Untangling emergent cortical dynamics: neurons from networks, noise from chaos

Thèse N° 9616

Présentée le 28 août 2019

à la Faculté des sciences de la vie
Programme doctoral en neurosciences

pour l'obtention du grade de Docteur ès Sciences

par

Max Christian NOLTE

Acceptée sur proposition du jury

Prof. J. Gräff, président du jury
Prof. H. Markram, Dr. E. B. Muller, directeurs de thèse
Prof. A. Destexhe, rapporteur
Prof. M. London, rapporteur
Prof. C. Petersen, rapporteur

2019

ÉCOLE POLYTECHNIQUE
FÉDÉRALE DE LAUSANNE

Truth springs from argument amongst friends.
— David Hume

In recognition of the rodents whose brains provided the neurobiological foundation for this simulation-based study.

Acknowledgements

Firstly, I would like to thank my supervisors, Henry Markram and Eilif Muller. Thank you for giving me the opportunity to pursue an exciting research topic in such a stimulating and supportive environment as the Blue Brain Project. Secondly, I would like to thank Michael Reimann, my closest collaborator and third supervisor. Your input has shaped this thesis in many ways. Thirdly, I would like to thank my guides through the world of algebraic topology, Kathryn Hess and Ran Levi.

I would like to thank the examiners of this thesis, Alain Destexhe, Mickey London, and Carl Petersen, for their careful reading of the thesis and valuable discussions, as well as the president of the jury, Johannes Gräff, for a well-organized oral exam.

I would like to thank Taylor Newton and Giuseppe Chindemi for your support in writing this thesis and the countless scientific and non-scientific discussions over the last few years.

This thesis builds on the work of many people and I would like to thank everyone at the Blue Brain Project that has supported me over the years, directly or indirectly, especially Werner Van Geit, Srikanth Ramaswamy, James (Jim) King, Christian Rössert, Richard Walker, Cyrille Favreau, Nicolas Antille, Dace Picot-Stiebrina, Alina Busuioc Jiménez, Cristina Colangelo, Natali Barros-Zulaica, Armando Romani, Lida Kanari, Eleftherios Zisis, András Ecker, Georgios Iatropoulos, Vishal Sood, Hugo Dictus, Sirio Bolaños Puchet, Marwan Abdellah, Akiko Sato, Francesco Cremonesi, Bruno Magalhães, Pramod Kumbhar, Dan Keller, Jay Coggan, Karin Holm, Rodrigo Perin, Ayah Khubieh, Jane Yi, Marc-Oliver Gewaltig, Felix Schürmann, and many more. Special thanks goes out to the HPC infrastructure team: I might only talk to you when things break, but I know that having an in-house supercomputer is a real privilege.

I would like to thank everyone at the Hebrew University of Jerusalem: Idan Segev, thanks for inviting me. Oren Amsalem, Eyal Gal, Michael Doron, thanks for great discussions. I would also like to thank everyone in the Laboratory for Topology and Neuroscience at EPFL, especially Martina Scolamiero, Katherine Turner, Gard Spreeman, Stefania Ebli, Daniela Egas Santander, Nicolas Ninin, and also Paweł Dłotko at Swansea University. Thanks to my official EPFL mentor, Wulfram Gerstner, for helpful discussions and giving me the opportunity to present at your lab meeting. Thanks to Alexandre Pouget for inviting me to present my work, and to his students, especially Michael Schartner, for great discussions and many COSYNE dinners. I would like to thank everyone I met at the Summer Workshop on the Dynamic Brain 2016, which greatly influenced my thesis, especially Team Cobra—Madineh Sedigh-Sarvestani & Phil Mardoum. I would further like to thank Michael Buice, Saskia de Vris, Anton Arkhipov, Adrienne Fairhall, and Christof Koch. Thanks also to Adrienne for introducing me to

computational neuroscience when at the University of Washington!
I would like to thank the Lunch Time Nomads and everyone that I kayaked, skied or hiked with over the years—thanks for keeping me sane. I would like to thank Tina Liebich for hosting me for almost my whole PhD, and tolerating all my kayaks in the garden. I would like to thank my family for enabling me to go abroad and study physics at the University of Edinburgh and University of Washington, which eventually led me to EPFL. My parents, Marietheres Nolte and Martin Nolte, and my siblings, Jens, Lukas and Henrike, thank you for supporting me. I would also like to thank my grandmother, Hildegard Lammert, and my late grandmother, Eva-Maria Nolte, for being proud of me and supporting me.
Last, but not least, I would like to thank my fiancée, Sacha Corby. Thank you for always being there for me, and for supporting my Swiss endeavor—without you this thesis would not exist.

M. N.

Abstract

The way in which cortical microcircuit components—most importantly *neurons*—and their connectivity—the *network*—shape and constrain emergent dynamics is a long-standing question in neuroscience. Experimentally observed dynamical properties can often be explained by circuit models with different simplifying assumptions for the underlying neuron models and their network structure, such as deterministic synapse models describing stochastic synapses, or a uniform network structure describing heterogeneous synaptic connectivity. Intrinsic neural variability, for example, can emerge from both stochastic synaptic properties (*noise*) and deterministic network dynamics (*chaos*). It is therefore often not clear if models with ad hoc simplifying assumptions for various biological details provide correct explanations for the emergence of cortical dynamics. In this thesis, we set out to advance our understanding of how detailed biological properties of cortical neurons and their network structure shape emergent dynamics by studying a model of a prototypical neocortical microcircuit that was reconstructed using all relevant available biological data. To make our predictions as biologically accurate as possible, we used a "zero tweak" strategy wherein parameters in the model were not adjusted to replicate specific experimentally observed dynamical properties, but instead were constrained by biological data. This allowed us to characterize the effect of two biological properties that are often abstracted away in ad hoc simplifications: stochastic synaptic transmission and a heterogeneous network structure with complex higher-order connectivity. Studying the model, we made several important predictions: (1) Stochastic synaptic transmission, in an interplay with recurrent network dynamics, causes rapid chaotic divergence of spontaneous activity. (2) Synaptic noise overshadows other local cellular noise sources. (3) Amid the noise and chaos, neurons can reliably respond to external inputs with millisecond spike-time precision. (4) This reliable response goes beyond mere feedforward suppression of recurrent dynamics and is driven by the circuit at a near-critical excitation-inhibition balance. (5) An abundance of high-dimensional cliques of all-to-all connected neurons which shape correlations between neurons in a hierarchical manner. (6) This effect is strongly reduced when synaptic connectivity is replaced by a rejected null model with reduced higher-order network structure. We conclude that a detailed representation of cellular noise sources and high-dimensional network structure is imperative to accurately model emergent cortical network dynamics. Models that make ad hoc simplifying assumptions need to carefully justify the exclusion of such details.

Keywords: neocortex, microcircuit, network dynamics, synaptic noise, chaos, variability, topology, model, simulation

Zusammenfassung

Wie die Komponenten von Mikroschaltkreisen im Cortex – vor allem *Nervenzellen* – und ihre Verbindungen – das *Netzwerk* – emergente Dynamik formen und einschränken, ist eine lang bestehende Frage der Neurowissenschaften. Viele theoretische und computergestützte Studien haben gezeigt, dass Schaltkreismodelle mit unterschiedlichen vereinfachenden Annahmen für Neuronenmodelle und Netzwerkstruktur oft so angepasst werden können, dass sie dieselbe experimentell beobachtete Dynamik erklären können. Intrinsische neuronale Variabilität kann zum Beispiel durch synaptisches *Rauschen* (englisch: *Noise*) und deterministisches Netzwerk*chaos* entstehen. Diese Studien können zwar potenzielle Mechanismen und neue Hypothesen aufzeigen, die in Experimenten getestet werden können, aber es ist oft nicht klar, ob die verwendeten Modelle auch korrekte biologische Erklärungen für die beobachtete Dynamik liefern. Das Ziel dieser Doktorarbeit war es ein besseres Verständnis dafür zu entwickeln, wie detaillierte biologische Eigenschaften der Nervenzellen des Cortex und ihre Netzwerkstruktur die entstehende Dynamik des Cortex formen und beschränken. Dazu untersuchten wir ein biologisch motiviertes Modell eines prototypischen Mikroschaltkreises des Neocortex mit einer "*Zero Tweak*"-Strategie: Der Mikroschaltkreis, der mit allen relevanten verfügbaren biologischen Daten rekonstruiert wurde, wurde nicht angepasst, um eine spezifische experimentell beobachtete Netzwerkdynamik zu simulieren. Bei der Untersuchung des Mikroschaltkreises konnten wir einige wichtige Vorhersagen treffen: (1) Die stochastische synaptische Übertragung verursacht im Zusammenspiel mit der rekurrenten Netzwerkdynamik eine schnelle chaotische Abweichung der spontanen Aktivität. (2) Wir sagen quantitativ vorher, dass das synaptische Rauschen andere lokale zelluläre Rauschquellen überschattet. (3) Wir beobachteten, dass Neuronen inmitten vom Rauschen und Chaos zuverlässig und mit einer Millisekunden-Zeitgenauigkeit auf externe Signale reagieren können. (4) Diese zuverlässige Reaktion geht über die bloße Unterdrückung der rekurrenten Dynamik hinaus und ist bei einem nahezu kritischen Gleichgewicht zwischen Erregung und Hemmung am stärksten. (5) Als wir tiefer in die Netzwerkstruktur eintauchten, fanden wir einen Überfluss an hochdimensionalen Cliquen aus miteinander verknüpften Nervenzellen, die hierarchische Korrelationen zwischen Nervenzellen formen. (6) In einem abgelehnten Nullmodell der synaptischen Verbindungen mit reduzierter Netzwerkstruktur höherer Ordnung war dieser Effekt stark reduziert. Wir schließen daraus, dass das detaillierte Modellieren zellulärer Rauschquellen und hochdimensionaler Netzwerkstruktur unerlässlich ist, um emergente Netzwerkdynamik zu simulieren. Vereinfachte Modelle mit Ad-hoc-Annahmen müssen die Auswirkungen der Nichtberücksichtigung dieser Details sorgfältig abwägen.

Contents

List of Figures

List of Tables

1 Introduction

1.1 Motivation

The neocortex is the newest addition to the mammalian brain (Rakic, 2009) and is involved in many higher-order brain functions, including decision-making (Walton et al., 2002).[1] Understanding the structure and function of the neocortex has been a goal of neuroscience for more than a century (Ramón y Cajal, 1911). The neocortex has a typical structure made up of six layers, which is roughly conserved across cortical areas and mammalian species, albeit with varying layer thicknesses across areas, varying total thickness, and drastically different surface areas (Douglas and Martin, 2004; Rakic, 2009; Rockel et al., 1980). Many studies have investigated the structure and function of neocortical circuitry in various mammalian species, yet there is still no integrated view of how this structure leads to the emergence of observed dynamics. In this thesis, we aim to shed light on the relationship between the structure and emergent dynamics of the cortex by studying a model of a prototypical neocortical microcircuit in the primary somatosensory cortex of the two-week old Wistar rat (*Rattus norvegicus domestica*). As the neocortex is the largest part of the cerebral cortex, and since many properties of one neocortical area have been shown to generalize to other areas and species (Douglas and Martin, 2004), we will often use the word "cortical" or "cortex" when in fact we mean the primary somatosensory cortex of the two-week old Wistar rat.

1.1.1 What is the nature of the cortical neural code?

Most cortical neurons send signals to other neurons in the form of action potentials, also called *spikes*. The nature of the neural code—i.e. how spikes encode information—appears to vary between brain regions. Broadly speaking, there are two classes of hypothesis regarding the implementation of this code (Shadlen and Newsome, 1994): The first is the idea that the exact

[1] While the cortex might indeed be important for many higher-order brain functions, it is interesting and humbling to note that rats can still sense with putatively relevant parts of the sensory cortex surgically removed (Hong et al., 2018), and male rats are able to copulate (and live) with the whole cortex removed (Whishaw and Kolb, 1985).

spike times and patterns of interspike intervals (ISIs), be it of a single neuron or a population, encode information—often referred to as *spike-time coding*. The other is that neurons are too noisy for exact spike times to reliably encode signals, and that only the firing rate encodes information, albeit with millisecond precision at the level of populations (Tchumatchenko et al., 2011)—often referred to as *spike-rate coding*. Spike-rate and spike-time coding are not as dichotomous as they seem, and they have been shown to coexist, for example for visual information encoded in the cat thalamus (Reinagel and Reid, 2000), and for tactile information recorded from human fingertip afferents (Johansson and Birznieks, 2004). In any case, the "neural code" is perhaps better seen as a metaphor that is not to be taken too literally, as some argue that the distributed and causal structure of the brain cannot be appropriately described in terms of "coding" (Brette, 2019). However, what we would certainly like to understand, is to what extent the occurrence of a particular spike in a cortical neuron matters. What is signal and what is noise?

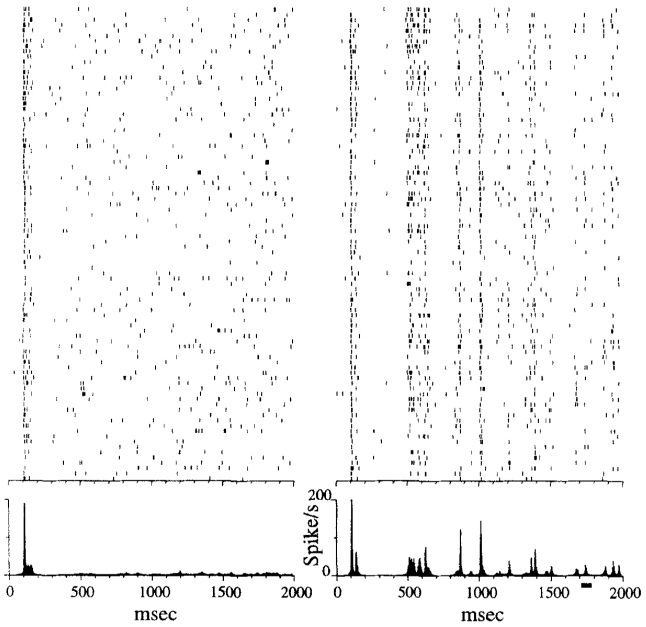

Figure 1.1 – Cortical variability: signal or noise? (Left) Spike trains of a neuron in the visual cortex of a behaving macaque monkey in response to randomly seeded dynamic dot visual stimuli, presented for two seconds each. (Right) Spike trains in response to a dynamic dot stimulus with a repeated seed. *Figure 1 of "Temporal Precision of Spike Trains in Extrastriate Cortex of the Behaving Macaque Monkey" by Wyeth Bair and Christof Koch in Neural Computation Volume 8, Issue 6, August 15, 1996, p.1185-1202, reprinted courtesy of The MIT Press* (Bair and Koch, 1996).

In the early stages of different sensory systems, very small numbers of spikes in single neurons carry significant information (Rieke et al., 1997). For example, neurons in the rat ventral posteromedial nucleus of the thalamus (VPM) are highly selective to certain whisker deflection features and respond with high temporal precision (Petersen et al., 2008), whereas neurons in

the somatosensory cortex that are innervated by the VPM and respond to the same deflection features are less reliable and need to be combined into populations to retrieve the same amount of information as one typical VPM neuron (Bale and Petersen, 2009). More generally in the cortex, high variability of neural activity in response to repeated stimuli is widely observed, including both a variable number of spikes and highly irregular interspike intervals (Dean, 1981; Tolhurst et al., 1983; Softky and Koch, 1992; Britten et al., 1993; Shadlen and Newsome, 1994; Stevens and Zador, 1998). Moreover, spike counts are often Poisson-like, or even more variable, with Fano Factors (variance of spike counts divided by mean spike count) ≥ 1 (Shadlen and Newsome, 1998; Softky and Koch, 1993; Kohn and Smith, 2005; Churchland et al., 2010; Nogueira et al., 2018). These results have led many people to conclude that the cortex cannot rely on individual spike times and must employ a spike-rate code. Moreover, it has been argued that computation itself might be inherently variable due to deterministic approximations (Beck et al., 2012), making precise spikes superfluous.

1.1.2 How does cortical neural variability emerge?

However, there are many examples of experiments from different cortical areas demonstrating precise and reliable spike times in response to stimulation (Petersen et al., 2001; Kayser et al., 2010; Hires et al., 2015). Bair and Koch (1996) showed that recordings that were thought to be highly variable (Newsome et al., 1989; Britten et al., 1992) were actually temporally precise when all "noise" was kept fixed in the stimulus. Figure 1.1 shows the response of a neuron to a dynamic visual stimulus with noise (left), and with frozen noise that is identical across trials (right) in the macaque visual cortex, re-analyzed by Bair and Koch (1996). In line with this observation, Kara et al. (2000) reported clearly sub-Poisson variability of neurons in the visual cortex. Yet, variability of cortical responses seems widespread. One explanation for the low variability could simply be that the recorded cortical cells receive feedforward input from the thalamus, and that these neurons are thus less variable than those receiving only cortical input (Movshon, 2000).

To further constrain the nature of the cortical neural code, we need to understand how the observed variability emerges and untangle to what extent it is "noise" that carries no signal, and to what extent it conveys signals that only *appear* variable to the observer (Renart and Machens, 2014). There are many potential sources of the observed variability (Fairhall, 2019) (summarized in Figure 1.2A). Two potential sources, namely intrinsic within-network dynamics—which theoretical models predict to be chaotic (van Vreeswijk and Sompolinsky, 1996, 1998; London et al., 2010)—and unobserved noisy inputs from other brain areas and the environment, imply that variability is at least partially true noise. There are, however, lines of evidence supporting the notion that most cortical variability only appears variable due to unobserved targeted inputs (Masquelier, 2013). Churchland et al. (2010) showed that at stimulus onset, spike count variability in many cortical areas decreases. Further, a large amount of variability can be explained by animal movement in addition to visual stimulation (Niell and Stryker, 2010), and all of the cortex is strongly modulated by global movement-related

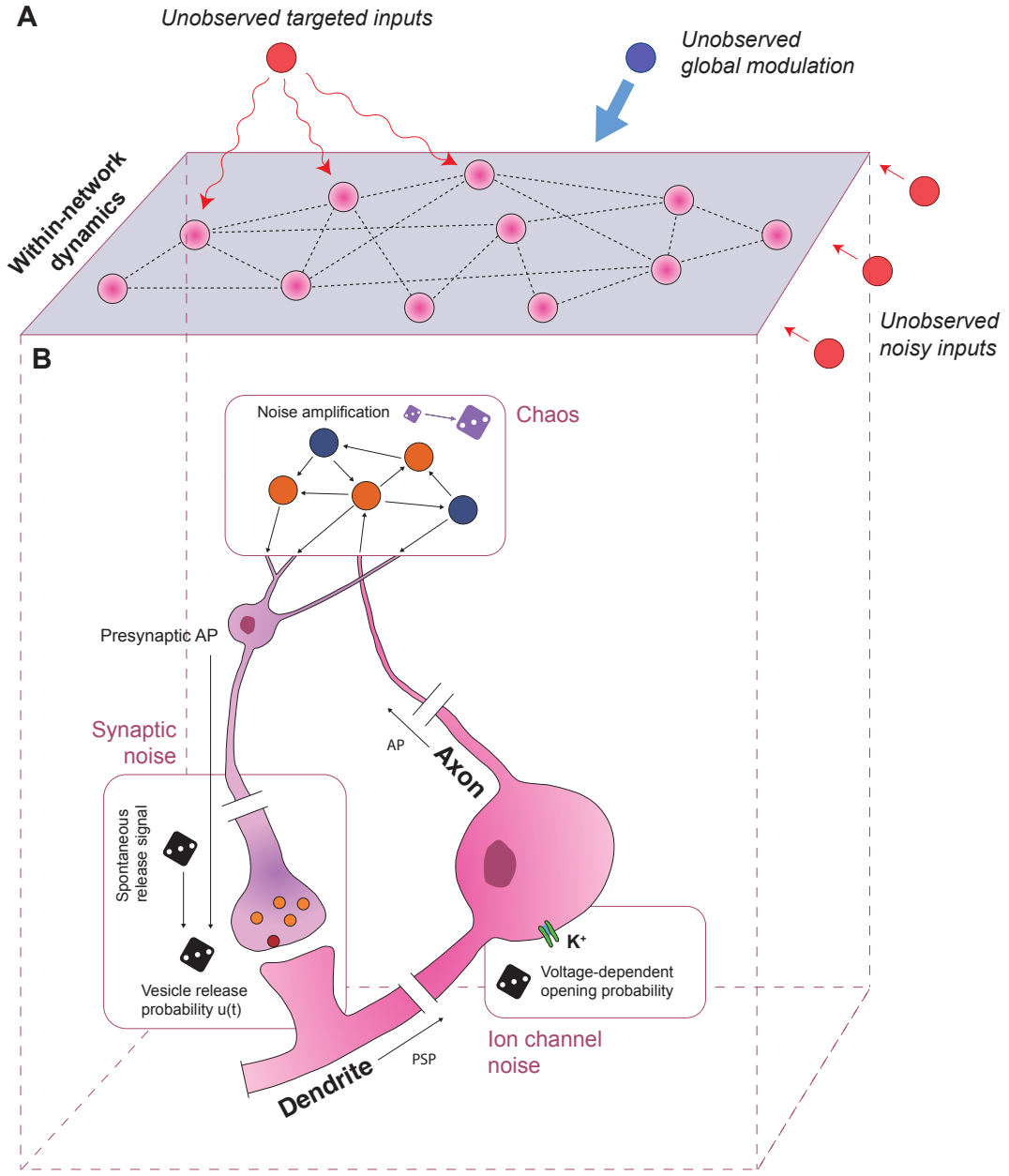

Figure 1.2 – Potential sources of cortical variability. (**A**) Potential sources of cortical variability can be divided into external inputs (including from other brain regions) and into intrinsic, within-network dynamics (Renart and Machens, 2014; Fairhall, 2019). *Redrawn from Fairhall (2019).* (**B**) Illustration of potential sources of variability of within-network dynamics: chaotic activity arising from a balance of excitation and inhibition (*chaos*) (van Vreeswijk and Sompolinsky, 1996, 1998; London et al., 2010), stochastic opening of voltage-dependent ion channels (*ion channel noise*) (Faisal et al., 2008), and stochastic synaptic neurotransmitter release (*synaptic noise*) (Allen and Stevens, 1994). Note that synaptic noise includes both *spontaneous* vesicle fusion and neurotransmitter release, and *failure* of vesicle fusion and neurotransmitter release upon action potential arrival.

activity (Musall et al., 2018). Finally, there is recent evidence that suggests that *most* variability is not noise, but true signal: Simultaneous recordings from ~10'000 neurons across the mouse brain show that most variability encodes behavioral information (Stringer et al., 2019). This study implies that variability, which was interpreted to be noise when recording from a single or a handful of neurons, is actually driven by brain-wide activity. It is thus likely that most observed cortical variability arises from unobserved targeted inputs and global modulation (Figure 1.2A).

1.1.3 Predicting emergent cortical network dynamics requires detailed modeling

But does this mean that each spike is reliable and encodes a signal, as some have argued (Masquelier, 2013)? The studies above look at average spiking over relatively large timescales (~1 second). To truly understand intrinsic cortical variability and the precision of spiking at the millisecond timescale, we would need to monitor *all* inputs to a neuron or local population of neurons, as cortical neurons respond with remarkable precision to small changes in membrane potential (Mainen and Sejnowski, 1995). This—at least for the moment—is not possible in vivo. An alternative, bottom-up approach is to study how the properties of single cortical neurons and local networks constrain spike-time variability and reliability (Figure 1.2B). Isolated cortical neurons in vitro are extremely reliable when they are injected with current (Mainen and Sejnowski, 1995). By contrast, under in vivo conditions, neurons receive synaptic inputs, which are subject to a considerable noise source: stochastic synaptic neurotransmitter release (*synaptic noise*)[2] (see Figure 1.2B). When a presynaptic spike arrives at a synapse, it triggers an influx of Ca^{2+}, which allows docked vesicles to fuse with the membrane and release neurotransmitter (Sudhof, 2004). This release mechanism is highly stochastic: quite often, presynaptic spikes fail to cause neurotransmitter release (Katz and Miledi, 1969; Allen and Stevens, 1994), and vesicles can also spontaneously fuse and release neurotransmitter (Katz and Miledi, 1969; Faisal et al., 2008).

To go beyond a single neuron and understand how the dynamics of local populations of neurons constrain variability, we can use models of neural networks, which have long been utilized to understand and predict in vivo cortical dynamics (Vogels et al., 2005). Many studies of network dynamics of balanced populations of excitatory and inhibitory neurons suggest that cortical network dynamics are chaotic (van Vreeswijk and Sompolinsky, 1996, 1998; London et al., 2010), meaning that any intrinsic noise such as synaptic noise would likely be amplified and lead to highly variable network activity. Nonetheless, deterministic networks with chaotic network dynamics can still be reliable (Rajan et al., 2010; Lajoie et al., 2013) and information can even be encoded by spike times (Lajoie et al., 2016). However, it has also been shown that synaptic noise in a recurrent cortical network can lead to Poisson-like spiking variability

[2] The term "synaptic noise" is sometimes used to describe the total "background noise" of a neuron, that is the membrane voltage fluctuations arising from a combination of "noisy" presynaptic inputs and stochastic synaptic release (Calvin and Stevens, 1968; Fellous et al., 2003; Destexhe et al., 2003). However, in this thesis, "synaptic noise" always refers to "stochastic synaptic release" alone, making no assumptions on the structure of presynaptic input (Faisal et al., 2008).

(Moreno-Bote, 2014). Yet, some models suggest that very few synchronous synaptic inputs can overcome synaptic noise and induce reliable spikes (Wang et al., 2010).[3]

The examples above illustrate that network models with varying degrees of biological detail can exhibit similar dynamics through different mechanisms. Another study showed that asynchronous network dynamics in simplified models can break down when accounting for heterogeneous connectivity data, but can be recovered by including spike-frequency adaptation mechanisms (Landau et al., 2016). Many of the classic balanced network models connect neurons completely at random and with spatially uniform probability distributions. However, it is known that distance-dependent connectivity can change emergent variability (Rosenbaum et al., 2017). Furthermore, intrinsic shared variability can arise when time scales of excitatory and inhibitory synapses are constrained using biological data (Huang et al., 2019). Yet, none of these models consider intrinsic noise sources such as synaptic noise, which has been shown to have a potentially large impact on emergent variability (Moreno-Bote, 2014). How additional biological details of cortical circuits, such as differences across layers, different cell types beyond excitatory and inhibitory populations, or higher-order connectivity motifs (Song et al., 2005; Perin et al., 2011) may impact variability and emergent dynamics more generally, is unknown.

Taken together, these studies demonstrate that neurobiological details matter, and that ad hoc simplifying assumptions that leave out details without knowledge of their impact could fundamentally alter emergent network dynamics. This, in turn, can lead to misguided predictions and incorrect explanations of observed phenomena. This is not to say that the use of simplified models is wrong in any context, or that more detail is always better. Simplified models have many advantages—they are easier to construct and more amenable to theoretical analysis. However, for interpreting how well these models capture neurobiological mechanisms, any simplification should ideally be informed and carefully justified.

In this thesis, we propose to study and untangle emergent cortical network dynamics using a model that takes relevant available biological data into account and provides an integrative view of neocortical microcircuitry (Markram et al., 2015). The goal is to make predictions about which details of cortical circuitry matter, thus providing a guide for informed simplifications and bridging levels of understanding.

[3] This result is likely due to an overestimated synaptic release probability, not adjusted from in vitro to in vivo conditions, as we will explain in Chapter 2.

1.2 Outline of the thesis

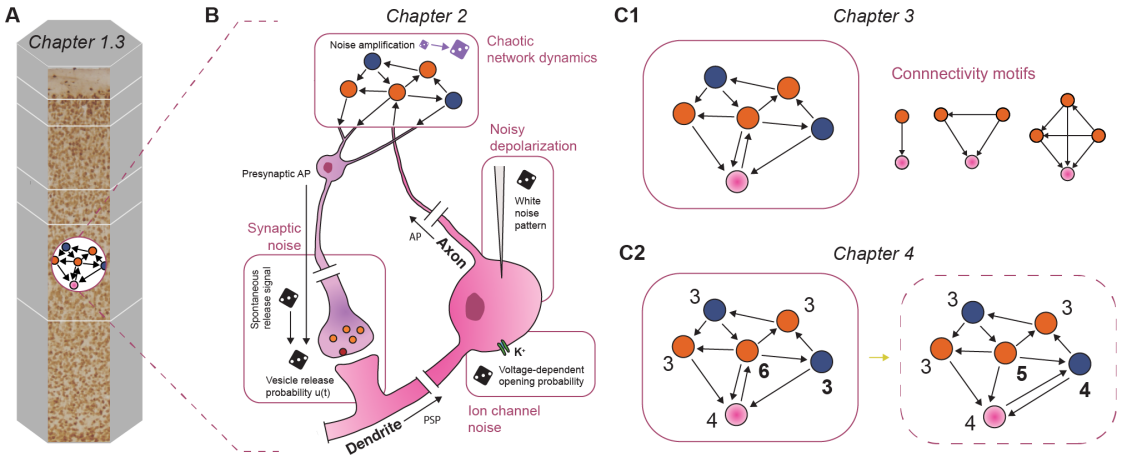

Figure 1.3 – Outline of the thesis. (**A**) Overview of the detailed neocortical microcircuit model studied in this thesis—the *NMC-model* (Chapter 1.3). (**B**) How do local network dynamics and cellular noise sources constrain spike variability and reliability (Chapter 2)? (**C1**) What is the role of the network topology in emergent dynamics (Chapter 3)? (**C2**) How do emergent dynamics change with a reduction in high dimensional topological network structure (Chapter 4)?

In Chapter 1.3 ("A detailed neocortical microcircuit model"), we give a brief introduction to the Blue Brain Project's neocortical microcircuit model (*NMC-model*), which provided the foundation for the research in this thesis (Figure 1.3A). In Chapter 1.3.2, we demonstrate why it is an adequate model to use for making predictions about in vivo neuronal activity. All of Chapter 1.3 is based on the publication "*Reconstruction and simulation of neocortical microcircuitry*" (Markram et al., 2015), and parts of Chapter 1.3.2 are original research as part of this thesis (see contributions at start of Chapter 1.3).

Chapter 2 ("Reliability amid noise and chaos") forms the backbone of this thesis, and answers questions about how neuronal variability and reliability emerge in the NMC-model (Figure 1.3B). The chapter is a revised and extended version of the preprint "*Cortical reliability amid noise and chaos*" (Nolte et al., 2018).

In Chapter 3 ("Cliques of neurons bound into cavities") and Chapter 4 ("Impact of higher-order network structure") we dive deeper into the structural connectivity of the NMC-model, and learn how components of the network topology of the NMC-model shape emergent dynamics (Figure 1.3C1-2). Chapter 3 is a postprint of a publication that arose from a collaboration with algebraic topologists called "*Cliques of neurons bound into cavities provide a missing link between structure and function*" (Reimann et al., 2017b). In Chapter 4, we extend on the findings from Chapter 3 by simulating a circuit model that has a substantial part of these elements of network topology removed. Chapter 4 will be submitted for publication as "*Impact of higher-order network structure on emergent cortical activity*".

Finally, in Chapter 5, we summarize the main contributions of this thesis and point to future directions.

1.3 A detailed neocortical microcircuit model

The following is a description of the detailed neocortical microcircuit model (*NMC-model*) studied in this thesis. First, we briefly summarize how the NMC-model was reconstructed from biological data and then used to simulate neuronal activity (Chapter 1.3.1). We then describe how the NMC-model reproduces findings of spontaneous and evoked activity in vivo (Chapter 1.3.2). Note that this chapter only provides a brief summary of the publication "*Reconstruction and simulation of neocortical microcircuitry*" in which the NMC-model is described in full detail (Markram et al. (2015); http://dx.doi.org/10.1016/j.cell.2015.09.029). Note that Chapter 2.4.1 provides a summary of additional details such as the synapse model.

Contribution: I analyzed simulations run by Eilif B. Muller and generated Figures 1.8A1–3. I contributed to the analysis and generation of Figures 1.9C–F together with Eilif B. Muller and Giuseppe Chindemi. I contributed to the captions and text describing the results shown in these two figures. I generated Figure 1.6 (not part of original publication).

1.3.1 Reconstruction and simulation of a neocortical microcircuit

Reconstruction

The NMC-model is a biologically detailed model of a prototypical microcircuit of the somatosensory cortex of the two-week old rat. One microcircuit contains 31'346 neurons that were reconstructed with detailed anatomy and physiology from sparse data. Detailed neuronal morphologies were reconstructed in vitro, and then repaired and cloned to replicate the morphological diversity of neurons in the neocortex (Figure 1.4A). Neuronal morphologies were then placed into a volume approximately defined to cover dendritic trees of neurons in the center of the volume, according to experimentally constrained densities and frequencies of individual morphological types (*m-types*) in each of the six layers (Figure 1.4B). Figure 1.5 is a detailed illustration of a subset of the 31'346 morphologies placed in the microcircuit volume, colored according to their layer (defined by soma location).

Synaptic connectivity between neurons was predicted algorithmically (Figure 1.4C), by considering all appositions of axons and dendrites in the microcircuit as potential synapse locations and then pruning connections according to biological constraints such as the number of synapses per connection and bouton densities (Reimann et al., 2015). The resulting connectome for a microcircuit of 31'346 neurons contains around ~8 million connections comprising ~36 million synapses. The connectome is a null-model with many predictions and interpolations, but emergent properties, such as synapse densities and interbouton intervals, were validated extensively against available biological data (Reimann et al., 2015).

Electrical models were generated by fitting ion-channel distributions to reproduce the behavior of distinct electrical neuron types (*e-types*) to somatic current injection protocols in vitro, using a genetic optimization algorithm (Van Geit et al., 2016). E-types were assigned to

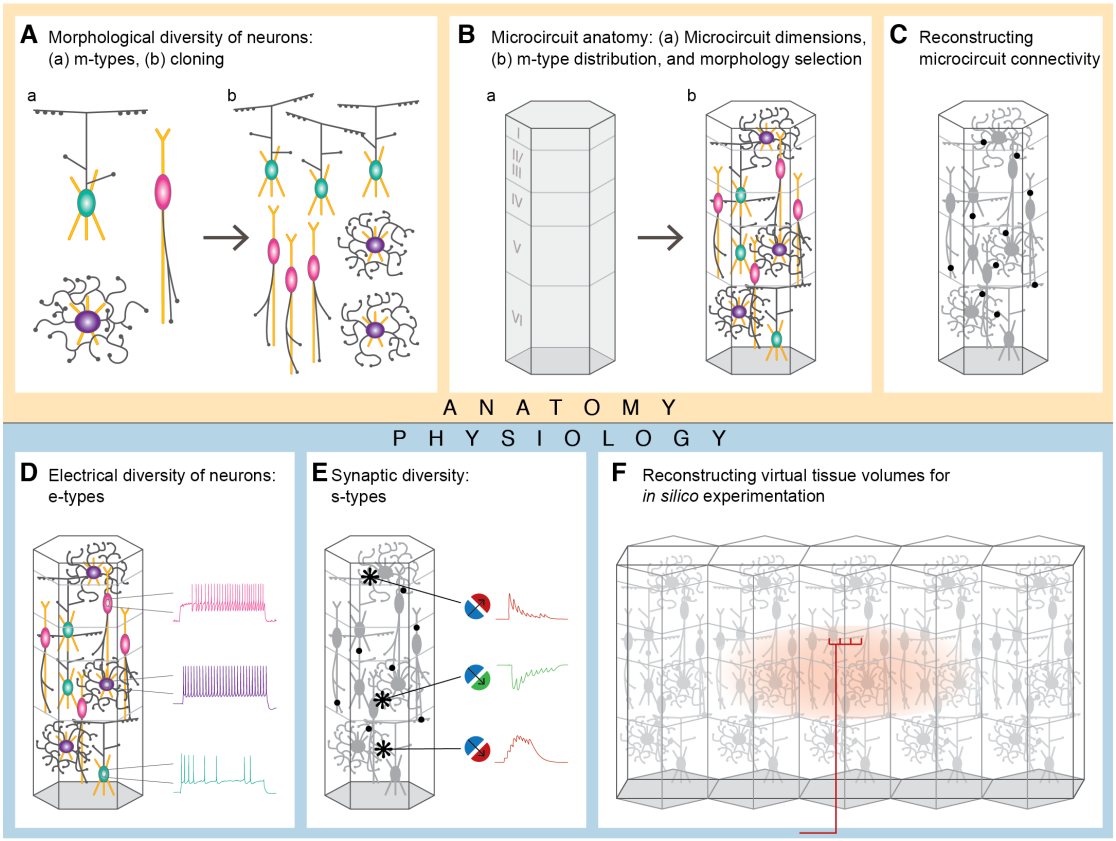

Figure 1.4 – Workflow for data-driven reconstruction of neocortical microcircuitry. (**A**) Morphological diversity of neurons. (a) Identify the morphological diversity in the neocortical microcircuit (m-types). (b) Repair and then clone the various m-types with statistical variations to enrich the number of exemplars. (**B**) Microcircuit anatomy. (a) Define the spatial dimensions of a unitary microcircuit. (b) Assemble individual neurons in 3D space according to the frequency of occurrence of each m-type per layer, selecting the appropriate m-type instance that satisfies laminar constraints on the axonal and dendritic distribution. (**C**) Reconstructing microcircuit connectivity. Derive the number and location of synaptic contacts formed between all neurons in the microcircuit, based on a series of synaptic connectivity rules. (**D**) Electrical diversity of neurons. Map and model the electrical types (e-types) of each m-type to account for the observed diversity of morpho-electrical subtypes (me-types). (**E**) Synaptic diversity of neurons. Map and model the diversity of synaptic types (s-types) observed between pre-post combinations of me-types, according to rules derived from synaptic physiology. (**F**) Reconstructing virtual tissue volumes. Apply the above strategy to reconstruct defined circuit volumes (microcircuits, slices, mesocircuits) for in silico experiments; insert synapses formed by thalamocortical fibers for stimulation experiments. *Figure 1 and corresponding caption from Markram et al. (2015), reprinted courtesy of Cell Press.*

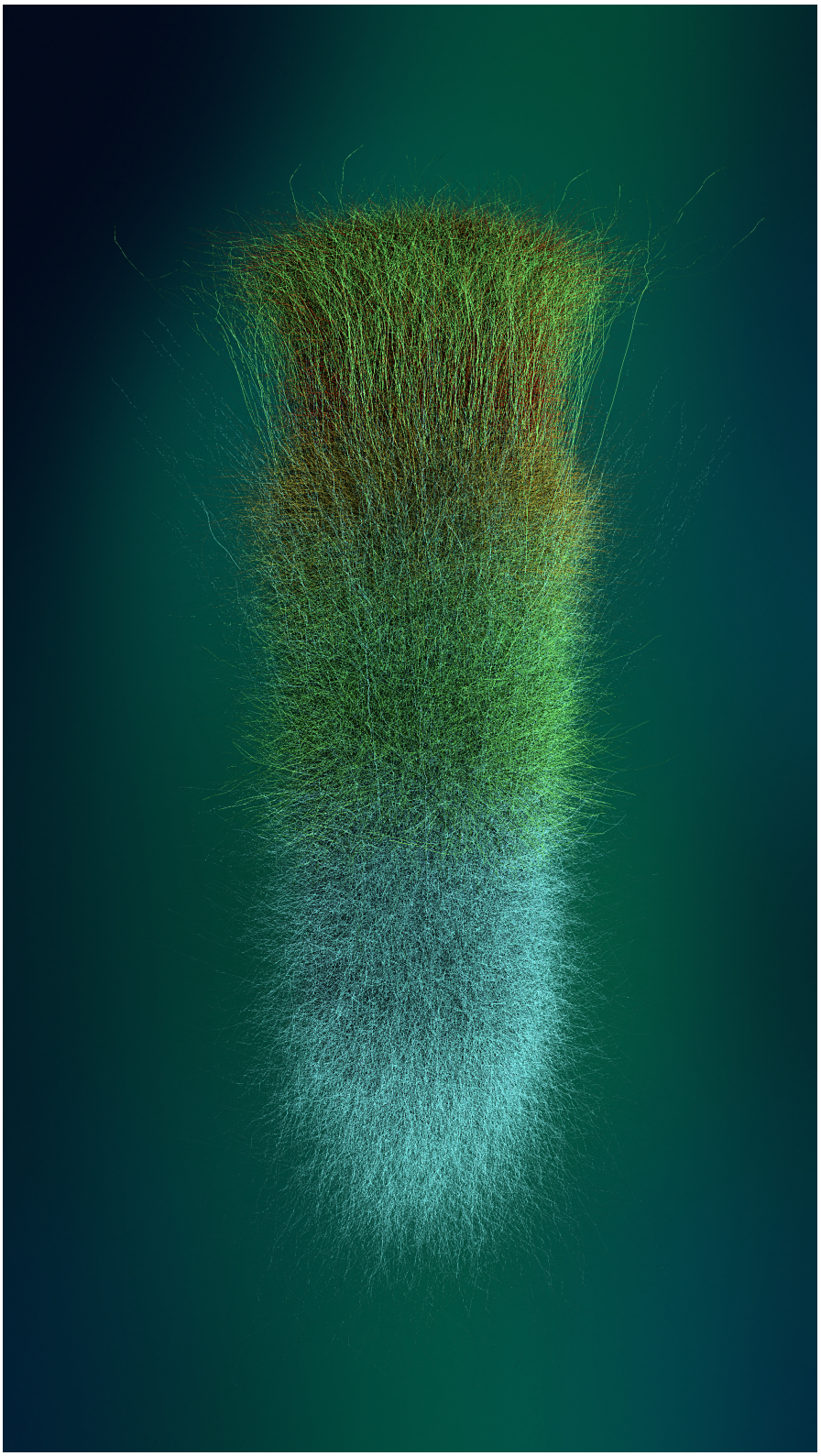

Figure 1.5 – Detailed visualization of a randomly selected subset of neurons in the NMC-model, colored according to cortical layer, from layer 1 at the top to layer 6 at the bottom. *Visualization: Cyrille Favreau & Blue Brain Scientific Visualization team.*

neurons according to their distributions in vitro (Figure 1.4D). 1'137 out of 31'346 neurons exhibit irregular firing behavior and use stochastic potassium channels models.

Synaptic transmission is modeled using the stochastic Tsodyks-Markram synapse model, which takes into account short-term plasticity including facilitation and depression, as well as the stochastic release of vesicles. Model parameters were constrained to capture the diversity of synapse types (*s-types*) observed in vitro (Figure 1.4E), resulting in six s-types. For a brief overview of the synapse model, see Chapter 2.4.1.

To evoke activity on top of intrinsic circuit dynamics, thalamic synapses from fibers coming from the ventral posteromedial nucleus (VPM) were added to the NMC-model. Each connection between a thalamic fiber and a cortical neuron contains several synapses, with experimentally constrained densities across layers, resulting in relatively more synapses near the borders between layers 2/3 and 4, and layers 5 and 6, respectively (Meyer et al., 2010).

Simulation of neuronal activity

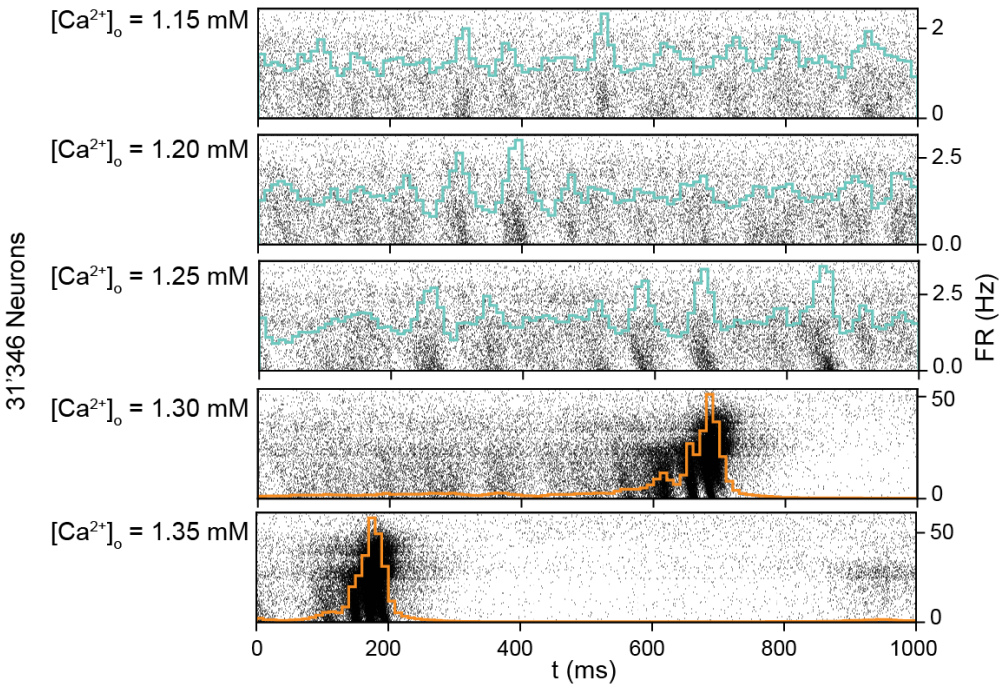

Figure 1.6 – Transition of neuronal activity. Spontaneous activity of all 31'346 neurons in the microcircuit at increasing $[Ca^{2+}]_o$ (100% depolarization). The line indicates the population firing rate.

The microcircuit has a unified set of network parameters constrained by the reconstruction process. However, there were two unknown parameters required for simulating neuronal network activity: Due to a difference in the chemical composition of the extracellular fluid between in vitro and in vivo conditions, and also due to missing long-range inputs (approx-

imately 80% of excitatory synapses come from long-range presynaptic neurons), neurons need to be injected with a tonic somatic depolarizing current to be active. We expressed this current as the percentage of the current required to drive a cell to threshold and make it spike (rheobase). Another unknown which is different to in vitro conditions is the precise extracellular Ca^{2+} concentration. $[Ca^{2+}]_o$ differentially modulates the release probability of inhibitory and excitatory synapses (Rozov et al., 2001), and consequently their effective strength. At $[Ca^{2+}]_o$ = 2.00 mM, the typical in vitro level of $[Ca^{2+}]_o$, excitation is so strong compared to inhibition that network dynamics are regenerative, with bursts of synchronous, microcircuit-wide activity. When decreasing $[Ca^{2+}]_o$ to values that are closer to in vivo conditions, excitation loses strength relative to inhibition, and activity transitions from this synchronous state to more asynchronous activity (Figure 1.6). Notably, this transition was also observed in a slice when lowering $[Ca^{2+}]_o$ (Markram et al., 2015).

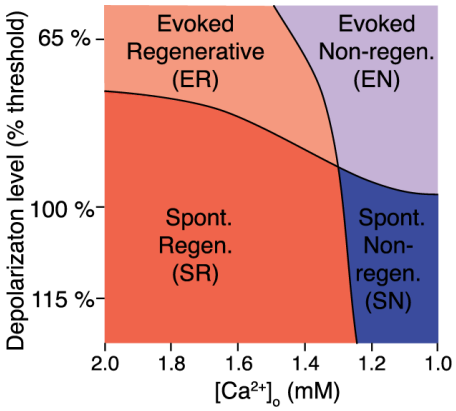

Figure 1.7 – The regime map. Characterization of spontaneous and evoked activity under different levels of depolarization and $[Ca^{2+}]_o$. *Figure 15D and corresponding caption from Markram et al. (2015), reprinted courtesy of Cell Press.*

Depending on the depolarization level, these bursts either form spontaneously (Figure 1.7, *spontaneous regenerative* regime) or need to be evoked with thalamic input (Figure 1.7, *evoked regenerative* regime). As $[Ca^{2+}]_o$ decreases, the dynamical regime suddenly and rapidly transitions from regenerative to non-regenerative activity. At a 100% depolarization level, this transition occurs between $[Ca^{2+}]_o$ = 1.30 to 1.275 mM.[4] As this change in dynamics is similar to a phase transition between two fundamentally different regimes in statistical physics, we define this point as a *critical* point. At $[Ca^{2+}]_o$ = 1.25 mM, activity is thus in near-critical regime, but still subcritical. It is *nearly* regenerative with synchronous bursts, but it is actually still asynchronous and non-regenerative. It is at this point that the NMC-model can reproduce an array of properties of spontaneous and evoked activity in vivo. We therefore refer to this point as the *in vivo-like state*, which we will further describe in Chapter 1.3.2 below.

[4] This value is specific to the NMC-model, and could change with any other mechanisms that differentially modulate the effective strength of excitatory and inhibitory synapses.

1.3.2 Reproducing in vivo-like cortical dynamics

The NMC-model was reconstructed from—and validated against—in vitro slice data. While it successfully reproduces a range of dynamic regimes including asynchronous activity, it was not clear if the NMC-model also provides a good model for making predictions about in vivo cortical activity. We therefore tested how well the microcircuit could reproduce properties of spontaneous and evoked activity in vivo. Importantly, no tweaking of parameters was performed—a "zero tweak" strategy. This is in contrast with many other models that often tune parameters to reproduce certain experimental findings—instead, the parameters of the NMC-model are constrained by biological data, and not tuned to match emergent function.

Spontaneous activity in vivo contains a rich structure of repeated spike patterns, including an overexpression of spike triplet patterns that cannot be explained by random spike correlations (Luczak et al., 2007). We found that the NMC-model exhibited these spike triplets, adding more weight to the hypothesis that they arise intrinsically from local circuit properties (Luczak et al., 2007). Notably, when moving from the near-critical state around $[Ca^{2+}]_o \approx 1.25$ mM to lower $[Ca^{2+}]_o$, the effect vanished, suggesting that the near-critical point close to the transition to synchronous, regenerative activity best describes in vivo-like activity in the NMC-model. Another feature of cortical spontaneous activity is a wide range of coupling to the local population, from soloist neurons, that are weakly correlated to the network population, to chorister neurons, that are highly correlated with the network population (Okun et al., 2015). This range of population coupling also only emerged at the near-critical point. At lower $[Ca^{2+}]_o$ (i.e. < 1.2), all neurons become weakly correlated, and at higher $[Ca^{2+}]_o$ (i.e. ≥ 1.3), all neurons fire in strongly correlated bursts of network activity. Finally, in the in vivo-like state at $[Ca^{2+}]_o = 1.25$ mM, asynchronous activity emerges due to anti-correlated inhibitory activity canceling out highly correlated excitatory activity (Figure 1.8B), as shown before in a theoretical analysis (Renart et al., 2010). This anti-correlation of inhibitory and excitatory inputs was previously observed in vivo (Okun and Lampl, 2008), another indication that the NMC-model captures many properties of in vivo cortical dynamics.

Neuronal responses to thalamic input

Experimental evidence suggests that cortical responses to thalamic inputs are largely driven by intrinsic cortical dynamics (MacLean et al., 2005). This implies that if the NMC-model can approximate in vivo cortical dynamics, it should also be able to reproduce some of the response structure to thalamic input. A recent study looked at the response of neurons in the (anesthetized) rat barrel cortex in response to a full whisker deflection (Reyes-Puerta et al., 2014). During such a whisker "flick", many VPM neurons are active, but the exact population response is unknown. We therefore gave the microcircuit a very simple thalamic stimulus consisting of a single pulse of activity in the central 60 VPM fibers. Interestingly, a wide array of cell-specific responses emerged in the microcircuit (Figure 1.8A). This included a diversity of responses in terms of peristimulus time histograms (PSTHs) (Figure 1.8A1), including ON cells that increased their firing, OFF cells that decreased their firing, and non-responding

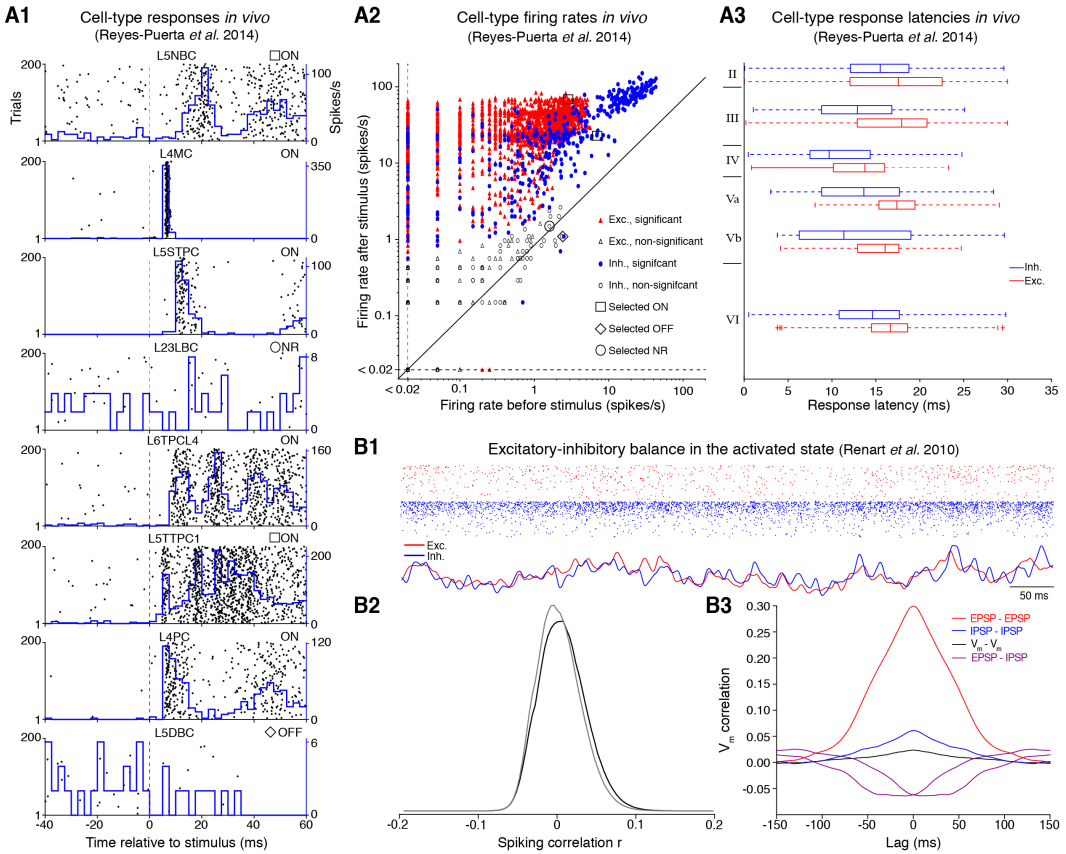

Figure 1.8 – Cell-type responses in vivo and E-I balance. (**A1**) Cellular response types to simulated single-whisker deflection. Each subplot represents the activity of an individual cell, containing the raster plot aligned to simulated whisker deflection and the PSTH. Upon simulated whisker deflection, neurons increased their firing rate (ON cells), showed no change in firing rate (NR cells), or decreased their firing rate (OFF cells). (**A2**) Comparison of mean firing rates before and after whisker deflection plotted in logarithmic scale (2630 excitatory and 550 inhibitory neurons). Empty symbols represent neurons showing no significantly different activity in both periods (NR cells), and filled symbols represent neurons showing significantly different ($p < 0.05$) activity (ON and OFF cells). (**A3**) Mean first-spike latencies of inhibitory (INH) and excitatory (EXC) neurons to simulated whisker deflection, defined by first spike occurrence within 30 ms after stimulation, mean over 200 trials, for all 31,346 neurons in the stimulated column. Each box plot represents median, interquartile, and range of latencies; crosses represent outliers (2.5 times interquartile range). (**B1**) Raster (top) of the spontaneous spiking activity of 500 excitatory (red) and inhibitory (blue) neurons under in-vivo-like conditions (100% depolarization and $[Ca^{2+}]_o$ = 1.25 mM). Bottom curves show tracking of instantaneous population-averaged activities (transformed to z-scores, bin size 3 ms). Average firing rates of E and I cells were 1.09 ± 1.0 Hz and 6.00 ± 8.95 Hz, respectively (n = 1,000; mean ± SD). (**B2**) Histogram of spike-spike correlations (black, count window 50 ms) and of jittered spike trains (gray, jitter ± 500 ms). (**B3**) Population-averaged cross-correlograms of the somatic membrane current, when cells are held at the reversal potential of inhibition (blue) or of excitation (red) in both cells, or at one potential for one cell and at the other potential for the other cell (magenta). The black curve is for pairs at resting potential. *Figure 17 and corresponding caption from Markram et al. (2015), reprinted courtesy of Cell Press.*

(NR) cells. The distribution of response types and trans-laminar response latencies were qualitatively similar to in vivo recordings by Reyes-Puerta et al. (2014) (Figure 1.8A2–3). These findings pose an important question: Renart et al. (2010) showed that a recurrent neural network can generate asynchronous activity even when there is shared excitatory input, by finely anti-correlated inhibitory input. A mechanism that we showed also contributes to the asynchronous activity in the NMC-model (Figure 1.8B). What, then, is the origin of the reliable responses we observe for thalamocortical stimulation? Chapter 2 addresses this question in detail.

Emergence of the in vivo-like state

The size of the NMC-model is not arbitrary, but was chosen to just encompass the full dendritic trees of neurons in the center of the microcircuit. However, is that size enough to make accurate predictions about integrated microcircuit dynamics? To test the relationship between the size of the circuit and its emergent dynamics, we compared activity in simulations with varying numbers of neurons in a *mesocircuit* made up of seven microcircuits (see Figure 2.2b1 for an illustration). Each microcircuit is split up into 310 *minicolumns*. However, by design of the reconstruction process, there is no boundary effect between either minicolumns or microcircuits. As the transition from non-regenerative, asynchronous dynamics to regenerative, synchronous dynamics for increasing $[Ca^{2+}]_o$ was fundamental for the observation of the in vivo-like properties described above, we compared how this transition changed for different circuit sizes (Figure 1.9A-B). With significantly fewer minicolumns (< 100) than the microcircuit (310), the point of transition from asynchronous to synchronous activity shifts towards higher $[Ca^{2+}]_o$. However in a circuit with 1000 minicolumns, more than three times the size of the NMC-model, the point of transition is shifted to only marginally lower $[Ca^{2+}]_o$, with no qualitative changes (Figure 1.9A-B). At the size of the NMC-model (310 minicolumns), the emergent transition from asynchronous to synchronous activity has thus become stabilized.

Another feature of in vivo neuronal activity is distance-dependence of correlations (Rosenbaum et al., 2017). We therefore analyzed how correlations between clustered groups of neurons at various spatial distances changed with circuit size (Figure 1.9C-F). We found a clear distance-dependence, with decreasing correlation of firing rates for increasing distances (Figure 1.9C). The overall correlation and its distance-dependence changed drastically from smaller (50 minicolumns) to larger circuit size (Figure 1.9C). While there is still a change when going from 300 to 400 and 1000 minicolumns, correlations, especially in the center of the microcircuit, are fairly stable at the size of the NMC-model (310 minicolumns) (Figure 1.9F). In summary, while the effect of circuitry beyond the size of the NMC-model clearly influences emergent dynamics, dynamics in the center of the microcircuit are less affected, and there are no qualitative changes.

We conclude that the NMC-model is suitable for making predictions about emergent cortical dynamics, as it was reconstructed from data, with no network parameter "tweaking," yet captures many properties of in vivo cortical activity. However, this comes with a caveat:

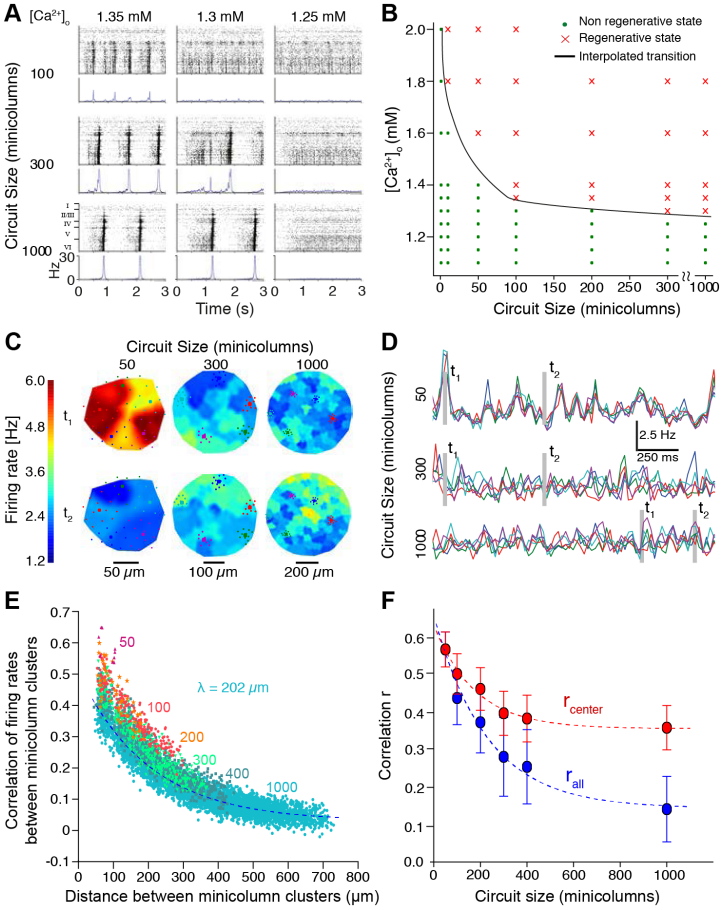

Figure 1.9 – Emergence. (**A**) Transition between regenerative and non-regenerative regimes as a function of circuit size and calcium concentration. Panels of raster plots (top) and PSTHs (bottom) of spontaneous activity are shown for a selection of circuit sizes and calcium concentrations (100% depolarization). (**B**) Overview of a broad range of circuit sizes and calcium concentrations as in A. Red crosses and green dots indicate regenerative and non-regenerative circuit behavior, respectively, as assessed by visual inspection. Black curve depicts interpolated transition between regenerative and non-regenerative regimes. (**C**) Spatial profile of instantaneous firing rates for circuits of increasing size. Mean instantaneous firing rates were estimated for contiguous groupings (clusters) of approximately ten minicolumns using a K-means algorithm. Six spatial firing rate profiles are shown, generated by interpolating these rate estimates (see Experimental Procedures *[in Markram et al. (2015)]*) at two selected times for three circuit sizes. Colored circles show five exemplary cluster centers. (**D**) Time traces of firing rates for selected clusters. Firing rate time courses are shown for the clusters in **C** in corresponding color for all three circuit sizes. Dashed boxes indicate the times, t_1 and t_2, at which spatial profiles are compared in **C**. (**E**) Pairwise cross-correlation coefficients of cluster firing rate time courses for all cluster combinations versus inter-cluster separation for varying circuit sizes (50 to 1,000 minicolumns). Pairwise correlation decays exponentially with distance (blue dashed line shows exponential fit to 1,000 minicolumn circuit dataset, space constant λ = 202 mm). (**F**) Mean pairwise cluster correlation coefficients versus circuit size for each circuit's centermost five clusters (red circles) and for all clusters (blue circles). Error bars indicate SD. Dashed curves indicate exponential fits to respective data. *Figure 20 and corresponding caption from Markram et al. (2015), reprinted courtesy of Cell Press.*

the microcircuit model was built from *sparse* data and makes many predictions that require experimental validation, including the cellular composition of the microcircuit, the lengths of dendrites and local axons, the total number of synapses, the number of connections and connection types, quantal synaptic conductances, excitation-inhibition ratios, and many more (see Markram et al. (2015) for a more complete overview). There are also many important neurobiological details missing, for example gap junctions, neuromodulation, glia, and functional and structural plasticity. Some of these will be discussed in Chapter 2.3 and Chapter 5. Nonetheless, the NMC-model integrates more detailed biological data than any other cortical microcircuit model to date. In Chapter 2, we begin to untangle how these details shape emergent network dynamics.

2 Reliability amid noise and chaos

This chapter is a preprint of joint work with Michael W. Reimann, James G. King, Henry Markram and Eilif B. Muller; it is currently under review. An earlier version is available as "*Cortical reliability amid noise and chaos*" on bioRxiv (Nolte et al. (2018); https://doi.org/10.1101/304121).

Contribution: I performed all simulations and analysis, and created all figures. J.K. developed the ability to switch random seeds after resuming a simulation. I wrote the original draft, with help by M.R.. All authors edited the draft manuscript. Further author contributions are listed at the end of the chapter.

Summary

Typical responses of cortical neurons to identical sensory stimuli are highly variable. It has thus been proposed that the cortex primarily uses a rate code. However, other studies have argued for spike-time coding under certain conditions. The potential role of spike-time coding is constrained by the intrinsic variability of cortical circuits, which remains largely unexplored. Here, we quantified this intrinsic variability using a biophysical model of rat neocortical microcircuitry with biologically realistic noise sources. We found that stochastic neurotransmitter release is a critical component of this variability, which, amplified by recurrent network dynamics, causes rapid chaotic divergence with a time constant on the order of 10-20 milliseconds. Surprisingly, weak thalamocortical stimuli can transiently overcome the chaos, and induce reliable spike times with millisecond precision. We show that this effect relies on recurrent cortical connectivity, and is not a simple effect of feedforward thalamocortical input. Our model shows that the noisy and chaotic network dynamics of recurrent cortical microcircuitry are compatible with stimulus-evoked, millisecond spike-timing reliability, resolving a long-standing debate.

2.1 Introduction

The typical electrical activity of cortical neurons is highly variable, in the sense that membrane potentials, spike times and interspike intervals vary during spontaneous activity as well as across trials with identical sensory stimuli (Mohajerani et al., 2013; Shadlen and Newsome, 1998; Stern et al., 1997; Tolhurst et al., 1983). While part of this variability could be due to intrinsic noise sources, a substantial part could also be due to hidden variables such as unknown input from other parts of the brain, environmental parameters, or brain state (Pachitariu et al., 2015; Renart and Machens, 2014). For instance, it has been shown in the visual cortex that the act of running modulates responses of neurons to identical stimuli (Niell and Stryker, 2010). Moreover, some neurons in sensory cortices can encode sensory input with high spike-time precision (Hires et al., 2015; Kayser et al., 2010; Petersen et al., 2001). Taken together, it is compelling to assume that intrinsic noise plays a negligible role, and that cortical variability is essentially deterministic (Masquelier, 2013), encoding hidden or unobserved variables. This view is also supported by the fact that neocortical neurons respond to somatic current injections in vitro with high reliability (Mainen and Sejnowski, 1995). However, there are two important reasons to believe that a large part of cortical variability is due to internally generated noise that carries no signal.

First, all cortical neurons are subject to well-established cellular noise sources, such as stochastic synaptic transmission and ion-channel noise (Faisal et al., 2008). These noise sources ultimately originate from proteins susceptible to thermodynamic fluctuations, and are therefore indeed truly intrinsic sources of noise (Faisal et al., 2008; Renart and Machens, 2014). In particular, synaptic transmission is based on a sequence of stochastic molecular events, where the low numbers of molecules involved do not allow stochastic properties to average out (Ribrault et al., 2011). In fact, in tightly controlled slice conditions in vitro, the probability of vesicle release upon action potential arrival at a single cortical synapse is low (~50% between thick tufted layer 5 pyramidal neurons (Markram et al., 1997a)), and estimated to be substantially lower in vivo (Borst, 2010) (~10% between same neurons (Markram et al., 2015)). The universal presence of synaptic noise suggests that cortical neurons respond far less reliably to presynaptic inputs than to current injections. It has been shown, moreover, that a simplified cortical network model with stochastic synapses can provide a sufficient explanation for variable spiking (Moreno-Bote, 2014). Furthermore, in vitro, some types of inhibitory neurons exhibit stochastic firing types. That is, they respond highly irregularly to constant somatic current injections (Petilla Interneuron Nomenclature Group et al., 2008). This is due to ion-channel noise that is amplified during action potential initiation (Mendonça et al., 2016). Even activity in regular firing excitatory neurons can be subject to ion-channel noise, for example during action potential propagation in thin axons (Faisal and Laughlin, 2007).

Second, models suggest (Vreeswijk and Sompolinsky, 1998; van Vreeswijk and Sompolinsky, 1996) and experiments show (London et al., 2010) that cortical networks have chaotic dynamics. This implies, by definition, that small perturbations, such as those due to intrinsic cellular

noise, are amplified. Thus, extra or missing spikes in the network, for example due to failed synaptic transmission, could fundamentally alter the trajectories of spiking activity in the network, leading in turn to large steady-state fluctuations.

In spite of their potential importance, the separate and combined impacts of network dynamics and cellular noise sources on cortical neuronal variability remain largely unexplored. There are several reasons why understanding what proportion of cortical neuronal variability is generated internally—and how this variability arises—is crucial for understanding the neural code.

First, strong internally generated variability due to chaotic network dynamics could prevent coding based on spike timing past the sensory periphery, and favor theories of firing rate coding (London et al., 2010). To test the feasibility of models of cortical coding that rely on spike timing (Gütig and Sompolinsky, 2006; Luczak et al., 2015; Thorpe et al., 2001), we need to understand internal variability and how it arises.

Second, variability could carry information and encode signals itself, for example perceptual uncertainty (Orbán et al., 2016). It is thus essential to understand how to separate intrinsically generated variability that is *bona fide* noise from variability that encodes an additional signal or brain state.

Third, and more generally, optimal coding strategies for neural circuits depend on where noise enters the circuit (Brinkman et al., 2016). That is, to understand the neural code, we need to understand the mechanisms responsible for internally generated variability. Currently, it is impossible to measure all external inputs to a local population of cortical neurons in vivo. As a result, we are still unable to quantify how much of the experimentally observed variability is generated internally by the local circuitry, and how much is generated externally.

In this study, we addressed these questions with a recently developed simulation-based approach, namely a biologically constrained model of a prototypical *neocortical microcircuit* in rat somatosensory cortex (the NMC-model; see Markram et al. (2015)). The NMC-model incorporates several prominent sources of noise, including stochastic synaptic transmission and ion channel noise, and reproduces a range of in vivo experiments with a unified parameter set. Each of the noise sources is constrained to replicate experimentally observed variability. This bottom-up modeling approach provides control over all noise sources, as well as external inputs and internal states.

Through a series of simulation experiments, in which we selectively enabled noise sources and recurrent network dynamics, we characterized intrinsic cortical variability and how it arises. When cellular noise sources were disabled, we found that the underlying deterministic network dynamics were chaotic, whereas when noise sources were enabled, an interplay of stochastic synaptic transmission and network dynamics determined the rate by which membrane potentials diverged. Surprisingly, the recurrent cortical circuitry can transiently overcome these chaotic network dynamics in response to weak thalamocortical inputs and

produce reliable spike timing. Thus, our model predicts that the recurrent cortical architecture can transform relatively weak inputs into reliable patterns of activity amid high cellular noise and chaotic network dynamics.

2.2 Results

2.2.1 Rapid divergence of spontaneous activity

Using the NMC-model of rat somatosensory cortex (31'346 neurons, ~8 million connections, and ~36 million synapses; see Figure 2.1a), we simulated in vivo-like spontaneous neuronal activity. The NMC-model contains three types of biological noise sources, all of which are required to replicate neuronal responses to paired recordings and current injections in vitro (Figure 2.1b). Each of the 36 million synapses in the model incorporates stochastic models of vesicle release with biologically constrained variability, which display both *failure* of vesicle release (*a*) and *spontaneous release* (*b*). The neuron types which exhibit irregular firing behavior (1'137 neurons) also contain models of *stochastic potassium channels* (*c*), which induce irregular firing in response to constant current injections in vitro. A fourth, tunable noise source consisted of a noisy current (*d*) injected at the soma of each of the 31'346 neurons in the model, used to account for other putative sources of depolarization in vivo (see Methods, Markram et al. (2015)) (Figure 2.1b). In our initial experiments, we maintained the magnitude of this generic noise far below the magnitude of the experimentally-constrained noise sources, using it later for sensitivity analysis.

Independent trials of the network activity were simulated up to a time t_0, at which point we saved the full dynamical state of the simulation (*base state*). We then *resumed* the simulation two times from the base state, i.e. we used identical initial conditions and histories in each case, but with different sequences of random numbers. This allowed us to obtain two equally valid probabilistic network trajectories for $t > t_0$ for each base state. We observed that somatic membrane potentials (V_m) for individual neurons, and the mean potentials for the population both diverged rapidly between the two simulations (Figure 2.1c).

To quantify the time course of the divergence for each neuron *n,* we calculated the *root-mean-square deviation* of its somatic membrane potential between two trials in time bins of size Δt starting from:

$$RMSD_V(n,k;t) = \sqrt{\frac{1}{\Delta t}\int_{t-\Delta t/2}^{t+\Delta t/2} [V_{m,1}(n,k;t') - V_{m,2}(n,k;t')]^2 dt'}, \tag{2.1}$$

where $V_{m,1}(n,k;t)$ and $V_{m,2}(n,k;t)$ denote the time series of somatic membrane potentials of neuron n in the two respective trials resuming from the same base state k. We consequently defined the mean root-mean-square deviation of the microcircuit $RMSD_V(t)$ as the mean

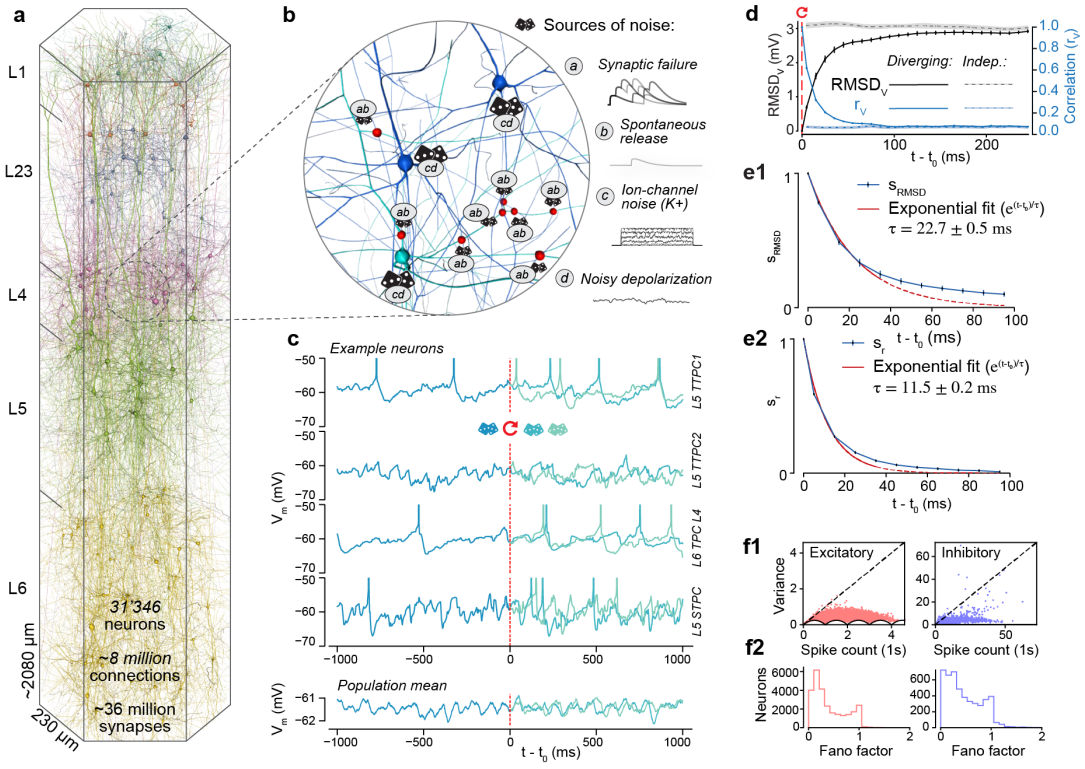

Figure 2.1 – Rapid divergence of spontaneous activity. (**a**) Morphologically-detailed model of a neocortical microcircuit (NMC); depicted are 100 randomly selected neurons, out of 31'346 in total (~0.3%). Neurons are colored according to their layer. (**b**) Examples of simulated noise sources in the NMC-model: stochastic synaptic transmission, including (*a*) vesicle release failure and (*b*) spontaneous vesicle release ('miniature PSPs') at all 36 million synapses; (*c*) probabilistic opening and closing of voltage-gated potassium channels in irregularly spiking inhibitory neurons (1'137 out of 31'346 neurons); (*d*) a constant depolarizing current with a weak white noise component ($\sigma_s^2 \ll \mu_s$) injected into the somata of all neurons. (**c**) The membrane potential of four sample neurons (and population mean of all 31'346 neurons) during a network simulation of in vivo-like spontaneous activity. At t_0, the state of the microcircuit is saved, and then resumed twice with identical initial conditions, but with different random seeds for all noise sources. (**d**) Root-mean square deviation ($RMSD_V(t)$) and correlation ($r_V(t)$) of the somatic membrane potentials between pairs of resumed simulations diverging from identical initial conditions (mean of all neurons and 40 saved base states ±95% confidence interval). The dashed lines depict the steady-state $RMSD_V(t)$ and $r_V(t)$ between independent simulations (i.e. resumed from different base states). (**e**) The similarity of the system (s_{RMSD} and s_r) defined as the difference between the diverging and steady-state $RMSD_V$ and r_V, normalized to lie between 1 (identical) and 0 (fully diverged) (mean ±95% confidence interval). Exponential fit of s_{RMSD} and s_r for $t - t_0 < 40$ ms (estimated time constant ±68% confidence interval of fit). (**f1**) Mean spike count and variance of spike count of 40 independent trials of 1000 ms duration for all neurons in the microcircuit, plotted separately for excitatory neurons (red) and inhibitory neurons (blue). The dashed lines indicate the expected values for a Poisson process. Black lines indicate minimum variance due to the fact that the spike count has to be an integer. (**f2**) Distribution of Fano factors (variance divided by mean spike count) corresponding to **f1**.

of $RMSD_V(n,k;t)$ over all base states ($K = 40$) and neurons ($N = 31'346$). We observed that $RMSD_V(t)$ diverged rapidly from zero and eventually converged towards a *steady-state* value $RMSD_\infty$, equal to the $RMSD_V$ of independent trials that did not share the same base state (Figure 2.1d, solid black and solid grey lines). The divergence was fast, with $RMSD_V(t)$ reaching more than 50% of its steady-state value within 20 ms.

While the $RMSD_V(t)$ of the circuit allowed us to accurately track the overall divergence of the whole circuit, $RMSD_V(n,k;t)$ for individual neurons and trials were too noisy for in-depth analysis (Supplementary Figure 2.9a1,b1). We note that while $RMSD_V(t)$ quantifies the absolute distance between membrane potentials, potentials can still be correlated independent of this distance. To this end, we analogously computed the *linear correlation* of somatic membrane potentials between two trials in time bins of size Δt, starting from t_0 (averaging over t' in each time bin of size Δt):

$$r_V(n,k;t) = \frac{\mathrm{cov}\left(V_{m,1}(n,k;t'), V_{m,2}(n,k;t')\right)}{\sigma\left(V_{m,1}(n,k;t')\right) \cdot \sigma\left(V_{m,2}(n,k;t')\right)}, \quad t - \frac{\Delta t}{2} < t' \leq t + \frac{\Delta t}{2} \tag{2.2}$$

We found that the mean correlation $r_V(t)$ diverged faster than the absolute distance as measured by $RMSD_V(t)$ (Figure 2.1d, dashed blue line), again with a broad distribution across individual neurons (Supplementary Figure 2.9a2,b2).

To better evaluate the difference between $r_V(t)$ and $RMSD_V(t)$, we defined the *similarity* $s_{RMSD}(t)$ of the microcircuit activity as the normalized difference between diverging and steady-state $RMSD_V(t)$ (and similarly $s_r(t)$ for $r_V(t)$). When similarity $s_{RMSD}(t) = 0$, membrane potential traces are identical; when $s_{RMSD}(t) = 1$ membrane potentials have reached their steady-state distance $RMSD_\infty$. Similarly, when $s_r(t) = 1$, membrane potentials have a perfect linear relationship; when $s_r(t) = 0$, they reached their steady-state correlation r_∞. Comparing $s_r(t)$ and $s_{RMSD}(t)$, we observed that $r_V(t)$ diverged approximately twice as fast as $RMSD_V(t)$ (Figure 2.1e1 vs. Figure 2.1e2). More precisely, an exponential fit to the first 40 milliseconds revealed divergence time constants of $\tau_{RMSD} = 22.7 \pm 0.5$ ms and $\tau_r = 11.5 \pm 0.2$ ms (68% confidence interval of fit). These were conserved for different bins sizes Δt in the range of 1 ms to 50 ms (Supplementary Figure 2.10b1,2). We observe, however, that a simple exponential decay does not provide an adequate description of the whole time-course of the similarity, as the time constant changes continuously, especially in the first several milliseconds (Supplementary Figure 2.10a). While the initial divergence is rapid, a small but statistically significant difference ($p < 0.025$) between diverging and independent activity persists for around 400 ms for $RMSD_V$ (Supplementary Figure 2.9c1) and around 200 ms for r_V (Supplementary Figure 2.9c2).

The observed rapid time-scale of divergence demonstrates that spontaneous activity in the NMC-model is inherently probabilistic, with a high internally generated variability. However, this does not automatically imply high spike-count variability. This variability is commonly

assessed using the Fano factor, which is 1 for a Poisson process (Moreno-Bote, 2014). Indeed, for most neurons we found that the variance of spike counts across independent trials was far lower than for a Poisson process, especially for larger firing rates (Figure 2.1f and Supplementary Figure 2.11). Thus, our model predicts that Poisson-like variability does not arise spontaneously in the microcircuit.

2.2.2 Variability is robust across dynamical states

In addition to the *microscopic* divergence of individual somatic membrane voltages, *macroscopic* fluctuations in population spiking activity (Figure 2.2a1) and population firing rate (Supplementary Figure 2.12a) also diverged rapidly for $t > t_0$. These global fluctuations indicate substantial *shared variability* between individual neurons. However, the nature of these global fluctuations depends on the balance between excitatory and inhibitory activity (EI-balance) in the network (Brunel, 2000).

In the NMC-model, the EI-balance is determined by the integrated anatomical and physiological data, and can be modulated by changes in extracellular calcium concentration ($[Ca^{2+}]_o$) through its effect on synaptic vesicle release probabilities (Borst, 2010; Markram et al., 2015). Excitatory synapses are more strongly affected by $[Ca^{2+}]_o$ changes than inhibitory synapses, whereby an increase in the concentration of $[Ca^{2+}]_o$ shifts the EI-balance of the network in favor of excitation. It was previously shown that such changes in $[Ca^{2+}]_o$ induce a sharp transition in network activity, from asynchronous to regenerative synchronous activity (Markram et al., 2015). This transition occurs around a *critical* point just above $[Ca^{2+}]_o = 1.25mM$, with activity below this point being *subcritical* (Figure 2.2a1) and activity above this point being *supercritical* (Figure 2.2a2).

In the in vivo-like state analyzed here ($[Ca^{2+}]_o = 1.25mM$), the microcircuit is in a just subcritical (Priesemann et al., 2014) state of asynchronous spontaneous activity, where it reproduces spontaneous and evoked network dynamics previously observed in vivo (Markram et al., 2015) While this asynchronous state might be important for efficient coding (Beggs and Plenz, 2003; Denève and Machens, 2016), the exact EI-balance in vivo is difficult to determine, and is likely to reconfigure dynamically as a function of the state of arousal and attentiveness of the animal (Constantinople and Bruno, 2011). We therefore investigated the relationship between the time course of divergence and different dynamical regimes. We observed that the rapid divergence of electrical activity was approximately conserved across these different dynamical states (Figure 2.2a3). While steady-state electrical activity was slightly more de-correlated in the in vivo-like state, the time course of divergence was remarkably similar. We also found that the synchronous state still displayed high shared variability, with unpredictable timing of population bursts (Figure 2.2a2, $t > t_0$). In our model, therefore, intrinsic variability, as quantified by the time course of divergence, is conserved across a spectrum of dynamical states and does not depend on the exact EI-balance.

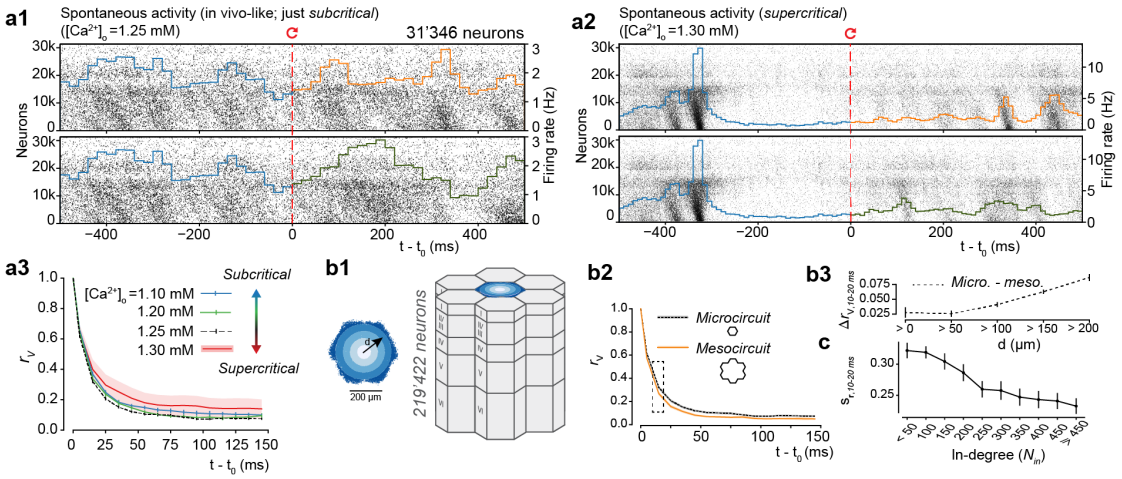

Figure 2.2 – Robust rapid divergence across dynamical states and microcircuit scale. (**a1**) Population raster plot and population peristimulus time histogram (PSTH) for all 31'346 neurons in the microcircuit, during in vivo-like spontaneous activity. Neurons are ordered according to cortical depth, with deep layers at the bottom and upper layers at the top. Each row represents the spikes of one neuron. For visibility, raster lines extend over dozens of rows for each neuron. For $t < t_0$, the top and bottom raster plots show the same simulation, whereas for $t > t_0$, the raster plots depict two simulations resuming from identical initial conditions at t_0, but using different random number seeds. (**a2**) Same as **a**, but for supercritical activity. (**a3**) $RMSD_V$ and r_V across dynamical regimes (20 saved base states, mean ± 95% confidence interval; same as Figure 2.1d for in vivo-like regime ($[Ca^{2+}]_o = 1.25mM$)). (**b1**) The microcircuit (center, blue), surrounded by 6 other microcircuits (grey), forming a continuous mesocircuit of ~220'000 neurons, with no boundary effects between the circuits. (**b2**) r_V for the center microcircuit when simulated without surrounding circuits (black), and of the center microcircuit when simulated as a mesocircuit (orange) (microcircuit: 40 saved base states; mesocircuit: 20 saved base states; mean ± 95% confidence interval). (**b3**) Quantifying edge effects. Difference of r_V between the same neurons in the microcircuit and the mesocircuit at 10-20 ms, plotted according to distance from horizontal center (mean ± 95% confidence interval). (**c**) Similarity s_r for subsets of neurons grouped by in-degree (bin size: 50; mean ± 95% confidence interval).

2.2.3 Variability is nearly saturated at the scale of the microcircuit

It is possible that the amount of internally generated variability depends not just on the dynamical state of the model circuit but also on its size. We have previously shown that increasing the size of the model beyond the size described above does not alter the observed dynamical states (Markram et al., 2015). At this size, dendritic trees and thus the afferent connections of neurons in the lateral center of the microcircuit are fully located within the microcircuit. However, a large fraction of their recurrent connections with neurons in the surrounding tissue are with neurons beyond the periphery of the microcircuit. Since these neurons were not included in the simulations, large portions of synaptic input to peripheral neurons were missing. To quantify the effect of this additional input on variability in the microcircuit, we surrounded the original microcircuit with six additional microcircuits, simulating a much larger *mesocircuit,* providing missing synaptic input to the neurons at the periphery of the microcircuit (Figure 2.2b1, blue and grey). Connectivity in this mesocircuit was homogeneous, both within and between the individual microcircuits.

When we compared the divergence of membrane potentials between micro- and mesocircuit simulations, we found that membrane potentials diverged slightly faster in the mesocircuit, although the time courses of divergence followed similar trends (Figure 2.2b2). The mean difference in $r_V(t)$ was always below 0.06, and the steady state difference below 0.03. Considering the difference at 10-20 ms (which we found to be a good predictor of the relative order of differences at any time), we found this difference to increase towards the periphery of the microcircuit (Figure 2.2b3). This suggests that additional direct synaptic input onto a neuron increases variability, but has only a weak effect on indirectly connected neurons. Thus, at the scale of the microcircuit, the amount of internally generated variability is nearly saturated, albeit underestimated for neurons at the periphery.

2.2.4 Highly connected neurons diverge faster

Next, we explicitly quantified how the time course of divergence depends on the amount of the synaptic input. To this end, we examined the relationship between the similarity $s_r(t)$ of a given neuron and the number of connections it receives from within the microcircuit (*in-degree*). Once more, we found that the time course of divergence was faster, the more synaptic inputs a neuron received, as summarized by $s_r(t)$ at 10-20 ms (Figure 2.2c). Thus, neurons which are more strongly coupled to the local population (Okun et al., 2015) diverge more quickly. Additionally, we found that for highly connected neurons, divergence increased with their ratio of excitatory vs. inhibitory inputs (Supplementary Figure 2.12b). Repetition of the analysis using $RMSD_V(t)$ instead of $r_V(t)$ gave qualitatively similar results (data not shown). We note that $RMSD_V(t)$ and $r_V(t)$ are generally highly correlated (Supplementary Figure 2.13a, *abcd*). In what follows, we hence present the divergence in terms of $r_V(t)$, except when there is a qualitative difference.

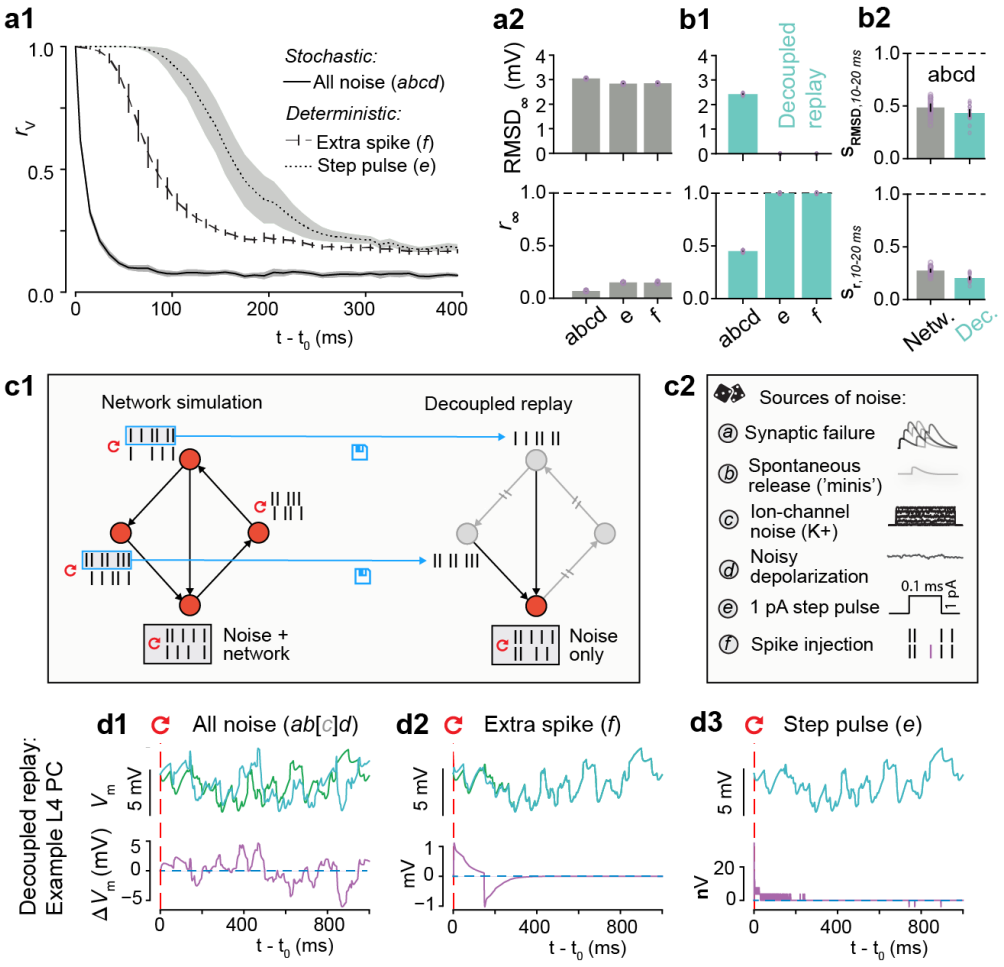

Figure 2.3 – Noise amplified by chaos determines internally generated variability. (**a1**) Time course of correlation r_V after resuming at t_0 from identical conditions with different forms of perturbation. Full cellular noise as before, solid line (*abcd*); no cellular noise, but perturbing with a single extra spike in one neuron, dashed line (*f*); a miniscule step pulse perturbation in all neurons, dotted line (*e*). (*abcd*: 40 saved base states; *e, f*: 20 saved base states; mean ± 95% confidence interval) (**a2**) Steady-state root-mean square deviation $RMSD_\infty$ and correlation r_∞ for stochastic (*abcd*) and deterministic simulations (*e, f*) as defined in **a1** (mean ± 95% confidence interval in black; individual base states in purple dots). (**b1**) As in **a2**, but for decoupled, replayed simulations. (20 saved base states) (**b2**) Similarity s_{RMSD} and s_r at 10-20 *ms* with all noise sources enabled, for network and decoupled simulations (mean ± 95% confidence interval). (**c1**) Decoupled replay paradigm. Presynaptic spike trains from a network simulation are saved and then replayed to the synapses of each neuron in a decoupled simulation, thereby removing variability due to feedback network dynamics. (**c2**) Overview of sources of noise and perturbations. (**d**) Decoupled replay simulations (see **c1**) for a representative L4 PC neuron, with somatic membrane potential differences between the two trials only due to cellular noise sources (*ab[c]d*), a single extra presynaptic spike (*f*) or a miniscule step-pulse perturbation (*e*). [*c*] indicates that for some neuron types in the NMC-model, such as L4 PCs, no stochastic ion-channels are present.

2.2.5 Noise amplified by chaos determines internally generated variability

Thus far, we have demonstrated a high level of variability which is robust across dynamical states and nearly saturated at the scale of the microcircuit. We have also shown that divergence is faster for neurons that are more tightly coupled to the local population (Figure 2.2c). This suggests that the variability of individual neuron activity is driven by the variability of local population activity, or that additional synaptic input simply adds more synaptic noise, or that the noise is determined by some combination of the two effects. In other words, while cellular noise is the only original source of variability in the NMC-model, the question remains to what degree this noise is amplified by recurrent network connectivity.

To address this question, and more generally, to study the interaction of noise sources and recurrent network dynamics, we performed two complementary sets of simulation experiments. In the first set, we sought insights into the role of network dynamics without noise sources, probing the sensitivity of a completely deterministic version of the model to a weak, momentary perturbation. In the second, we studied the opposite case of variability due to stochastic noise sources without amplification by the network.

To implement the first set of simulations, we disabled stochasticity of cellular noise sources, including synaptic transmission, by using a fixed sequence of random numbers, which made the random outcome deterministic (or alternatively by completely replacing the stochastic model with a deterministic one, see below). This enabled us to observe amplification of perturbations through the network without the effect of continuously varying cellular noise sources. As the sole source of perturbation, we injected a single extra spike into one of the neurons in the microcircuit (see Methods). We observed that the network diverged rapidly (Figure 2.3a1, dashed line), though more slowly than with noise sources enabled (Figure 2.3a1, solid line). In fact, even a miniscule current injection, which shifted the majority of spike times by less than 0.05 ms (see Methods), eventually led to a divergence of membrane potentials similar to the divergence observed in the full model with noise sources (Figure 2.3a1, dotted line). The slightly higher steady-state correlation r_∞ in the deterministic simulation was due to identical spontaneous release of neurotransmitter, identical ion-channel opening probabilities, and the small, but identical, noisy component of the depolarizing current injection. However, the relative difference in $RMSD_\infty$ was much smaller than the difference between the deterministic and the stochastic simulations (Figure 2.3a2, top vs. bottom). That is, any perturbation to the system eventually led to a similarly large steady-state divergence. We conclude that the underlying dynamics of the circuit are chaotic, in the sense that small perturbations, such as one injected spike, lead to completely different activity trajectories.

It is important to note that when using a fixed random seed to make the stochastic version of the Tsodyks-Markram synapse model deterministic (Markram et al., 2015; Tsodyks and Markram, 1997), any extra or missing presynaptic spike can change the outcome for the next spike by advancing the sequence of random numbers. To avoid this difficulty, we ran equivalent simulations using the deterministic version of the Tsodyks-Markram synapse

model (see Methods). In these simulations, extra spikes and small perturbations produced qualitatively similar divergence time courses (Supplementary Figure 2.14a vs. 2.14b, dark green and pink lines).

We had shown that the network amplifies extra spikes or even small perturbations of membrane potentials. This leads to chaotic divergence of activity with similar steady-state variability, but different time courses. It remained to be seen whether this high level of variability requires network amplification or whether it could be generated by the noise sources alone.

To address this question, we implemented a second set of simulations to study the case of ongoing noise sources without network propagation. In these *decoupled replay* simulations, in contrast to regular *network simulations,* synaptic mechanisms were activated by spikes at fixed times, recorded in an earlier simulation experiment (Figure 2.3c1). In this way, the network was no longer able to amplify neuronal variability and neuronal variability was entirely due either to cellular noise sources or perturbations (Figure 2.3d). We found with all noise sources turned on, somatic membrane potentials still diverged rapidly, as quantified by $s_{r,10-20ms}$ (Figure 2.3b2) (as mentioned above, we found s_r at 10-20 ms to be a good predictor of the relative order of s_r at any time). However, steady-state r_∞ was higher and $RMSD_\infty$ was lower than in the network simulations (Figure 2.3b1 vs. Figure 2.3a2). When the decoupled replay paradigm was used with the deterministic version of the model, single extra spikes and brief current injections only evoked small, transient perturbations (Figure 2.3d2,3). It follows that the high level of variability observed in network simulations was due to chaotic network dynamics which amplified rapid perturbations of activity from cellular noise sources.

2.2.6 Synaptic noise dominates variability

To understand the contribution of individual noise sources in this interplay of noise and recurrent network dynamics, we designed a series of simulation experiments where we selectively disabled specific subsets of noise sources. We observed that disabling all noise sources except synaptic failure produced a time course for $r_V(t)$ and steady-state divergence r_∞ which was very similar to observations with all noise sources combined (Figure 2.4a1, black and green lines). On the other hand, disabling all but ion channel noise or all but the noisy current injection led to much slower divergence (Figure 2.4a1, orange and purple lines). As before, we quantified the speed of divergence by the similarity s_r at 10-20 ms after t_0 ($s_{r,10-20,ms}$) (Figure 2.4a3, cyan). Our results suggest that simulations with synaptic failure give rise to rapid divergence, whereas steady-state r_∞ and $RMSD_\infty$ depend on noise sources only weakly (Figure 2.3a2). We conclude that in the NMC-model, the time course of divergence depends on synaptic noise, a combination of synaptic failure and spontaneous release, and that other noise sources add little to no additional variability.

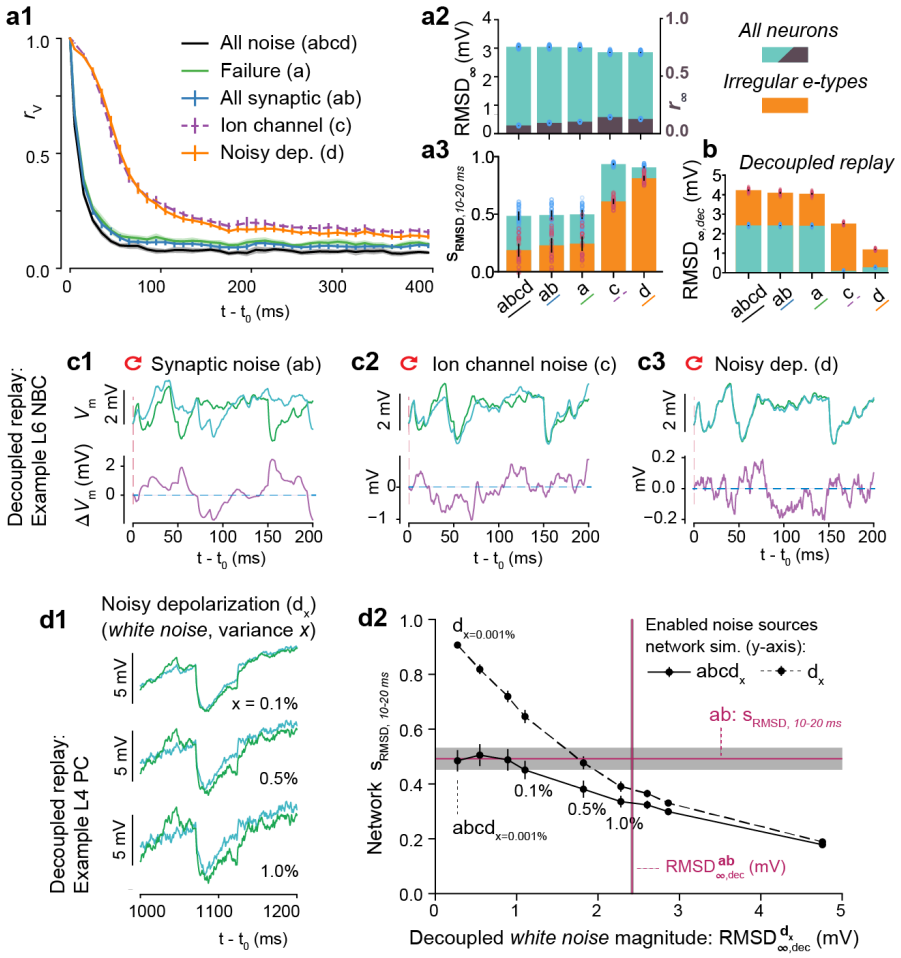

Figure 2.4 – Synaptic noise dominates variability. (**a1**) Time course of correlation after resuming at t_0 from identical conditions with different noise sources enabled (*abcd*: 40 bases states; *a, ab, c, d*: 20 base states; mean ± 95% confidence interval). (**a2**) Steady-state root-mean square deviation $RMSD_\infty$ (cyan) and correlation r_∞ (purple) with different noise sources enabled. Dots indicate individual trials; black error bars indicate 95% confidence interval. (**a3**) Similarity s_{RMSD} at 10-20 ms with different noise sources enabled, for all neurons (cyan) and irregular e-types (orange). (**b**) Steady-state root-mean square deviation for decoupled simulations, $RMSD_{\infty,dec}$, for all neurons (cyan) and irregular e-types (orange) (20 saved base states). Only irregular e-types in (c), 1,137 out of 31,346 neurons. (**c**) Decoupled replay simulations for a representative L6 NBC neuron, with somatic membrane potential differences between the two trials only due to synaptic noise (*ab*), ion-channel noise (*c*) or a noisy current injection (*d*). (**d1**) The effect of changing random seeds for the noisy depolarization only, for different noise strengths in a decoupled simulation. *x*: white noise variance as percentage of mean injected current (**d2**) The decoupled steady-state membrane potential fluctuations $RMSD^d_{\infty,dec}$ evoked by different magnitudes of white noise without network dynamics, versus the similarity s_{RMSD} at 10-20 *ms* during network simulations when either turning on only the white noise depolarization (*d*) or all noise sources (*abcd*). Similarly, in purple, $RMSD^{ab}_{\infty,dec}$ for synaptic noise versus the similarity at 10-20 *ms* when only turning on synaptic noise (*ab*). All error bars and shaded areas indicate 95% confidence intervals. Means for **d2** are based on ten base states.

2.2.7 Ion-channel noise in irregular firing neurons is overshadowed by synaptic noise

Synaptic noise in the NMC-model is modeled at every single synapse, while ion-channel noise is limited to irregular firing e-types (Markram et al., 2015; Petilla Interneuron Nomenclature Group et al., 2008). Irregular e-types are defined by high intrinsic spike-time variability in response to constant current injections in vitro, even in the absence of synaptic noise. In the NMC-model, irregular spiking is modeled with a subset of stochastic ion-channels, in accordance with in vitro findings on the source of the irregular spiking patterns observed in cortical interneurons (Mendonça et al., 2016). In contrast, regular firing e-types do not require noisy ion-channels to replicate in vitro spiking behavior. To better understand the interplay of ion-channel noise and synaptic noise, we focused our next analysis solely on irregular firing e-types. We observed that irregular firing e-types diverged significantly faster than the whole population (Figure 2.4a3, orange vs. cyan). However, synaptic noise still dominated over ion-channel noise. Enabling ion-channel noise in addition to synaptic noise led to only marginal gains in divergence rate; when ion-channel noise was enabled on its own, divergence was significantly slower (Figure 2.4a3, orange, *ab* vs. *abcd* and *c*). This suggests that in in vivo conditions, noise from stochastic ion-channels is overshadowed by synaptic noise.

2.2.8 Synaptic noise acts as a threshold for other noise sources

Several smaller noise sources are not included in our model (see Discussion). To understand how additional noise sources of various magnitudes could influence divergence, we quantified the somatic voltage fluctuations due to the previously used combinations of cellular noise using the decoupled replay paradigm, i.e. with network propagation removed ($RMSD_{\infty,dec}$) (Figure 2.4b; see Figure 2.4c1-3 for representative examples). We found that the rate of divergence in a network simulation, $s_{RMSD,10-20ms}$, is inversely proportional to $RMSD_{\infty,dec}$ (Figure 2.4a3; see also Supplementary Figure 2.15 for an extensive comparison of noise sources across simulation paradigms). In the NMC-model, synaptic noise leads to the largest $RMSD_{\infty,dec}$ and determines the rate of divergence. How strong would any other noise source have to be to increase network variability beyond the level due to synaptic noise? To answer this question, we studied how the magnitude of a generic white noise depolarizing current affects the time course of divergence. Previously, the variance σ_s^2 had been set to 0.001% of the firing threshold for each neuron—a level far lower than other sources of noise. When we increased the variance to values from 0.01% up to 10%, and disabled all other noise sources, we observed that increasing variance led to more rapidly diverging network dynamics (Supplementary Figure 2.16a). However, when other noise sources were also enabled, the noisy current injection only affected network dynamics beyond a certain threshold (Supplementary Figure 2.16b).

To characterize this threshold, we determined the magnitude of white noise required to cause a noticeable change in the network divergence rate. To this end, we used a decoupled replay paradigm with only noisy current injection (as above), for various levels of σ_s^2 (Figure

2.4d1). As above, we quantified the somatic voltage fluctuations due to this noise source, denoted by $RMSD^{d_x}_{\infty,dec}$ (d_x: only white noise, with magnitude x). In the corresponding network simulations, the rate of divergence was strongly dependent on $RMSD^{d_x}_{\infty,dec}$, with larger values leading to faster divergence (Figure 2.4d2, dashed line). In contrast, when *all* noise sources were enabled (Figure 2.4d2, solid line), there was only a meaningful influence of the noise injection when it was beyond a threshold in the range 0.1%–0.5%. At this threshold, $RMSD^{d}_{\infty,dec}$ was just above 1 mV, approximately half of the value for synaptic noise sources ($RMSD^{ab}_{\infty,dec}$, Figure 2.4d2, vertical purple line "*ab*"). When σ_s^2 is increased even more, the curves for $s_{r,10-20ms}$ with noisy current alone and with all noise sources eventually converge. Thus, when $RMSD^{d}_{\infty,dec}$ was larger than $RMSD^{ab}_{\infty,dec}$ the noisy current injection dominated other noise sources. This suggests that the strongest source of cellular noise dominates over other sources, unless they are of a comparable magnitude. Taken together, under biological conditions, we predict that synaptic noise is the most important cellular noise source, determining the variability of neuronal responses to presynaptic inputs in vivo. This prediction is consistent with previous findings that cortical neurons respond highly reliably to current injections in vitro, where synaptic noise plays no role (Mainen and Sejnowski, 1995).

2.2.9 Rapid divergence of evoked, reliable activity

In the NMC-model, thalamic inputs can evoke responses with varying degrees of reliability (Markram et al., 2015; Reimann et al., 2017b). What then are the roles of synaptic noise and chaotic network dynamics during these evoked responses? To answer this question, we simulated electrical activity in response to a naturalistic thalamocortical stimulus (Figure 2.5a1), consisting of spike trains recorded in the ventral posteromedial nucleus (VPM) during replayed whisker deflection in vivo (Bale et al., 2015). These spike trains were then applied to different feedforward VPM fibers in the model to achieve a biologically-inspired, time-varying synchronicity among inputs (Figure 2.5a3; see Methods; see Reimann et al. (2017b)). To avoid introducing external variability on top of the intrinsically generated microcircuit variability, presynaptic inputs were kept identical across trials, but with thalamocortical synapses subject to the same synaptic noise as cortical synapses. The thalamocortical presynaptic inputs were not subject to recurrent network dynamics. Since this condition excludes variability in the system up to and including the thalamus, it can be considered an intermediate stage between the decoupled replay and regular network simulations. The simulations allowed us to identify an upper bound on the reliability of thalamocortical responses. Mean $r_V(t)$ during evoked activity was stronger than during spontaneous activity, moving between ~0.1 and ~0.4 (Figure 2.5a2), indicating that external input increases neuronal reliability.

To characterize the nature of chaotic network dynamics during this evoked, reliable activity, we again resumed from identical initial conditions, with t_0 at various times relative to the stimulus onset at t = 0 ms (Figure 2.5b, for t_0 = 100 ms). The population spiking activity across pairs of trials after resuming appeared almost identical, even for time intervals much larger than the divergence time characterized above (Figure 2.5b). At first glance, it would

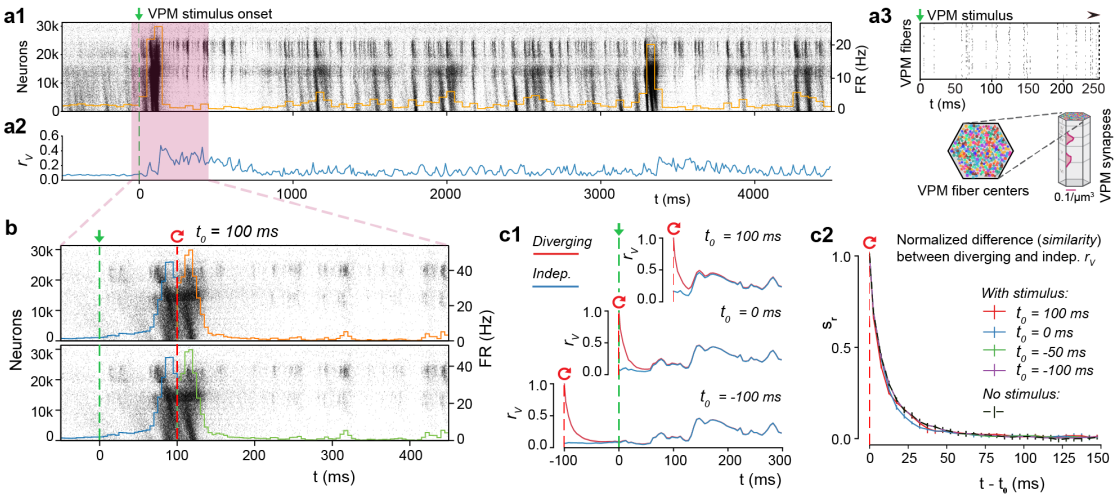

Figure 2.5 – Rapid divergence of evoked, reliable activity. (**a1**) Population raster plot and population peristimulus time histogram (PSTH) for all 31'346 neurons in the microcircuit, during evoked activity with a thalamic (VPM) stimulus. Neurons are ordered according to cortical depth, with deep layers at the bottom and upper layers at the top, and each row representing the spikes of one neuron. For visibility, raster lines extend over dozens of rows for each neuron. (**a2**) Mean somatic membrane potential correlation r_V between independent simulations of the same VPM stimulus (mean ± 95% confidence interval). (**a3**) Schematic of the VPM stimulus. Top: Raster plot spike times for the first 250 ms of the thalamic stimulus. Bottom: 310 VPM fiber centers are assigned 30 colors, and those with identical colors are provided with duplicate spike trains. The synapse density profile across layers for each fiber is shown to the right. (**b**) For $t < 100$, the top and bottom raster plots show the same simulation, whereas for $t > 100$, the raster plots depict two resumed simulations starting from the same saved state at $t_0 = 100$, using different random number seeds. (**c1**) Resuming from identical initial conditions at different times: during (top), at onset (middle), or before the stimulus (bottom). Mean r_V between independent simulations (blue, as in **a2**), and mean r_V between simulations starting from the same base state (red; mean ± 95% confidence interval). (**c2**) The similarity, s_r, defined as the difference between the r_V of diverging and independent trials, normalized to lie between 1 (identical) and 0 (fully diverged) (mean ± 95% confidence interval). Means are based on 20 base states.

appear that the input had fully overcome the chaotic divergence. However, quantification of variability by time course of divergence of membrane potentials, $r_V(t)$, showed that it dropped rapidly towards the independent trial average (Figure 2.5c1, top). When we resumed from identical initial conditions at different times, for example at the onset of evoked activity (Figure 2.5c1, middle) or before onset (Figure 2.5c1, bottom), $r_V(t)$ dropped in the same way, subsequently converging to the average for independent trials. Indeed, $s_r(t)$, the normalized difference between the resumed and independent $r_V(t)$, showed a pattern of divergence remarkably similar to the divergence observed in simulations of spontaneous activity (Figure 2.5c2). Resuming from a base state at the peak of evoked activity, $s_{RMSD}(t)$ drops even faster (Supplementary Figure 2.17a). A simpler stimulus, designed to imitate a whisker flick-type experiment (Markram et al., 2015), yielded comparable results (Supplementary Figure 2.17b,c). Hence, any neuronal activity, whether spontaneous and unpredictable, or evoked and reliable, is ultimately subject to similar chaotic network dynamics.

2.2.10 Evoked reliable activity amid noise and chaos

At first glance, our observations of evoked reliable activity and chaotic divergence of membrane potentials seem to be contradictory. To better understand how the reliable responses can emerge, we quantified the respective contribution of network propagation and cellular noise sources to variability. As before, we compared network simulations with decoupled replay simulations (Figure 2.6a3). Unsurprisingly, $r_V(t)$ was much larger in the decoupled simulations (Figure 2.6a1, black) than in the network simulations (Figure 2.6a1, red; same as Figure 2.5a2). However, the difference between the two was always smaller during evoked activity (Figure 2.6a2, after 0 ms) than during spontaneous activity (Figure 2.6a2, before 0 ms). This suggests that network dynamics play a reduced role in generating variability during evoked activity.

Indeed, when we focused on individual neurons (Figure 2.6b), we saw that that the difference between network and decoupled $r_V(t)$ collapsed to zero at times (Figure 2.6c). This is in stark contrast to spontaneous activity, where there is always a large difference between network and decoupled $r_V(t)$ (Supplementary Figure 2.18a,c1). Hence, it appears that, in response to a stimulus, membrane potential variability due to network dynamics can intermittently be completely overcome, with remaining variability being solely due to cellular noise—at least for a sub-population of neurons in the network.

2.2.11 Spike-timing reliability

So how does the decreased membrane potential variability relate to spike-timing reliability? Spike-timing is determined by a non-linear transformation of the somatic membrane potential. First, we observed that during spontaneous activity, the increase in membrane potential reliability in a decoupled replay does not directly translate into an increase in spike-timing reliability (Supplementary Figure 2.18b,c2). In fact, we found a small negative correlation (Supplementary Figure 2.18b,c3). However, during evoked activity, we observed from our

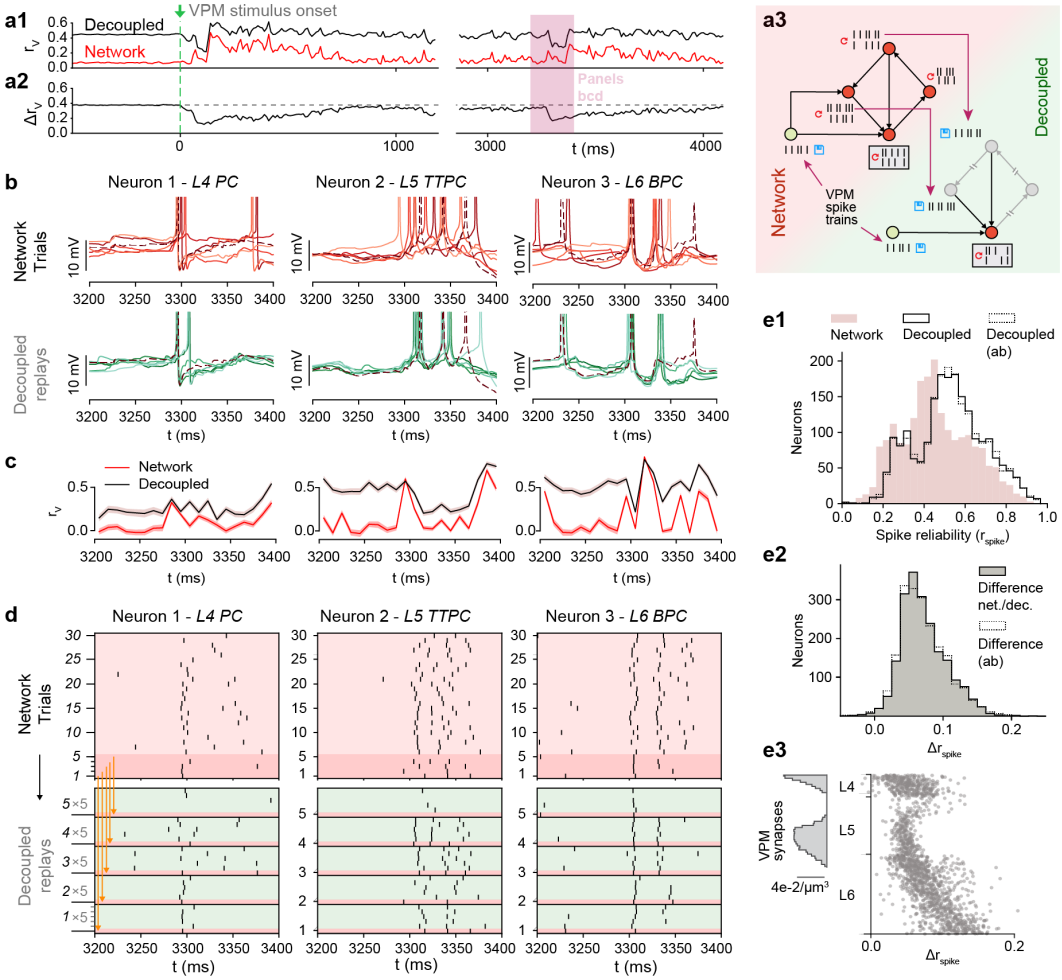

Figure 2.6 – Spike-timing reliability amid noise and chaos. (**a1**) Mean somatic membrane potential correlation, r_V, between independent simulations, and between decoupled replays of those simulations (network simulation identical to Figure 7A2). (**a2**) Difference in r_V for decoupled and network simulations. (**a3**) Schematic of network and decoupled replay simulation paradigms, including thalamic input. (**b**) Somatic membrane potentials (V_m) of three representative neurons for the time interval highlighted by the red box in **a**. Top: during six independent trials. Bottom: five decoupled replay trials (green) with the same presynaptic input as during the original network simulation trial (red), but with different random seeds. (**c**) Network and decoupled r_V as in **a**, but only for the three sample neurons in **b**. (**d**) Top: Raster plot of spike times of the same three example neurons as in **b**, during 30 independent trials of evoked activity. Bottom: Decoupled replay trials (green) of the same input received during 5 of the 30 original trials (dark red). (**e1**) Mean spike-timing reliability r_{spike} of 2024 pyramidal neurons from layers 4, 5, and 6 between independent network simulations, and between decoupled replay simulations with identical presynaptic inputs. (**e2**) Difference between r_{spike} of decoupled and replayed simulations. (**e3**) Difference between r_{spike} of decoupled and replayed simulations versus position of somata across layers 4,5 and 6 of microcircuit (1675 neurons).

example neurons that there are periods of reliable spiking where network variability can go to zero (Figure 2.6c vs. Figure 2.6d, top).

So far, we have analyzed the variability of spiking activity of neurons in terms of the Fano factor of their spike count (Figure 2.1, see above). This measure quantifies average variability over relatively long time-windows and therefore cannot quantify the transient periods of reliability we observed. Therefore, we used a correlation-based measure, r_{spike} (Schreiber et al., 2003), to compare simulations with and without network dynamics for a population of neurons during evoked activity (Figure 2.6d,e1). Contrary to the Fano factor, this measure is affected by the precise timing of spikes in smaller time windows. We observed that removing network dynamics only moderately increased spike-timing reliability (Figure 2.6e1, red vs solid black line). In fact, increases in reliability were small for all neurons (Figure 2.6e2, solid black line). In stark contrast to the spontaneous case (Supplementary Figure 2.18c2), a small population of neurons in the evoked network simulations achieved close to perfect spike-timing reliabilities (Figure 2.6e1). As expected, most of the noise effects could be explained by synaptic noise alone (Figure 2.6e1,2, dotted black line).

We conclude that during spontaneous activity, the reliability of spike generation across time-scales is directly, and severely constrained by synaptic noise, even without amplification through network dynamics. However, external stimuli can sparsely and transiently overcome chaotic network dynamics for sub-populations of neurons, with a residual variability—caused by synaptic noise—that is much smaller than during spontaneous activity.

2.2.12 High reliability requires recurrent cortical connectivity

It is conceivable that the spike-timing reliability we observed could simply be a result of direct and feedforward thalamic input (Wang et al., 2010). Indeed, when we look at changes in reliability without network dynamics, the strongest increase in reliability is in neurons at the bottom of layer six that receive comparatively little direct VPM input (Figure 2.6e3). On the other hand, the VPM input was weak compared to the recurrent connectivity, making up only 7% of the connections onto neurons in layer 4, 4% for layer 5, and less than 3% for layer 6. To test whether the intermittent suppression of chaotic dynamics is simply an effect of the feedforward input, we compared simulations of single cells with network simulations. To this end, we designed a new simulation paradigm similar to our previous decoupled replay, where each neuron received a combination of replayed presynaptic inputs from a simulation of spontaneous activity and from the direct feedforward VPM input it received in the evoked network simulations (Figure 2.7a1). That is, each neuron receives input as in a spontaneous activity trial through its recurrent synaptic contacts, and input as in an evoked trial through its feedforward synaptic contacts.

In this *mixed replay* paradigm, the population response was much weaker (Figure 2.7a2). While in simulations of evoked activity, all neurons showed higher reliability than in simulations of spontaneous activity (Figure 2.7b1), in the mixed replay, the only cells that showed increased

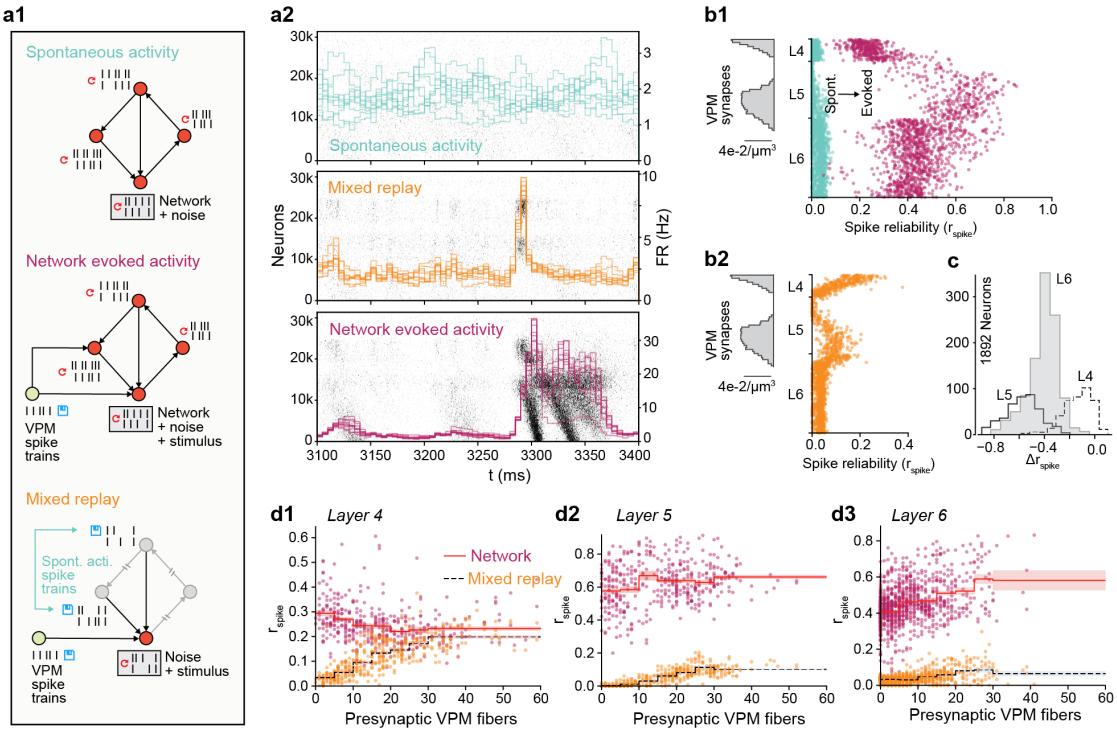

Figure 2.7 – High reliability requires recurrent cortical connectivity. (**a1**) Overview of three simulation paradigms: *spontaneous activity*, *network evoked activity* (with network propagation intact and VPM input), and *mixed replay* (with network propagation replaced by replays of spontaneous activity spike trains, and VPM input) (**a2**) Examples of population spiking activity during the three simulation paradigms. (**b1**) Spike-timing reliability, r_{spike}, during spontaneous (blue) and evoked (purple) activity for 1675 excitatory neurons in the center of layers 4, 5 and 6. (**b2**) Spike-timing reliability, r_{spike}, during a mixed replay with VPM input but with network propagation disabled for the same neurons as in **b1**. (**c**) Difference in r_{spike} between evoked activity with and without network propagation for 1892 excitatory neurons in the center of layers 4, 5 and 6 (same for **d1-3**). (**d1**) The number of presynaptic VPM fibers from which each neuron receives input versus r_{spike} in evoked simulations with (*network*) and without (*mixed replay*) network propagation. All reliabilities per neuron (points) are based on 30 trials. Mean of neurons per bin indicated by line; shaded area depicts standard error of mean of neurons in bin. Bins: 0-4, 5-9, 10-14, 15-19, 20-24, 25-29, 30+ VPM fibers.

reliability were those close to the VPM synapses (Figure 2.7b2). Furthermore, the only neurons to display similar reliability, with and without recurrent network propagation, were a small group in layer 4 (Figure 2.7c). Taken together, these findings suggest that feedforward VPM input alone is not enough to make the majority of neurons spike reliably.

To test this hypothesis, we compared the reliability between the two simulation paradigms to the number of presynaptic VPM fibers innervating each neuron (Figure 2.7d1-3). We can see that neurons in layer 4 that receive little direct VPM input responded more reliably with the network enabled than neurons that receive a lot of VPM input in the mixed replay case (Figure 2.7d1). Neurons in layers 5 and 6 were more reliable in mixed replays when they had more presynaptic VPM connections. However, this reliability increases drastically when network dynamics are enabled (Figure 2.7d2,3). We conclude that the reliable spiking observed in response to VPM inputs is propagated and amplified by recurrent cortical connectivity. This is true both for neurons that receive large direct VPM input, and for neurons that receive little or no such input. In brief, in spontaneous activity, recurrent connectivity amplifies variability; in the evoked state, it amplifies reliability.

2.2.13 High reliability emerges near a critical EI-balance

What mechanisms allow the recurrent cortical circuitry to respond so reliably? We have shown above that dynamics in the NMC-model depend on the balance between excitatory and inhibitory activity (EI-balance). This balance can be altered by the extracellular calcium concentration ($[Ca^{2+}]_o$), which differentially modulates the effective strength of excitatory and inhibitory synapses (see Markram et al. (2015) for full details). At $[Ca^{2+}]_o \approx 1.25mM$, the circuit exhibits in vivo-like dynamics (Figure 2.8a2; Figure 2.2a1). For lower $[Ca^{2+}]_o$, activity becomes more and more asynchronous (Figure 2.8a1), for higher $[Ca^{2+}]_o$, activity reaches a critical point and abruptly transitions to synchronous, regenerative (supercritical) behavior (Figure 2.8a3; Figure 2.2a2).

To understand how this affects spike-timing reliability, we repeated 30 trials of the thalamic stimulus at eight different levels of $[Ca^{2+}]_o$ (Figure 2.8a and Figure 2.8b). As we go from asynchronous to synchronous dynamics, the response properties visibly change (Figure 2.8a) and spiking becomes more reliable (Figure 2.8c). As we approach the in vivo-like state at $[Ca^{2+}]_o = 1.25mM$, reliability increases sharply (Figure 2.8c), whereas the overall EI-balance increases gradually (Figure 2.8d). As we transition to supercritical regenerative, synchronous behavior the reliability begins to plateau. At the same time the population response becomes erratic, with all-or-nothing network bursts (Figure 2.8b, Supplementary Figure 2.19).We previously showed that stimulus discriminatory power breaks down in this supercritical regime, as it does far into the asynchronous regime (Markram et al., 2015).

We conclude that spike-timing reliability in the microcircuit is adaptive: any neuromodulator that differentially targets inhibitory and excitatory synapses could adapt the response in the microcircuit according to computational tasks by fine-tuning the global EI-balance.

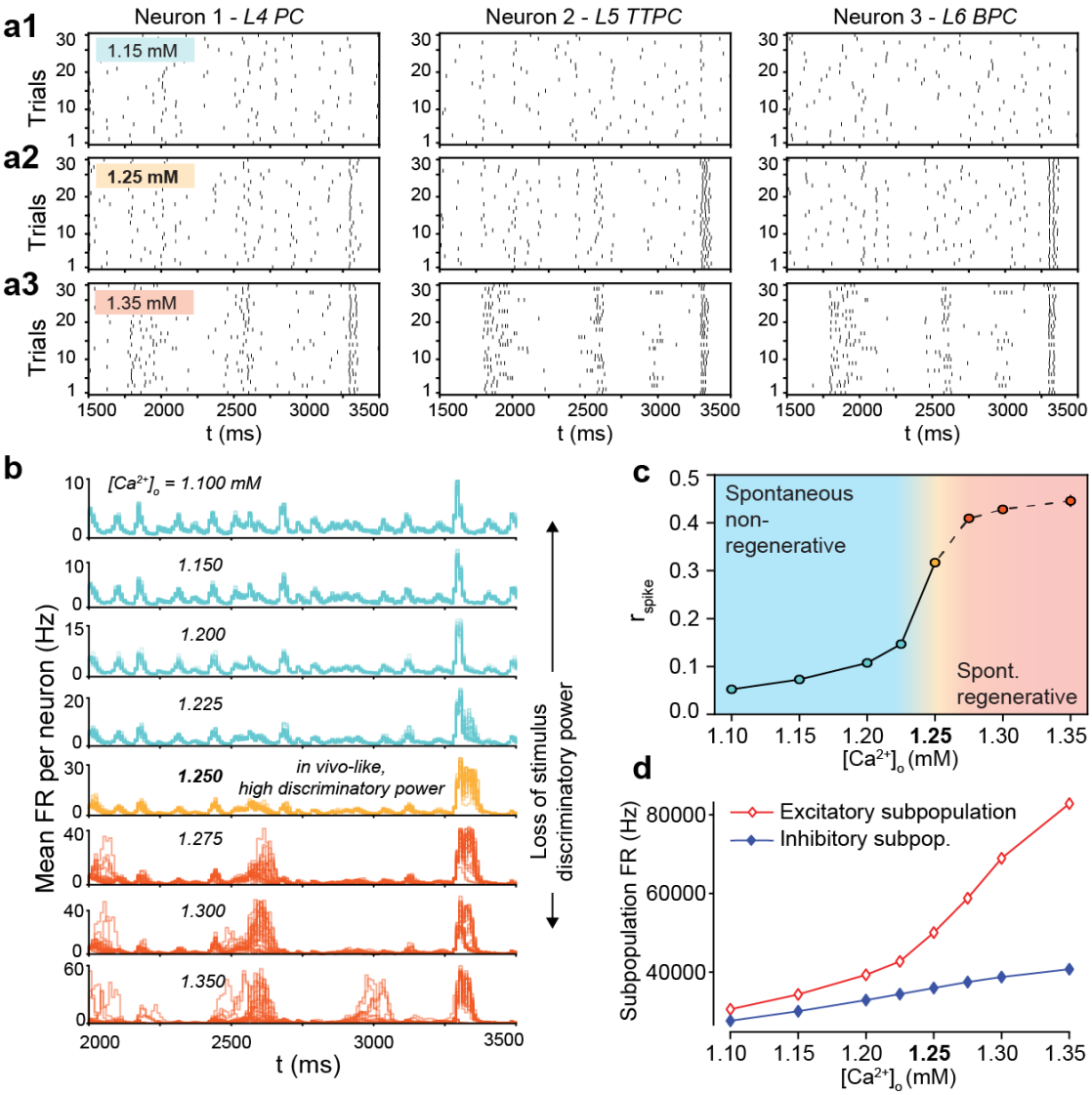

Figure 2.8 – High reliability emerges near a critical EI-balance. (**a1-3**) Raster plot of spike times of the same three example neurons as in Figure 2.6d, during 30 independent trials of evoked activity, for three different extracellular calcium concentrations ($[Ca^{2+}]_o$ = 1.15, 1.25, 1.35 mM). (**b**) Population firing rates for all 30 trials for eight different extracellular calcium concentrations. Loss of stimulus discriminatory power away from $[Ca^{2+}]_o$ = 1.25 mM as observed by Markram et al. (2015). (**c**) Mean reliability of 2024 pyramidal neurons from layers 4, 5 and 6 during the evoked response vs. extracellular calcium concentration (mean of 30 trials ± 95% confidence interval). (**d**) Total population firing rates for excitatory and inhibitory subpopulations in the whole microcircuit during the evoked response.

2.3 Discussion

In the present study, we used a biologically constrained model of a prototypical neocortical microcircuit (Markram et al., 2015) to estimate the intrinsic variability of local neocortical activity (Figures 2.1-2.4) and explore the implications for reliable stimulus encoding (Figures 2.5-2.8). We found that cortical circuitry supports millisecond-precision spike-timing reliability amid highly variable, chaotic network activity. This resolves a long-standing question: Is the cortex too noisy for the precise timing of a spike to matter (Hires et al., 2015; London et al., 2010; Mainen and Sejnowski, 1995; van Vreeswijk and Sompolinsky, 1996)? Put simply, if spiking is unreliable, information must be coded by firing rates estimated in populations of neurons (London et al., 2010; van Vreeswijk and Sompolinsky, 1996), whereas if it is reliable, precise spike timing of single neurons could contain significant information (Hires et al., 2015; Mainen and Sejnowski, 1995). Here, we demonstrated that cortical circuitry naturally supports both regimes.

This debate has persisted for decades, because the experimental manipulations required to untangle the noise sources in the brain, and evaluate their impact on spike reliability, are impossible to perform in vitro or in vivo. Using the NMC-model, we were able to perform a series of simulation-based manipulations where we systematically added and removed noise sources to quantify their impacts. These manipulations yielded several novel insights.

First, we found that spontaneous activity in cortical circuitry is intrinsically variable, both at the single neuron and population level (Figures 2.1,2.2). While some of the effects of cellular noise sources on variability had been studied in single biophysical Hodgkin-Huxley type neuron models (Diba et al., 2006; Mendonça et al., 2016; Singh and Levy, 2017; Wang et al., 2010), this is the first estimate of internally generated variability in an integrated, biologically constrained model of a cortical circuit. Our results confirm previous predictions of simplified network models that showed that biological details such as distance dependent connectivity (Rosenbaum et al., 2017), feedback inhibition(Stringer et al., 2016), and differences in synaptic time scales(Huang et al., 2019)—all intrinsically part of our model—can lead to internally generated variability.

Our second insight was that stochastic synaptic transmission is amplified by chaotic network dynamics to drive a rapid, chaotic divergence of the network, resulting in the above-mentioned variability (Figures 2.3,2.4). Chaotic network dynamics without synaptic noise have been extensively studied (London et al., 2010; van Vreeswijk and Sompolinsky, 1996, 1998), and it has been suggested that synaptic noise can generate high neural variability in postsynaptic neurons (Reich and Rosenbaum, 2013) and recurrent networks (Moreno-Bote, 2014). In contrast to previous predictions from a simplified network (Moreno-Bote, 2014), our model shows that synaptic noise and recurrent network dynamics do not necessarily lead to Poisson-like spike-count variability (Figure 2.1f).

A third insight was that spike times were unreliable during spontaneous activity, but became reliable during evoked activity (Figures 2.5,2.6). Comparatively weak thalamocortical input

could switch the network to a highly reliable spiking regime. Left alone, the network is in a chaotic regime, but transient inputs can push the network towards a temporally precise regime where millisecond-precise spike-timing reliability is possible. This confirms that results of deterministic models (Lajoie et al., 2016) are correct also in the presence of strong cellular noise and weak thalamic inputs, and explains how patterns of activity generated by cortical circuitry in response to sensory stimuli can often have millisecond spike-timing precision (Luczak et al., 2015; Sato et al., 2012).

The fourth—and perhaps most surprising insight—is the mechanism for this dichotomous behavior. We determined that the recurrent network architecture causes both the amplification of synaptic noise during spontaneous activity, and the quenching of the noise sources in the presence of input. In the former case, the network is driven towards a chaotic, divergent regime, whereas in the latter, a temporally precise regime emerges (Figure 2.7). The critical role of the recurrent network stands in contrast to previous modelling work which showed that relatively few synchronous thalamic inputs maximize reliability in single neurons in cat visual cortex (Wang et al., 2010). However, this study likely overestimated synaptic reliability—synaptic release probabilities are lower in vivo than in vitro, both in general (Borst, 2010) and in this specific pathway (Sedigh-Sarvestani et al., 2017). We conclude that the thalamic input is the trigger, but that the input can only pull the neurons out of chaos with the help of the network.

What network mechanisms achieve this? We found that the reliability of the response strongly depended on the overall EI-balance in the network (Figure 2.8). The response reliability rapidly increases towards a just subcritical dynamical state where the microcircuit reproduces several in vivo findings and neurons have maximum discriminatory power to different stimuli (Markram et al., 2015). Above the critical state, microcircuit dynamics are characterized by whole-network bursts that lead to reliable but non-discriminating spiking. Fine-tuning of the EI-balance by extracellular calcium or neuromodulators thus allows to adapt the microcircuit response according to computational tasks.

The exact mechanism for this triggering of reliable spiking, and the means by which signals are reliably propagated through the circuitry amid variable activity remains a subject for future investigation. In a first step towards a characterization, we found that synchronous inputs that arrive within in several milliseconds are well suited to elicit reliable responses (Supplementary Figure 2.21), in line with previous predictions for single cells (Wang et al., 2010). One possible explanation for the propagation of reliable activity is that certain connectivity motifs could amplify reliability through redundant connectivity. Candidate motifs have already been identified in the NMC-model, such as common neighbor motifs (Perin et al., 2011) and high-dimensional cliques that shape spike correlations between neurons (Reimann et al., 2017b). In fact, we found that neurons with high in-degrees were more reliable (Supplementary Figure 2.20a), and that neurons are less reliable the fewer higher-dimensional cliques (Reimann et al., 2017b) they are part of (at similar in-degrees, Supplementary Figure 2.20b). Dendritic nonlinearities, such as N-methyl-D-aspartate (NMDA)-mediated plateau potentials evoked by

clustered synaptic inputs onto the dendritic tree could also play an important role (Antic et al., 2018; Wilson et al., 2016).

The predicted mechanism of suppression of chaotic dynamics does not yet have a direct experimental confirmation. However, the effect is related to the often observed quenching of variability—in terms of trial-to-trial spike counts—at the onset of stimuli (Churchland et al., 2010). In the NMC-model, spike count variance is low both during spontaneous (Figure 2.1f) and evoked activity to the same stimulus (Supplementary Figure 2.22b1). However, in the intact animal, a neocortical microcircuit is integrated with the rest of the brain and constantly receiving input: around 80% of corticocortical synapses are formed with non-local neurons (Markram et al., 2015), which are not yet accounted for in the NMC-model. In the behaving brain, most of this external input to the microcircuit will likely contain signals: for example, visual cortex is strongly modulated by movement-related activity (Musall et al., 2018). Indeed, when we stimulated the NMC-model with in vivo recordings of thalamic input that was recorded across multiple trials (Supplementary Figure 2.22a1-3), instead of perfectly identical input, Poisson-like spike count variances sometimes emerged (Supplementary Figure 2.22b2). When we stimulated the NMC-model with variable thalamic input to account for the effect of hidden inputs, Fano factors increased to values observed in rat somatosensory cortex in vivo (Bale and Petersen, 2009) (Supplementary Figure 2.23a1,a3,b1,b2,c2, $t < 0$ ms). When we added reliable input on top of the variable input, spike count variability was quenched (Supplementary Figure 2.23a1,a3,b1,b2,c2, $t > 0$ ms), consistent with previous reports (Churchland et al., 2010). Importantly, repeating one specific input out of the set of variable inputs once again led to a low spike count variance (Supplementary Figure 2.23a2,c1). Taken together, these results support the hypothesis that the observed cortical spike count variability in vivo is actually a reliable response to unobserved input, i.e. variable inputs projecting from diverse locations throughout the brain (Fairhall, 2019; Muller et al., 2018). From this point of view, the observed quenching of variability at stimulus onset (Churchland et al., 2010) reflects the statistical impact of knowledge of the stimulus (Masquelier, 2013).

2.3.1 Potential effects of missing biological detail

While the NMC-model is one of the most detailed models of neocortical circuitry to date, several biological details are lacking. In terms of noise sources, the most important missing detail is ion-channel noise. Other electrical noise sources such as thermal noise are orders of magnitude smaller (Faisal et al., 2008).

The ion-channel noise in irregular firing neurons in the NMC-model (which is responsible for the irregular initiation of action potentials in vitro (Mendonça et al., 2016)) is overshadowed by synaptic noise under in vivo-like conditions (Figure 2.4). But how would additional ion-channel noise in axons and dendrites of all neurons impact variability? In dendrites, ion-channel noise is thought to evoke little to no variability in isolated back-propagating action potentials (Diba et al., 2006). Thus, mean ion-channel models are likely sufficient for accurate

action potential initiation.

Action potentials reliably permeate axonal arbors of neocortical pyramidal neurons without failures (Cox et al., 2000). But as action potentials propagate along axons, their timing becomes increasingly variable. Simulations predict that ion-channel noise affects action potential timing in all axons with a diameter below 0.5 μm, with the standard deviation of action potential variability predicted to increase by 0.6 ms per 2 mm in 0.2 μm diameter axons (Faisal and Laughlin, 2007). In the NMC-model, axons have a mean axonal diameter of around 0.3 μm and are modeled deterministically. Therefore, ion-channel noise in longer axons could increase variability of spike timing by up to several milliseconds.

The missing ion-channel noise might push the circuit towards a more variable state. On the other hand, adding missing detail to the synapse models might increase reliability: The reliability of synaptic transmission increases with the number of readily releasable vesicles (Rudolph et al., 2015). Some studies have found *univesicular* synaptic transmission at cortical synapses (Silver et al., 2003), while others have estimated there may be as many as ten releasable vesicles per synapse (Loebel et al., 2009).

The current version of the NMC-model assumes one readily releasable vesicle per synapse, and thus potentially underestimates synaptic reliability. To estimate the potential impact of *multivesicular* release, we repeated the simulation experiments with an increasing number of readily releasable vesicles (n_{rrp}) at all synapses (Supplementary Figure 2.24). As expected, the time course of divergence slowed with increasing n_{rrp}. Nonetheless, for mean n_{rrp} values which reproduce cortical PSP variability data ($n_{rrp} = 2-3$; data not shown), synaptic noise remains the dominant source of noise driving the rapid chaotic divergence. In addition, n_{rrp} may vary between and across synapse types, but a systematic exploration thereof is beyond the scope of the present study.

There are other intrinsic mechanisms not yet included in the NMC-model such as gap junctions, intra-circuit neuromodulation (Engelhardt et al., 2007) or active information transfer from glia to neurons (Fiacco and McCarthy, 2018; Savtchouk and Volterra, 2018), whose contributions to variability within cortical circuits are as yet poorly understood. However, for these mechanisms to contribute significantly as additional noise sources above and beyond synaptic noise, they would have to cause somatic membrane potential fluctuations on the order of 1 mV ($RMSD_V$) (Figure 2.4).

2.3.2 Concluding remarks

This study provides, for the first time, a data-constrained biophysical framework that supports theories of cortical coding along a spectrum from population firing rates to reliable individual spike times. This study does not claim that cortex generally employs codes that rely on individual spike-timing, only that it is principally capable of such codes. Even a highly reliable cortex might be variable due to computational strategies that are intrinsically variable, such as

sub-optimal inference (Beck et al., 2012), or due to overcomplete representation of inputs, with distributions of spike patterns encoding the same stimulus (Moreno-Bote and Drugowitsch, 2015). Encoding strategies might further be adjusted according to computational needs by fine-tuning of the network near criticality (Wilting et al., 2018), for example due to neuromodulation that shifts the balance between excitation and inhibition and with it spike-timing reliability.

We hypothesize that population firing rates might encode attentional states, general movement-related activity, or other slow variables, whereas patterns of spikes with high temporal precision (Luczak et al., 2015) might encode more particular information, such as the touch of a whisker or, perhaps, perception of a specific object. The critical role of the recurrent network for the reliable representation of information in these spike patterns further suggests that such patterns might play an important role in computations across the hierarchy of cortical regions (VanRullen and Thorpe, 2002). The present study provides a solid foundation for future studies in this direction, and ultimately towards a deeper understanding of cortical information processing.

2.4 Methods

2.4.1 Simulation

Model of neocortical microcircuitry (NMC)

Simulations of electrical activity were performed on a previously published model of a neocortical microcircuit based on data from two-week old rats. Reconstruction and simulation methods are described extensively by Markram et al. (2015). In our study, we used a microcircuit consisting of 31,346 biophysical Hodgkin-Huxley NEURON models and around 7.8 million connections forming roughly 36.4 million synapses. Synaptic connectivity between 55 distinct morphological types of neurons (*m-types*) was predicted algorithmically by integrating anatomical data, such as layer-dependent cell type densities, morphologies and bouton densities, to generate a wiring diagram (Reimann et al., 2015) with highly heterogeneous connectivity (Gal et al., 2017; Reimann et al., 2017b,a). Consequently, the NMC-model exhibits a naturally emerging structural and functional EI-balance (Gal et al., 2017), without relying on assumptions about the exact level of coupling between excitatory and inhibitory currents. The densities of ion-channels on morphologically-detailed neuron models were optimized to reproduce the behavior of different electrical neuron types (*e-types*) as recorded in vitro (Van Geit et al., 2016). We also used a larger mesocircuit comprising seven microcircuits (mean of 36.5 million synapses per circuit), with no boundaries between the peripheral circuits and the original microcircuit in the center (shown in Figure 2.2b). Simulations were run on a BlueGene/Q supercomputer (BlueBrain IV) and an HPE SGI 8600 supercomputer (BlueBrain V). NEURON (Hines and Carnevale, 1997) models and the connectome are available online at bbp.epfl.ch/nmc-portal (Ramaswamy et al., 2015).

Simulation of in vivo-like spontaneous activity

In the in vivo-like state, release probabilities for all synapses were modulated according to the extracellular calcium concentration found in vivo, leading to substantially lower reliability than in vitro (Borst, 2010). As described by Markram et al. (2015), the U_{SE} parameter for synaptic transmission was modulated differentially as a function of extracellular calcium concentration ($[Ca^{2+}]_o$), resulting in transitions from in vitro to in vivo-like dynamics. Neurons were depolarized with a somatic current injection, with currents expressed as a percent of first spike threshold for each neuron, to mimic, for example, the effect of depolarization due to missing neuromodulators. Apart from a small white-noise component (with a variance of 0.001% of the mean injected current per neuron, unless stated otherwise), the current injection was constant. With mean injected currents at around 100% of first spike threshold and $[Ca^{2+}]_o$ at 1.25 mM, the microcircuit exhibits in vivo-like spontaneous activity (Markram et al., 2015).

Simulation of evoked activity

The microcircuit is innervated by 310 (virtual) thalamic fibers (Markram et al., 2015). In vivo spike train recordings from 30 VPM neurons were randomly assigned to the 310 fibers, to achieve varying degrees of naturalistic synchronous thalamic inputs. Spike trains were recorded during replayed whisker motion in anesthetized rats (Bale et al., 2015). Full methods are described in Reimann et al. (2017b). A variable version of the naturalistic input used in vivo spike train recordings of the same 30 VPM neurons during 30 trials of the same replayed whisker motion (Bale et al., 2015). Another stimulus consisted of synchronous spikes at the 60 central thalamic fibers, with all 60 virtual thalamic neurons firing simultaneously, to approximate a whisker 'flick' (see Markram et al. (2015)).

Save-resume

After running a simulation for some amount of biological time, the final states of all variables in the system were written to disk using NEURON's *SaveState* class. For large-scale simulations, this required the various processes to coordinate how much data each needed to write, so that each rank could then seek the appropriate file offset and together write in parallel without interfering with the others. After restoring a simulation, the user could specify new random seeds (see below).

Random numbers

In our simulations, we used random number generators (RNGs) to model all stochastic processes: noisy current injection, stochastic ion channels, probabilistic release of neurotransmitters and generation of spontaneous release events. Each synapse had two RNGs. One was used to determine vesicle release on the arrival of an action potential. The other determined

the spontaneous release signal. Similarly, each stochastic K^+-channel model had an RNG determining voltage-dependent opening and closing times. Finally, the white noise process underlying the noisy depolarization was determined by one RNG per neuron. By using different random seeds to initialize the RNGs, we obtained different sequences of random numbers, and consequently different but equally valid simulation outcomes. In earlier versions of the NEURON microcircuit simulation software, the user was given only a single random seed parameter with which to alter the random number streams generated by all RNGs. We added the option to separately change random seeds for RNGs for a specific type of stochastic component. For example, "IonChannelSeed <value>" allows the specification of a seed which is only given to the RNGs used by ion channel instances.

Stochastic synapses

The synapse models including parameters are described in detail in Markram et al. (2015), and the models used can be found online at bbp.epfl.ch/nmc-portal. The model is based on two previous models (Fuhrmann et al., 2002; Loebel et al., 2009). In short, each synapse has a pool of readily releasable vesicles of size n_{rrp} which are in one of two states: *recovered* or *depleted*. Upon action potential arrival at the synapse, each recovered vesicle stochastically releases with dynamic probability $U(t)$. The probability of vesicle release $U(t)$ is dynamic, to implement synaptic facilitation, and is governed by an event-based equation:

$$U(t) = U(t_{syn}) \cdot e^{-\frac{t-t_{syn}}{\tau_{fac}}} + U_{SE} \cdot (1 - U(t_{syn}) \cdot e^{-\frac{t-t_{syn}}{\tau_{fac}}}) \tag{2.3}$$

where U_{SE} is the release probability of a synapse that has not been activated in a long time, t_{syn} is the time of arrival of the last presynaptic spike at the synapse, and τ_{fac} is the facilitation time constant. For each released vesicle, postsynaptic AMPAR and NMDAR models are activated with a conductance g_{max}/n_{rrp} where g_{max} is the maximal postsynaptic conductance. After successful vesicle release, the vesicle location is in a *depleted* state in which it has no vesicle to release. The transition from the *depleted* state back to the *recovered* state is governed by a Poisson process, according to a survival function:

$$P_{surv}(t) = e^{-\frac{t-t_{syn}}{\tau_{dep}}} \tag{2.4}$$

where $P_{surv}(t)$ is the probability of remaining in the *depleted* state in the interval $[t_{syn}, t]$, and is the depression time constant. The univesicular case ($n_{rrp} = 1$) is modeled, unless stated otherwise.

A second stochastic process is used to generate event times for spontaneous 'miniature'

postsynaptic potentials. Spontaneous release is modelled as an independent Poisson process with a rate λ_{spont} at each synapse. When the synapse receives the signal for a spontaneous release event, it is treated as a presynaptic action potential.

Deterministic synapse model

The deterministic synapse model is implemented as previously described (Fuhrmann et al., 2002). In this formulation, $U(t)$ is interpreted as the fraction of consumed resources, rather than a release probability. Each release event activates a fraction of postsynaptic conductance proportional to $U(t) \cdot R(t)$, where *R(t)* is the fraction of vesicles in the recovered state. These two state variables are governed by the following equations (Fuhrmann et al., 2002):

$$\frac{dR}{dt} = \frac{1-R}{\tau_{rec}} - U_{SE} \cdot R \cdot \delta(t - t_{syn}), \tag{2.5}$$

$$\frac{dU_{SE}}{dt} = -\frac{U_{SE}}{\tau_{facil}} + U1 \cdot (1 - U_{SE}) \cdot \delta(t - t_{syn}), \tag{2.6}$$

where τ_{rec} and τ_{facil} are the recovery and facilitation relaxation time constants, U_{SE} is a dynamic variable that increases by an amount determined by $U1$ for each presynaptic spike, and t_{syn} is the time of arrival of presynaptic spikes at the synapse. The deterministic models implemented in this way are equivalent to their stochastic (multivesicular) counterparts in the limit as $n_{rrp} \to \infty$.

Stochastic ion-channels

In some interneuron models, a potassium channel type with a stochastic implementation was added using previously-described methods (Diba et al., 2006; Markram et al., 2015; Mendonça et al., 2016; Steinmetz et al., 2000) to model ion channel noise. The full model is available online at bbp.epfl.ch/nmc-portal. In brief, instead of a mean field model, the equations used explicitly track the number of channels in a certain state and allow these numbers to evolve stochastically, according to a binomial distribution, with the probability of transition between states computed according to the deterministic rate functions α and β:

$$Open \underset{\beta}{\overset{\alpha}{\rightleftharpoons}} Closed \tag{2.7}$$

Single spike injection

We injected single spikes in twenty different layer 4 pyramidal neurons (and twenty random neurons across the circuit, data not shown) by *replaying* (see below) an additional spike event in one neuron per simulation. Thus, there were no shifted or missing spikes, as may occur when injecting a spike in vivo. The spike was injected *0.1 ms* after resuming the simulation from identical initial conditions.

Step-pulse perturbation

We applied a microscopic current step-pulse to all neurons at their soma *0.1 ms* after resuming the simulation (duration: 0.1 ms, amplitude: *1* pA,). The current was chosen to have an almost negligible effect on individual neurons, and was near the limit of the NEURON integrator. On average, 108 ± 8 neurons out of 31,346 neurons had any changes in their spike times (mean of 19 trials ± STD). The majority of the shifted spikes were shifted by less than 0.05 ms (59.1%: < 0.05 ms; 33.1%: < 1 ms; 5.5%: < 20 ms; 1.8%: < 100 s; 0.5%: < 1 s). Finally, 3 ± 2 neurons had extra or missing spikes. The median first occurrence of an extra or missing spike was at 257 ms (min: 11 ms, max: 946 ms after resuming).

Decoupled replay

When resuming a simulation at t_0, we decoupled all connections by setting the connection weights to zero, ensuring that action potentials would be delivered to the synapses of postsynaptic neurons. At the same time, we started *replaying* action potential times from a previous resumed simulation, activating the synapses of postsynaptic neurons as if the presynaptic neuron had fired an action potential, but actually replaying presynaptic action potentials from the previous simulation. For computational reasons, spikes that had not been delivered at the save time t_0, were not delivered in the decoupled replay (meaning that a couple of presynaptic spikes per neuron may have been lost, leading to a slight underestimation of divergence).

2.4.2 Analysis

RMSD and correlation

All analysis was performed using custom scripts written in Python 2.7 using the *NumPy, matplolib* and *SciPy* libraries. Scripts were executed on a Linux cluster connected to the same IBM GPFS file system that the simulation output was written to. Root-mean-square deviation $RMSD_V$ and correlation r_V as defined in Equations 2.1 and 2.2 were implemented with *NumPy*.

Similarity

The similarity measure $s(t)$ was defined as the normalized difference between diverging $r_V(t)$ (or $RMSD_V(t)$), and steady-state $r_V(t)$ (or $RMSD_V(t)$). The steady-state value was defined as the continuous $r_{V,shuffle}(t)$ computed by shuffling the soma voltages between simulation trials, so that instead of 40 deviating pairs of trajectories, we compared 40 independent pairs of trajectories. Alternatively, we defined it as the mean stationary, fully deviated r_∞ for $t > 1000$ *ms* after resuming from identical initial conditions.

Firing rate

Firing rate was defined as the average number of spikes in a time interval of size Δt, divided by Δt ($\Delta t = 10ms$, unless stated otherwise).

Neuron selection

We selected all excitatory neurons in layers 4, 5 and 6 that belonged to the 30 *minicolumns* (out of 310 in total) in the center of microcircuit (n = 2024). The analysis was restricted to neurons that spiked at least once in each of the compared simulation paradigms.

Spike-timing reliability

Spike-timing reliability was measured using a correlation-based measure first proposed by Schreiber et al. (2003). Briefly, the spike times of each neuron in each trial were convolved with a Gaussian kernel of width $\sigma_S = 5ms$ to yield filtered signals $s(n,k,;t)$ for each neuron n and each trial k ($\Delta t_S = 1ms$). The spike-timing reliability for each neuron was then defined as the mean inner product between pairs of signals divided by their magnitude: $r_{spike}(n) = \frac{2}{K(K-1)} \sum_{k \neq l} \frac{s(n,k;t) \cdot s(n,l;t)}{|s(n,k;t)| \cdot |s(n,l;t)|}$, (K = 30; independent trials). Decoupled replay: there are M=5 replays of each of the K=30 trials, and thus $r_{spike}(n) = \frac{2}{KM(M-1)} \sum_m \sum_{k \neq l} \frac{s_m(n,k;t) \cdot s_m(n,l;t)}{|s_m(n,k;t)| \cdot |s_m(n,l;t)|}$.

Errors and statistical tests

Error bars and shaded areas indicate 95%-confidence intervals (CI), unless stated otherwise. t-based CIs (n = 20; or n = 40 if stated) were computed using *scipy.stats.sem* and *scipy.stats.t.ppf* to compute P-values from the CIs (one-sided). Errors for fit parameters, obtained with *scipy.optimize.curve_fit*, are given as the square-root of the variance of the parameter estimate.

Data availability

NEURON models, microcircuit information, and the connectome are available for download at https://bbp.epfl.ch/nmc-portal/downloads. The integrated microcircuit model is available

upon reasonable request. Output spike times and output somatic membrane potentials are available upon reasonable request.

Code availability

Software used for visualization of neurons in Figure 1 is available at https://github.com/BlueBrain/RTNeuron. The NEURON simulation environment is available at https://www.neuron.yale.edu/neuron/. The custom-written Python analysis and figure generation scripts are available at https://github.com/maxnolte/deciphering_variability.

Author contributions

Conceptualization, M.N., M.R., H.M., E.M.; Methodology, M.N., M.R., H.M., E.M.; Software, M.N., J.K.; Validation, M.N., J.K.; Investigation, M.N; Visualization, M.N.; Writing – Original Draft, M.N., M.R.; Writing – Review & Editing, M.N., M.R., H.M., E.M.; Supervision, H.M., E.M.; Funding Acquisition, H.M.

Acknowledgements

We thank Giuseppe Chindemi, Srikanth Ramaswamy, and Werner Van Geit for help with synapse and ion channel models, and the rest of the Blue Brain team for developing and maintaining the microcircuit model and computational infrastructure. We thank Taylor Newton, Madineh Sedigh-Sarvestani, Richard Walker and Mickey London for discussions and critical comments on the manuscript. We thank Oren Amsalem, Idan Segev, Wulfram Gerstner and Alexandre Pouget for helpful discussions. This work was supported by funding from the ETH Domain for the Blue Brain Project. The Blue Brain Project's IBM BlueGene/Q system, BlueBrain IV, and HPE SGI 8600 system, BlueBrain V, were funded by the ETH Board and hosted at the Swiss National Supercomputing Center (CSCS).

2.5 Supplementary figures (2.9 to 2.24)

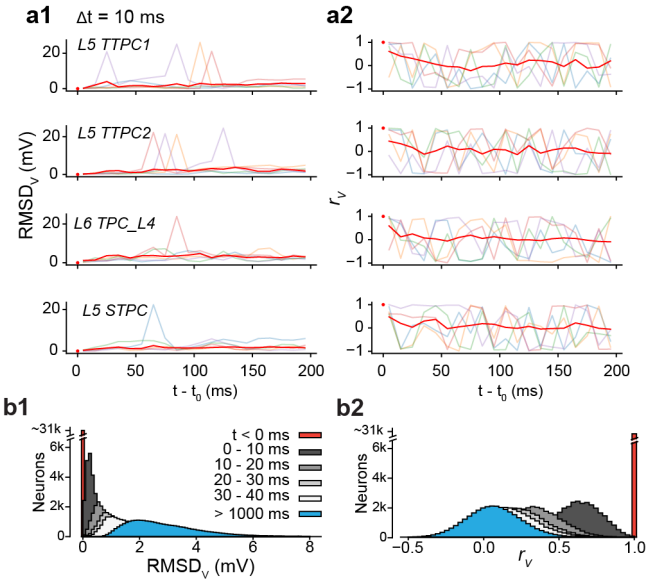

Figure 2.9 – Rapid divergence of electrical activity. (**a**) Root-mean square deviation ($RMSD_V$) and correlation (r_V) of the somatic membrane potentials between pairs of resumed simulations diverging from identical conditions, for five different base states (faded colors) and the mean of 40 saved base states (red), with $\Delta t = 10$ ms. Same neurons as in Figure 2.1c. (**b**) Time evolution of distributions of mean $RMSD_V$ and r_V values for individual neurons.

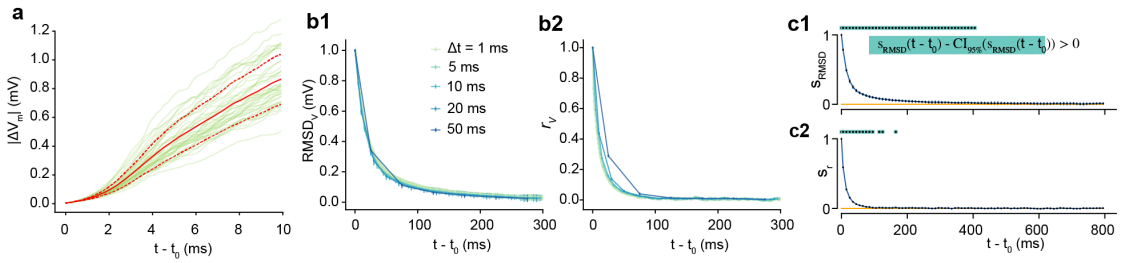

Figure 2.10 – Quantifying the rapid divergence of electrical activity. (**a**) Mean divergence in the first 10 *ms*, with $\Delta t_V = 0.1$ ms (mean of all neurons and 40 saved base states ± standard deviation). (**b**) $RMSD_V$ and r_V for different analysis bin sizes Δ_t. The time step for the soma voltage is $\Delta t_V = 0.1$ ms. (**c**) The similarity (s_{RMSD} and s_r) (mean ± 95% confidence interval). Dots signal time bins where s_{RMSD} and s_r are larger than 0, by a 95% confidence interval ($p < 0.025$).

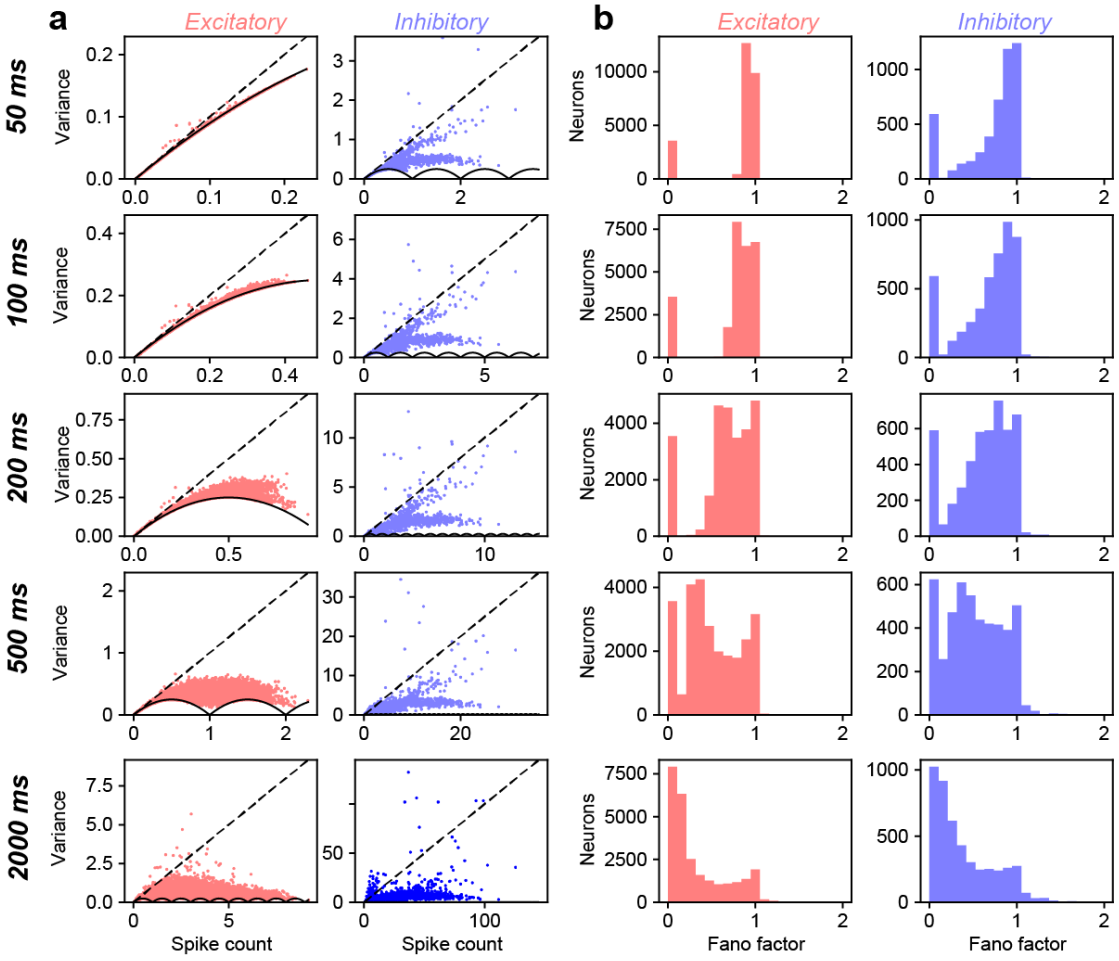

Figure 2.11 – Fano factors. (**a**) Mean spike count and variance of spike count of 40 independent trials of increasing duration for all neurons in the microcircuit, plotted separately for excitatory neurons (red) and inhibitory neurons (blue). The dashed lines indicate the expected values for a Poisson process. (**b**) Distribution of Fano factors (variance divided by mean spike count) corresponding to **a**.

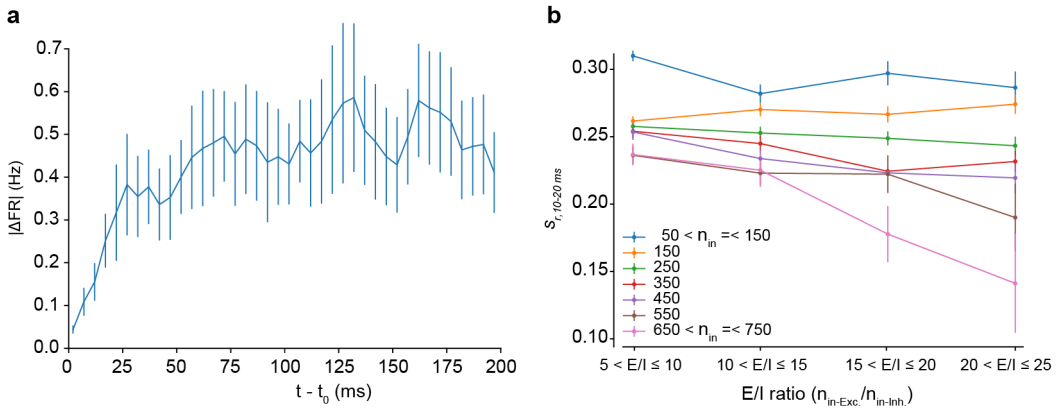

Figure 2.12 – Rapid divergence of population activity; in-degree and EI-balance. (**a**) Mean population firing rate difference (Δt = 5 ms) between pairs of simulations diverging from identical initial conditions (mean of all neurons and of 40 saved base states ± 95% confidence interval). (**b**) Similarity s_r for subsets of neurons grouped by in-degree, and by the ratio of excitatory presynaptic connections over inhibitory connections (mean ± 95% confidence interval).

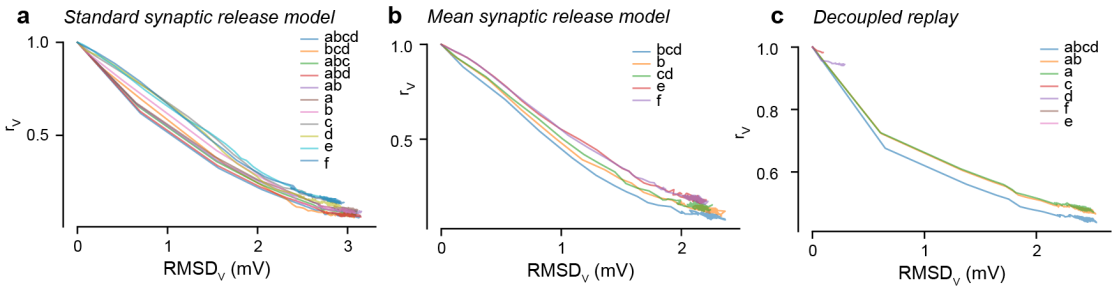

Figure 2.13 – Linear relationship between $RMSD_V$ and r_V. Root-mean square deviation ($RMSD_V$) and correlation (r_V) of the somatic membrane potentials between pairs of simulations diverging from identical initial conditions (mean of all neurons and saved base states). (**a**) Changing random seeds for subsets of noise sources with the standard stochastic release model. (**b**) Changing random seeds for subsets of noise sources with a mean release model. (**c**) Standard stochastic release model for decoupled, replayed simulations. *abcd*: 40 base states; all others: 20 base states.

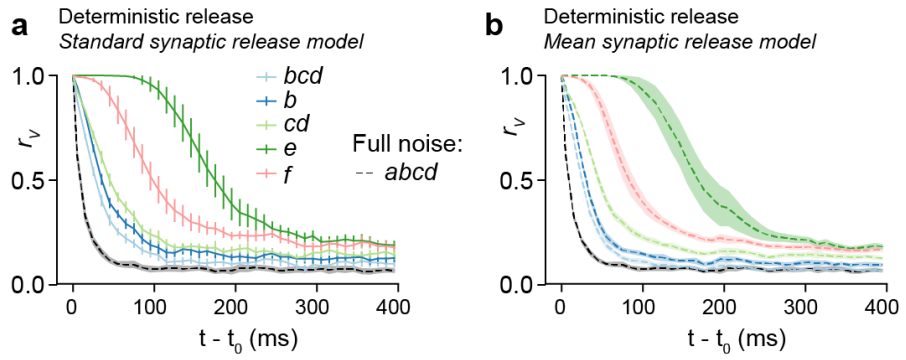

Figure 2.14 – Mean synaptic release model. (**a**) Correlation r_V (as in Figure 2.4 and Supplementary Figure 2.13), with pseudo-deterministic synaptic release by not changing the random seeds for vesicle release (but with a change in '*mini*' signals for *b*). (**b**) As in **a**, but with deterministic synaptic release (mean release model), apart from *abcd* which has the fully stochastic model. Based on 20 saved base states (*abcd*: 40 saved base states); mean of base states ± 95% confidence interval.

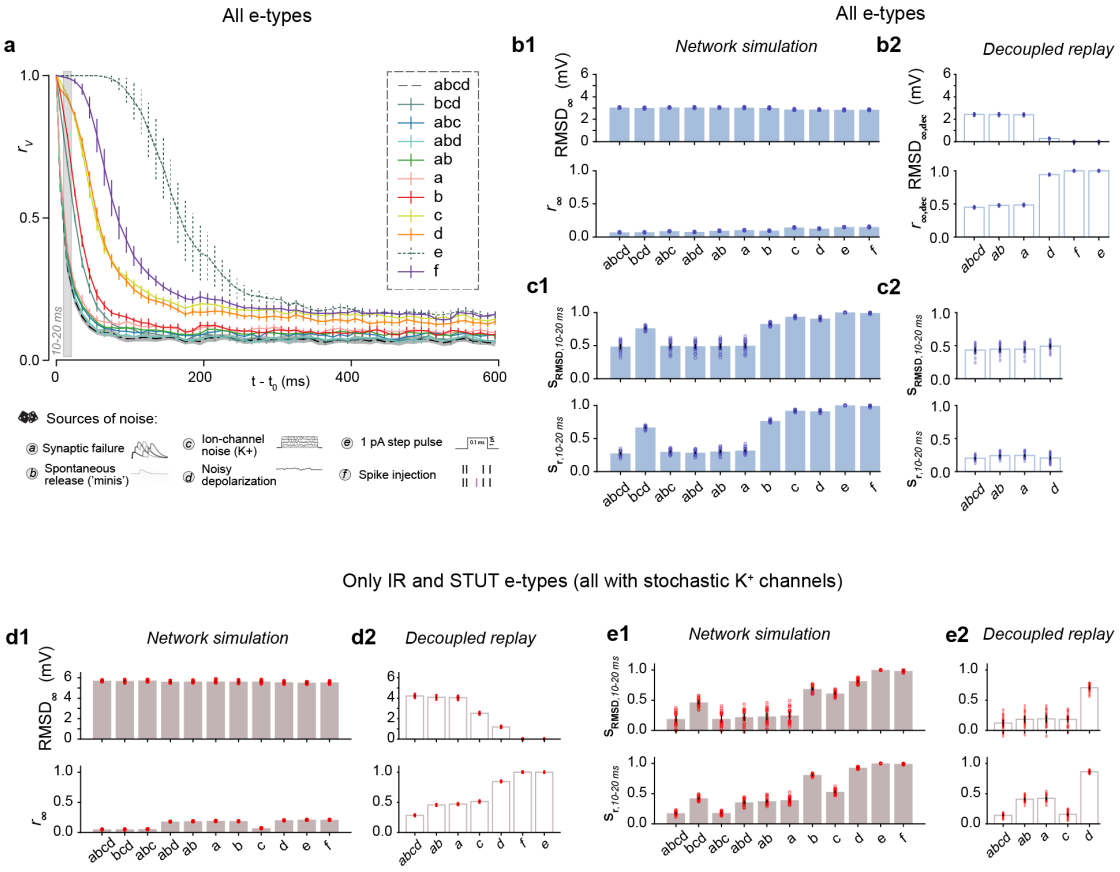

Figure 2.15 – Unravelling noise sources. (**a**) Correlation r_V from identical initial conditions with different cellular noise sources turned on, and when turning of cellular noise, but perturbing the system by a single extra spike (in one neuron) or a miniscule perturbation in all neurons. (**b**) Steady-state membrane potential fluctuations ($RMSD_\infty$) and correlations (r_∞) for network simulations (**b1**) and decoupled, replayed simulations (**b2**) for different noise sources. (**c**) Similarity $s_{r/RMSD}$ at 10-20 *ms* for network simulations (**c1**) and decoupled, replayed simulations (**c2**) for different noise sources. (**d-e**) Same as **b-c**, but only for the subset of neurons that have stochastic ion-channels (irregularly firing e-types, 1'137 out of 31'346 neurons). All error bars indicate 95% confidence intervals, based on 20 pairs of simulations (40 for *abcd*). Blue and red dots indicate individual simulation pairs.

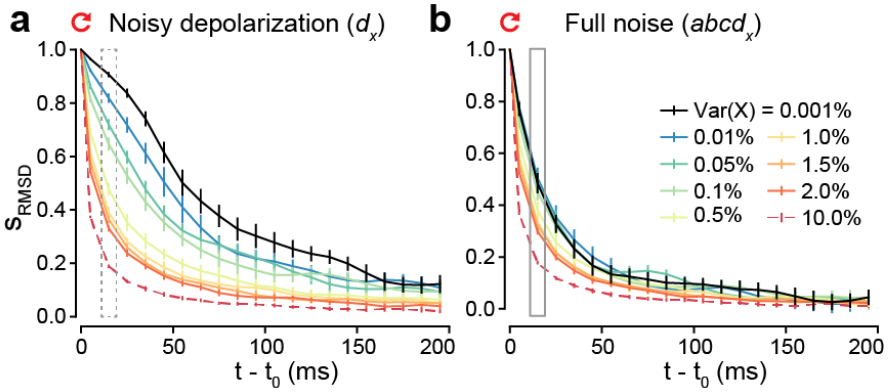

Figure 2.16 – Predicting impact of other noise sources. (**a**) Similarity s_{RMSD} when only changing random seeds for noisy depolarization, but with different magnitudes of noise. (**b**) As in **a**, but with all noise sources enabled by changing random seeds. Based on 10 saved base states; mean of base states ± 95% confidence interval.

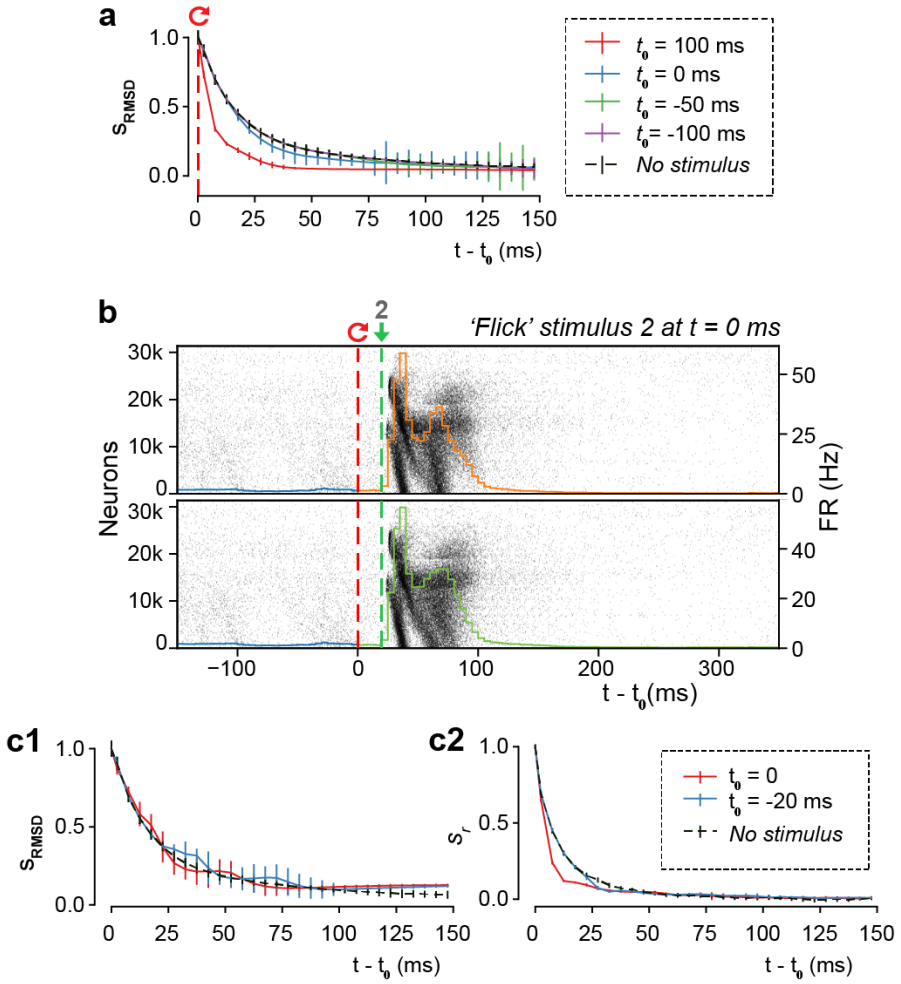

Figure 2.17 – Divergence of evoked activity. (**a**) The similarity s_{RMSD} defined as the difference between the $RMSD_V$ of diverging and independent trials, normalized to lie between 1 (identical) and 0 (fully diverged) (mean ± 95% confidence interval, 20 saved base states), for the thalamic stimulus. (**b**) Population raster plot and population peristimulus time histogram (PSTH) of all 31'346 neurons in the microcircuit, during evoked activity with a simplified "whisker flick" stimulus (60 VPM neurons are firing at the same time, one spike). (**c1**) As **a**, but for the "whisker flick" stimulus. (**c2**) As **c1**, but for s_r instead of s_{RMSD}.

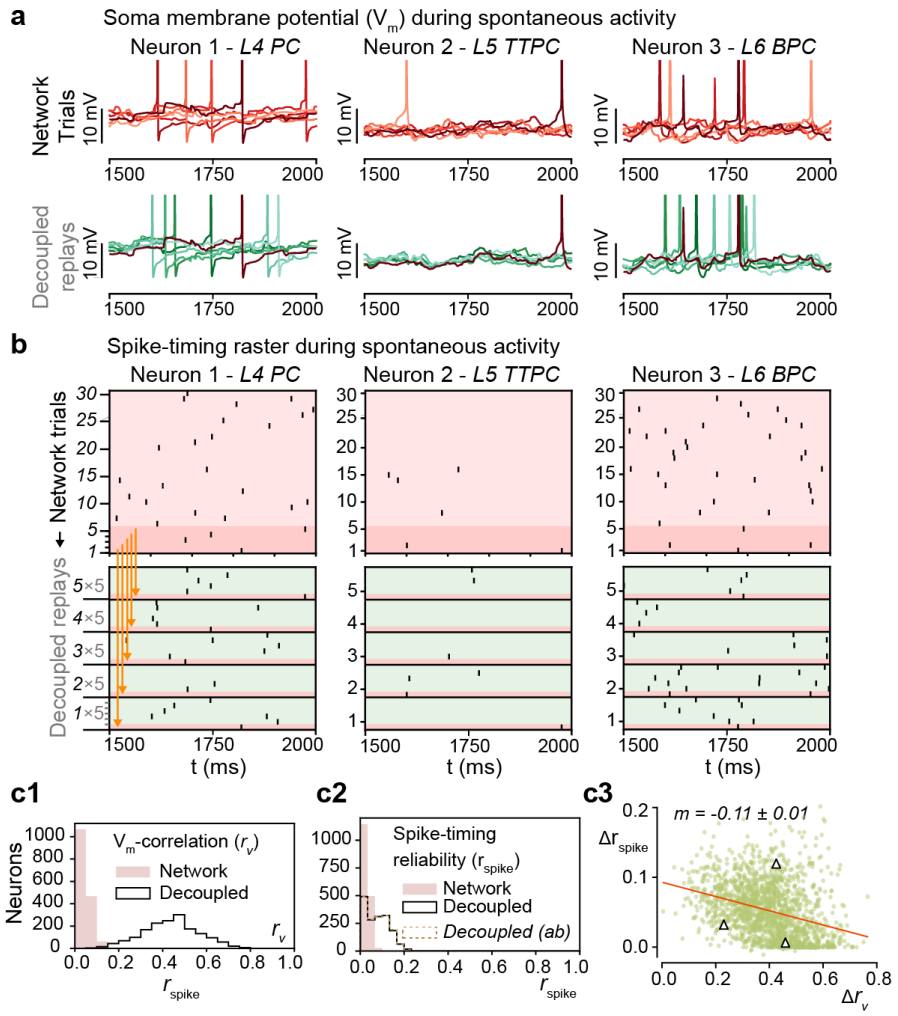

Figure 2.18 – Low trial-by-trial spike-timing reliability during spontaneous activity. (**a**) Somatic membrane potentials (V_m) of three representative neurons. Top: during six independent trials of spontaneous activity. Bottom: five decoupled replay trials (green) with the same presynaptic input as during the original network simulation trial (red), but with different random seeds. (**b**) Top: Raster plot of spike times for the same example neurons as in **a**, during 30 independent trials of spontaneous activity. Bottom: 5 decoupled replay trials (green) of the same input received during 5 of the 30 original trials (dark red). (**c1**) Mean somatic membrane potential correlation r_V of the 1666 (*ab*: 1670) most central (and spiking) pyramidal neurons from layers 4, 5, and 6 between independent network simulations, and between decoupled replay simulations with identical presynaptic inputs. (**c2**) Mean spike-timing reliability r_{spike} of the same neurons. Decoupled and decoupled (ab) are overlapping. (**c3**) Change in correlation, Δr_V, versus change in spike-timing reliability, Δr_{spike}, for each neuron for decoupled replay simulations relative to network simulations (linear fit with 68% confidence interval on slope m, red line). Triangles indicate values of representative neurons in panel B.

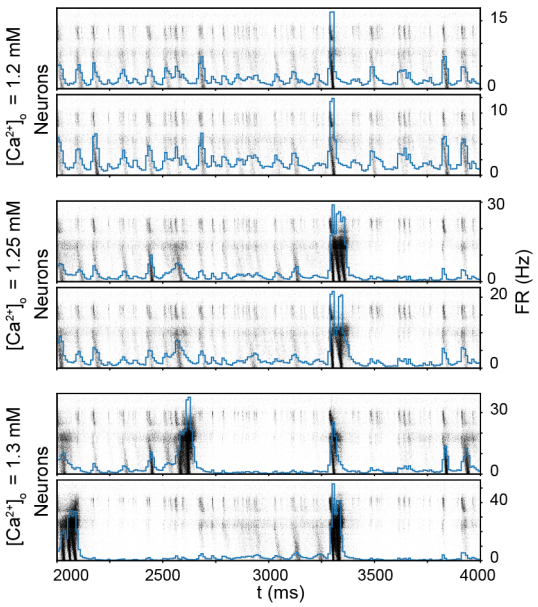

Figure 2.19 – Population response at different calcium concentrations. Spike raster of all neurons in the microcircuit and mean population firing rate for two trials of evoked activity with the same thalamic stimulus, for three different extracellular calcium concentrations.

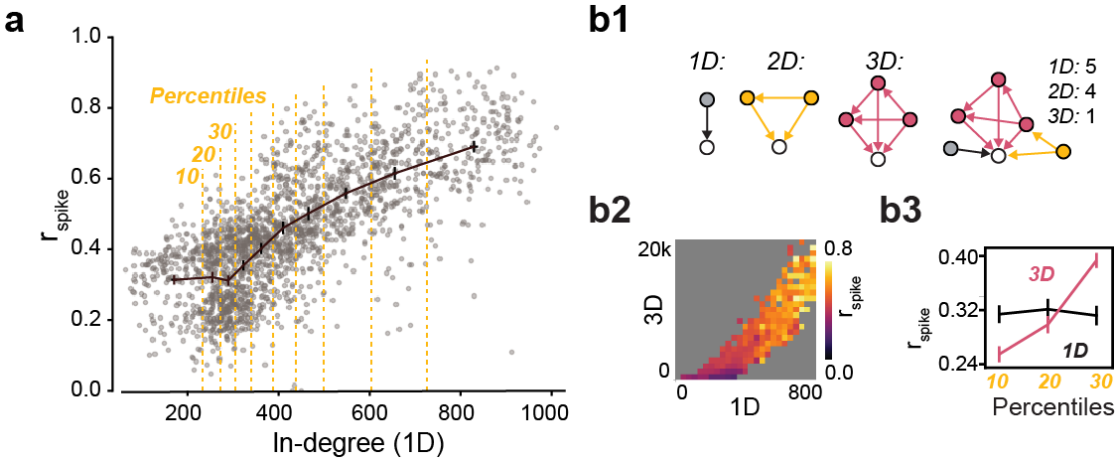

Figure 2.20 – In-degree and higher-dimensional connectivity. (**a**) In-degree (number of presynaptic connections) vs. spike-timing reliability, for the same neurons as in Figure 2.8. Mean of in-degree percentiles (the 10% of neurons with the lowest in-degree, the 10% of neurons with the 2nd lowest indegree, etc.). Error bars indicate 95%-confidence interval. (**b1**) Higher order connectivity. *1D*: number of presynaptic neurons (one-dimensional directed cliques). *2D*: number of two-dimensional directed cliques a neuron is the sink of. *3D*: Number of three-dimensional directed cliques a neuron is the sink of. Example network: the white neuron is the sink of 5 1D-cliques, 4 2D-cliques, and 1 3D-cliques, according to the definition of directed cliques to the left. (**b2**) In-degree (1D) vs. number of 3D-directed-cliques a neuron is the sink of (3D). Raster plot shows mean reliability of all neurons in a pixel. Grey indicates that no neuron falls in this pixel. (**b3**) The 30% of neurons with the lowest indegree in black (same as first three percentiles in **a**). Red: The same neurons reordered according to number of 3D-directed-cliques a neuron is the sink of.

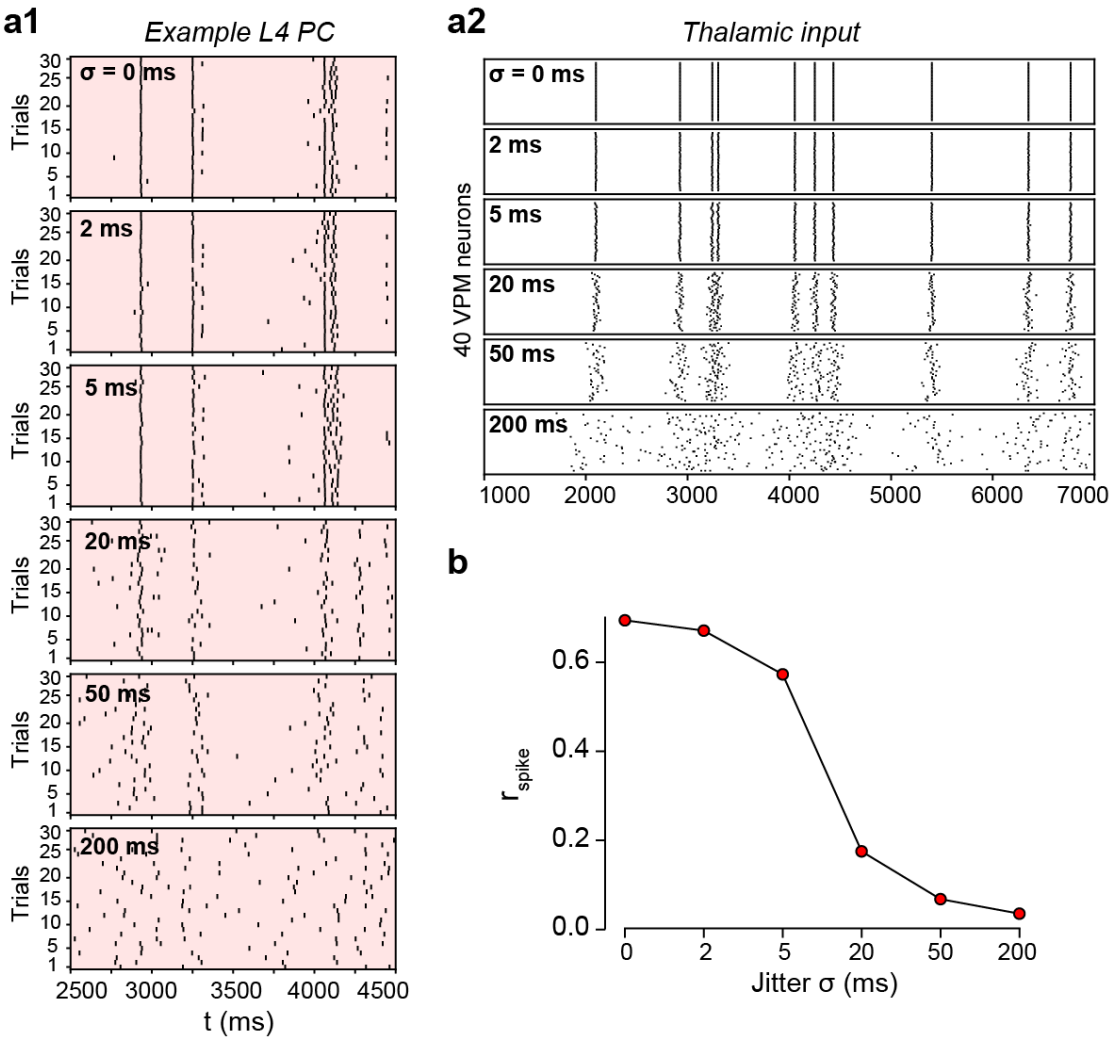

Figure 2.21 – Input synchrony and reliability. (**a1**) Response of a layer 4 pyramidal cell to a simple thalamic stimulus consisting of 40 synchronous spikes with increasing jitter (but frozen across trials). (**a2**) The thalamic stimulus, with increasing normally-distributed jitter with standard deviation σ. The stimulus is kept identical across 30 repetitions to study only intrinsic cortical variability, as before. (**b**) Mean spike-timing reliability of 2024 pyramidal neurons from layers 4, 5 and 6 (as before) versus jitter standard deviation σ (mean of 30 trials, 95%-CI smaller than marker symbols).

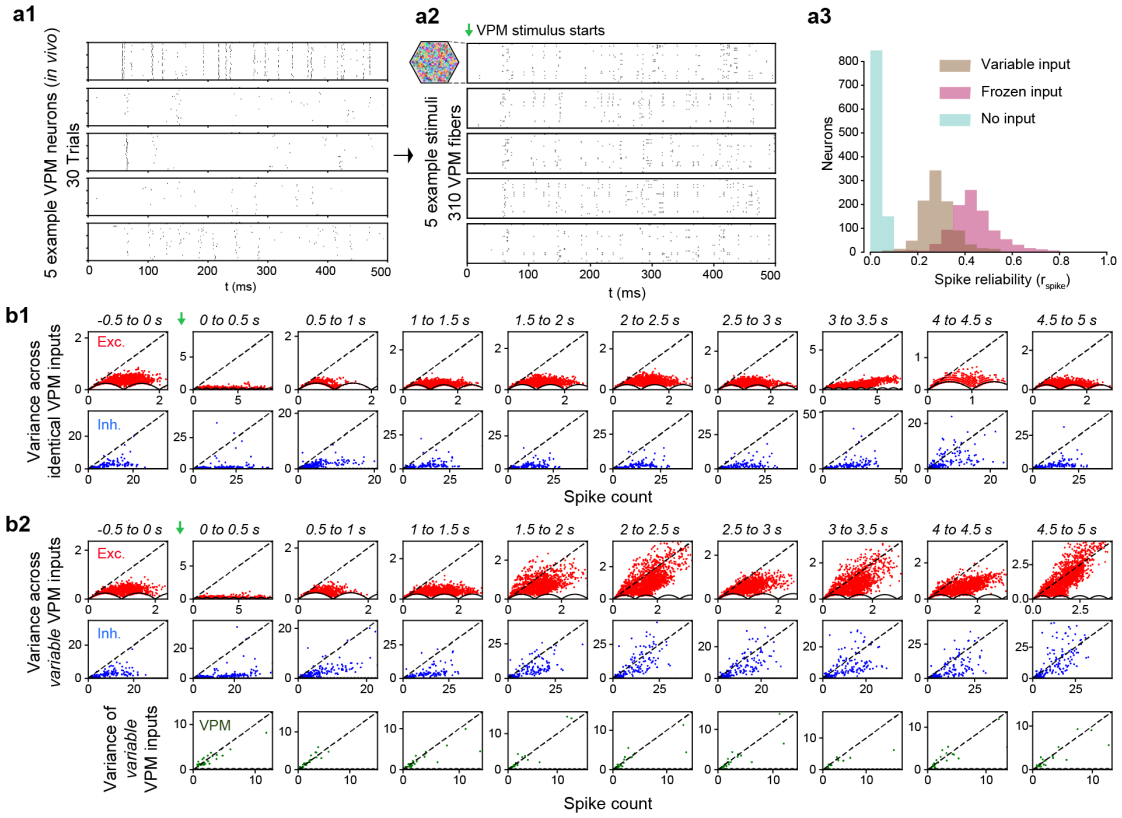

Figure 2.22 – Variable thalamic input. (**a1**) In vivo recordings of five thalamic neurons during 30 trials of replayed whisker deflection. (**a2**) Variable input created from in vivo recordings. (**a3**) Spike-timing reliability for no input (spontaneous activity), frozen input (same as Figures 2.5-2.8) and for variable input, for the same pyramidal neurons analyzed in Figures 2.5-2.8. (**b1**) Variance vs. mean spike count of all neurons in the microcircuit over 30 trials with identical inputs (same input as in Figures 2.5-2.8), for adjacent time bins of 500 ms duration. (**b2**) Variance vs. mean spike count with variable input, and Fano factors of VPM input, across 30 trials.

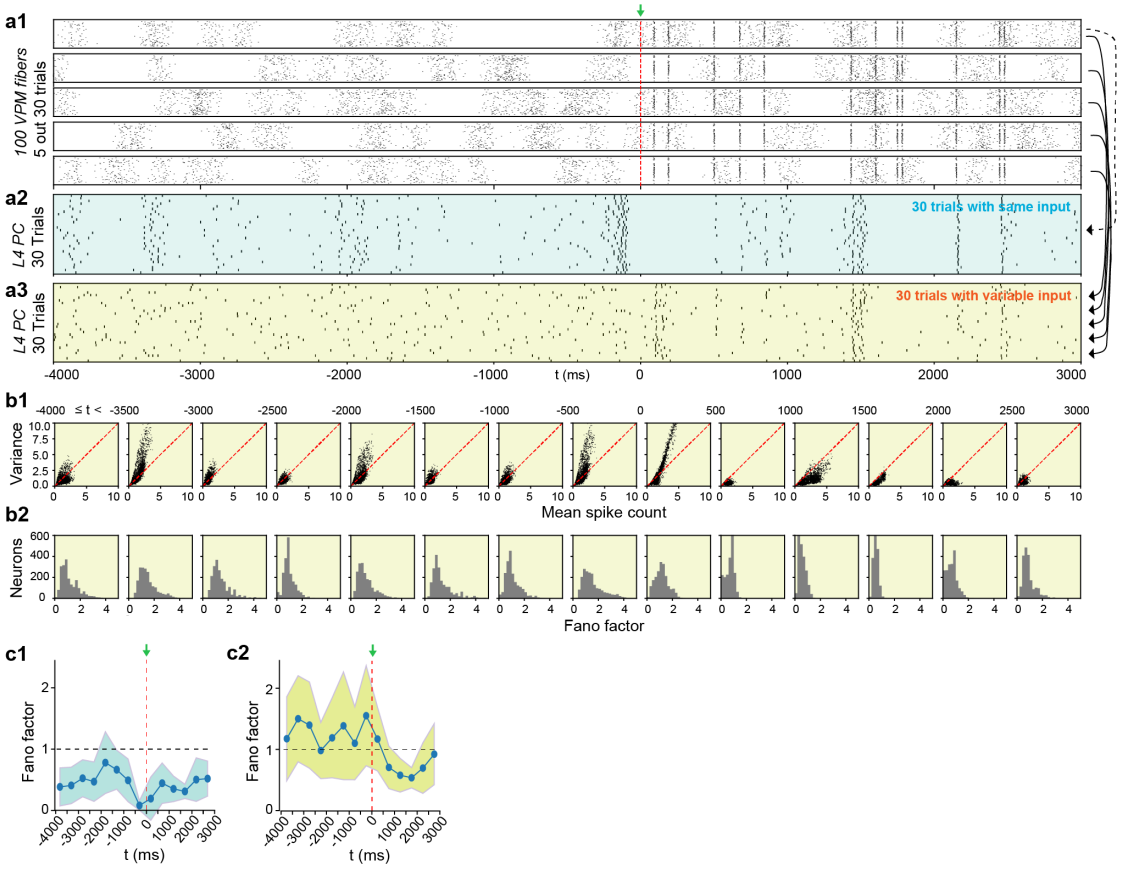

Figure 2.23 – Quenching of spike count variability. (**a1**) The central 100 VPM fibers innervating the microcircuit are activated with different inputs: 60 randomly chosen fibers contain variable inputs that are correlated between the fibers (Poisson-spike train, FR = 4 Hz, σ_{corr} = 50 ms), and different in each of 30 trials (5 shown). The other 40 fibers contain a reliable signal (FR = 4 Hz) of randomly distributed spikes, that is highly correlated between the fibers (σ_{corr} = 2 ms) and always arriving at roughly the same time between trials. The variable input lasts from -4000 to 3000 ms, whereas the reliable input only starts after t = 0 ms. (**a2**) Spike response of example L4 PC across 30 trials to *one* of the 30 inputs from **a1** (top stimulus). (**a3**) Spike response of same example L4 PC across 30 trials to *all* 30 inputs from a1. (**b1**) Variance of spike count vs. mean spike count of central 2024 excitatory neurons in layers 4, 5, and 6 (as before) for the 30 variable input trials, split in bins of 500 ms duration. (**b2**) Fano factors for the same neurons and time bins as in **b1**. (**c1**) Mean Fano factor (blue) and standard deviation (light blue) across trials with the same identical input. (**c2**) Mean Fano factor (blue) and standard deviation (green) of the neurons in **b1** and **b2** across trials with variable input.

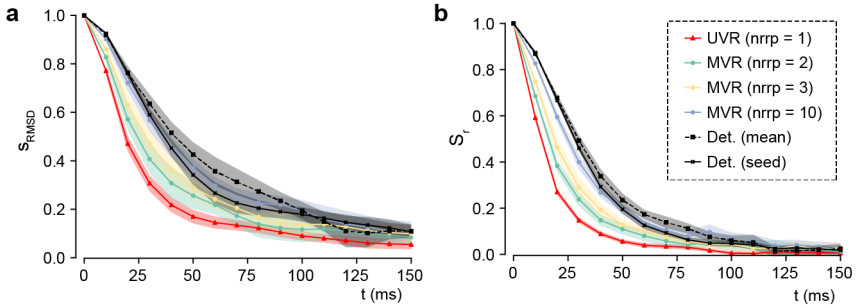

Figure 2.24 – Multivesicular release. Change in divergence time course depending on the size of the pool of readily releasable vesicles (n_{rrp}), quantified by similarity of the somatic membrane potentials diverging from identical initial conditions: (**a**) s_{RMSD} and (**b**) s_r. (mean of all neurons and n base states ± 95% confidence interval; UVR: $n = 40$; all others: $n = 20$).

3 Cliques of neurons bound into cavities

This chapter is a postprint of joint work with Michael W. Reimann, Martina Scolamiero, Katharine Turner, Rodrigo Perin, Giuseppe Chindemi, Paweł Dłotko, Ran Levi, Kathryn Hess and Henry Markram; it has been published as "*Cliques of neurons bound into cavities provide a missing link between structure and function*" in Frontiers in Computational Neuroscience (Reimann et al. (2017b); https://doi.org/10.3389/fncom.2017.00048).

Contribution: I applied custom software written by M.R. and P.D. to compute all connection matrices and all simplicial complexes. I designed the thalamic stimulus and ran all simulations of evoked activity. M.R. and I jointly contributed to the analysis in Figure 3.2. I solely performed the analysis of the simplicial architecture and how simplices shape correlations in Figures 3.3 and 3.4. I created Figure 3.6 jointly with M.R.. I assembled all final figures, other than Figure 3.1. The original draft was written jointly with M.R., R.L., K.H. and H.M.. Further author contributions are listed at the end of the chapter.

Summary

The lack of a formal link between neural network structure and its emergent function has hampered our understanding of how the brain processes information. We have now come closer to describing such a link by taking the direction of synaptic transmission into account, constructing graphs of a network that reflect the direction of information flow, and analyzing these directed graphs using algebraic topology. Applying this approach to a local network of neurons in the neocortex revealed a remarkably intricate and previously unseen topology of synaptic connectivity. The synaptic network contains an abundance of cliques of neurons bound into cavities that guide the emergence of correlated activity. In response to stimuli, correlated activity binds synaptically connected neurons into functional cliques and cavities that evolve in a stereotypical sequence towards peak complexity. We propose that the brain processes stimuli by forming increasingly complex functional cliques and cavities.

3.1 Introduction

How the structure of a network determines its function is not well understood. For neural networks specifically, we lack a unifying mathematical framework to unambiguously describe the emergent behavior of the network in terms of its underlying structure (Bassett and Sporns, 2017). While graph theory has been used to analyze network topology with some success (Bullmore and Sporns, 2009), current methods are usually constrained to analyzing how local connectivity influences local activity (Chambers and MacLean, 2016; Pajevic and Plenz, 2012) or global network dynamics (Hu et al., 2014), or how global network properties like connectivity and balance of excitatory and inhibitory neurons influence network dynamics (Renart et al., 2010; Rosenbaum et al., 2017). One such global network property is small-worldness. While it has been shown that small-worldness optimizes information exchange (Latora and Marchiori, 2001), and that adaptive rewiring during chaotic activity leads to small world networks (Gong and Leeuwen, 2004), the degree of small-worldness cannot describe most local network properties, such as the different roles of individual neurons.

Algebraic topology (Munkres, 1984) offers the unique advantage of providing methods to describe quantitatively both local network properties and the global network properties that emerge from local structure, thus unifying both levels. More recently, algebraic topology has been applied to functional networks between brain regions using fMRI (Petri et al., 2014) and between neurons using neural activity (Giusti et al., 2015), but the underlying synaptic connections (structural network) were unknown. Furthermore, all formal topological analyses have overlooked the direction of information flow, since they analyzed only undirected graphs.

We developed a mathematical framework to analyze both the structural and the functional topology of the network, integrating local and global descriptions, enabling us to establish a clear relationship between them. We represent a network as a directed graph, with neurons as the vertices and the synaptic connections directed from pre- to postsynaptic neurons as the edges, which can be analyzed using elementary tools from algebraic topology (Munkres, 1984). The structural graph contains all synaptic connections, while a functional graph is a sub-graph of the structural graph containing only those connections that are active within a specific time bin (i.e. in which a postsynaptic neuron fires within a short time of a presynaptic spike). The response to a stimulus can then be represented and studied as a time series of functional graphs.

Networks are often analyzed in terms of groups of nodes that are all-to-all connected, known as *cliques*. The number of neurons in a clique determines its size, or more formally, its *dimension*. In directed graphs it is natural to consider *directed cliques*, which are cliques containing a single source neuron and a single sink neuron and reflecting a specific *motif* of connectivity (Perin et al., 2011; Song et al., 2005), wherein the flow of information through a group of neurons has an unambiguous direction. The manner in which directed cliques bind together can be represented geometrically. When directed cliques bind appropriately by sharing neurons, and without forming a larger clique due to missing connections, they form

cavities ("*holes*", "*voids*") in this geometric representation, with high-dimensional cavities forming when high-dimensional (large) cliques bind together. Directed cliques describe the flow of information in the network at the local level, while cavities provide a global measure of information flow in the whole network. Using these naturally arising structures, we established a direct relationship between the structural graph and the emergent flow of information in response to stimuli, as captured through time series of functional graphs.

We applied this framework to digital reconstructions of rat neocortical microcircuitry that closely resemble the biological tissue in terms of the numbers, types, and densities of neurons and their synaptic connectivity (a "microconnectome" model for a cortical column, Figures 3.1A and 3.1B, see Markram et al. (2015); Reimann et al. (2015)). Simulations of the reconstructed microcircuitry reproduce multiple emergent electrical behaviors found experimentally in the neocortex (Markram et al., 2015). The microcircuit, formed by ~8 million connections (edges) between ~31'000 neurons (vertices), was reconstructed from experimental data, guided by biological principles of organization, and iteratively refined until validated against a battery of independent anatomical and physiological data obtained from experiments. Multiple instantiations of the reconstruction provide a statistical and biological range of microcircuits for analysis.

We found a remarkably high number and variety of high-dimensional directed cliques and cavities, which had not been seen before in neural networks, either biological or artificial, and in far greater numbers than those found in various null models of directed networks. Topological metrics reflecting the number of directed cliques and cavities not only distinguished the reconstructions from all null models, they also revealed subtle differences between reconstructions based on biological datasets from different animals, suggesting that individual variations in biological detail of neocortical microcircuits are reflected in the repertoire of directed cliques and cavities. When we simulated microcircuit activity in response to sensory stimuli, we observed that pairwise correlations in neuronal activity increased with the number and dimension of the directed cliques to which a pair of neurons belongs, indicating that the hierarchical structure of the network shapes a hierarchy of correlated activity. In fact, we found a hierarchy of correlated activity between neurons even within a single directed clique. During activity, many more high-dimensional directed cliques formed than would be expected from the number of active connections, further suggesting that correlated activity tends to bind neurons into high-dimensional active cliques.

Following a spatio-temporal stimulus to the network, we found that during correlated activity, active cliques form increasingly high-dimensional cavities (i.e. cavities formed by increasingly larger cliques). Moreover, we discovered that while different spatio-temporal stimuli applied to the same circuit and the same stimulus applied to different circuits produced different activity patterns, they all exhibited the same general evolution, where functional relationships among increasingly higher dimensional cliques form and then disintegrate.

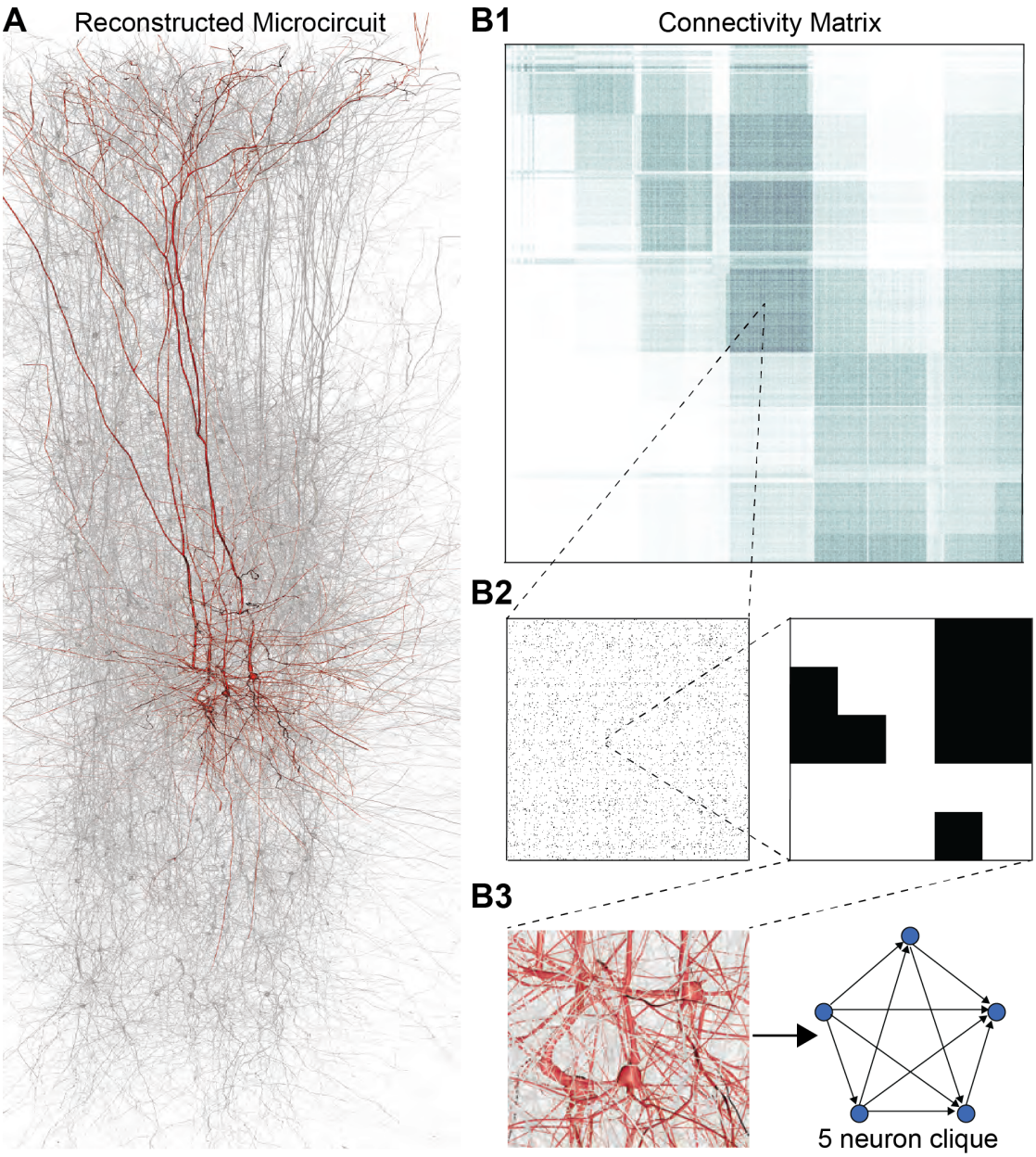

Figure 3.1 – A: Thin (10 μm) slice of a in silico reconstructed tissue. Red: A clique formed by five pyramidal cells in layer 5. **B1**: Full connection matrix of a reconstructed microcircuit with 31'146 neurons. Neurons are sorted by cortical layer and morphological type within each layer. Pre-/postsynaptic neurons along the vertical/horizontal axis. Each grayscale pixel indicates the connections between two groups of 62 neurons each, ranging from white (no connections) to black (≥8% connected pairs). **B2**: Zoom into the connectivity between two groups of 434 neurons each in layer 5, i.e., 7 by 7 pixels in **A**, followed by a further zoom into the clique of 5 neurons shown in **A**. Black indicates presence, and white absence of a connection. **B3**: Zoom into the somata of the clique in A and representation of their connectivity as a directed graph.

3.2 Results

3.2.1 The case for directed simplices

Networks of neurons connected by electrical synapses (gap junctions) can be represented as undirected graphs, where information can flow in both directions. Networks with chemical synapses, which impose a single direction of synaptic communication from the pre- to the postsynaptic neuron (Figures 3.1B2 and B3), are more accurately represented as directed graphs. Sub-sampling networks of neurons experimentally has revealed small motifs of synaptic connectivity, but not large cliques of neurons (Perin et al., 2011; Song et al., 2005). Knowing the complete directed network of neurons, as we do in the case of the microcircuit, enables us to detect all cliques, directed and otherwise (Figure 3.1).

When the direction of connections is not taken into account, a great deal of information is lost. For example, in the undirected case, there is only one possible configuration for a clique of four fully connected neurons (Figure 3.2A1, left). However, in the directed case, there are $3^6 = 729$ possible configurations, as each of the six connections can be in one of three states (i $\rightarrow$ j, j $\leftarrow$ i, or i $\leftrightarrow$ j connection types; Figure 3.2A1 right).

A clique with reciprocal connections contains two or more cliques consisting only of uni-directional connections (Figure 3.2A2). When only uni-directional connections are considered, there are 2^6 possible configurations of four fully connected neurons, which are of two types: those that contain cycles (40 configurations; Figure 3.2A3 left; Materials and Methods 3.4.1) and those that do not (24 configurations; Figure 3.2A3 right). Directed cliques are exactly the acyclic cliques. The *net directionality* of information flow through any motif can be defined as the sum over all neurons of the squares of the differences between their in-degree and their out-degree (see Equation 3.2, Figure S3.7). Directed cliques have the highest net directionality among all cliques with no reciprocal connections (Figure S3.7; Materials and Methods 3.4.1). A clique that contains cycles always decomposes into directed cliques with the same number of neurons or fewer, at the very least any single connection between two neurons forms a 2-clique. A cyclical clique of three neurons therefore decomposes into three 2-cliques. Following the conventions in algebraic topology, we refer to directed cliques of n neurons as *directed simplices of dimension n-1* or *directed (n-1)-simplices* (which reflects their natural geometric representation as (n-1)-dimensional polyhedra) (see Figure S3.8; Materials and Methods 3.4.1). Correspondingly, their sub-cliques are called *sub-simplices*.

3.2.2 An abundance of directed simplices

Reconstructed neocortical microcircuitry

We analyzed 42 variants of the reconstructed microconnectome, grouped into six sets, each comprised of seven statistically varying instantiations (Markram et al. (2015); Materials and Methods 3.4.3). The first five sets were based on specific heights of the six layers of the

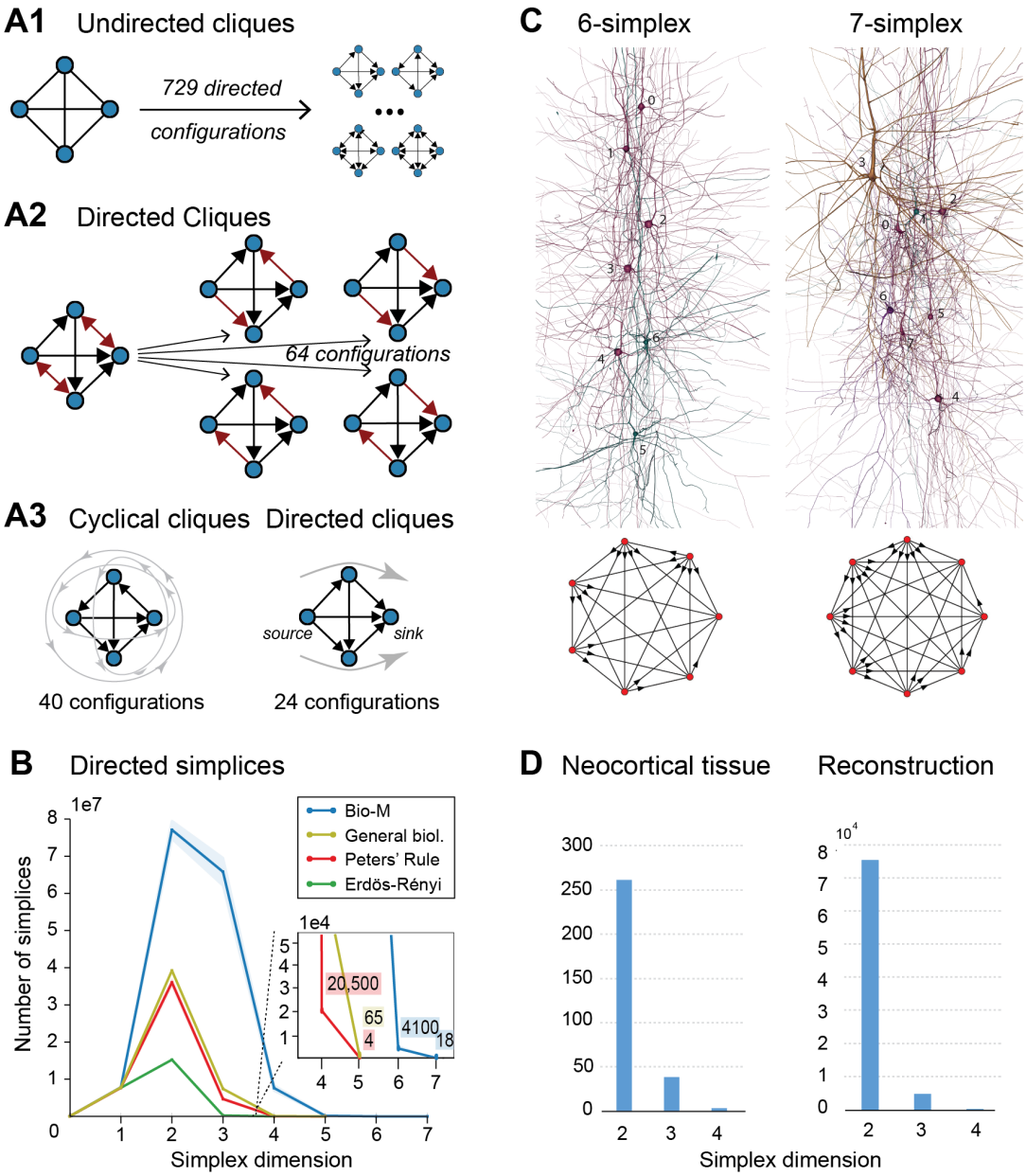

Figure 3.2 – A1: A 4-clique in the undirected connectivity graph has one of 729 *configurations* in the directed graph. **A2**: Configurations containing bidirectional connections are resolved by considering all sub-graphs without bidirectional connections. **A3**: Without bidirectional connections 64 possible configurations remain, 24 of which are acyclic, with a clear sink-source structure (*directed simplices*, in this case of dimension 3). **B**: Number of simplices in each dimension in the reconstruction (shaded area: standard deviation of seven instances) and in three types of random control networks. **C**: Examples of neurons forming high-dimensional simplices in the reconstruction. Bottom: Their representation as directed graphs. **D**: (Left) Number of directed simplices of various dimensions found in 55 in vitro patch-clamp experiments sampling groups of pyramidal cells in layer 5. (Right) Number of simplices of various dimensions found in 100'000 in silico experiments mimicking the patch-clamp procedure.

neocortex, cell densities, and distributions of different cell types experimentally measured in five different rats (Bio1-5), while the sixth represents the mean of these measurements (Bio-M). Individual instantiations within a set varied with the outcome of the stochastic portions of the reconstruction process. Surprisingly, we found that the reconstructions consistently contained directed simplices of dimensions up to 6 or 7, with as many as 80 million directed 3-simplices (Figure 3.2B; blue). This is the first indication of the existence of such a vast number of high-dimensional directed simplices in the neocortical microcircuitry, or in any neural network.

Control models

To compare these results with null models, we examined how the numbers of directed simplices in these reconstructions differed from those of artificial circuits and from circuits in which some of the biological rules of connectivity were omitted (see Materials and Methods 3.4.4). For one control, we generated five Erdős-Rényi random graphs (ER) of equal size (~31'000 vertices) and the same average connection probability as the Bio-M circuit (~0.8%; ~8 million edges) (Figure 3.2B; dark green). For another, we constructed a circuit with the same 3D model neurons as the Bio-M circuit, but connected the neurons using a random connectivity rule ("Peters' Rule" (Peters and Feldman, 1976), PR; Figure 3.2B, red). For the last control we connected the neurons in the Bio-M circuit according to the distance-dependent connection probabilities between the different morphological types of neurons. Since this control is similar to deriving connectivity from the average overlap of neuronal arbors (Shepherd et al., 2005), it retains the general biological (GB) features of connectivity between different types of neurons (Reimann et al., 2015), excluding only explicit pairwise connectivity between individual neurons, which is determined by the overlap of their *specific* arbors (Figure 3.2B, yellow). In all cases, the number of directed simplices of dimensions larger than 1 was far smaller than in the Bio-M circuit. In addition, the relative differences between the Bio-M and the null models increased markedly with dimension.

In vitro

Simplices of high dimensions (such as those depicted in Figure 3.2C) have not yet been observed experimentally, as doing so would require simultaneous intracellular recording of large numbers of neurons. To obtain an indication of the presence of many high-dimensional directed simplices in the actual neocortical tissue, we performed multi-neuron patch-clamp experiments with up to 12 neurons at a time in in vitro slices of the neocortex of the same age and brain region as the digitally reconstructed tissue (Materials and Methods 3.4.5). Although limited by the number of neurons we could simultaneously record from, we found a substantial number of directed simplices up to dimension 4 in just 55 multi-neuron recording experiments (Figure 3.2D, left). We then mimicked these experiments on the reconstructed microcircuit by repeating the same multi-neuron patch-clamp recordings in silico (Materials and Methods 3.4.5) and found a similar shape of the distribution of 4-, 3- and 2-simplices, though in lower

frequencies than in the actual tissue (Figure 3.2D, right). These findings not only confirm that high-dimensional directed simplices are prevalent in the neocortical tissue, they also suggest that the degree of organization in the neocortex is even greater than that in the reconstruction, which is already highly significant (see Discussion).

C. elegans

To test whether the presence of large numbers of high-dimensional directed simplices is a general phenomenon of neural networks rather than a specific phenomenon found in this part of the brain of this particular animal and at this particular age, we computed the numbers of directed simplices in the C. elegans connectome (Varshney et al., 2011) (Materials and Methods 3.4.6). Again, we found many more high-dimensional simplices than expected from a random circuit with the same number of neurons (Figure S3.9).

Simplicial architecture of neocortical microcircuitry

To understand the simplicial architecture of the microcircuit, we began by analyzing the sub-graphs formed only by excitatory neurons, only by inhibitory neurons, and only in individual layers by both excitatory and inhibitory neurons. Restricting to only excitatory neurons barely reduces the number of simplices in each dimension (Figure 3.3A1), while simplex counts in inhibitory sub-graphs are multiple orders of magnitude smaller (Figure 3.3A2), consistent with the fact that most neurons in the microcircuitry are excitatory. Analyzing the sub-graphs of the layers in isolation shows that layers 5 and 6, where most of the excitatory neurons reside (Markram et al., 2015), contain the most simplices and the largest number of high-dimensional simplices (Figure 3.3A3).

The large number of simplices relative to the number of neurons in the microcircuit implies that each neuron belongs to many directed simplices. Indeed, when we counted the number of simplices to which each neuron belongs across dimensions, we observed a long-tailed distribution such that a neuron belongs on average to thousands of simplices (Figure 3.3B). Both the mean maximal dimension and the number of simplices a neuron belongs to are highest in the deeper cortical layers (Figure 3.3C). Neurons in layer 5 belong to the largest number of simplices, many spanning multiple layers (Figure 3.3D), consistent with the abundance of neurons with the largest morphologies, which are connected to all layers. On the other hand, layer 6 has the largest number of simplices that are fully contained in the layer (Figure 3.3A3), consistent with the fact that layer 6 contains the most neurons. While the number of simplices that can form in the microcircuitry depends essentially on the number of neurons, the number of simplices to which a single neuron belongs depends fundamentally on its number of incoming and outgoing connections (its *degree*), which in turn depends on its morphological size (Figure 3.3E).

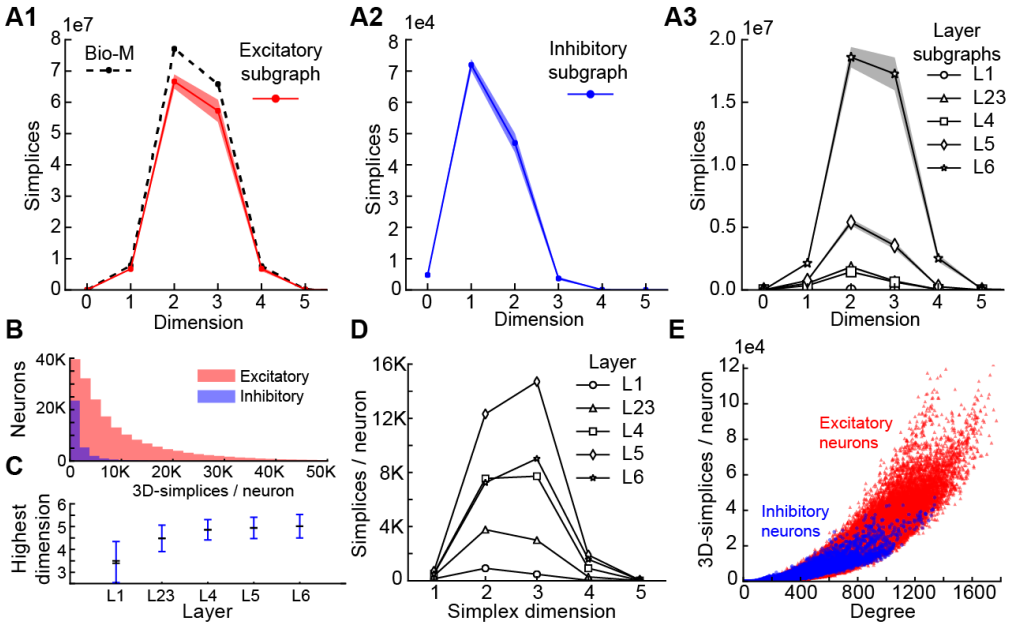

Figure 3.3 – A1: Number of simplices in each dimension in the excitatory subgraph (shaded area: standard deviation across seven instantiations). **A2**: Same, for the inhibitory subgraph. **A3**: Same, for the subgraphs of individual layers. **B**: Distribution across seven instantiations of the complete graph of the number of 3-simplices an excitatory (red) or inhibitory (blue) neuron belongs to (simplices / neuron). **C**: Mean over neurons in individual layers of the highest dimension of a simplex that they belong to. **D**: Correlation of 3-simplices / neuron and degree in the graph for all neurons. **E**: Simplices / neuron by layer and dimension.

3.2.3 Topology organizes spike correlations

The presence of vast numbers of directed cliques across a range of dimensions in the neocortex, far more than in null models, demonstrates that connectivity between these neurons is highly organized into fundamental building blocks of increasing complexity. Since the structural topology of the neural network takes into account the direction of information flow, we hypothesized that emergent electrical activity of the microcircuitry mirrors its hierarchical structural organization. To test this hypothesis, we simulated the electrical activity of the microcircuit under in vivo-like conditions (Markram et al., 2015).

Stimuli, configured as nine different spatio-temporal input patterns (Figure 3.4A), were injected into the reconstructed microcircuit through virtual thalamo-cortical fibers in which spike trains were induced using patterns recorded in vivo (Bale et al. (2015); Figure S3.10; Materials and Methods 3.4.7). These stimuli differed primarily in the degree of synchronous input received by the neurons. As expected, the neurons in the microcircuit responded to the inputs with various spiking patterns, in a manner that depended on their positions within simplices (Figures 3.4B1 and 3.4B4). We then calculated for each connected pair of neurons the correlation of their spiking activity (Figure 3.4C) and found a broad distribution of correlation coefficients, with only ~12% of connections where either the pre- or postsynaptic neuron

failed to respond during all stimuli.

To avoid redundant sampling when testing the relationship between simplex dimension and activity, we restricted our analysis to *maximal simplices*, i.e., directed simplices that are not part of any higher-dimensional simplex (Materials and Methods 3.4.1). A connection can be part of many higher dimensional maximal simplices, unless it is itself a maximal 1-simplex. Despite the restriction to maximal simplices, we retained all information about the structure of the microcircuit because the complete structure is fully determined by its list of maximal simplices (Materials and Methods 3.4.1). Correlations were calculated from histograms of the average spiking response (peri-stimulus time histogram, PSTH; bin size, 25 ms) to five seconds of thalamo-cortical input over 30 repetitions of a given input pattern (Figure 3.4B3). We then calculated the normalized cross-covariance of the histograms for all connections (Figure 3.4B4; Materials and Methods 3.4.8) and compared it to the number of maximal simplices associated with each connection in each dimension (see Figure 3.4D).

The neurons forming maximal 1-simplices displayed a significantly lower spiking correlation than the mean (Figure 3.4D), an indication of the fragility and lack of integration of the connection into the network. The mean correlation initially decreased with the number of maximal 2-simplices a connection belongs to, and then increased slightly. We observed that the greater the number of maximal 2-simplices a connection belongs to, the less likely it is to belong to higher dimensional maximal simplices, with the minimum correlation occurring when no connection belongs to any simplices of dimension higher than 3. In higher dimensions, the correlation increased with the number of maximal simplices to which a connection belongs. While very high mean correlation can be attained for connections belonging to many maximal 3- or 4-simplices, the mean correlation of connections belonging to just one maximal 5- or 6-simplex was already considerably greater than the mean. These findings reveal a strong relationship between the structure of the network and its emergent activity and specifically that spike correlations depend on the level of participation of connections in high-dimensional simplices.

To determine the full extent to which the topological structure could organize activity of neurons, we examined spike correlations between pairs of neurons within individual simplices. These correlations increased with simplex dimension (Figure 3.4E, blue), again demonstrating that the degree of organization in the activity increases with structural organization. Spike correlation between pairs of neurons is normally an ambiguous measurement of connection strength because it is influenced by the local structure, specifically by indirect connections and/or shared inputs (Brody, 1999; Palm et al., 1988). However, since in our case the local structure is known and described in terms of directed simplices, we could infer how the local structural organization influences spike correlations. We compared the impact of indirect connections and of shared inputs on correlated activity by calculating the average correlation of pairs of neurons at different positions in a simplex when ordered from source to sink (Figure 3.4E, right panel). The number of indirect connections is highest for the pair consisting of the first (source) and last (sink) neurons (Figure 3.4E, purple), while the number of shared

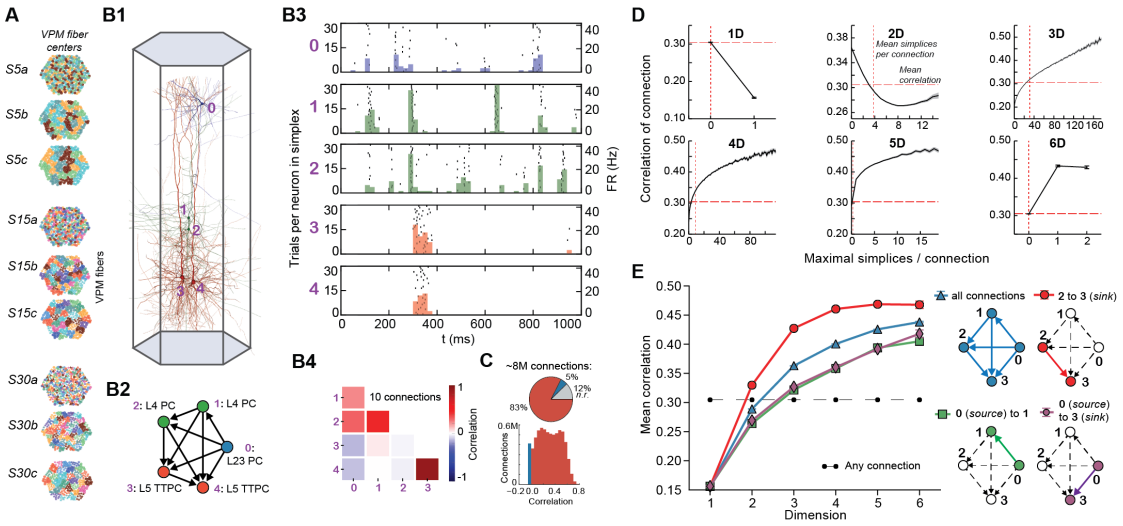

Figure 3.4 – A: Patterns of thalamic innervation in the reconstruction. Each circle represents the center of innervation of a thalamic fiber. Each color represents a unique thalamic spike train assigned to that fiber. **B1**: Exemplary directed simplex in a microcircuit. **B2**: Connectivity and morphological types of neurons in the exemplary simplex. **B3**: Raster plot and PSTH (Δt =10 ms) of spiking response of neurons in B1,2 to stimulus S30b. **B4**: Correlation coefficients of all pairs of PSTHs in B3. **C**: Correlation coefficients of PSTHs for all stimuli and all connected pairs of neurons in a microcircuit (Δt =25 ms). **D**: Mean correlation coefficients for connected pairs of neurons against the number of maximal simplices the edge between them belongs to, dimension by dimension. Means of fewer than 1000 samples omitted. **E**: Mean correlation coefficient of pairs of neurons, given their position within a simplex and its dimension.

inputs is highest for the last and second-to-last neurons (Figure 3.4E, red). The first (source) and second neurons (Figure 3.4E, green) serve as a control because they have the smallest numbers of both indirect connections and shared inputs in the simplex.

We found that correlations were significantly higher for the last two neurons in the simplex, suggesting that shared input generates more of the pairwise correlation in spiking than indirect connections in directed simplices ($p < 8{\cdot}10^{-6}$, all dimensions except 1D). Moreover, the spiking correlation of the source and sink neurons was similar to the correlation of the first and second neurons (Figure 3.4E, green and purple), further suggesting that spike correlations tend to increase as shared input increases. These results hold for a range of histogram time bin sizes (Figure S3.11). The specific positions of neurons in local structures such as directed simplices therefore shape the emergence of correlated activity in response to stimuli.

3.2.4 Cliques of neurons bound into cavities

Simplices are the mathematical building blocks of the microcircuitry. To gain insight into how its global structure shapes activity, it is necessary to consider how simplices are bound

together. This can be achieved by analyzing the *directed flag complex*, which is the set of all directed simplices, together with the set of all sub-simplices for each simplex (Figure S3.12, Materials and Methods 3.4.1). The directed flag complex is a complete representation of the graph, including in particular the cycles neglected when examining directed simplices in isolation. The relationship between any two directed simplices depends on how they share sub-simplices. Just as any simplex can be realized as a polyhedron, a directed flag complex can be realized as a geometric object, built out of these polyhedra. If two simplices share a sub-simplex, the corresponding polyhedra are glued together along a common face (Figure 3.5A). The "shape" (or, more precisely, the topology) of this geometric object fully describes the global structure of the network.

To analyze directed flag complexes we computed two descriptors, the *Euler characteristic* and *Betti numbers* (Materials and Methods 3.4.1). The Euler characteristic of a flag complex is given by the alternating sum of the number of simplices in each dimension, from zero through the highest dimension (Figure 3.5A). The Betti numbers together provide an indication of the number of cavities (or more precisely, *homology classes*) fully enclosed by directed simplices in the geometric object realizing the directed flag complex, where the dimension of a cavity is determined by the dimension of the enclosing simplices. The n^{th} Betti number, denoted β_n, indicates the number of n-dimensional cavities. For example, in Figure 3.5A, there is one 2-dimensional cavity (and therefore $\beta_2 = 1$) enclosed by the eight triangles; if an edge were added between any two non-connected nodes, then the geometric object realizing the corresponding flag complex would be filled in with solid tetrahedra, and the cavity would disappear. In the flag complexes of the reconstructions, it was not possible to compute more than the zero and top nonzero Betti numbers, as lower dimensions were computationally too expensive (Materials and Methods 3.4.2). We could easily compute all Betti numbers for the C. elegans connectome, however, as it has many fewer nodes and edges (Figure S3.9).

The Betti number computations showed that there are cavities of dimension 5 (cavities completely enclosed by 5-simplices/six-neuron directed cliques) in all seven instances of each of the reconstructions (Bio1-Bio5, Figure 3.5B; Bio-M not shown). In contrast, the ER- and PR-control models have no cavities of dimension higher than 3, and the GB-model has no cavities of dimension higher than 4, demonstrating that there are not only non-random building blocks in the reconstruction, but also non-random relationships among them. We found as well that the information encoded in β_5 and the Euler characteristic together captures enough of the structure of the flag complex of a reconstruction to reveal subtle differences in their connectivity arising from the underlying biological data (Figure 3.5B, different colors).

3.2.5 Cliques and cavities in active sub-graphs

Thus far we have shown that the structural network guides the emergence of correlated activity. To determine whether this correlated activity is sufficiently organized to bind neurons together to form active cliques and cliques together to form active cavities out of the structural graph,

we represented the spiking activity during a simulation as a time series of sub-graphs for which we computed the corresponding directed flag complexes. Each sub-graph in this series comprises the same nodes (neurons) as the reconstruction, but only a subset of the edges (synaptic connections), which are considered *active*, i.e., the presynaptic neuron spikes in a time bin of size Δt_1 and the postsynaptic neuron spikes within a time Δt_2 after the presynaptic spike (Figures 3.5C and S3.13, Materials and Methods 3.4.9). By considering subsequent, non-overlapping time bins of constant size Δt_1, we obtain a time series of *transmission-response* (TR) graphs reflecting correlated activity in the microcircuitry. We converted the time series of TR graphs in response to the different patterns of thalamo-cortical inputs (see Figure 3.4A) into time series of directed flag complexes. We found significantly more simplices in the TR graphs ($\Delta t_1 = 5$ ms, $\Delta t_2 = 10$ ms) than would be expected based on the number of edges alone (Figure 3.5D), indicating that correlated activity becomes preferentially concentrated in directed simplices.

The nine stimuli generated different spatio-temporal responses and different numbers of active edges (Figure 3.6A). The variation in Betti numbers and Euler characteristic over time indicates that neurons become bound into cliques and cavities by correlated activity (Figures 3.6A and S3.14). When we plotted the number of cavities of dimension 1 (β_1) against the number of those of dimension 3 (β_3) (the highest dimension in which cavities consistently occur), the trajectory over the course of approximately 100 ms (Figure 3.6B) began ~50 ms after stimulus onset with the formation of a large number of 1-dimensional cavities, followed by the emergence of 2-dimensional (not shown) and 3-dimensional cavities. The decrease in β_1 began while β_3 was still increasing and continued until β_3 reached its peak, indicating that higher dimensional relationships between directed simplices continued to be formed by correlated activity as the lower dimensional relationships subside.

Different stimuli led to Betti number trajectories of different amplitudes, where higher degrees of synchrony in the thalamic input produced higher amplitudes. The trajectories all followed a similar progression of cavity formation towards a peak level of functional organization followed by relatively rapid disintegration. The center of the projection of each trajectory onto the β_1-axis (its β_1-center) was approximately the same. Together, these characteristics of the trajectories reveal a stereotypical evolution of cliques and cavities in response to stimuli. These observations are consistent with experimentally recorded in vivo responses to sensory stimuli in terms of onset delay, response duration, and the presence of distinct phases of the response (Luczak et al., 2015).

To determine the neurons involved in this robust evolution of functional organization, we recorded the mean levels of spiking activity at different spatial locations within the microcircuit for one exemplary stimulus (Figure 3.6C). The activity started at depths that correspond to the locations of the thalamo-cortical input (Markram et al., 2015; Meyer et al., 2010), increasing in layer 4 and at the top of layer 6, before propagating downwards, reaching the top of layer 5 and the center of layer 6 as β_1 peaks, consistent with the finding that most directed simplices are in these layers. The transition from increasing β_1 to increasing β_3 coincided with the

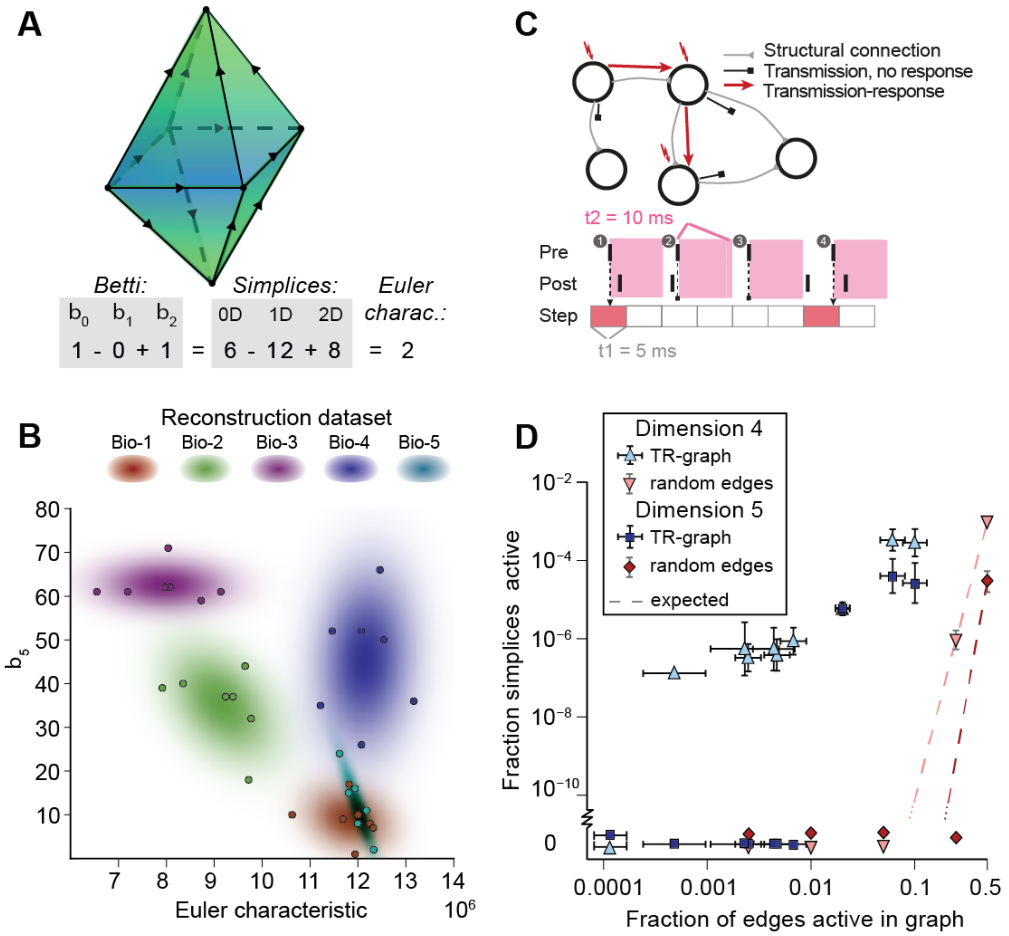

Figure 3.5 – A: Example of the calculation of the Euler characteristic of a directed flag complex as an alternating sum of Betti numbers or simplex counts. **B**: Euler characteristic against the highest non-zero Betti number (β_5) for seven instances of reconstructed microcircuits based on five different biological datasets (Bio 1-5). **C**: Top: The transmission-response (TR) graph of the activity of a microcircuit is a subgraph of its structural connectivity containing all nodes, but only a subset of the edges (connections). Bottom: An edge is contained if its presynaptic neuron spikes in a defined time bin and its postsynaptic neurons spikes within 10 ms of the presynaptic spike. **D**: Fraction of edges active against fraction of high-dimensional simplices active in TR graphs for various time bins of a simulation. Error bars indicate the standard deviation over 10 repetitions of the simulation. Blue triangles: 4-dimensional simplices, blue squares: 5-dimensional simplices. Red symbols and dashed lines indicate the results for choosing edges randomly from the structural graph and the number expected for random choice, respectively.

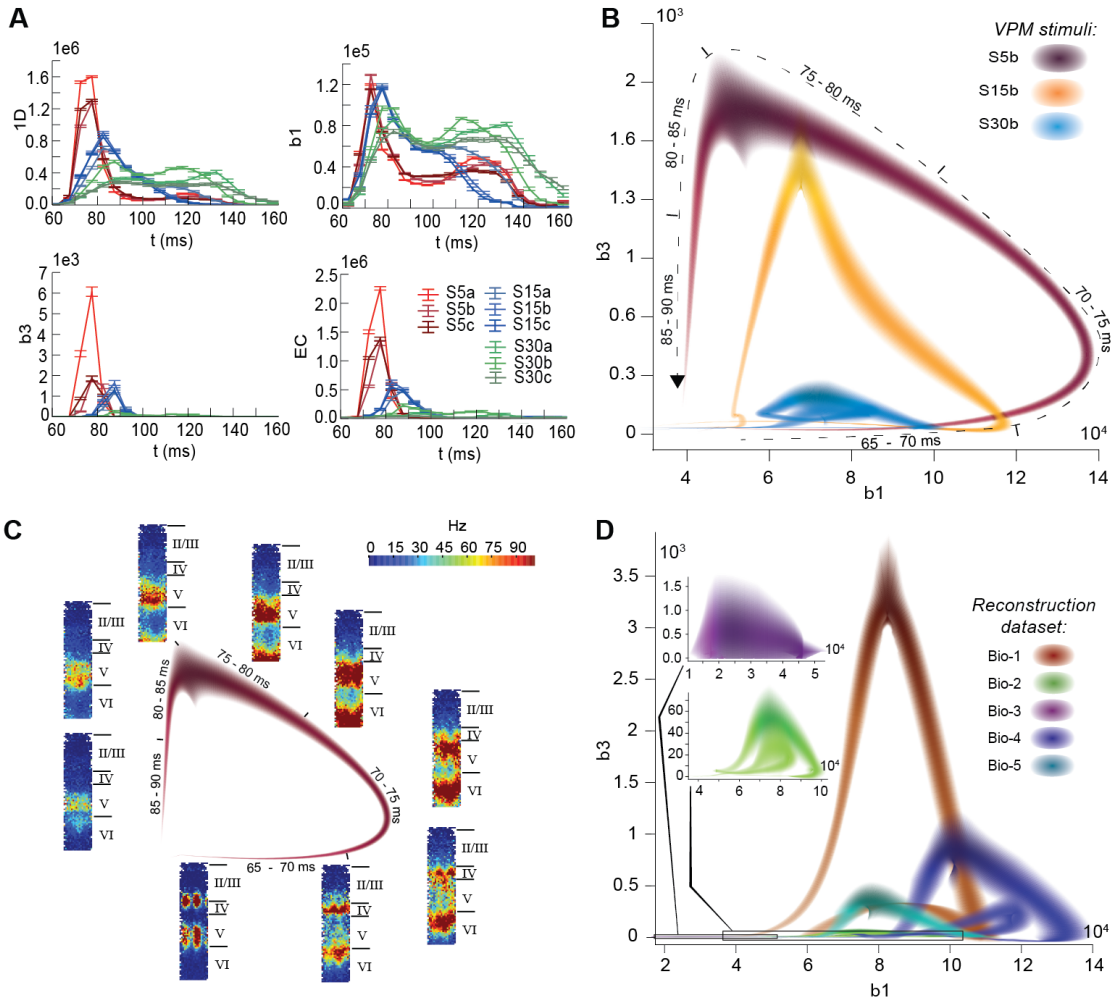

Figure 3.6 – A: Number of edges, β_1, β_3 and Euler characteristic of the time series of TR graphs in response to the stimulus patterns shown in Figure 3.4 (mean and SEM of 30 repetitions of each stimulus). **B**: Trace of the time series of β_1 against β_3 for three of the stimuli. Shading of colors indicates Gaussian profiles at each time step with means and standard deviations interpolated from 30 repetitions of each stimulus. **C**: Trace for one of the stimuli in B, along with the mean firing activity at different locations of the microcircuit during time steps of 2 ms. **D**: Like B, but for TR graphs of Bio 1-5, in response to stimulus S15b.

spread of the upper activity zone deeper into layer 5 and the top of layer 6, consistent with the presence there of the highest dimensional directed simplices. The bottom activity zone also continued moving deeper, until it eventually subsided. As the top activity zone reached the bottom of layer 5, β_3 attained its peak. The zones of activity at the peaks of β_1 and β_3 are highly complementary: zones active at the peak of β_1 were generally inactive at the peak of β_3 and vice versa. The activity zone then remained in layer 5 until the cavities collapsed.

Finally, we applied the same stimulus to the reconstructions based on variations in the underlying biological data (see Figure 3.5B, Bio-1 to 5) and found similar Betti number trajectories, indicating that the general sequence of cavity formation toward peak functional organization followed by disintegration is preserved across individuals. On the other hand, we observed markedly different amplitudes, indicating that biological variability leads to variation in the number of high-dimensional cavities formed by correlated activity (Figure 3.6D). We also found that, unlike the case of different stimuli applied to the same microcircuit (Figure 3.6B), trajectories arising from different biological variations have different β_1-centers. In some cases, we observed reverberant trajectories that also followed a similar sequence of cavity formation, though smaller in amplitude. The general sequence of cavity formation and disintegration, however, appears to be stereotypic across stimuli and individuals.

3.3 Discussion

This study provides a simple, powerful, parameter-free, and unambiguous mathematical framework for relating the activity of a neural network to its underlying structure, both locally (in terms of simplices) and globally (in terms of cavities formed by these simplices). Using this framework revealed an intricate topology of synaptic connectivity containing an abundance of cliques of neurons and of cavities binding the cliques together. The study also provides novel insight into how correlated activity emerges in the network and how the network responds to stimuli.

Such a vast number and variety of directed cliques and cavities had not been observed before in any neural network. The numbers of high-dimensional cliques and cavities found in the reconstruction are also far higher than in null models, even in those closely resembling the biologically-based reconstructed microcircuit, but with only some of the biological constraints released. We verified the existence of high-dimensional directed simplices in actual neocortical tissue. We further found similar structures in a nervous system as phylogenetically different as that of the worm C. elegans (Varshney et al., 2011) suggesting that the presence of high-dimensional topological structures is a general phenomenon across nervous systems.

We showed that the spike correlation of a pair of neurons strongly increases with the number and dimension of the cliques they belong to and that it even depends on their specific position in a directed clique. In particular, spike correlation increases with proximity of the pair of neurons to the sink of a directed clique, as the degree of shared input increases. These observations indicate that the emergence of correlated activity mirrors the topological

complexity of the network. While previous studies have found a similar link for motifs built from 2-dimensional simplices (Chambers and MacLean, 2016; Pajevic and Plenz, 2012), we generalize this to higher dimensions. The fact that each neuron belongs to many directed cliques of various dimensions explains in vivo observations that neurons can "flexibly join multiple ensembles" (Miller et al., 2014). Braids of directed simplices connected along their appropriate faces could possibly act as synfire chains (Abeles, 1982), with a superposition of chains (Bienenstock, 1995) supported by the high number of cliques each neuron belongs to.

Topological metrics reflecting relationships among the cliques revealed biological differences in the connectivity of reconstructed microcircuits. The same topological metrics applied to time-series of transmission-response sub-graphs revealed a sequence of cavity formation and disintegration in response to stimuli, consistent across different stimuli and individual microcircuits. The size of the trajectory was determined by the degree of synchronous input and the biological parameters of the microcircuit, while its location depended mainly on the biological parameters. Neuronal activity is therefore organized not only within and by directed cliques, but also by highly structured relationships between directed cliques, consistent with a recent hypothesis concerning the relationship between structure and function (Luczak et al., 2015).

The higher degree of topological complexity of the reconstruction compared to any of the null models was found to depend on the morphological detail of neurons, suggesting that the local statistics of branching of the dendrites and axons is a crucial factor in forming directed cliques and cavities, though the exact mechanism by which this occurs remains to be determined (but see Stepanyants and Chklovskii (2005)). The number of directed 2-, 3-, and 4-simplices found per 12-patch in vitro recording was higher than in the digital reconstruction, suggesting that the level of structural organization we found is a conservative estimate of the actual complexity. Since the reconstructions are stochastic instantiations at a specific age of the neocortex, they do not take into account rewiring driven by plasticity during development and learning. Rewiring is readily triggered by stimuli as well as spontaneous activity (Le Be and Markram, 2006), which leads to a higher degree of organization (Chklovskii et al., 2004; Holtmaat and Svoboda, 2009) that is likely to increase the number of cliques. The difference may also partly be due to incomplete axonal reconstructions that would lead to lower connectivity, but such an effect would be minor because the connection rate between the specific neurons recorded for this comparison is reasonably well constrained (Reimann et al., 2015).

The digital reconstruction does not take into account intracortical connections beyond the microcircuit. The increase in correlations between neurons with the number of cliques to which they belong should be unaffected when these connections are taken into account because the overall correlation between neurons saturates already for a microcircuit of the size considered in this study, as we have previously shown (Markram et al., 2015). However, the time course of responses to stimuli and hence the specific shape of trajectories may be affected by the neighboring tissue.

In conclusion, this study suggests that neocortical columns process information through a stereotypical progression of clique and cavity formation and disintegration, consistent with a recent hypothesis of common strategies for information processing across the neocortex (Harris and Shepherd, 2015). We conjecture that a stimulus may be processed by binding neurons into cliques of increasingly higher dimension, as a specific class of cell assemblies, possibly to represent *features* of the stimulus (Braitenberg, 1978; Hebb, 1949), and by binding these cliques into cavities of increasing complexity, possibly to represent the *associations* between the features (Engel and Singer, 2001; Knoblauch et al., 2009; Willshaw et al., 1969).

3.4 Materials and methods

3.4.1 The topological toolbox

Specializing basic concepts of algebraic topology, we have formulated precise definitions of cliques (*simplices*) and cavities (as counted by *Betti numbers*) associated to directed networks. What follows is a short introduction to directed graphs, simplicial complexes associated to directed graphs, and homology, as well as to the notion of directionality in directed graphs used in this study. We define, among others, the following terms and concepts (Table 3.1 below).

Table 3.1 – The topological toolbox

Term	Description	Page
Directed graph	Network where each edge has a *source* and a *target*	86
Simplex	Clique of all-to-all connected nodes	87
Directed simplex	Simplex in a directed graph, with a *source* and a *sink*	88
Source (of simplex)	The node that is only a source of edges in a directed simplex	88
Sink (of simplex)	The node that is only a target of edges in a directed simplex	88
Face (of simplex)	Obtained by leaving out one node of a simplex	87
Simplicial complex	Description of a graph in terms of its simplices and their relations	87
Maximal simplex	Not a face of any larger simplex	87
Directionality	Formalized, intuitive measure of directionality in a graph	88
Betti numbers	Description of a graph in terms of the number of *cavities*	89
Euler characteristic	Alternating sum of number of simplices	90

Directed graphs

A *directed graph* $\mathcal{G}$ consists of a pair of finite sets (V,E) and a function $\tau = (\tau_1,\tau_2)\colon E \to V \times V$. The elements of the set V are the *vertices* of $\mathcal{G}$, the elements of E are the *edges* of $\mathcal{G}$, and the function τ associates with each edge an ordered pair of vertices. The *direction* of an edge e with $\tau(e) = (v_1, v_2)$ is taken to be from $\tau_1(e) = v_1$, the *source vertex*, to $\tau_2(v) = v_2$, the *target*

vertex. The function τ is required to satisfy the following two conditions.

1. There are no (self-) loops in the graph (i.e., for each $e \in E$, if $\tau(e) = (v_1, v_2)$, then $v_1 \neq v_2$).
2. For any pair of vertices (v_1, v_2), there is at most one edge directed from v_1 to v_2 (i.e., the function τ is injective).

Notice that a directed graph may contain pairs of vertices that are reciprocally connected, i.e., there may exist edges $e, e' \in E$ such that $\tau(e) = (v_1, v_2)$ and $\tau(e') = (v_2, v_1)$ (Figure S3.12A1(ii)).

A vertex $v \in \mathcal{G}$ is said to be a *sink* if there exists no $e \in E$ such that $v = \tau_1(e)$, but there is at least one edge $e' \in E$ such that $\tau_2(e') = v$. Similarly v is said to be a *source* is if there exists no $e \in E$ such that $v = \tau_2(e)$, but there is at least one $e' \in E$ such that $\tau_1(e') = v$ (Figure S3.12A1(i) and (iii)). A *path* in a directed graph $\mathcal{G}$ consists of a sequence of edges $(e_1, ..., e_n)$ such that for all $1 \leq k < n$, the target of e_k is the source of e_{k+1}, i.e., $\tau_2(e_k) = \tau_1(e_{k+1})$ (Figure S3.12A1(iii)). The *length* of the path $(e_1, ..., e_n)$ is n. If, in addition, target of e_n is the source of e_1, i.e., $\tau_2(e_n) = \tau_1(e_1)$, then $(e_1, ..., e_n)$ is an *oriented cycle*. A graph that contains no oriented cycles is said to be *acyclic* (Figure S3.12A1(i)).

A directed graph is said to be *fully connected* if for every pair of distinct vertices, there exists an edge from one to the other, in at least one direction.

Simplices, simplicial complexes, and flag complexes

An *abstract directed simplicial complex* is a collection $\mathcal{S}$ of finite, *ordered* sets with the property that if $\sigma \in \mathcal{S}$, then every subset τ of σ, with the natural ordering inherited from σ, is also a member of $\mathcal{S}$. A *subcomplex* of an abstract directed simplicial complex is a sub-collection $\mathcal{S}' \subseteq \mathcal{S}$ that is itself an abstract directed simplicial complex. Abstract directed simplicial complexes are a variation on the more common ordinary *abstract simplicial complexes*, where the sets forming the collection $\mathcal{S}$ are not assumed to be ordered. To be able to study directed graphs, we use this slightly more subtle concept. Henceforth, we always refer to abstract directed simplicial complexes as *simplicial complexes*.

The elements σ of a simplicial complex $\mathcal{S}$ are called its *simplices*. We define the *dimension* of σ (denoted $\dim(\sigma)$) to be the cardinality of the set σ minus one. If σ is a simplex of dimension n, then we refer to σ as an *n-simplex* of $\mathcal{S}$. The set of all n-simplices of $\mathcal{S}$ is denoted $\mathcal{S}_n$. A simplex τ is said to be a *face* of σ if τ is a subset of σ of a strictly smaller cardinality. A *front face* of an n-simplex $\sigma = (v_0, ..., v_n)$ is a face $\tau = (v_0, ..., v_m)$ for some $m < n$. Similarly, a *back face* of σ is a face $\tau' = (v_i, \ldots, v_n)$ for some $0 < i < n$. If $\sigma = (v_0, \ldots, v_n) \in \mathcal{S}_n$ then, for each $0 \leq i \leq n$, the i^{th} *face* of σ is the $(n-1)$-simplex σ^i obtained from σ by removing the vertex v_{n-i}. A simplex that is not a face of any other simplex is said to be *maximal*. The set of all maximal simplices of a simplicial complex determines the entire simplicial complex, since every simplex is either maximal itself or a face of a maximal simplex.

A simplicial complex gives rise to a topological space by *geometric realization*. A 0-simplex is realised by a single point, a 1-simplex by a line segment, a 2-simplex by a (filled in) triangle, and so on for higher dimensions (see Munkres (1984), Section 1). To form the geometric realization of the simplicial complex, one then glues the geometrically realized simplices together along common faces. The intersection of two simplices in $\mathscr{S}$, neither of which is a face of the other, is a proper subset, and hence a face, of both of them. In the geometric realization this means that the geometric simplices that realize the abstract simplices intersect on common faces, and hence give rise to a well-defined geometric object.

If $\mathscr{S}$ is a simplicial complex, then the union $\mathscr{S}^{(n)} = \mathscr{S}_n \cup \cdots \cup \mathscr{S}_0$, called the *n-skeleton* of $\mathscr{S}$, is a subcomplex of $\mathscr{S}$. We say that $\mathscr{S}$ is *n-dimensional* if $\mathscr{S} = \mathscr{S}^{(n)}$, and n is minimal with this property. If $\mathscr{S}$ is n-dimensional, and $k \leq n$, then the collection $\mathscr{S}_k \cup \ldots \cup \mathscr{S}_n$ is not a subcomplex of $\mathscr{S}$ because it is not closed under taking subsets. However if one adds to that collection all the faces of all simplices in $\mathscr{S}_k \cup \ldots \cup \mathscr{S}_n$, one obtains a subcomplex of $\mathscr{S}$ called the *k-coskeleton* of $\mathscr{S}$, which we will denote by $\mathscr{S}_{(k)}$. Coskeleta are important for computing homology (see Materials and Methods 3.4.2).

Simplicial complexes of directed graphs

Directed graphs give rise to directed simplicial complexes in a natural way. The directed simplicial complex associated to a directed graph $\mathscr{G}$ is called the *directed flag complex* of $\mathscr{G}$ (Figure S3.12A2). This concept is a variation on the more common construction of a *flag complex* associated with an undirected graph Aharoni et al. (2005). If $\mathscr{G} = (V, E, \tau)$ is a directed graph, then the directed flag complex associated to $\mathscr{G}$ is the abstract directed simplicial complex $\mathscr{S} = \mathscr{S}(\mathscr{G})$, with $\mathscr{S}_0 = V$ and whose *directed n-simplices* $\mathscr{S}_n$ for $n \geq 1$ are $(n+1)$-tuples $(v_0, \ldots, v_n)$, of vertices such that for each $0 \leq i < j \leq n$, there is an edge in $\mathscr{G}$ directed from v_i to v_j. The vertex v_0 is called the *source* of the simplex $(v_0, \ldots, v_n)$, as there is an edge directed from v_0 to v_i for all $0 < i \leq n$. Conversely, the vertex v_n is called the *sink* of the simplex $(v_n, \ldots, v_n)$, as there is an edge directed from v_i to v_n for all $0 \leq i < n$.

Notice that because of the assumptions on τ, an n-simplex in $\mathscr{S}$ is characterized by the (ordered) sequence $(v_0, \ldots, v_n)$, but not by the underlying set of vertices. For instance (v_1, v_2, v_3) and (v_2, v_1, v_3) are distinct 2-simplices with the same set of vertices.

Directionality of directed graphs

We give an intuitive, mathematical definition of the notion of directionality in directed graphs, and prove that directed simplices are fully connected directed graphs with maximal directionality. Let $\mathscr{G} = (V, E, \tau)$ be a directed graph. For each vertex $v \in \mathscr{G}$, define the *signed degree* of v to be

$$\mathrm{sd}(v) = \mathrm{Indeg}(v) - \mathrm{Outdeg}(v). \tag{3.1}$$

Note that for any finite graph $\mathscr{G}$, $\sum_{v\in\mathscr{G}} \mathrm{sd}(v) = 0$. We define the *directionality* of $\mathscr{G}$, denoted $\mathrm{Dr}(\mathscr{G})$, to be the sum over all vertices of the square of their signed degrees (Figure S3.7),

$$\mathrm{Dr}(\mathscr{G}) = \sum_{v\in V} \mathrm{sd}(v)^2. \tag{3.2}$$

Let $\mathscr{G}_n$ denote a directed n-simplex, i.e., a fully connected directed graph on $n+1$ vertices such that every complete subgraph has a unique source and a unique sink. Note that a directed n-simplex has no reciprocal connections. If $\mathscr{G}$ is any directed graph on $n+1$ vertices, then $\mathrm{Dr}(\mathscr{G}) \leq \mathrm{Dr}(\mathscr{G}_n)$. If additionally $\mathscr{G}$ is a fully connected directed graph without reciprocal connections, then equality holds if and only if $\mathscr{G}$ is isomorphic to $\mathscr{G}_n$ as a directed graph. A full proof of these statements is given in the supplementary methods (Appendix A.1.1).

Homology

Betti numbers and *Euler characteristic* are numerical quantities associated to simplicial complexes that arise from an important and very useful algebraic object one can associate with any simplicial complex, called *homology*. Homology serves to measure the "topological complexity" of simplicial complexes, leading us to refer to Betti numbers and Euler characteristic as *topological metrics*. In this study we use only *mod-2 simplicial homology*, computationally the simplest variant of homology, which is why it is very commonly used in applications (Bauer et al., 2017). What follows is an elementary description of homology and its basic properties.

Betti numbers Let $\mathbb{F}_2$ denote the field of two elements. Let $\mathscr{S}$ be a simplicial complex. Define the *chain complex* $C_*(\mathscr{S},\mathbb{F}_2)$ to be the sequence $\{C_n = C_n(\mathscr{S},\mathbb{F}_2)\}_{n\geq 0}$, such that C_n is the $\mathbb{F}_2$-vector space whose basis elements are the n-simplices $\sigma \in \mathscr{S}_n$, for each $n \geq 0$. In other words, the elements of C_n are formal sums of n-simplices in $\mathscr{S}$.

For each $n \geq 1$, there is a linear transformation called a *differential*

$$\partial_n \colon C_n \to C_{n-1} \tag{3.3}$$

specified by $\partial_n(\sigma) = \sigma^0 + \sigma^1 + \cdots + \sigma^n$ for every n-simplex σ, where σ^i is the i-th face of σ, as defined above. Having defined ∂_n on the basis, one then extends it linearly to the entire vector space C_n. The n-th Betti number $\beta_n(\mathscr{S})$ of a simplicial complex $\mathscr{S}$ is the $\mathbb{F}_2$-vector space dimension of its n-th mod 2 *homology group*, which is defined by

$$H_n(\mathscr{S},\mathbb{F}_2) = \mathrm{Ker}(\partial_n)/\mathrm{Im}(\partial_{n+1}) \tag{3.4}$$

for $n \geq 1$ and

$$H_0(\mathscr{S},\mathbb{F}_2) = C_0/\mathrm{Im}(\partial_1). \tag{3.5}$$

For all $n \geq 1$, there is an inclusion of vector subspaces $\mathrm{Im}(\partial_{n+1}) \subseteq \mathrm{Ker}(\partial_n) \subseteq C_n$, and thus the

definition of homology makes sense.

Computing the Betti numbers of a simplicial complex is conceptually very easy. Let $|\mathscr{S}_n|$ denote the number of n-simplices in the simplicial complex $\mathscr{S}$. If one encodes the differential ∂_n as a $\big(|\mathscr{S}_{n-1}| \times |\mathscr{S}_n|\big)$-matrix D_n with entries in $\mathbb{F}_2$, then one can easily compute its *nullity*, $\mathrm{null}(\partial_n)$, and its *rank*, $\mathrm{rk}(\partial_n)$, which are the $\mathbb{F}_2$-dimensions of the null-space and the column space of D_n, respectively. The *Betti numbers* of $\mathscr{S}$ are then a sequence of natural numbers defined by

$$\beta_0(\mathscr{S}) = \dim_{\mathbb{F}_2}(C_0) - \mathrm{rk}(\partial_1), \quad \text{and} \quad \beta_n(\mathscr{S}) = \mathrm{null}(\partial_n) - \mathrm{rk}(\partial_{n+1}). \tag{3.6}$$

Since $\mathrm{Im}(\partial_{n+1}) \subseteq \mathrm{Ker}(\partial_n)$ for all $n \geq 1$, the Betti numbers are always non-negative. The n-th Betti number β_n gives an indication of the number of "n-dimensional cavities" in the geometric realization of $\mathscr{S}$.

Euler characteristic If $\mathscr{S}$ is a simplicial complex, and $|\mathscr{S}_n|$ denotes the cardinality of the set of n-simplices in $\mathscr{S}$, then the Euler characteristic of $\mathscr{S}$ is defined to be

$$\chi(\mathscr{S}) = \sum_{n \geq 0} (-1)^n |\mathscr{S}_n|. \tag{3.7}$$

There is a well known, close relationship between Euler characterstic and Betti numbers (Munkres, 1984, Theorem 22.2), which is expressed as follows. If $\{\beta_n(\mathscr{S})\}_{n \geq 0}$ is the sequence of Betti numbers for $\mathscr{S}$, then

$$\chi(\mathscr{S}) = \sum_{n \geq 0} (-1)^n \beta_n(\mathscr{S}). \tag{3.8}$$

3.4.2 Computation of simplices and homology

Generating directed flag complexes with hasse diagrams

To obtain the simplices, Betti numbers and Euler characteristic of a directed graph, we first generate the directed flag complex associated to the graph. Our algorithm encodes a directed graph and its flag complex as a *Hasse diagram*. The Hasse diagram then gives immediate access to all simplices and simplex counts. The algorithm to generate the Hasse diagrams is fully described in the Supplementary Methods Section 2.2, and the C++ implementation of the code is publicly available at http://neurotop.gforge.inria.fr/.

Homology computations

Betti numbers and Euler characteristic are computed from the directed flag complexes. All homology computations carried out for this paper were made with $\mathbb{F}_2$ coefficients, using the boundary matrix reduced by an algorithm from the PHAT library (Bauer et al., 2017).

The complexity of computing the n-th Betti numbers scales with the number of simplices in dimensions $n-1$, n and $n+1$. In particular, it requires the computation of rank and nullity of matrices with shapes $(n-1)\times n$ and $n\times(n+1)$. Due to the millions of simplices in dimensions 2 and 3 in the reconstructed microcircuits (see Results), the calculation of Betti numbers above 0 or below 5 was computationally not viable. Nevertheless, our Euler characteristic computations imply that at least one of β_2 or β_4 must be nonzero, and it is highly likely the β_k is nonzero for all $k \leq 5$.

3.4.3 Model of neocortical microcircuitry

Analyses of connectivity and simulations of electrical activity are based on a previously published model of neocortical microcircuitry and related methods (Markram et al., 2015). We analyzed microcircuits that were reconstructed with layer height and cell density data from five different animals (Bio-1-5), with seven microcircuits per animal forming a mesocircuit (35 microcircuits in total). In addition, we analyzed microcircuits that were reconstructed using average data (Bio-M, seven microcircuits). Simulations were run on one microcircuit each of Bio-1-5 and Bio-M. Each microcircuit contains approximately 31,000 neurons and approximately 8 million connections. Data about the microcircuit and the neuron models used in the simulations is available on https://bbp.epfl.ch/nmc-portal/ (Ramaswamy et al., 2015).

3.4.4 Control networks

Additional control models of connectivity were constructed by removing different biological constraints on connectivity. We created three types of random matrices of sizes and connection probabilities identical to the connectivity matrices of the reconstructed microcircuits.

ER-model (random-independent graph)

An empty square connection matrix of the same size as the connection matrix of the reconstruction was instantiated and then randomly selected off-diagonal entries were activated. Specifically, entries were randomly selected with equal probabilities until the same number of entries as in the reconstruction were active. The directed graph corresponding to such a matrix is the directed analog of an Erdős-Rényi random graph (Erdos and Rényi, 1960).

PR-model (morphology-only, “Peters’ rule”)

A square connection matrix was generated based on the existence of spatial appositions between neurons in the reconstruction, i.e., instances where the axon of one neuron is within 1 μm of a dendrite of the other neuron. Appositions were then randomly removed from the matrix with equal probabilities until the same number of connections as in the reconstruction

remained.

GB-model (shuffled, preserving distance dependence)

The connection matrix of a reconstructed microcircuit was split into 55^2 submatrices based on the morphological types of pre- and postsynaptic neurons. Each submatrix was then randomized by shuffling its connections as follows. Connections in a sub-matrix were first grouped into bins according to the distance between the somata of their pre- and postsynaptic cells. Next, for each connection a new postsynaptic target was randomly selected from the same distance bin. We selected a distance bin size of $75\,\mu m$, which was the largest bin size that preserved the distribution of soma-distances of connected pairs of neurons in all sub-matrices (no statistically significant difference; $p > 0.05$, KL-test).

3.4.5 Patch clamp experiments

In vitro

Connectivity between layer 5 thick-tufted pyramidal cells was analyzed using multiple somatic whole-cell recordings (6 to 12 cells simultaneously) on 300 μm slices of primary somatosensory cortex of fourteen- to sixteen-day-old rats. Monosynaptic, direct excitatory connections were identified by stimulation of a presynaptic cell with a 20-70 Hz train of 5-15 strong and brief current pulses (1 - 2 nA, 2 - 4 ms). Experiments were carried out according to the Swiss national and institutional guidelines. Further details are explained in the supplementary methods (Appendix A.1).

In silico

In order to obtain in silico cell groups comparable to their patched in vitro counterparts, we designed a cell selection procedure approximating several of the experimental constraints of the in vitro patch-clamp setup used in this study and explained above. In brief, layer 5 thick-tufted pyramidal cells were selected from a volume with dimensions of $200\,\mu m \times 200\,\mu m \times 20\,\mu m$. The size of the volume was chosen to match the field of view usually available in the in vitro patch-clamp setup and to account for the tendency to patch nearby cells, which increases the probability of finding connected cells. The total number of cells was then reduced by randomly discarding a fraction of them, approximating the limited number of patching pipettes available in vitro (twelve) and the failure rate of the patching. This filtering step was optimized to match the in silico and in vitro cluster size distributions.

3.4.6 C. elegans connectome

We analyzed part of the C. elegans connectome (Varshney et al., 2011), consisting of 6393 directed chemical synapses, obtained from www.wormatlas.org/neuronalwiring.html.

3.4.7 Simulation of electrical activity

We performed simulations of neuronal electrical activity during stimulation with spatio-temporal patterns of thalamic input at the in vivo-like state (as in Markram et al. (2015)), in the central microcircuit of Bio-M. Additionally, we repeated the same simulations in the central microcircuits of the Bio-1-5 reconstructions. We ran simulations using nine different organizations of thalamic input spike trains (see below).

Thalamic stimulation

We used spike trains of 42 VPM neurons extracted from extracellular recordings of the response to texture-induced whisker motion in anesthetized rats, with up to nine cells in the same barreloid recorded simultaneously (Bale et al., 2015). Each reconstructed microcircuit is innervated by 310 virtual thalamo-cortical fibers (Markram et al., 2015). To generate sets of stimuli with different degrees of synchronous input, we assigned to each fiber one of 5 (SS5), 15 (SS15) or 30 (SS30) spike trains, recorded from distinct VPM neurons. In addition, we used k-means clustering to form clusters of fibers of size 1 (SSa), 5 (SSb), and 10 (SSc) (scikit-learn, sklearn.cluster.KMeans, Pedregosa et al. (2011)) that were assigned the same spike train. This leads to different spatial arrangements of the identical thalamic inputs, and therefore to different degrees of synchronous input to individual neurons in the microcircuit.

3.4.8 Spike train correlations

We constructed post-stimulus time histograms (PSTHs) for each neuron for each stimulus, using the mean response to 30 trials of five seconds of thalamic stimulation (with bin size of 25 ms; for additional control, bin sizes of 10, 50, 100, 250, and 500 ms were also used). We then computed the normalized covariance matrix of the PSTHs of all neurons

$$R_{ij} = \frac{C_{ij}}{\sqrt{C_{ii}C_{jj}}}, \tag{3.9}$$

where C_{ij} is the covariance of the PSTHs of neurons i and j. PSTHs of simulations with different thalamic stimuli were concatenated for each neuron to yield an average correlation coefficient for all stimuli. In total, correlations are based on the response of all neurons during 30 trials of nine stimuli for five seconds of activity (22.5 minutes).

3.4.9 Transmission-response matrices

The temporal sequence of transmission-response matrices associated to a simulation of neuronal activity of duration T is defined as

$$TR(\Delta t_1, \Delta t_2) := \{A(n) = A(n, \Delta t_1, \Delta t_2)\}_{n=1}^{N}, \tag{3.10}$$

where the n-th matrix, $A(n)$, is a binary matrix describing spiking activity in the time interval $[n \cdot \Delta t_1, (n+1) \cdot \Delta t_1 + \Delta t_2]$, and where $N = T/\Delta t_1$. The (j,k)-coefficient of $A(n)$ corresponding to the n-th time bin is 1 if and only if the following three conditions are satisfied, where s_i^j denotes the time of the i-th spike of neuron j.

(1) The (j,k)-coefficient of the structural matrix is 1, i.e., there is a structural connection from the neuron with GID j to the neuron with GID k, so that they form a pre-post synaptic pair.

(2) There is some i such that $n\Delta t_1$ ms $\leq s_i^j < (n+1)\Delta t_1$ ms, i.e., the neuron with GID j spikes in the n-th time bin.

(3) There is some l such that 0 ms $< s_l^k - s_i^j < \Delta t_2$ ms, i.e., the neuron with GID k spikes after the neuron with GID j, within a Δt_2 ms interval.

In other words, a non-zero entry in a transmission-response matrix denotes a presynaptic spike, closely followed by a postsynaptic spike, maximizing the possibility of a causal relationship between the spikes. Based on firing data from spontaneous activity in the reconstructed microcircuit, we optimized the Δt_i, such that the resulting transmission-response matrices best reflect the actual sucessful transmission of signals between the neurons in the microcircuit (see supplementary methods, Appendix A.1). Unless noted otherwise, $\Delta t_1 = 5$ ms and $\Delta t_2 = 10$ ms were used throughout the study.

3.4.10 Data analysis and statistical tests

Analysis of the model and simulations was performed on a Linux computing-cluster using Python 2.7, including the numpy and scipy libraries (Jones et al., 2001), and custom Python scripts. We calculated p-values using Welch's t-test (scipy.stats), unless noted otherwise.

Conflict of interest statement

The authors declare that the research was conducted in the absence of any commercial or financial relationships that could be construed as a potential conflict of interest.

Author contributions

H.M. and R.L. developed and initially conceived the study over 10 years of discussions. H.M., R.L. and K.H. conceived and directed the final study. K.H. and R.L. directed the applicability of concepts in algebraic topology to neuroscience. H.M. directed the relevance of algebraic topology in neuroscience. The Blue Brain Project team reconstructed the microcircuit and developed the capability to simulate the activity. M.N. performed the simulations. M.N., M.R. and P.D. generated the directed flag complexes from the connection matrices for analysis.

K.H. and R.L. developed the theory for directed cliques and directed simplicial complexes. M.R. and R.L. developed the definition of directionality within motifs and directed cliques. M.R. developed the definition for transmission response matrices. P.D. developed the code to isolate simplices and directed simplices and performed initial computations. M.S. performed topological and statistical analyses on the flag complexes and on the C. elegans connectome. K.T. helped with initial statistical analysis of network responses to stimuli. M.R. and M.N. analyzed the simulation data, mapped it onto the topological data and generated the figures. R.P. performed the patch-clamp experiments. G.C. and M.R. performed the corresponding in silico experiments. H.M., K.H., R.L., M.R. and M.N. wrote the paper.

Acknowledgments

This work was supported by funding from the ETH Domain for the Blue Brain Project and the Laboratory of Neural Microcircuitry. The Blue Brain Project's IBM BlueGene/Q system, BlueBrain IV, is funded by the ETH Board and hosted at the Swiss National Supercomputing Center (CSCS). M.S. was supported by the NCCR Synapsy grant of the Swiss National Science Foundation. Partial support for P.D. was provided by the GUDHI project, supported by an Advanced Investigator Grant of the European Research Council and hosted by INRIA. We thank Eilif Muller for providing input on the analysis, Magdalena Kedziorek for help with proving maximality in directed cliques, Gard Spreemann for help with the analysis of the C. elegans connectome, and Taylor H. Newton for helpful discussions about statistical methods.

Supplementary material

Supplementary material contains supplementary methods (Appendix A.1) and supplementary figures (Section 3.5).

3.5 Supplementary figures (3.7 to 3.14)

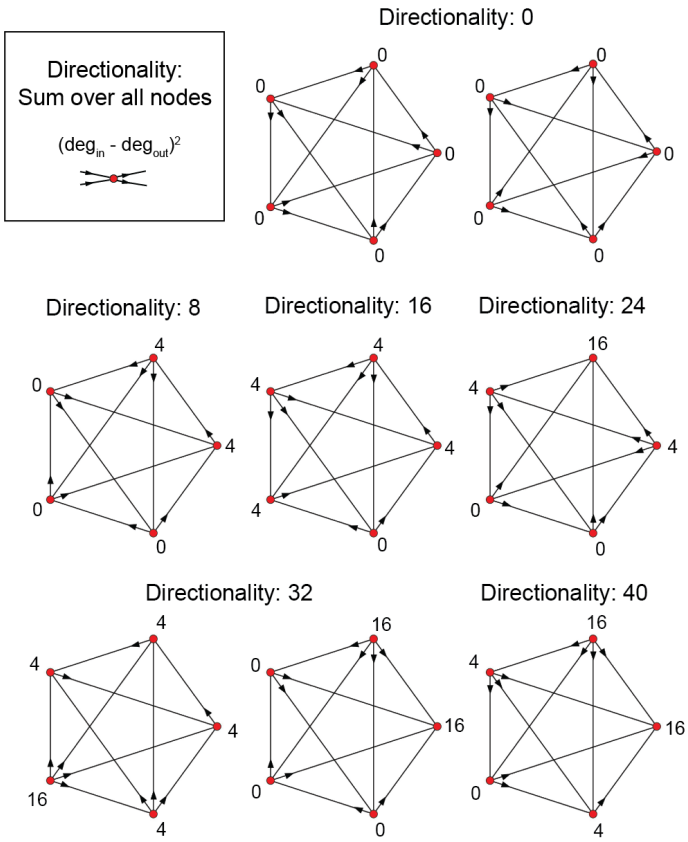

Figure 3.7 – Examples of 5-cliques with various degrees of directionality, as well as the square of the difference of the in-degree and out-degree of all their nodes.

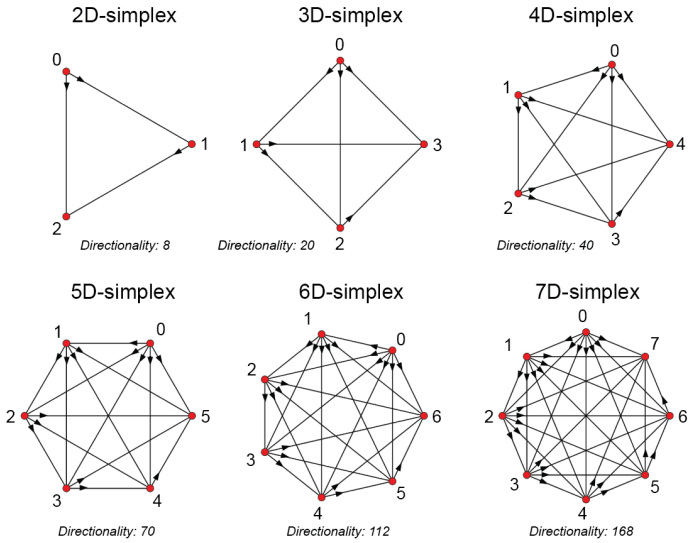

Figure 3.8 – Directed simplices of dimensions 2-7, directionality as in Figure S3.7

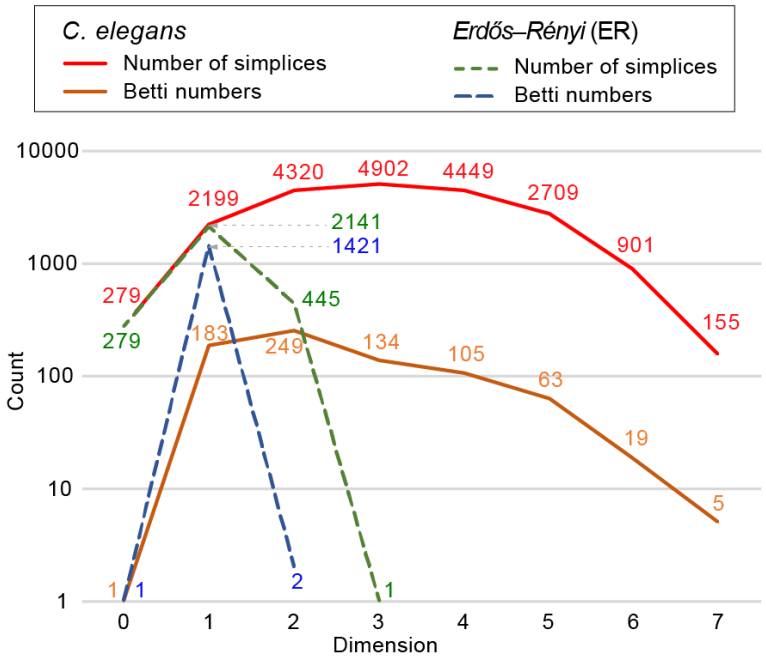

Figure 3.9 – The number of simplices and Betti numbers for the C. elegans connectome, and for an ER-graph with the same number of nodes and the same connection probability.

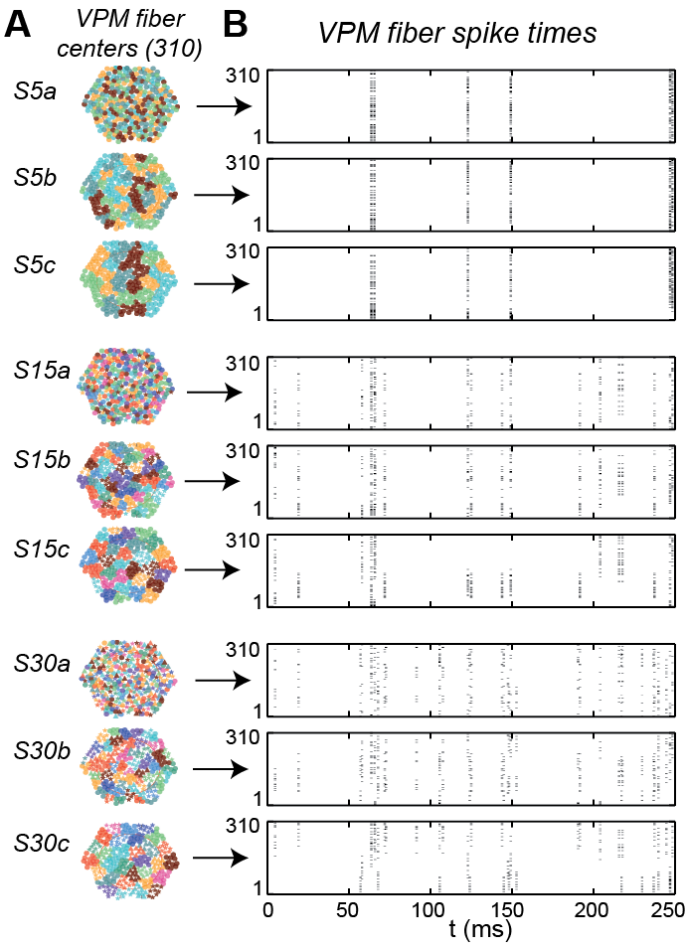

Figure 3.10 – A: Same as Figure 3.4A. Each symbol represents the center of innervation of one of 310 thalamic fibers. **B**: Spike trains assigned to each thalamic fiber, during first 250 ms of each stimulus.

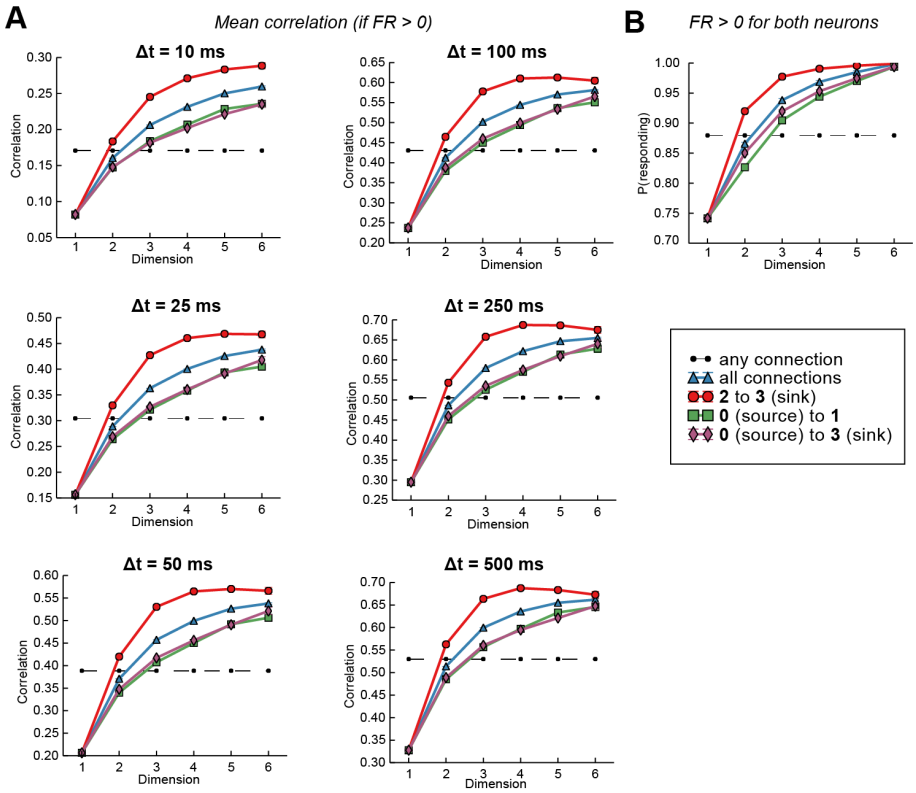

Figure 3.11 – A: Same as Figure 3.4E, but for different PSTH time bin sizes. **B**: Probability of both neurons in a connection firing at least once during all stimuli.

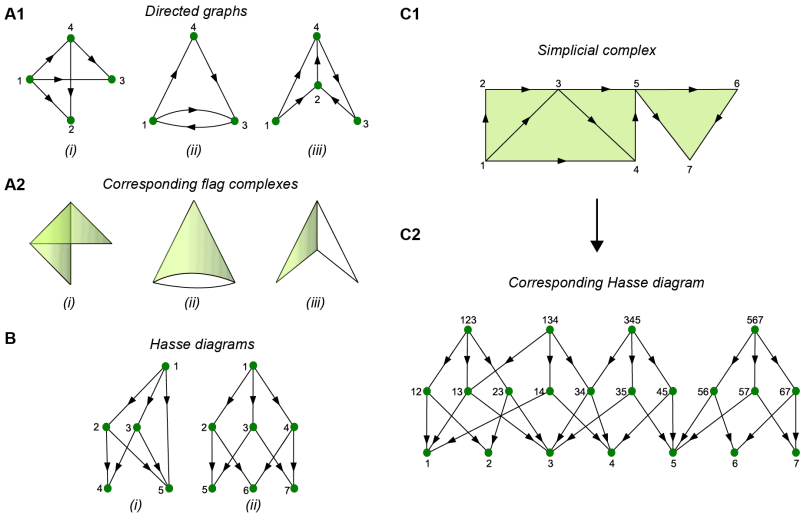

Figure 3.12 – A1: Examples of directed graphs. (i) An acyclic graph. Vertex 1 is a source. Vertices 2 and 3 are sinks. (ii) A graph with one reciprocal connection, two cycles and no sources or sinks. (iii) A graph containing a cycle on the vertices 2, 3 and 4. Vertex 1 is a source. There are two directed paths from vertex 1 to vertex 3: 1-4-3 and 1-2-4-3. **A2**: Directed flag complexes associated to the directed graphs in A1. (i) Two 2-simplices correspond to the two directed 3-cliques. (ii) One 2-simplex corresponds to one directed 3-clique. The reciprocal connection contributes an additional 1-simplex, but not another 2-simplex. (iii) One 2-simplex corresponds to a single directed 3-clique. The cycle does not contribute a 2-simplex. **B**: (i) A Hasse diagram that is not stratified, due to the edge from the vertex 1 to 5. (ii) A stratified Hasse diagram, where vertices 5, 6, and 7 are the vertices of level 0, vertices 2, 3, and 4 are of level 1, and vertex 1 is of level 2. This is also an admissible Hasse diagram, where the outgoing edges are ordered from left to right. Vertex 2 is a front face of vertex 1, while vertex 3 is neither a front nor a back face of a vertex 1, and vertex 4 is back face of a vertex 1. **C1**: The geometric realization of a simplicial complex consisting of seven 0-simplices (labeled 1,...,7), ten 1-simplices, and four 2-simplices. The orientation on the edges is denoted by arrows, i.e., the tail of an arrow is its source vertex, while the head of an arrow is its target. **C2**: The Hasse diagram corresponding to the simplicial complex above. Level k vertices correspond to k-simplices of the complex and are labeled by the ordered sets of vertices that constitute the corresponding simplex. Note that, e.g., vertex 23 is a back face of a vertex 123 and a front face of a vertex 234.

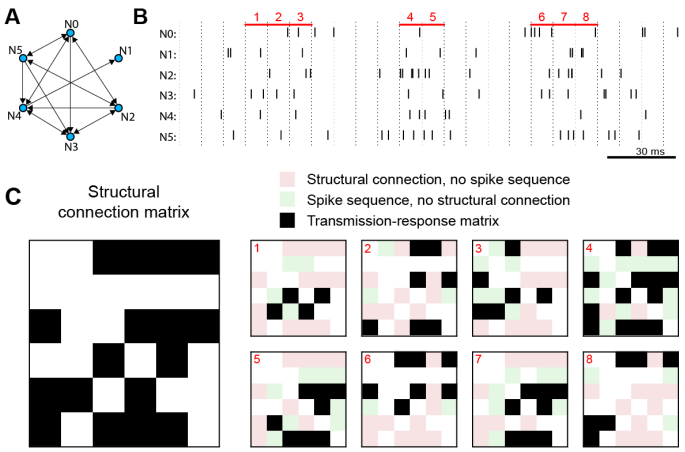

Figure 3.13 – A: Exemplary connectivity motif of six neurons **B**: Random spikes generated for all six neurons. Dashed lines indicate time steps of 10 ms. **C**: Left: Structural connection matrix, Right: Resulting transmission-response (TR) matrices for eight time steps indicated in B. Additionally, structural connections that are not active in the TR graph are indicated in red, and instances of a spike sequence within $\Delta t = 7.5$ ms that lack a structural connection are indicated in green.

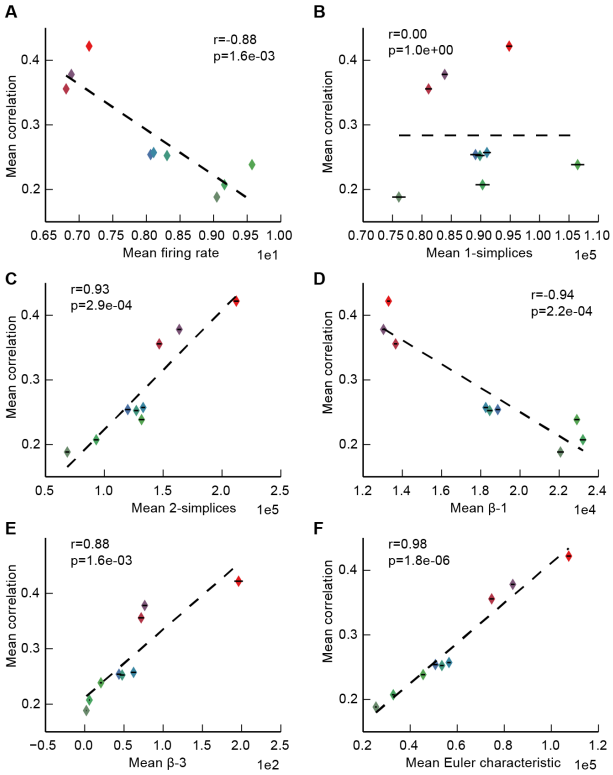

Figure 3.14 – A: Mean pairwise correlation of neurons in microcircuit during the first 250ms of each stimulus, vs. mean firing rate in the same time range. **B-F**: Correlation vs. topological metrics.

4 Impact of higher-order network structure

This chapter is a preprint of joint work with Eyal Gal, Eilif B. Muller, Henry Markram and Michael W. Reimann, to be submitted for publication as "*Impact of higher-order network structure on emergent cortical activity.*"

Contribution: I performed all simulations and analysis, and created all figures. M.R. developed the control circuit models. E.G. computed small-worldness. I wrote the original draft with help by M.R.. Further author contributions are listed at the end of the chapter.

Summary

Synaptic connectivity between neocortical neurons is highly structured. The network structure of synaptic connectivity includes first-order properties, such as strengths of connections between different neuron types and distance-dependent connectivity, and higher-order properties, such as an abundance of cliques of all-to-all connected neurons and small-world topology. The relative impact of first- and higher-order structure on emergent cortical network activity is unknown. Here, we compared network topology and emergent activity in two neocortical microcircuit models with different null models of synaptic connectivity. Both models have a similar first-order structure, but only one model includes higher-order structure arising from morphological diversity within neuronal types. We found that morphological diversity within neuronal types creates more heterogeneous degree distributions, increases in-degrees at the bottom of layer six, increases the number of cliques, and contributes to a small-world topology. The increase in higher-order network structure was accompanied by more nuanced changes in neuronal firing patterns, including increased activity and response reliability at the bottom of layer six. Without this structure, the dependence of pairwise correlations on the positions of neurons in cliques was reduced. Our study shows that circuit models with very similar first-order structure of synaptic connectivity can have a drastically different higher-order network structure, and suggests that the higher-order structure imposed by morphological diversity within neuronal types has an impact on emergent cortical activity.

4.1 Introduction

Local synaptic connectivity between neocortical neurons is highly structured (Song et al., 2005; Perin et al., 2011). Details of *first-order structure* that can be described by pairwise statistics include distinct mean connection strengths between different neuron types, distance-dependent connectivity that changes between neuron types, and a bias for reciprocal connections (Markram et al., 2015). This first-order structure is undoubtedly important for emergent electrical activity, for example by constraining the interlaminar flow of spiking activity (Reyes-Puerta et al., 2014) and constraining the excitation-inhibition balance (Rosenbaum et al., 2017).

Local synaptic connectivity also contains significant *higher-order structure*, that cannot be described by pairwise statistics (Benson et al., 2016). Examples are an overexpression of certain triplet motifs of neurons (Song et al., 2005; Perin et al., 2011), an abundance of cliques of all-to-all connected neurons (Reimann et al., 2017b) and increased small-worldness (Gal et al., 2017). Such higher-order structure has been hypothesized to be important for computation (Braitenberg, 1978; Hebb, 1949; Willshaw et al., 1969; Knoblauch et al., 2009). On the other hand, modern artificial neural networks have demonstrated impressive computational capabilities without complex higher-order micro-structures (Simonyan and Zisserman, 2014). Whether computation in the cortex relies on higher-order structure such as multi-neuron motifs on top of evidently already complex first-order structure is unknown.

Answering this question in vivo will require simultaneous access to both detailed synaptic connectivity and electrical activity. While detailed synaptic connectivity of larger areas encompassing thousands of neurons might soon become available (Kasthuri et al., 2015), it will remain difficult to study the direct impact of the network structure on electrical activity, and even then it would be difficult to quantify the relative impact of first- and higher-order structure. A modelling approach can help bridge this gap. An algorithmic approach can use available data to generate emergent connectivity in a neocortical microcircuit model with diverse morphologies (Reimann et al., 2015). When simulated, this neocortical microcircuit model (*NMC-model*) can reproduce an array of in vivo-like neuronal activity (Markram et al., 2015), and allows us to compare and manipulate detailed—predicted—structure and function.

Here, we utilized a recent finding that first-order connectivity is largely constrained by morphological diversity between neuronal types, and higher-order connectivity by morphological diversity within neuronal types (Reimann et al., 2017a). Both aspects are captured by the NMC-model, leading to a biologically realistic micro-structure (Gal et al., 2017).

By connecting neurons according to average axonal and dendritic morphologies (*cloud-model*) (Figure 4.1), we created a control circuit that has very similar first order structure, but highly reduced higher-order structure. We found that this reduced higher-order structure—caused by disregarding morphological diversity within neuronal types—included more homogeneous degree distributions, reduced in-degrees at the bottom of layer six, less cliques, and decreased small-world topology. When we compared electrical activity in the two circuit models, we

found that the changes in higher-order connectivity were accompanied by nuanced, but significant changes in neuronal firing patterns, firing rates, response reliabilities and pairwise correlations.

Our study introduces a rigorous method to reduce higher-order network structure of a neocortical microcircuit model while leaving first-order structure largely intact, and suggests that higher-order network topology of neocortical microcircuitry shapes cortical function.

4.2 Results

4.2.1 Reducing higher-order network structure

We studied a previously published neocortical microcircuit model (*NMC-model*) (Markram et al., 2015). The NMC-model consists of 31'346 neurons belonging to 55 different morphological types (*m-types*). Synaptic connectivity between the neurons was derived by considering appositions of dendrites and axons as potential synapse locations (Figure 4.1A, left), which were then filtered according to biological constraints (Reimann et al., 2015). While this connectome is merely a null model of connectivity, it matches a large array of biological measurements, both in terms of its *first-order structure* (which we define as structure that can be described by pairwise statistics, e.g. connection strengths between different m-types and distance-dependent connectivity) and its *higher-order structure* (which we define as structure involving more than two neurons, e.g. common-neighbor bias, over-representation of cliques of all-to-all connected neurons, and also degree distributions). Neuronal and synaptic physiology in the model are equally well constrained (Markram et al., 2015).

To assess the specific role of the higher-order synaptic structure on neuronal activity, we had to reduce the higher-order structure while simultaneously impacting the first-order structure as little as possible. To this end, we used an alternative cloud-based approach to derive synaptic connectivity based on the overlap of average dendritic and axonal shapes of the various morphological neuron types (Figure 4.1A, bottom, right; *cloud-model*) instead of specific axo-dendritic appositions of individual neurons. This approach yields similar properties of first-order structure of the microcircuit connectome, such as distinct connection strengths between different m-types (and consequently between layers), distance-dependent connectivity and a bias for reciprocal connections (Reimann et al., 2017a). However, the cloud-model cannot reproduce an experimentally observed bias for connected neocortical neurons to share a common neighbor (Perin et al., 2011; Reimann et al., 2017a), indicating a reduced complexity of its higher-order structure. By comparing electrical activity between the NMC-model and the cloud-model in a number of simulation experiments, we can thus study the relative impact of first- and higher-order structure on electrical activity.

To build the control cloud-model, we first generated alternative cloud-based connectomes for the NMC-model (Figure 4.1B1, red to green), using methods introduced by Reimann et al. (2017a). Briefly, average axon and dendrite shapes were calculated from reconstructions for

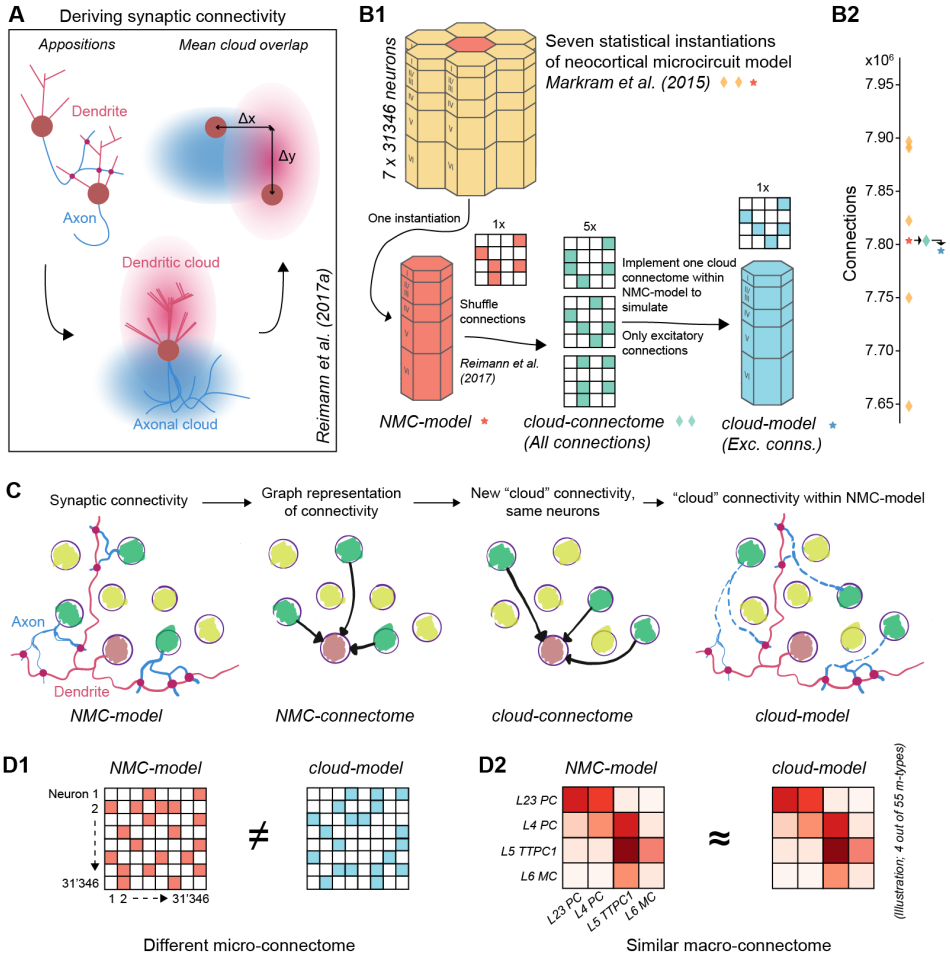

Figure 4.1 – Reducing higher-order network structure in a neocortical microcircuit model. (A) Deriving synaptic connectivity between neocortical neurons: Connectivity in the NMC-model is based on a touch-based approach that considers appositions of dendrites and axons (Reimann et al., 2015). Connectivity in the control cloud-model considers overlap of average dendritic and axonal clouds (Reimann et al., 2017a). (B1) We computed network properties for seven statistical instantiations of the microcircuit (Markram et al., 2015), and simulated one of them (the *NMC-model*). The connectome of the NMC-model can be rewired by using the existing neurons, but reassigning synaptic connectivity according to the cloud-based approach (see panel A). We then implemented one of the alternative connectomes within the existing synapses of the NMC-model, resulting in the *cloud-model*. The rewiring was restricted to excitatory connections. (B2) Number of connections across connectomes. By design, the cloud-connectomes have roughly the same number of connections as the NMC-model. The implemented cloud-model has 0.12% less total connections due to a mismatch in new connections and available synapses. (C) The cloud connectome is implemented within the NMC-model by using existing synapses of the same connection type, that is identical combinations of pre- and postsynaptic morphological neuron types (*m-type*). (D) The NMC- and cloud-models have a completely different micro-connectome in terms of connections between individual neurons (D1) but very similar macro-connectome in terms of number of connections between the 55 different m-types in the model (D2).

all morphological neuron types. Next, for each combination of neuron types, their axon- and dendrite volumes were convolved (see Figure 4.1A, top, right) to yield the expected strength of their overlap for all possible relative soma locations. Soma locations of neurons were taken from the NMC-model and used to look up the overlap strengths for all neuron pairs. Connection probabilities for all pairs were then proportional to the square of the overlap and normalized such that the total number of connections for each combination of neuron types matches the NMC-model (Figure 4.1B2, red asterisk and green diamond).

A neuron-to-neuron connection matrix was then instantiated from the probabilities (the *cloud-connectome*) and transplanted into the NMC-model, to generate an instance of the *cloud-model* that was identical to the NMC-model in terms of neuronal composition, and morphology and physiology of all individual neurons (Figure 4.1B1). Similarly, the physiology of individual synapses (strength, kinetics and short-term dynamics) and their locations on dendrites were taken from the NMC-model; we only changed which presynaptic neurons innervated them to implement the cloud-based connection matrix (Figure 4.1C). This re-assignment of innervation was constrained to select a new innervating neuron only from the same morphological type that innervated it in the NMC-model to preserve the pathway-specific synaptic physiology, where a *pathway* is defined as a specific combination of pre- and postsynaptic m-types, e.g. L4 PC (layer 4 pyramidal cell) to L5 MC (layer 5 Martinotti cell). However, while synaptic physiology is conserved in this approach, the axonal path length, the time it takes for a action potential to propagate from the soma to the synapse, is potentially incorrect. While the average path lengths per pathway are conserved, an action potential might potentially arrive earlier or later than is appropriate for the distance between pre- and postsynaptic neuron.

In the cloud-based connection matrix, a small number of neurons received input from m-types that did not innervate them in the NMC-model. Consequently, a small fraction of connections could not be instantiated within the existing synapses of the NMC-model and had to be left out. The loss was minor for excitatory connections (0.12% loss of connections), but posed a significant problem for inhibitory connections. We therefore implemented the cloud-connectome only for excitatory connections and kept inhibitory connectivity in the cloud-model identical to the NMC-model. Supplementary Figures 4.6B and 4.6C provide an overview of connection losses in the cloud-model. However, note that the loss of connections is very small compared to the variability in connections between statistical instantiations of the NMC-model (Figure 4.1B2, orange diamonds), which all have very similar dynamical properties (Markram et al., 2015).

To control for the minor loss of excitatory connectivity and the shuffling of axonal path lengths within pathways, we generated an additional control circuit, NMC-model$_{\text{cloud-control}}$: a total of 0.12% of excitatory connections were randomly removed from the NMC-model to match the pathway-specific connection losses in the cloud-model (as in Supplementary Figure 4.6B). Connections with the the same presynaptic excitatory m-type for *each* neuron were then shuffled and assigned new synapses to account for the scrambling of axonal path lengths in

Table 4.1 – Overview of circuit models and connectomes analyzed in this study.

Circuit	Description
NMC-model	Simulated neocortical microcircuit model (Markram et al., 2015).[a]
NMC-connectomes ($n = 6$)	Additional statistical instantiations of NMC-model (Markram et al., 2015).[a]
cloud-connectomes ($n = 5$)	Alternative connectomes for the NMC-model (Reimann et al., 2017a).
cloud-model	Implementation of one cloud-connectome in NMC-model (excitatory connections only).
NMC-model$_{\text{cloud-control}}$	Control for axon path length shuffle and 0.12% connection loss in cloud-model.

[a] mc2_Column and mc[0, 1, 3-6]_Column respectively at bbp.epfl.ch/nmc-portal/downloads → AVERAGE.

Table 4.2 – Overview of control model conservation of NMC-model properties.

Microcircuit properties	cloud-model	NMC-model$_{\text{cloud-control}}$
Specific neuron electrophysiology & morphology	✓	✓
Pathway-specific synaptic physiology	✓	✓
Average (pathway specific) axonal path length	✓	✓
Macro-connectome (between m-types)	(✓)[a]	(✓)[a]
Micro-connectome (between specific neurons)	x	(✓)[a]
Specific axonal path length	x	x

[a] 0.12% excitatory connection loss.

the cloud-model (See Figure 4.1C). All circuits and connectomes analyzed in this study are summarized in Table 4.1.

In summary, our approach ensured that for each neuron in the NMC-model, there was a corresponding neuron in the cloud-model with identical location, morphology, electrophysiology, synaptic physiology, inhibitory innervation and average innervation patterns. On a larger scale, both models also had nearly identical *macro-connectomes* in terms of the number of connections between morphological types (Figure 4.1D2, Supplementary Figure 4.6A and 4.6B), and consequently also between layers, and between excitatory and inhibitory sub-populations (Supplementary Figure 4.6C1-3). Only the micro-connectomes defined by connections between individual neurons were changed within tight global constraints (Figure 4.1D1). An overview of what is conserved between NMC-model and cloud-model, and NMC-model$_{\text{cloud-control}}$ can be found in Table 4.2.

4.2.2 Decreased heterogeneity of degree-distributions in cloud-model

As the many features of higher-order connectivity are intrinsically linked, it is virtually impossible to predict how changing one will affect the others. As such, we started our analysis

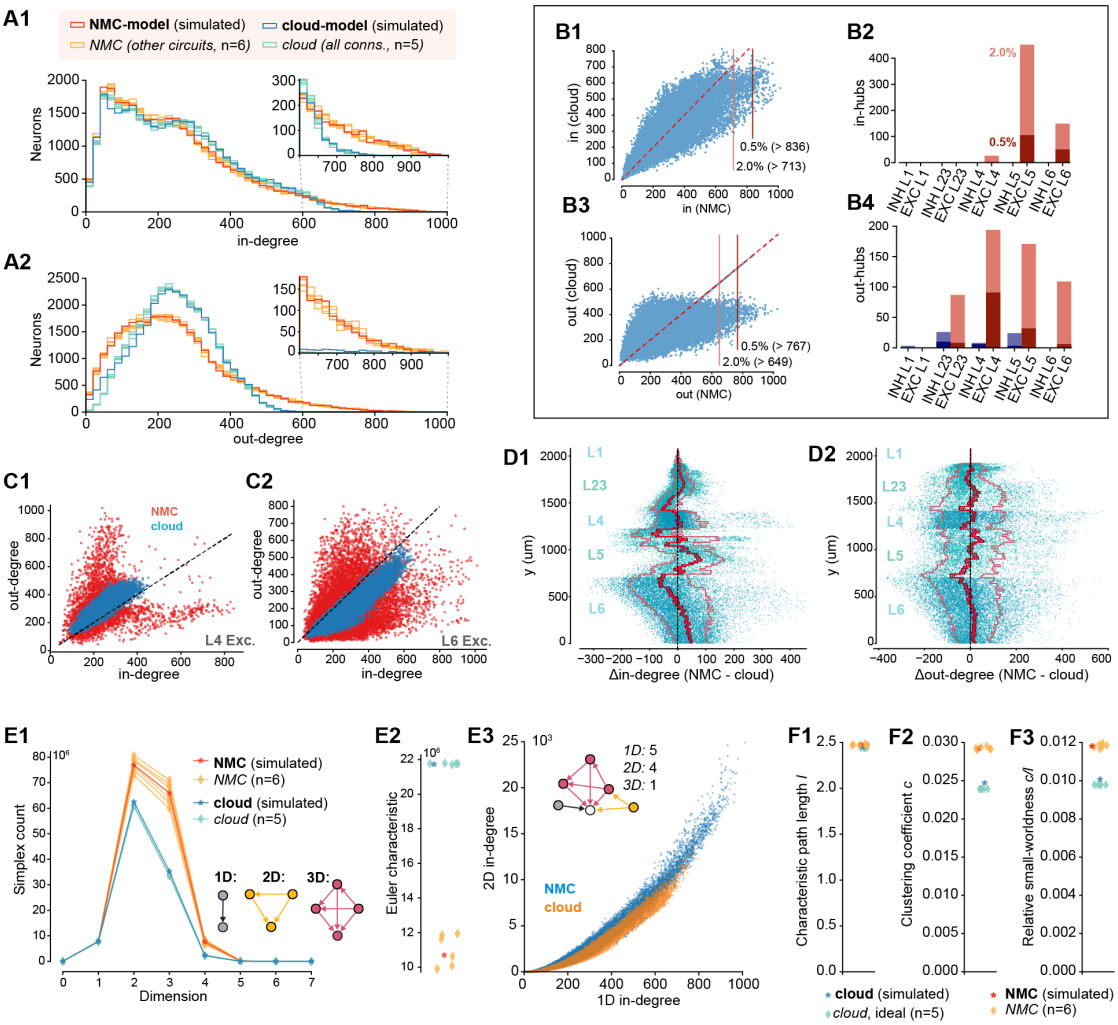

Figure 4.2 – Higher-order structure differences between NMC- and cloud-models. (A1) In-degree distributions of neurons in NMC-model (red), additional NMC-connectomes (orange), the cloud-model (blue), and the five cloud-connectomes (light blue). Insets show the same distributions starting from 600 for easier comparison. (A2) As A1, but for out-degree distributions. (B) Hub-neurons in NMC- and cloud-models. (B1) Scatter plot of in-degree in NMC- vs. cloud-model for the same neurons. Horizontal lines indicate 2.0% and 0.5% percentile in NMC-model. (B2) In-hubs in NMC-model by neuronal type in red, in-hubs in cloud-model in blue (larger than 2.0% and 0.5% percentile in NMC-model). (B3) As B1 but for out-degree. (B4) As B2 but for out-degree. (C1) In- vs. out-degree scatter plot for NMC-and cloud model for excitatory neurons in layer 4. (C2) In- vs. out-degree scatter plot for NMC-and cloud model for excitatory neurons in layer 6. (D1) Difference in in-degree of neurons between NMC- and cloud model, across cortical depth. The bright red line indicates the mean across y-bins, the dark red line the standard error of the mean, and the outer, faded line the standard deviation. (D2) As D1, but for out-degree. (E1) Number of directed cliques (simplices) per dimension in the different connectomes. (E2) Euler characteristic. (E3) Participation at the sink of 1D simplices vs. 2D simplices. (F1) Characteristic path length l of the different connectomes. (F2) Clustering coefficient c of the different connectomes. (F3) Relative small-worldness c/l of the different connectomes.

by fully characterizing the anatomical differences in the micro-structure of NMC-model and cloud-model. As shown before (Reimann et al., 2017a), the cloud-model has a reduced higher-order structure in terms of a bias for two connected neurons to share common neighbors (*common neighbor bias*). Another important higher-order characteristic of a network are the in- and out-degree distributions, which directly shape cortical network dynamics (Landau et al., 2016). We can see that both in- and out-degree distributions are much more heterogeneous in the NMC-model than in the cloud-model (Figure 4.2A1 and 4.2A2, red), across all layers (Supplementary Figure 4.7).

To better understand the significance of this discrepancy, we next analyzed the connectivity of the additional six statistical variants of the NMC-model (Figure 4.2 A1, A2 orange). Similarly, we analyzed the five instances of the cloud-connectome (of which we used one for simulations where only the excitatory connections were changed, see above) (Figure 4.2 A1, A2 teal). The difference between cloud-connectome (cloud-based excitatory *and* inhibitory connections) and the cloud-model (which differs from the NMC-model only in the *excitatory* connections) is very small, showing that inhibitory connections would only have a minor impact on higher-order structure differences between NMC-model and cloud-model.

The stark difference in connectivity between NMC- and cloud-models is also reflected by hub neurons, previously defined as the top 0.5% of neurons in terms of in- or out-degree (Gal et al., 2017), which almost vanish in the cloud-model when using the same cut-off value as in the NMC-model (Figure 4.2B). This increased heterogeneity of degree distributions in the NMC-model vs. the cloud-model also extends to the correlations between in- and out-degree (Figure 4.2C1 and 4.2C2 for excitatory neurons in layers 4 and 6, see Supplementary Figure 4.8 for all neurons), indicating a stronger specialization into input- and output neurons in the NMC-model. We further found that there was a redistribution of connectivity in terms of in- and out-degree from the bottom to the top of layer 6 in the cloud-model compared to the NMC-model (Figure 4.2D1 and 4.2D2). In summary, the cloud-model has a strongly reduced heterogeneity of connectivity in terms of distributions of in- and out-degrees.

4.2.3 Fewer directed simplices and decreased small-worldness in cloud-model

In addition to the common neighbor bias and heterogeneous degree distributions, the NMC-model also contains an abundance of all-to-all connected cliques of neurons called simplices (Reimann et al., 2017b), high-dimensional Betti-numbers describing the topological complexity of the network in terms of cavities formed by the simplices (Reimann et al., 2017b), and is a small-world network (Gal et al., 2017). While simplices of the same dimensions are present in cloud- and NMC-models (Supplementary Figure 4.9A), the numbers of simplices of the same dimension are much larger in the NMC- than in the cloud-model (Figure 4.2E1). A very different Euler Characteristic (Figure 4.2E2) and different Betti-numbers (Supplementary Figure 4.9B) further illustrate the drastic change in global properties of network topology between NMC- and cloud-models (see Methods). The increase in simplex numbers in the

NMC-model is correlated with the more heterogeneous degree distributions, as neurons with larger degrees are generally part of more simplices (Figure 4.2E3). Simplex counts in the cloud-model are much closer to the NMC-model than in simpler control models (Reimann et al., 2017b). In a previously used control that conserves only the distance-dependence of connectivity, but ignores the shapes of axonal and dendritic clouds, we found a more drastic decrease from around 80 million to 40 million 2D-simplices (Reimann et al., 2017b), while the cloud-model has more than 60 million 2D-simplices.

The decrease in higher-order structure also manifests itself in a change in small-worldness due to decreased clustering. The characteristic path length l between cloud- and NMC-model is very similar (Figure 4.2F1), while the clustering coefficient c is much larger in the NMC-model (Figure 4.2F2), meaning that the NMC-model is more of a small-world network (c/l) than the cloud-model (Figure 4.2F3). The decrease in the global clustering coefficient can be attributed to the previously described reduction in the common-neighbor bias (Reimann et al., 2017a). In summary, the cloud model—with its disregard for morphological diversity within neuronal types—has strongly reduced numbers of high-dimensional cliques and reduced small-worldness.

4.2.4 Simulating neuronal activity in NMC- and cloud-models

Impact of higher-order structure on spontaneous activity

We have established that the cloud-model has strongly reduced structural heterogeneity, which can affect the structural and, consequently, functional excitation-inhibition (EI) balance (Landau et al., 2016). The functional EI-balance also depends on the extracellular calcium level ($[Ca^{2+}]_o$), which differentially modulates the release probability of excitatory and inhibitory synapses (Markram et al., 2015). In the NMC-model, at low $[Ca^{2+}]_o$, the network is in an asynchronous state of activity (Figure 4.3A1, $[Ca^{2+}]_o$ = 1.2 mM, 1.25 mM). At high $[Ca^{2+}]_o$, the circuit is in a non-biological synchronous state of activity with spontaneous network bursts (Figure 4.3A1, $[Ca^{2+}]_o$ = 1.3 mM, 1.35 mM). At $[Ca^{2+}]_o$ = 1.25 mM, just before the transition from the asynchronous to synchronous state, activity in the microcircuit is in a in vivo-like state in which it exhibits many properties of in vivo spontaneous and evoked activity (Markram et al., 2015).

The transition from asynchronous to synchronous states in the cloud-model remains remarkably similar to the NMC-model (Figure 4.3A2). The cloud-model appears to transition at lower $[Ca^{2+}]_o$ than the NMC-model, but firing rates are nearly identical at $[Ca^{2+}]_o$ = 1.25 mM (Figure 4.3B1–3). However, this effect could simply be due to the stronger loss of $E \rightarrow I$ connections (Supplementary Figure 4.6E1, 1.1% loss) than of $E \rightarrow E$ connections (Supplementary Figure 4.6D1, 0.09% loss), rather than the reduced higher-order structure. We therefore also simulated a control model that takes the connection loss (and also the non-conserved axonal path lengths) into account (NMC-model$_{\text{cloud-control}}$; see Tables 4.1 & 4.2). Interestingly, the inhibitory firing in the NMC-model$_{\text{cloud-control}}$ is significantly reduced compared to the cloud-

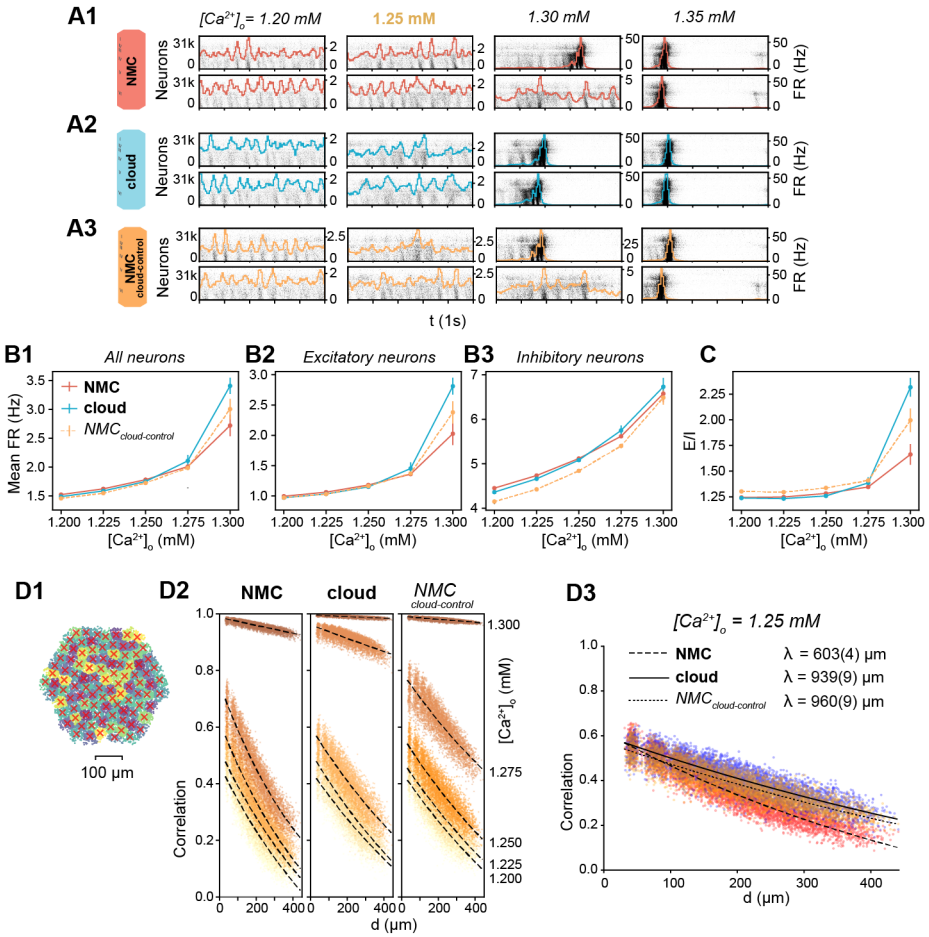

Figure 4.3 – Simulating spontaneous activity in NMC- and cloud-models. (A1) Spontaneous activity of all neurons in the NMC-model for two trials at different levels of $[Ca^{2+}]_o$. Each spike is represented by a vertical line, whose position on the y-axis is ordered by soma position in the microcircuit, which was then rasterized. Colored lines depict the population firing rate ($\Delta t = 10$ ms). (A2) Spontaneous activity of all neurons in the cloud-model. (A3) Spontaneous activity of all neurons in the NMC-model$_{\text{cloud-control}}$. (B1) Mean firing rate during spontaneous activity for all neurons. Mean of 20 trials of 1000 ms, error bars indicate standard error of the mean. (B2) Mean firing rate during spontaneous activity for excitatory neurons. Mean of 20 trials of 1000 ms, error bars indicate standard error of the mean. (B3) Mean firing rate during spontaneous activity for inhibitory neurons. Mean of 20 trials of 1000 ms, error bars indicate standard error of the mean. (C) Total spike count of excitatory neurons divided by the spike count of inhibitory neurons. Mean of 20 trials of 1000 ms, error bars indicate standard error of the mean. (D1) All neurons in the microcircuit were divided into 100 interlaminar clusters (k-means clustering). The red cross marks the geographic center of all neurons for each cluster. (D2) Correlation-coefficients between combined PSTHs of all neurons of each combination of clusters vs. distance between clusters. From $[Ca^{2+}]_o = 1.200$ mM (bottom fitted curve, bright yellow dots) to $[Ca^{2+}]_o = 1.300$ mM (top fitted curve, dark brown dots). The fitted line indicates an exponential fit $e^{-d/\lambda} + c$. (D3) As in D2, but at $[Ca^{2+}]_o = 1.25$ mM. The fitted line indicates an exponential fit $e^{-d/\lambda} + c$, parentheses indicate the standard error of the fit.

model (Figure 4.3B3), while excitatory firing is conserved (Figure 4.3B2), despite both models having the same amount of lost connections compared to the NMC-model. Taken together, this implies that the increased higher-order structure in the NMC-model shifts the ratio of excitatory and inhibitory activity towards more excitation (Figure 4.3C).

Correlation coefficients of spiking activity between neurons decrease with distance (Markram et al., 2015). The overall strength of these correlations and their dependence on distance also depend on $[Ca^{2+}]_o$, as we can see in Figure 4.3D2. At the transition from asynchronous to synchronous activity, correlations coefficients rapidly increase. However, we can see that at $[Ca^{2+}]_o$ = 1.25 mM correlations between cloud-and NMC-model are very similar (Figure 4.3D3). While correlations drop slightly faster in the cloud- than in the NMC-model, this can be fully explained by the non-topological changes controlled for in the NMC-model$_{\text{cloud-control}}$. We thus conclude that the higher-order network structure has an impact on emergent dynamics, such as the increase in effective excitation, but does not fundamentally alter the dynamics of spontaneous activity.

Impact of higher-order structure on evoked activity

We next stimulated the NMC- and cloud-models with thalamic input (Figure 4.4A1) to compare more detailed dynamic properties between the models, such as spike responses to stimuli, response reliability (Nolte et al., 2018) and correlations between individual neurons (Reimann et al., 2017b). Similar to spontaneous activity, the response of the circuits to the input depended on $[Ca^{2+}]_o$ (Figure 4.4A2-3). As we established that the NMC-model and cloud-models have a slightly different transition between dynamic states, we compared evoked activity for up to five $[Ca^{2+}]_o$ values around the in vivo-like state at $[Ca^{2+}]_o$ = 1.25 mM. Overall, evoked activity in the cloud-model looks very similar to evoked activity in the NMC-model (Figure 4.4A2-3). However, over shorter timescales, spike patterns are altered, depending on $[Ca^{2+}]_o$ (Figure 4.4B1-3). Activity in NMC-model and NMC-model$_{\text{cloud-control}}$ is very similar (Supplementary Figure 4.10A1–3 and 4.10B1–3), and we thus conclude that the difference in activity between NMC- and cloud-models arises primarily from the change in higher-order network structure.

The ratio of overall excitatory to inhibitory activity is increased in the cloud-model, mainly through a decrease of inhibitory activity at all $[Ca^{2+}]_o$ levels (Figure 4.4C1-2). However, consistent with our observation for spontaneous activity, inhibitory activity in the NMC-model$_{\text{cloud-control}}$ is even lower than in the cloud-model (Supplementary Figure 4.10C), suggesting that most of the loss in inhibitory firing was due to the 1.1% loss of excitatory connections innervating inhibitory neurons and the reduction of higher-order structure in the cloud-model partly restored it. Similarly, excitatory activity is also higher in the cloud-model than in the NMC-model$_{\text{cloud-control}}$, further demonstrating that higher-order structure leads to a small net loss in neuronal spiking activity. To gain a deeper understanding, we next looked at the changes in firing rates between models for individual neurons. Excitatory firing rates varied according to the change in in-degree across cortical depth (Figure 4.4D2 vs. Figure 4.2D1),

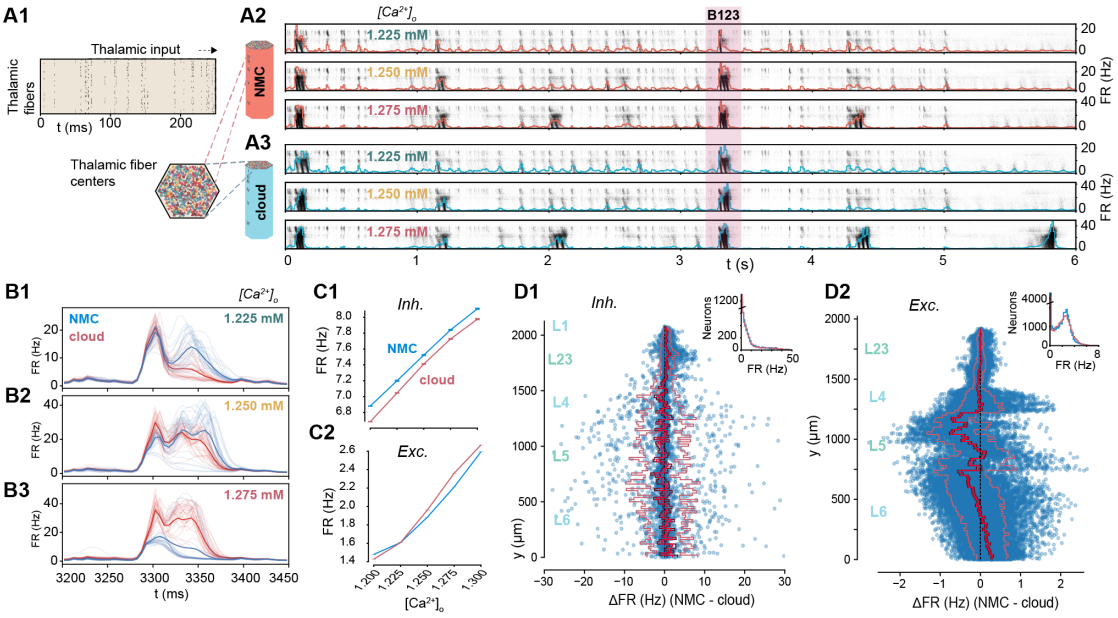

Figure 4.4 – Simulating evoked activity in NMC- and cloud-models. (A1) Illustration of the first 250 ms of the thalamic input stimulating the microcircuit from $t = 0$ to 5 s. (A2) Evoked activity for all neurons in the NMC-model in response to input from A1 at three different $[Ca^{2+}]_o$-levels. (A3) Evoked activity for all neurons in the cloud-model at three different $[Ca^{2+}]_o$-levels. (B1) Population firing rate for NMC-model (blue) and cloud-model (red) for a 250 ms time period during the evoked activity (shaded red area in A23) at $[Ca^{2+}]_o = 1.225$ mM. Faint lines: population means for all 30 trials. Thick line: mean of all 30 trials. Bins size: $\Delta t =$ 5 ms. (B2) As B1, but for $[Ca^{2+}]_o = 1.25$ mM. (B3) As B1 and B2, but for $[Ca^{2+}]_o = 1.275$ mM. (C1) Mean population firing rate of inhibitory neurons during evoked activity at different $[Ca^{2+}]_o$-levels. Error bars indicate standard error of the mean over 30 trials. Note that error bars for excitatory neurons are smaller than linewidth. (C2) Mean population firing rate of excitatory neurons during evoked activity at different $[Ca^{2+}]_o$-levels. Error bars indicate standard error of the mean over 30 trials. (D1) Difference in firing rate of inhibitory neurons during evoked activity at $[Ca^{2+}]_o = 1.25$ mM. Blue dots indicate values for individual neurons, ordered along their soma positions with respect to the y-axis (cortical depth). Lines indicate, mean (bright red), standard-error (dark red), and standard deviation. Inset: Distribution of all mean firing rates. (D2) As D1, but for excitatory neurons.

but not inhibitory firing rates (Figure 4.4D1). The mean change directly reflects the change in in-degree shown in Figure 4.2D1—which is not surprising as any change in in-degree in the cloud-model is restricted to excitatory connections. The higher-order structure is thus directly affecting the structural EI-balance of individual neurons in the network and consequently shaping firing rates.

We previously showed that the in-degree also influences the spike-timing reliability (Nolte et al., 2018)—that is how precisely spikes occur at the same time in response to repeated trials of a thalamic stimulus. Overall, there is little change in spike-timing reliability going from NMC- to cloud-model (Supplementary Figure 4.11A1 and 4.11A2). However, we found that there was a drop in reliability near the top of layer 5, which also displays a large in-degree reduction in the cloud model. We further noted that as the neurons have reduced in-degrees towards the bottom of layer 6 and spike less, they also become less reliable (Supplementary Figure 4.11B1–2). While neurons in the cloud-model seem to be generally slightly more reliable (Supplementary Figure 4.11C1), this can be explained by the slightly shifted EI-balance (Supplementary Figure 4.11C2). Similar to the firing rate, the change in spike-timing reliability is clearly correlated with the change in in-degree (Supplementary Figure 4.13A and 4.13B). Consequently, the change in reliability is also strongly correlated with the change in firing rate (Supplementary Figure 4.12C1–2 and Supplementary Figure 4.12D). A comparison against the NMC-model$_{\text{cloud-control}}$ (Supplementary Figure 4.13) confirms that the observed shift in reliability is primarily caused by the change in higher-order network structure.

Impact on ordering of correlations in cliques

We showed that numbers of directed simplices in the cloud-model are strongly reduced (see Figure 4.2E1). We previously observed that average pairwise correlations between neurons in simplices increased with the dimension of the simplex, and also with the position of the pair of neurons in the simplex (Reimann et al., 2017b). To assess whether there was a change in this relationship in the cloud-model, we computed pairwise correlations of spiking activity in response to the thalamic stimulus between all pairs of active neurons (Figure 4.5A). Similar to correlations between populations of neurons (see Figure 4.3D2), correlation distributions between individual neurons were very similar between NMC- and cloud-models. The cloud-model was, however, slightly closer to the transition from asynchronous to synchronous activity, with consequently generally higher correlation coefficients. Next, we calculated the average correlation coefficient of a pair of neurons in a n-dimensional simplex. To fairly compare correlations in NMC- and cloud-models, we compared correlation coefficients at various $[Ca^{2+}]_o$-levels (Figure 4.5B1–2). We found that the average correlation increased with dimension and position for both NMC- and cloud-models (Figure 4.5B1–2). However, the magnitude of the dependence on the position of the connection within the simplex changed: The difference between average correlation coefficients for connections at the *source* and the *sink* position was highly reduced in the cloud-model (Figures 4.5B1–2 and 4.5B3). Note that to avoid redundancy, the average correlation in Figures 4.5B1–3 is for *maximal* simplices,

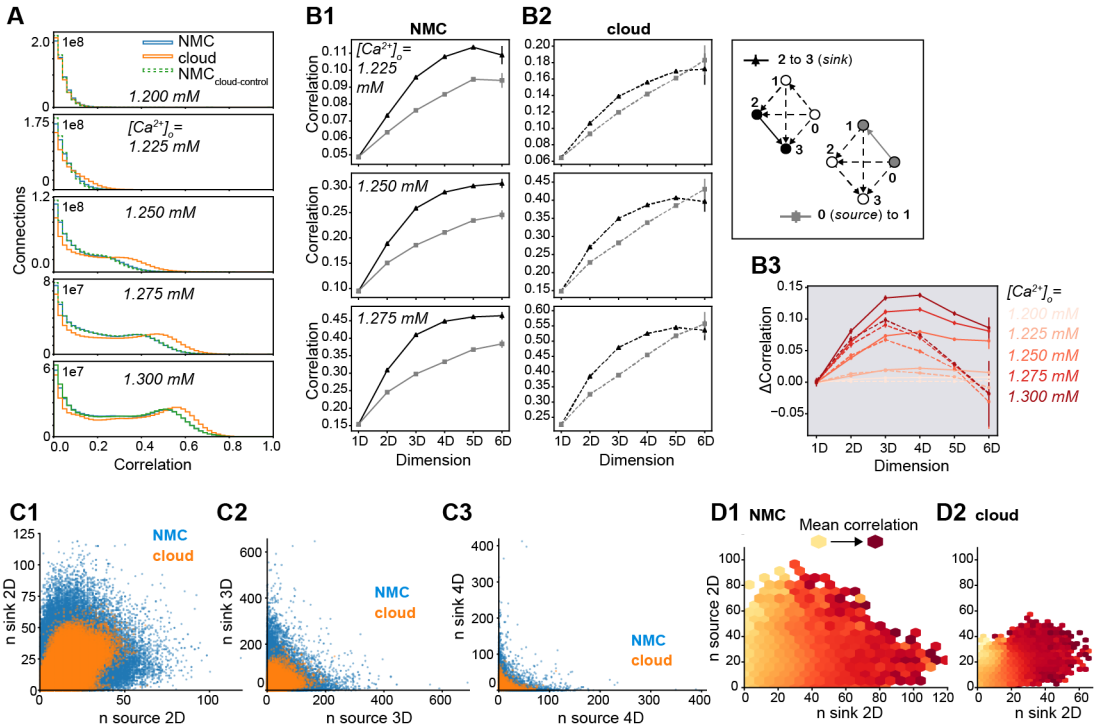

Figure 4.5 – Simplices and correlations in NMC- and cloud-models. (A1) Correlation coefficients of the firing rates ($\Delta t = 20$ ms) of all connected pairs of active neurons in the microcircuit for NMC-model, cloud-model, and NMC-model$_{\text{cloud-control}}$, during the 30 trials of the thalamic stimulus. (B1) Average correlation coefficient of a connected pair of neurons in a (maximal) simplex of a certain dimension, depending on the position of the pair in the simplex; for the NMC-model, for three different $[Ca^{2+}]_o$-levels. Black triangles indicate the average correlation for a pair of neurons at the *sink* of a simplex, grey squares the average correlation for a pair at the *source* of a simplex. (B2) As B1, but for cloud-model. (B3) Difference in average correlation coefficient for connections of neurons at the sink and the source of a (maximal) simplex. Solid lines: NMC-model; dashed lines: cloud-model. (C1) Participation of connections in the source vs. sink of (non-maximal) 2D-simplices in NMC- and cloud-models (constrained to connections at the center of layers 4, 5, 6). (C2) Participation of connections in the source vs. sink of (non-maximal) 3D-simplices in NMC- and cloud-models (constrained to connections at the center of layers 4, 5, 6). (C3) Participation of connections in the source vs. sink of (non-maximal) 4D-simplices in NMC- and cloud-models (constrained to connections at the center of layers 4, 5, 6). (D1) Mean correlation given the participation of a connection in (non-maximal) 2D-simplices at the source and sink, from bright yellow (low correlation) to dark red (high correlation); in NMC-model, constrained to connections at the center of layers 4, 5, 6. (D2) As D1, but for the cloud-model.

simplices that are not part of any higher dimensional simplices (Reimann et al., 2017b).

A possible explanation for this diminished hierarchical organization of correlations in simplices could be the higher homogeneity of connectivity in terms of correlations of in- and out-degrees (see Figure 4.2C1). In fact, this effect extends from the in- and out-degree of individual neurons to the *participation* of connections at the source and sink of simplices. The correlation between the participation of pairs of neurons in simplices as the sink or the source was highly reduced (Figure 4.5C1–3). Similar to in- and out-degrees for individual neurons, pairs of neurons in the NMC-model are thus also more specialized into input and output connections. In fact, we found that the expected correlation of a connection is highly influenced by the participation in simplices as the sink, but not as the source (Figure 4.5D1–2). Taken together, this illustrates that the increased heterogeneity of synaptic connectivity from cloud- to NMC-model extends to higher-dimensional motifs of neurons, and shapes the correlation structure of emergent activity.

4.3 Discussion

We introduced a method to reduce the higher-order structure of synaptic connectivity in a neocortical microcircuit model, based on a previously published control connectome with a reduced common-neighbor bias (Reimann et al., 2017a). In this control cloud-model, excitatory synaptic connectivity between neurons was derived from average morphologies rather than appositions of axons and dendrites of individual neurons, as was done in the original NMC-model (Figure 4.1). We showed that the reduction in higher-order structure in the cloud-model includes more homogeneous in- and out-degree distributions, the disappearance of hub neurons, less connectivity towards the bottom of layer 6, less all-to-all directed cliques of neurons and reduced small-worldness (Figure 4.2). Spontaneous and evoked dynamics in the NMC-model and cloud-model are superficially very similar (Figures 4.3-4.4), a result that is not surprising given the conserved first-order structure, including conserved interlaminar connectivity, structural EI-balance and distance-dependent connectivity. However, some properties of neuronal activity changed. Global firing patterns diverged, and spike counts and spike time-reliability of individual neurons changed according to in-degrees (Figure 4.4 & Supplementary Figure 4.11). Most importantly, a hierarchical dependence of correlation strength on the position of a pair of neurons in directed cliques (*simplices*) was weaker in the cloud-model than in the NMC-model (Figure 4.5). In summary, we established a method that can reduce the higher-order structure of cortical circuitry without changing first-order structure, leading to very similar global dynamical properties. Nuanced changes in electrical activity, such as the more homogenous correlation structure in directed cliques, suggest that higher-order network structure is important for computation in the cortex, for example in shaping functional plasticity by influencing correlations (Hebb, 1949; Markram et al., 1997b; Kempter et al., 1999).

Our definition of higher-order structure includes degree distributions of neurons, since these

cannot be described by the properties of neurons (edges) or connections (vertices) alone, consistent with previous definitions of higher-order network structure (Benson et al., 2016). Nevertheless, reducing higher-order network structure while keeping degree distributions fixed is possible, and such higher-order structure can have an impact on network dynamics (Ritchie et al., 2014). To better understand the respective impact of changes in in- and out-degrees on one side, and clustering and high-dimensional motifs on the other side, it will be necessary to create a more refined control model that conserves degree distributions on top of first-order structure.

The comparison between NMC- and cloud-models comes with several caveats. Distance-dependent connectivity in the cloud-model is not perfectly preserved for all m-type combinations (Reimann et al., 2017a). Distance-dependance is however much better conserved than in a previous control model that disregarding the average shapes of m-types, resulting in much fewer simplices (Reimann et al., 2017b). The cloud-model further neglects to account for inhibitory higher-order structure. However, the structural similarity between cloud-connectomes (changed excitatory and inhibitory connectivity) and the cloud-model (changed excitatory connectivity only) suggests that the contribution of inhibitory connections to higher-order network structure in the NMC-model is negligible. This could potentially be due to an underestimation of inhibitory higher-order structure in the NMC-model, either due to insufficient biological data constraining the connectivity, or because inhibitory structure might only emerge through plasticity (Vogels et al., 2011).

Indeed, this brings us to the most important caveat: The NMC-model is a statistical reconstruction of a prototypical microcircuit from sparse data. While it captures a high level of detail of synaptic connectivity (Gal et al., 2017), with strong constraints on the space of connectivity that can be explored by structural plasticity (Reimann et al., 2017a), the model has not learned to respond to specific stimuli or perform certain computations. This is illustrated by the fact that the discrimination accuracy to thalamic stimuli targeting different areas of the microcircuit is almost identical between NMC- and cloud-models (see Supplementary Figure 4.14). A comparison of numbers of simplices observed in in vitro slice experiments with similar in silico recordings replicated in the NMC-model shows that the number of simplices in the NMC-model is likely underestimated by an order of magnitude (Reimann et al., 2017b). This suggests that a large fraction of biological higher-order structure is not captured by the NMC-model. This leads to at least two interesting questions to be explored in the future: Firstly, what is the functional impact of that additional higher-order structure on network dynamics? Secondly, given a biologically plausible model of structural plasticity, could the network reach similar higher-order structure starting from both NMC- and cloud-models?

Our method of separating first and higher-order structure need not only be applied to models that use detailed morphologies, but might also be useful for the interpretation of future dense reconstructions of brain tissue using electron microscopy (Kasthuri et al., 2015). Once a volume large enough to contain several neurons of different m-types can be reconstructed, comparing the “cloud” connectivity of average reconstructed neurons to the actual biological connectivity

could serve as a powerful control to interpret the structure of synaptic connectivity.

In summary, we introduced a rigorous method for investigating the functional impact of higher-order network structure of neocortical microcircuitry by comparing a detailed microcircuit model (Markram et al., 2015) with a control model that disregards morphological diversity within neuronal types, resulting in a conserved first-order, but reduced higher-order network structure (Reimann et al., 2017a). Going beyond the common neighbor bias described by Reimann et al. (2017a), our analysis demonstrates just how many higher-order structural properties are constrained by neuronal diversity within neuronal types. In line with previous theoretical work showing that higher-order structure can impact network dynamics (Ritchie et al., 2014), our comparison between the two models suggests that the higher-order network structure of cortical synaptic connectivity impacts emergent dynamics and might be a non-negligible component of cortical function.

4.4 Methods

4.4.1 Circuit models

Neocortical microcircuit model (NMC-model)

Methods are based on a previously published model of a neocortical microcircuit of the somatosensory cortex of the two week-old rat, here called the *NMC-model* (Markram et al., 2015). Synaptic connectivity (with adjacency matrix M^{NMC}) between 31'346 neurons belonging to 55 different morphological types (m-types) was derived algorithmically starting from the appositions of dendrites and axons, and then taking into account further biological constraints such as number of synapses per connection and bouton densities (Reimann et al., 2015). Neuronal activity in the NMC-model was then simulated in the NEURON simulation environment (www.neuron.yale.edu/neuron/). Detailed information about the circuit, NEURON models and the seven connectomes of the different statistical instantiations of the NMC-model analyzed in this study are available at bbp.epfl.ch/nmc-portal/ (Ramaswamy et al., 2015). Simulations and analysis were performed on an HPE SGI 8600 supercomputer (BlueBrain V).

cloud-connectome

Synaptic connectivity based on average morphologies (with adjacency matrix M^{cloud}) was computed with methods previously described by Reimann et al. (2017a). In brief, for each m-type m_i out of the 55 m-types, we computed $V_{m_i}^{dendrite}(x,y)$ and $V_{m_i}^{axon}(x,y)$, the mean dendrite and axon density of each m-type, based on 10 reconstructed morphologies per m-type, with a resolution of 2 $\mu m \times 2$ μm. Next, we computed for all combinations of m-types the convolution of axon and dendrite densities $V_{m_i \to m_j}^{\text{cloud-overlap}}(\Delta y, \Delta x) = V_{m_i}^{dendrite} * V_{m_j}^{axon}$. This yielded a measure of the expected strength of the overlap of axon and dendrite for pairs of neurons at all potential relative soma positions. We then looked up this value for all pairs of

neurons of a given combination of m-types $m_i \rightarrow m_j$, based on their locations in the NMC-model and formed a matrix of overlap strengths $O^{\text{cloud}}_{m_i \rightarrow m_j}$ (stored in a table). We next applied a transfer function $\tilde{O} = O^2$, which was chosen to conserve distance-dependent connectivity from the NMC-model for most m-type combinations (Reimann et al., 2017a). We then normalized the matrix $\tilde{O}^{\text{cloud}}_{m_i \rightarrow m_j}$ to yield a matrix of connection probabilities such that the expected number of connected pairs equals the number of pairs in the NMC-model:

$$P^{\text{cloud}}_{m_i \rightarrow m_j} = \frac{\tilde{O}^{\text{cloud}}_{m_i \rightarrow m_j}}{c} \text{ with c chosen such that } \overline{P^{\text{cloud}}_{m_i \rightarrow m_j}} = \overline{M^{\text{NMC}}_{m_i \rightarrow m_j}}, \tag{4.1}$$

where $\overline{P^{\text{cloud}}_{m_i \rightarrow m_j}}$ is the average connection probability for $m_i \rightarrow m_j$ in the cloud-model, and $\overline{M^{\text{NMC}}_{m_i \rightarrow m_j}}$ is the average connection probability for $m_i \rightarrow m_j$ in the NMC-model. The adjacency matrix M^{cloud} was then randomly generated from the normalized connection probabilities for all 55×55 $m_i \rightarrow m_j$ combinations.

Five example connectomes for each of the seven NMC-connectomes are available at bbp.epfl.ch/nmc-portal/downloads → AVERAGE (Reimann et al., 2017a).

cloud-model

We implemented one of the cloud model connectomes(M^{cloud}) within the existing NMC-model, using pre-existing synapses from the NMC-model. To keep physiological properties such as mean number of synapses per connection conserved, we rewired connections by changing the *source* of *netCon* in NEURON for all synapses in a connection to a new presynaptic neuron according to M^{cloud}, and we constrained this rewiring to connections with the same presynaptic m-type in the cloud- as in the NMC-model. If there were less connections of a $m_i \rightarrow m_j$ combination than required by M^{cloud}, we duplicated connections and their synapses. As some neurons receive input in M^{cloud} from neurons that they did not receive input in in M^{NMC}, some connections could not be implemented. This was a particular problem for inhibitory connections, and we therefore only implemented M^{cloud} for excitatory neurons. This resulted in a connectivity matrix $M^{\text{cloud-model}}$ that uses M^{cloud} for excitatory connections (with a 0.12% loss of connections), and conserved connectivity M^{NMC} for inhibitory connections.

NMC-model$_{\text{cloud-control}}$

To ensure that any changes in emergent activity were not due to the 0.12% of missing connections, or to a shuffling of path lengths (shuffled delays of action potential propagation from soma to synapse), we created a control circuit in which we randomly removed exactly the same number of connections per pathway (0.12%) from the NMC-model as could not be

implemented in the cloud-model, i.e.:

$$\overline{M^{\text{NMC}_{\text{cloud-control}}}_{m_i \to m_j}} = \overline{M^{\text{cloud-model}}_{m_i \to m_j}} \tag{4.2}$$

We then shuffled connections with the same presynaptic m-type for each postsynaptic neuron (only for excitatory neurons), keeping the connectivity matrix identical but the locations of synapses randomized as in the cloud-model (and consequently incorrect axonal path lengths).

4.4.2 Simulation

Spontaneous activity

Simulation methods are identical to methods described by Markram et al. (2015): To simulate spontaneous activity, neurons were injected with a depolarizing somatic current, with currents expressed as a percent of first spike threshold for each neuron (100% current used). The U_{SE} parameter for synaptic transmission of inhibitory and excitatory synapses was then differentially modulated by changing the extracellular calcium concentration $[Ca^{2+}]_o$. At $[Ca^{2+}]_o$ = 1.25 mM, the circuit was in an in vivo-like state of asynchronous activity with a global balance of excitation and inhibition. We simulated 20 trials of spontaneous activity (2 seconds) in the NMC-model, cloud-model, and NMC-model$_{\text{cloud-control}}$ at five different $[Ca^{2+}]_o$ concentrations around the in vivo-like state at $[Ca^{2+}]_o$ = 1.25 mM. We further added two trials of two second duration at other $[Ca^{2+}]_o$ concentrations to illustrate the transition from asynchronous to synchronous activity. The first second of activity was discarded, as the circuit has not yet reached a resting state.

Evoked activity

We simulated spontaneous activity for seven seconds, as described above. After one second (at t = 0 ms, as we discard the first second) we apply a thalamic stimulus through synapses of 310 VPM fibers that innervate the microcircuit. The stimulus lasts five seconds (t = 0 to 5 s) and is identical to a previously described stimulus (Reimann et al., 2017b; Nolte et al., 2018) based on in vivo thalamic recordings to whisker deflection (Bale et al., 2015). We simulated 30 trials of the same stimulus in the NMC-model, cloud-model and NMC-model$_{\text{cloud-control}}$ at five different $[Ca^{2+}]_o$ concentrations around the in vivo-like state at $[Ca^{2+}]_o$ = 1.25 mM.

Spatial discrimination

We stimulated the microcircuit by activating five different clusters of five thalamic fibers at five different locations in the microcircuit ($-50, -25$, 0, 25, and 50 μm from center). We simulated activity in the NMC-model and cloud-model 20 times each for the five different stimulus locations at three $[Ca^{2+}]_o$ concentrations around the in vivo-like state at $[Ca^{2+}]_o$ = 1.25 mM. The stimulus consists of a single spike in each of the five fibers at t = 0, 50, 100, 150, 200, and

250 ms.

4.4.3 Analysis

In-degree

Number of presynaptic connections a neuron forms with other neurons in the microcircuit.

Out-degree

Number of postsynaptic connections a neuron forms with other neurons in the microcircuit.

Simplices

A *simplex* is a clique of all-to-all connected neurons. Methods and definitions were adapted from Reimann et al. (2017b). In brief, if $G = (V, E)$ is a directed graph, where V is a set of vertices (neurons) and E a set of ordered pairs of vertices (directed connections between neurons), then its *directed nD-simplices* for $n \geq 1$ are $(n+1)$-tuples $(v_0, \ldots, v_n)$ of vertices such that for each $0 \leq i < j \leq n$, there is an edge in G directed from v_i to v_j. Neuron 0 (the vertex v_0), the *source* of the simplex $(v_0, \ldots, v_n)$, receives no input from within the simplex, but innervates all neurons in the simplex (there is an edge directed from v_0 to v_i for all $0 < i \leq n$). Neuron 1 (v_1), receives input from Neuron 0, and innervates Neurons 2 (v_1) to n (v_n), and so forth. Neuron n, the *sink*, receives input from all neurons in the simplex, but does not innervate any (there is an edge directed from v_0 to v_i for all $0 < i \leq n$). See Figure 4.2E1 for an illustration. Note that reciprocal connections are counted separately: an n-simplex in G is defined by the (ordered) sequence $(v_0, \ldots, v_n)$, but not by the underlying set of vertices (neurons). For instance (v_1, v_2, v_3) and (v_2, v_1, v_3) are distinct $2D$-simplices with the same neurons. We computed simplices using *flagser* (https://github.com/luetge/flagser).

Higher-order in-degree

We define the ND-in-degree as the number of ND-simplices a neuron is the sink of. For 1D-simplices (a pair of connected neurons), this is simply the in-degree.

Simplex participation of pairs of neurons

We define as the ND-participation of connections at the source or the sink of a simplex how many ND-simplices a connection is part of as the source (neurons 0 and 1) or at the sink (neurons $N-1$ and N). See inset next to Figure 4.11B for an illustration.

Betti numbers

In brief, Betti numbers describe the number of "cavities" or "holes" formed by the simplices in each dimension. Betti numbers were computed using *flagser* (https://github.com/luetge/flagser). Detailed methods are as previously described by Reimann et al. (2017b).

Euler characteristic

The alternating sum of the number of simplices in each dimension (and of non-zero Betti-Numbers).

Small-worldness

Methods are as defined by Gal et al. (2017) and were computed using the Brain Connectivity Toolbox (Rubinov and Sporns, 2010). In brief, we first computed the characteristic path length of the network, defined as the mean shortest path length of all pairs of neurons ($N = 31346$):

$$l = \frac{1}{N(N-1)} \sum_{i \neq j} l_{ij} \tag{4.3}$$

We next defined the network-wide clustering coefficient as:

$$c = \frac{1}{N} \sum_{i} \frac{(M + M^T)^3_{ii}}{2(d_i^{\text{tot}}(d_i^{\text{tot}} - 1) - 2M_{ii}^2)} \tag{4.4}$$

where M is the binary connection matrix and d_i^{tot} the combined in- and out-degree of each neuron i. Thus, $c = 0$ indicates that there are no common neighbors, and $c = 1$ indicates that all neighbors are mutually connected. The ratio of c/l gives indication about the small-worldness of the network. We showed previously that the NMC-model has a small-world topology by comparing it to different control models (Gal et al., 2017). A smaller value of c/l for the cloud-than NMC-model thus shows that small-worldness decreases.

Firing rate

We defined the firing rate (FR) as the average number of spikes in a time bin of size Δt, divided by Δt.

Spike-timing reliability

Spike-timing reliability was quantified with a correlation-based measure (Schreiber et al., 2003). The spike times of each neuron n in each trial k ($K = 30$ trials) were convoluted with a Gaussian kernel of width $\sigma_S = 5$ ms to result in filtered signals $s(n, k, ; t)$ for each neuron n and each trial k ($\Delta t_S = 0.5$ ms). For each neuron n, the spike-timing reliability is defined as the

mean inner product between all pairs of signals divided by their magnitude:

$$r_{spike}(n) = \frac{2}{K(K-1)} \sum_{k \neq l} \frac{s(n,k;t) \cdot s(n,l;t)}{|s(n,k;t)| \cdot |s(n,l;t)} \tag{4.5}$$

Computation of spike-timing reliability is identical to a previous study (Nolte et al., 2018).

Correlation coefficients

We computed peristimulus time histograms (PSTHs) for each neuron i to the 30 trials of the thalamic stimulus (with a bin size Δt=20 ms), and next computed the normalized covariance matrix of the PSTHs of all neurons:

$$R_{ij} = \frac{C_{ij}}{\sqrt{C_{ii} C_{jj}}} \tag{4.6}$$

C_{ij} is the covariance of PSTHs of neurons i and j. The analysis is replicating a previous analysis by Reimann et al. (2017b).

Logistic regression

We used *scikit-learn* "sklearn.linear_model.LogisticRegression" (solver='liblinear', max_iter=100, multi_class='ovr'; otherwise default parameters) (Pedregosa et al., 2011) to classify the spike-count responses of neurons in layers 4, 5, and 6 in response to five different stimuli at three $[Ca^{2+}]_o$ concentrations. We used the total spike count for each of 20 trials for each neuron between t = 0 and 300 ms. We randomly picked 1, 10, 20, ..., or 100 neurons from layer 4, upper layer 5, lower layer 5, upper layer 6 or lower layer 6. For each of the 11 × 5 × 3 combinations (number of neurons × neuron location × $[Ca^{2+}]_o$), we randomly selected the right number of neurons and then kept 80% as a training and 20% as a test set. Classification accuracy was then based on the mean accuracy of 300 runs with randomly selected neurons.

Supporting information

Supporting information includes Supplementary Figures 4.6-4.14.

Acknowledgments

We thank the Blue Brain team for developing and maintaining the microcircuit model and computational infrastructure. We thank Kathryn Hess and Idan Segev for helpful discussions. We thank Taylor H. Newton for help in editing the manuscript. This work was supported by funding from the ETH Domain for the Blue Brain Project. The Blue Brain Project's HPE SGI 8600 system, BlueBrain V, was funded by the ETH Board and hosted at the Swiss National

Supercomputing Center (CSCS).

Author contributions

Conceptualization, M.N., M.R., H.M.; Methodology, M.N., M.R.; Software, M.N., M.R.; Validation, M.N., M.R.; Investigation, M.N., E.G.; Visualization, M.N.; Writing – Original Draft, M.N.; Writing – Review & Editing, M.N., M.R.; Supervision, M.R., H.M., E.M.; Funding Acquisition, H.M.

4.5 Supplementary figures (4.6 to 4.14)

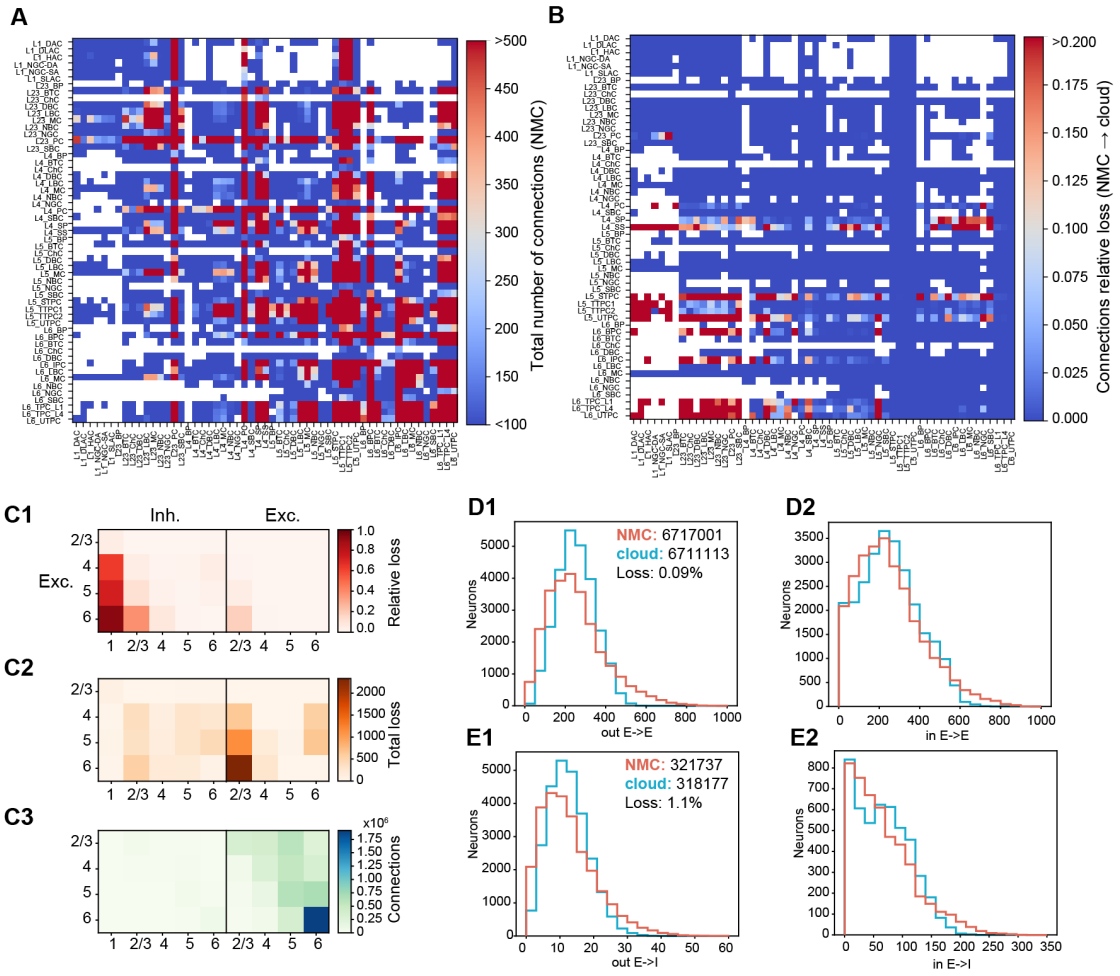

Figure 4.6 – Macro-connectome of NMC- and cloud-models. (A) Total number of connections between m-types in NMC-model. (B) Relative loss of connections from NMC- to cloud-model between each pathway (combination of pre- and postsynaptic m-types). (C1) Relative loss of connections from NMC- to cloud-model between layers and excitatory and inhibitory neurons. (C2) Total loss of connections from NMC- to cloud-model between layers and excitatory and inhibitory neurons. (C3) Total number of connections in NMC-model between layers and excitatory and inhibitory neurons. (D1) Out-degree of excitatory neurons counting only excitatory (E) connections. Numbers describe total numbers of E-to-E connections in NMC- and cloud-models. (D2) In-degree of excitatory neurons counting only excitatory connections. (E1) Out-degree of excitatory neurons counting only connections formed with postsynaptic inhibitory (I) neurons. Numbers describe total numbers of E-to-I connections in NMC- and cloud-models. (E2) In-degree of inhibitory neurons counting only excitatory connections.

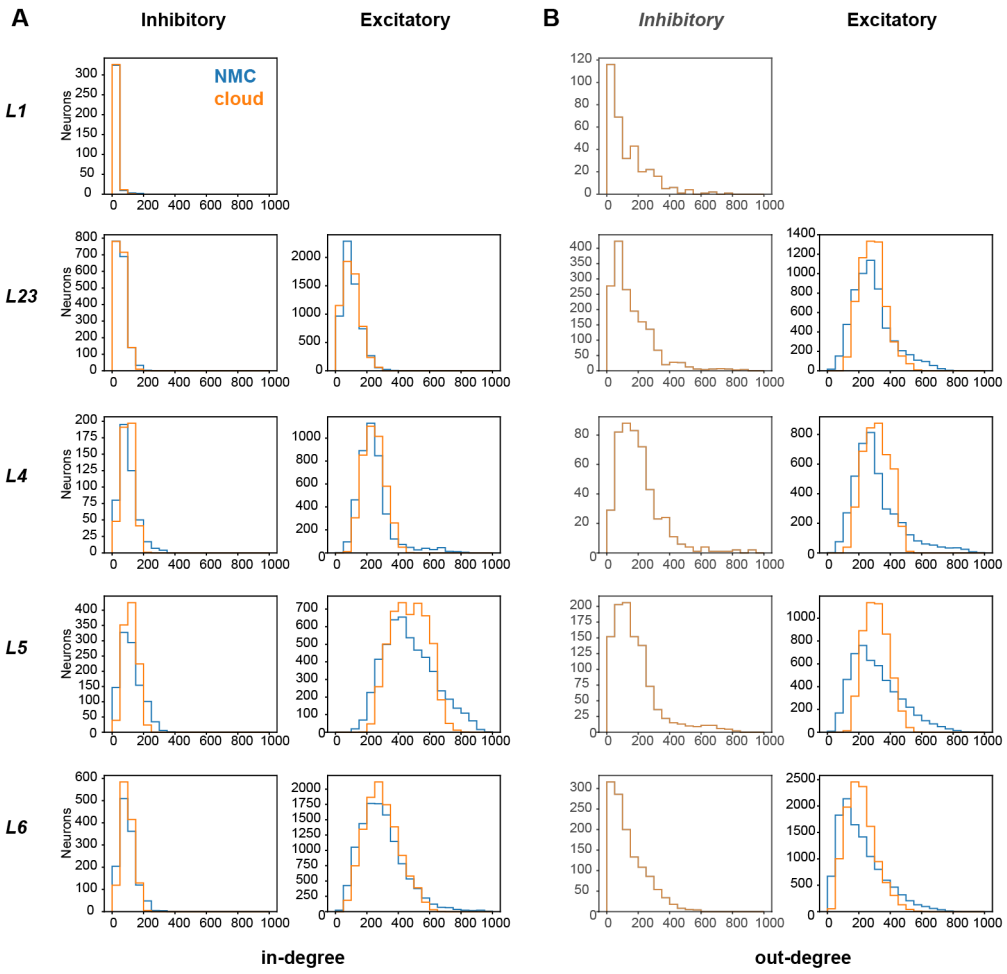

Figure 4.7 – In- and out-degrees across layers. (A) In-degrees of neurons in NMC- and cloud-models, by layer and excitatory/inhibitory sub-type. (B) Out-degrees of neurons in NMC- and cloud-models, by layer and excitatory/inhibitory sub-type.

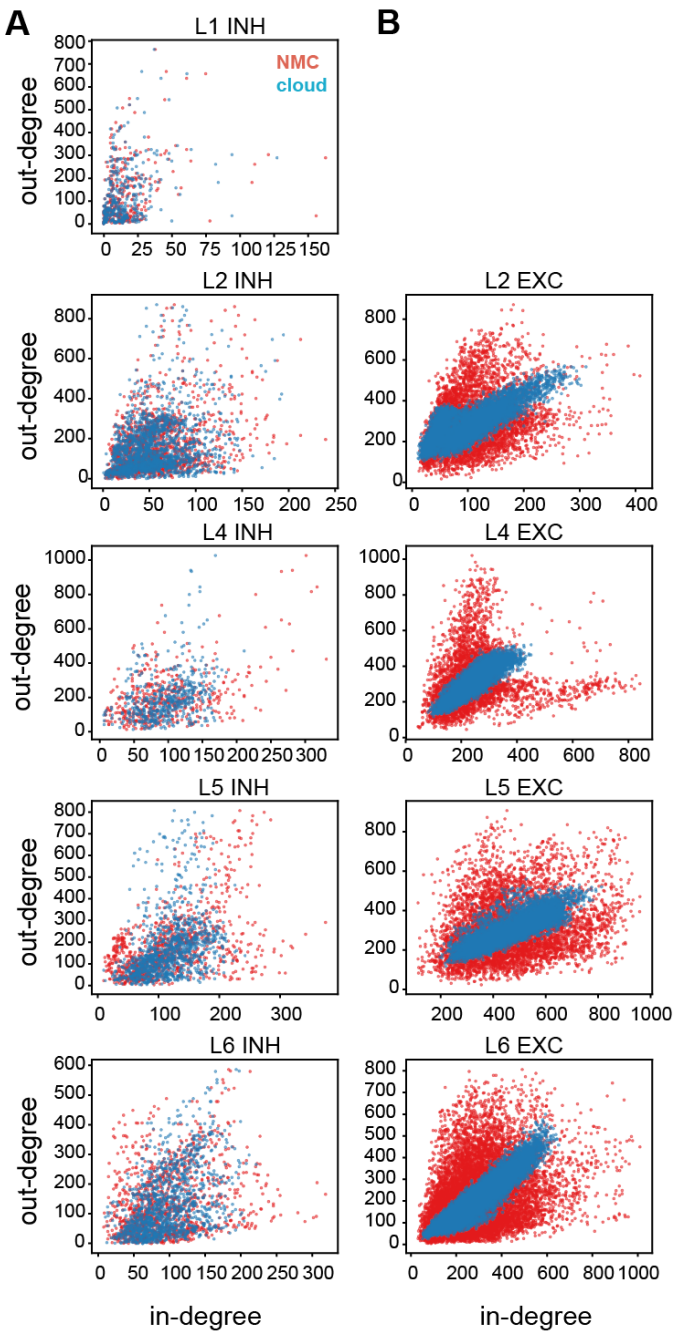

Figure 4.8 – In- and out-degree correlations. (A) Correlations between in- and out-degree for all inhibitory neurons in NMC- and cloud-models, sorted by layer. (B) Correlations between in- and out-degree for all excitatory neurons in NMC- and cloud-models, sorted by layer.

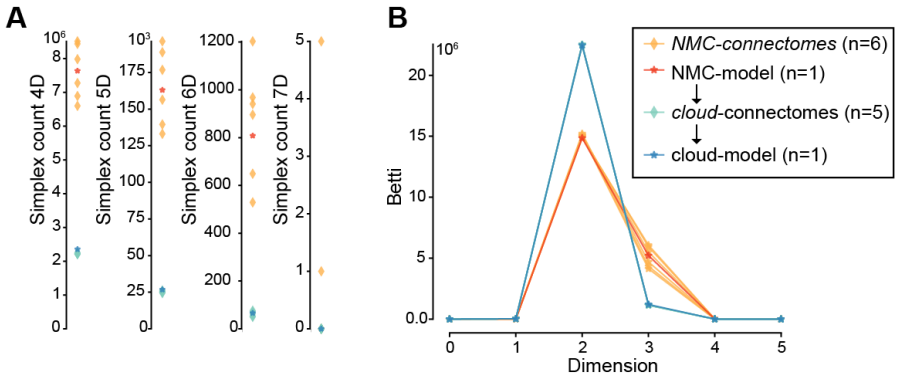

Figure 4.9 – Simplices and Betti-numbers. (A) Number of simplices of dimensions 4, 5, 6 and 7 across circuits. Same legend as B. (B) Betti-numbers across circuits.

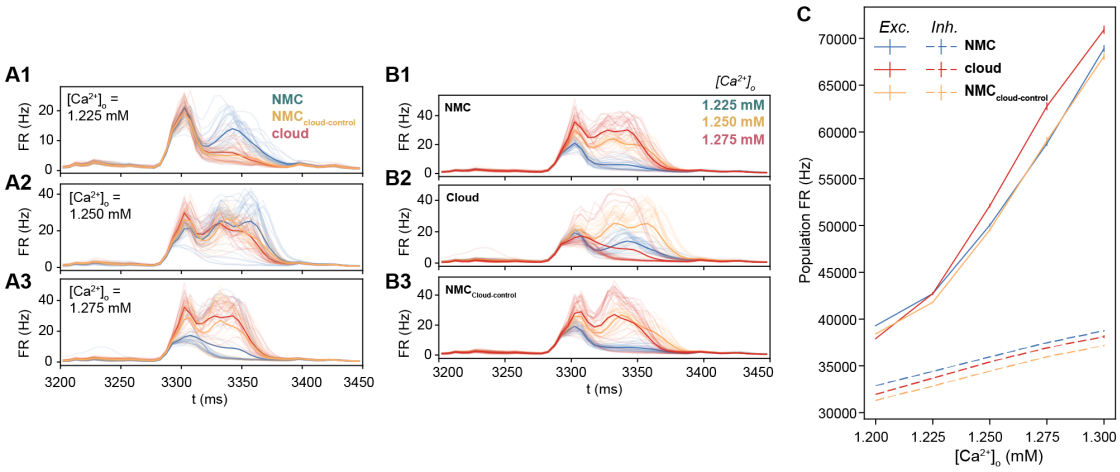

Figure 4.10 – PSTHs and firing rates. (A1-3) Peristimulus time histograms (PSTHs) for NMC-model, cloud model and NMC-model$_{\text{cloud-control}}$ for different $[Ca^{2+})]_o$ levels. Thick line indicates the mean of 30 trials, the faint lines show the individual trials. (B1-3) Same data as in A1-3, but ordered by model instead of $[Ca^{2+})]_o$. (C) Population firing rate during evoked activity at different $[Ca^{2+})]_o$ levels, across models and excitatory and inhibitory sub-populations.

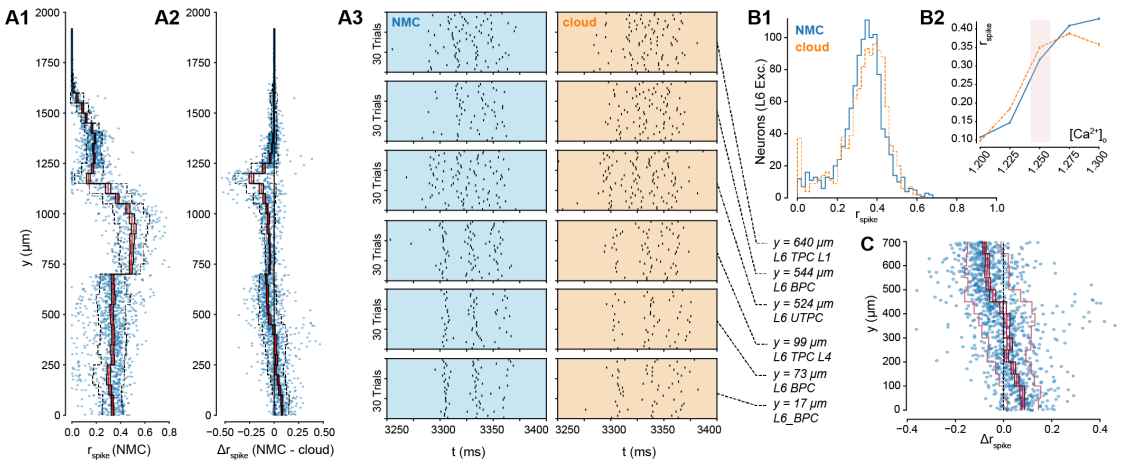

Figure 4.11 – Spike-timing reliability. (A1) Spike-timing reliability r_{spike} in NMC-model at $[Ca^{2+}]_o$ = 1.25 mM. The bright red line indicates the mean of all neurons per 50 μm bin, solid black lines indicate standard error of the mean, and the outer dashed lines the standard deviation, for around 3000 excitatory neurons in the center of the microcircuit. (A2) Difference in spike-timing reliability Δr_{spike} between NMC- and cloud-models at $[Ca^{2+}]_o$ = 1.25 mM. The bright red line indicates the mean of all neurons per 50 μm bin, solid black lines indicate standard error of the mean, and the outer dashed lines the standard deviation, for around 3000 excitatory neurons in the center of the microcircuit. (B1) Spike raster of neurons at different locations in layer 6, in NMC- and cloud-models. (B2) Difference in spike-timing reliability Δr_{spike} between NMC- and cloud-models at $[Ca^{2+}]_o$ = 1.25 mM. The bright red line indicates the mean of all neurons per 50 μm bin, dark red lines indicate standard error of the mean, and the outer lines the standard deviation, for 1092 excitatory neurons in the center of layer 6. (C1) Spike-timing reliability r_{spike} in NMC- and cloud-models at $[Ca^{2+}]_o$ = 1.25 mM, for 1092 excitatory neurons in the center of layer 6. (C2) Spike-timing reliability r_{spike} NMC- and cloud-models at different $[Ca^{2+}]_o$-levels, for 1092 excitatory neurons in the center of layer 6.

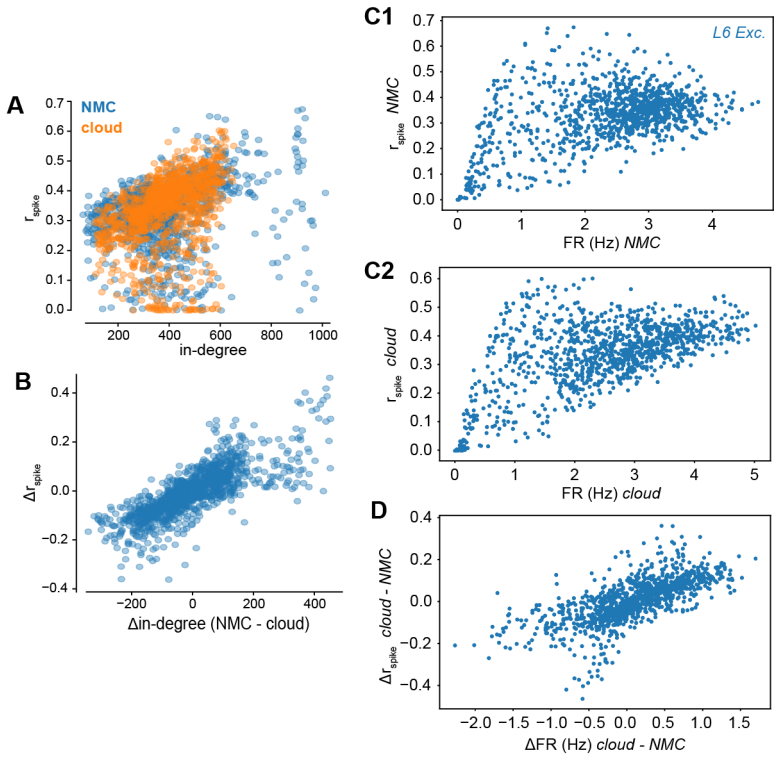

Figure 4.12 – Spike-timing reliability and firing rate. (A) In-degree vs. spike-timing reliability r_{spike} for NMC- and cloud-models for 1092 excitatory neurons in the center of layer 6.. (B) Difference in in-degree vs. difference in spike-timing reliability Δr_{spike} between NMC- and cloud-models for 1092 excitatory neurons in the center of layer 6. (C1) Firing rate vs. spike-timing reliability for 1092 layer 6 excitatory neurons in the center of the NMC-model. (C2) Firing rate vs. spike-timing reliability for selected layer 6 excitatory neurons in NMC-model. (D) Difference in Firing rate vs. spike-timing reliability between NMC- and cloud-models (same neurons as in A–C).

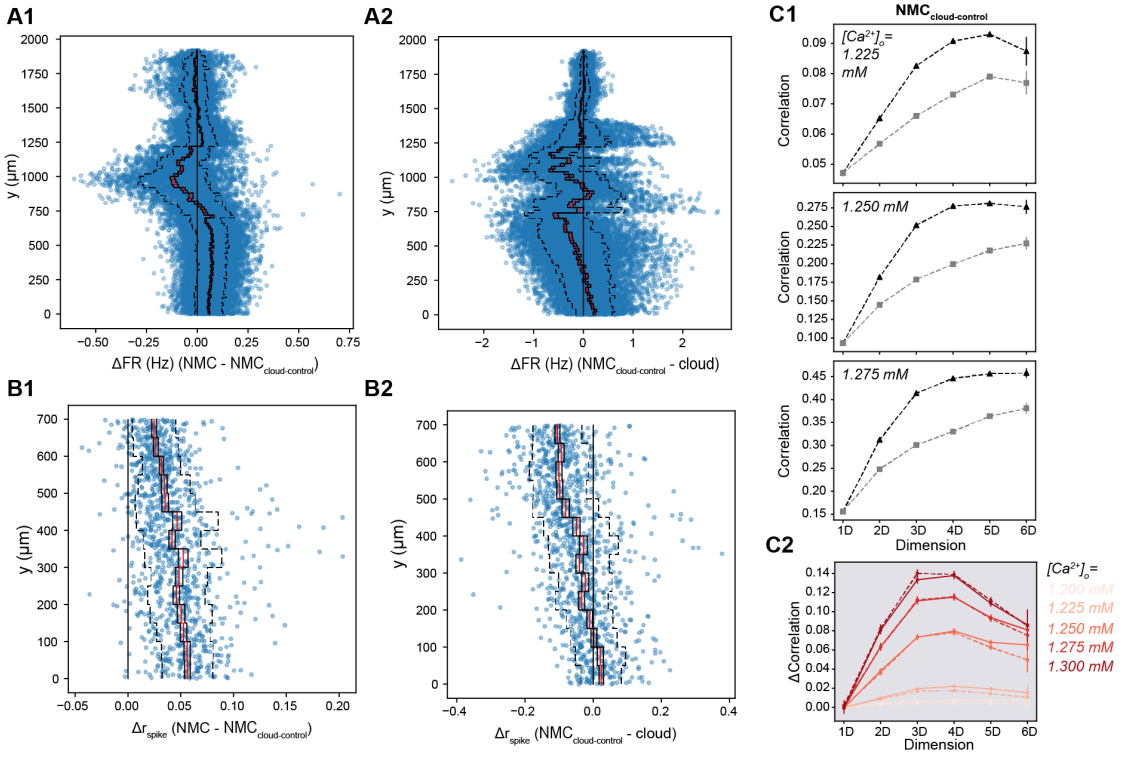

Figure 4.13 – Spike-timing reliability and firing rate in NMC-model$_{\text{cloud-control}}$. (A1) Difference in firing rate of excitatory neurons during evoked activity at $[Ca^{2+}]_o$ = 1.25 mM between NMC-model and NMC-model$_{\text{cloud-control}}$. Blue dots indicate values for individual neurons, ordered along their soma positions with respect to the y-axis (cortical depth). Lines indicate mean (bright red), standard-error (black), and standard deviation (dashed). (A2) As A1, but between NMC-model$_{\text{cloud-control}}$ and cloud-model. (B1) As A1, but for spike-timing reliability in L6. (B2) As B1, but between NMC-model$_{\text{cloud-control}}$ and cloud-model. (C1) Expected correlation coefficients between connections of neurons at the sink and the source of a simplex of a given dimension, for NMC-model$_{\text{cloud-control}}$. (C2) Difference in expected correlation coefficients between connections of neurons at the sink and the source of a simplex of a given dimension, for NMC-model and NMC-model$_{\text{cloud-control}}$.

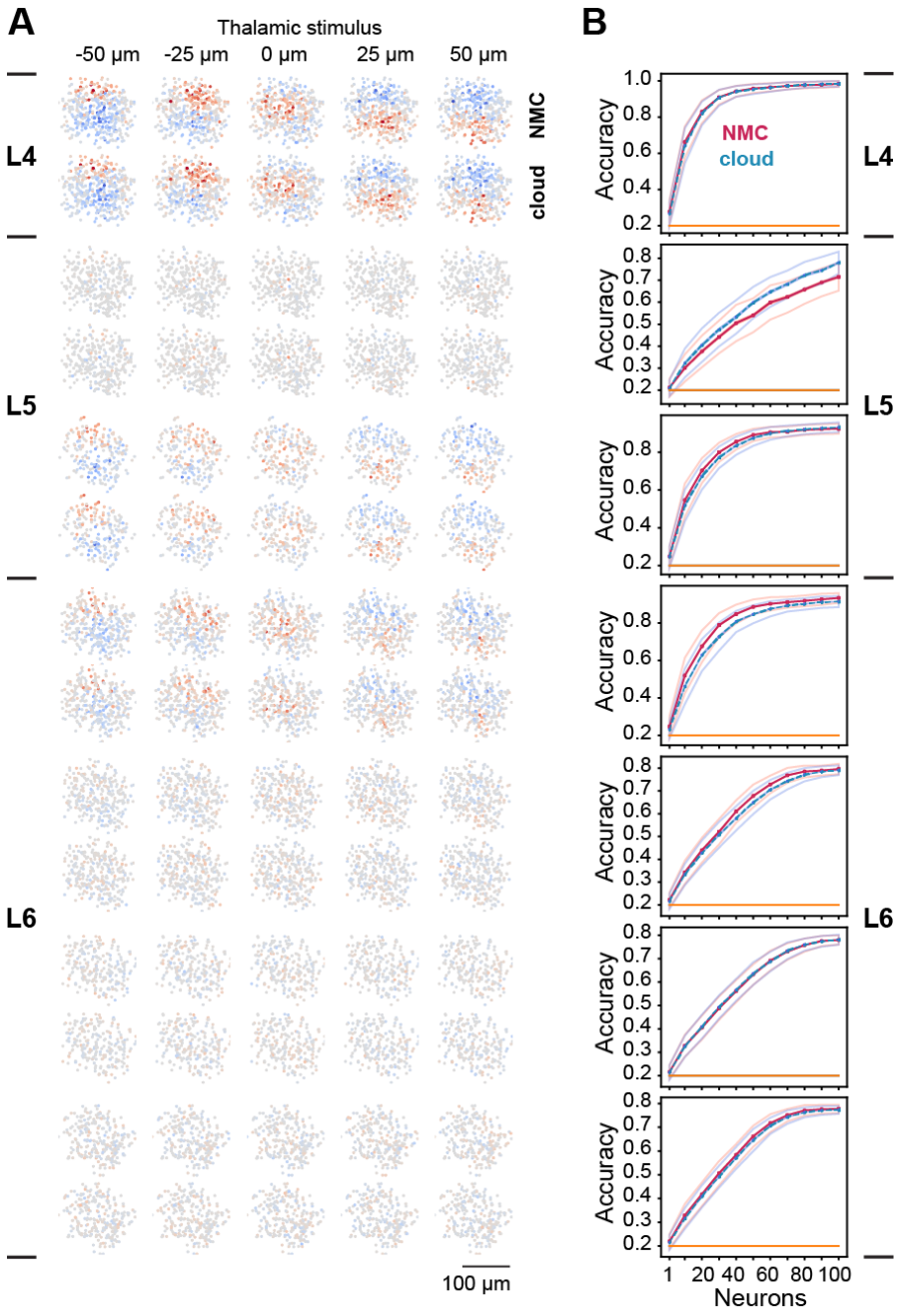

Figure 4.14 – Stimulus discrimination (A) Deviation of firing rate to mean in response to a stimulus at different positions ($-50\ \mu m$ to $-50\ \mu m$ from center) (B) Discrimination accuracy given the number of randomly chosen neurons used to classify the stimulus with logistic regression.

5 Conclusion

At the beginning of this thesis, we set out to *untangle emergent cortical dynamics*. This was motivated by the observation that in vivo responses of cortical neurons to the same stimulus are often highly variable across trials, but sometimes extremely reliable. There are many competing explanations for how the observed variability might emerge within a local network of cortical neurons, from *neuronal* properties—such as synaptic *noise*—to *network* properties—such as *chaos*. It remained unclear how reliable responses arise and how they relate to the observed variability.

To tackle this question, we chose a simulation-based approach in order to have a complete view of, and exert full control over, the structure and function of a local neocortical microcircuit. Given the state of current technology, this is still rather difficult to achieve in vitro or in vivo. We argue that making meaningful qualitative and quantitative predictions about how observed cortical dynamics emerge requires a data-constrained model without ad hoc simplifying assumptions (Chapter 1.1.3). Different models can often explain the same function, making it hard to interpret how the mechanisms of the model relate to the true neurobiological mechanisms (Landau et al., 2016). For example, different cellular noise sources and chaotic network dynamics can provide explanations for observed cortical variability in vivo (Moreno-Bote, 2014; London et al., 2010). Therefore, making predictions about the impact of these sources of variability requires data-constrained estimates of their magnitudes.

5.1 Summary of main conclusions

We simulated neuronal activity in a neocortical microcircuit model of the somatosensory cortex of the two-week old rat—the *NMC-model* (Markram et al., 2015)—to make predictions about how the dynamics of spontaneous and evoked activity emerge from the structure of neocortical microcircuitry. Below is a summary of the most important original findings that form part of this thesis:

1. *Cell-type specific whisker flick responses emerge at the microcircuit level* (Chapter 1.3.2).

We showed that the NMC-model, which was reconstructed according to available biological data without ad hoc simplifying assumptions, exhibits fundamental properties of spontaneous and evoked neocortical activity in vivo. In particular, in response to a strong thalamic stimulus imitating a whisker 'flick', reliable and cell-type specific responses emerged, as previously observed in vivo (Reyes-Puerta et al., 2014). This adds to the growing evidence that many spike-patterns arise from the general structure of neocortical microcircuitry (MacLean et al., 2005; Luczak et al., 2007). This result also raised an important question which we were able to address using our model: How can reliable responses emerge in a microcircuit that models many biological noise sources, which, according to a signifcant body of theoretical and experimental evidence, is ostensibly chaotic (van Vreeswijk and Sompolinsky, 1996, 1998; London et al., 2010)?

2. *Synaptic noise forms an integral part of cortical chaotic network dynamics* (Chapter 2). We confirmed that intrinsic cortical network dynamics in a deterministic version of the NMC-model are chaotic, but found that the timescale of chaotic divergence is orders of magnitude faster when simulating biological noise sources, most importantly synaptic noise. Stochastic synaptic release is often not taken into account, for example even when studying origins of internally generated variability (Huang et al., 2019). Our finding adds to the growing evidence that synaptic noise is a non-negligible component of cortical network dynamics (Moreno-Bote, 2014).

3. *Synaptic noise overshadows other local cellular noise sources* (Chapter 2). We added additional noise to predict the impact of missing ion-channel noise, and found that it would have to be almost as large as synaptic noise ($\geqslant 1$ mV) to have an impact on intrinsic chaotic dynamics beyond synaptic noise. While a comparison with more detailed models of missing cellular noise sources is required, this suggests that other intrinsic noise sources need not always be modeled when incorporating voltage fluctuations due to synaptic noise.

4. *Reliable responses and chaotic, divergent dynamics are not mutually exclusive* (Chapter 2). We observed that the dynamics of chaotic divergence during evoked, reliable activity followed exactly the same timescale as during spontaneous activity. This adds to the theoretical evidence that reliability and chaos can coexist in cortical networks (Rajan et al., 2010; Lajoie et al., 2013, 2016), even in the face of intrinsic biological noise sources driving the chaotic dynamics with constant perturbations.

5. *A near-critical EI-balance enables cortical circuitry to respond reliably amid noise and chaos* (Chapter 2). We found that the reliability of the response strongly depends on the global EI-balance, with a steep increase in reliability near the "critical" point of transition from asynchronous to synchronous activity, adding to the growing evidence that the brain maintains a near-critical state (Shew et al., 2009), and specifically supporting the hypothesis that the cortex operates just *below* the critical threshold (Priesemann et al., 2014). The reliability of the response can thus be fine-tuned by any mechanism that shifts the EI-balance, such as neuromodulation (Colangelo et al., 2019).

6. *Poisson-like spike count variability does not emerge at the microcircuit level, but reflects reliable responses to uncontrolled inputs to the local circuitry* (Chapter 2). Even though intrinsic variability in the NMC-model was high in terms of chaotic divergence, we found fairly low spike count variability in the absence of external inputs, contradicting a previous simplified study (Moreno-Bote, 2014). Our findings suggest that Poisson-like spike count variability does not arise from intrinsic, within-network dynamics, but is caused by unobserved inputs, be it hidden inputs from other brain areas, external noise, or global modulation (Fairhall, 2019; Musall et al., 2018; Muller et al., 2018).

7. *Cortical circuitry contains an abundance of directed, all-to-all connected cliques of neurons called simplices* (Chapter 3 & 4). We applied basic methods of algebraic topology to the microcircuit model and observed an abundance of all-to-all connected cliques of neurons (Chapter 3) that was highly diminished in control models (Chapters 3 & 4), providing further evidence of the highly non-random structure of cortical circuitry (Song et al., 2005; Perin et al., 2011).

8. *These simplices shape a hierarchy of spiking correlations* (Chapters 3 & 4). We found that these simplices shape pairwise spike correlations between neurons, with a hierarchical ordering of expected correlation coefficients according to simplex dimension and position of a connection within the simplex (Chapter 3). When we simulated a neurobiologically invalid control model with a substantial reduction in higher-order structure (Reimann et al., 2017a) (and consequently far fewer simplices), this position-dependence was notably weaker (Chapter 4).

Taken together, these simulation results show that neurobiological details such as stochastic synaptic release and higher-order structure of synaptic connectivity shape emergent cortical network dynamics, and that the impact of omitting such details in a simplified cortical network model requires careful evaluation.

5.2 Future directions

The predictions of the NMC-model come with many caveats. The NMC-model, while very detailed and constrained to biological data, uses interpolation and generalization to fill in gaps where data is missing. Notably, there are several important features of local cortical microcircuitry that could shift dynamics in the NMC-model—though in which direction these shifts would occur remains to be seen. We discussed many of these details extensively in Chapter 2.3. Below, we address what we identify as the three most significant caveats for the predictions in this thesis, which will need to be tested in the near future: the role of dendritic non-linearities such as NMDA-spikes (Figure 5.1A), structural and functional plasticity (Figure 5.1B), and whole-brain integration (Figure 5.2).

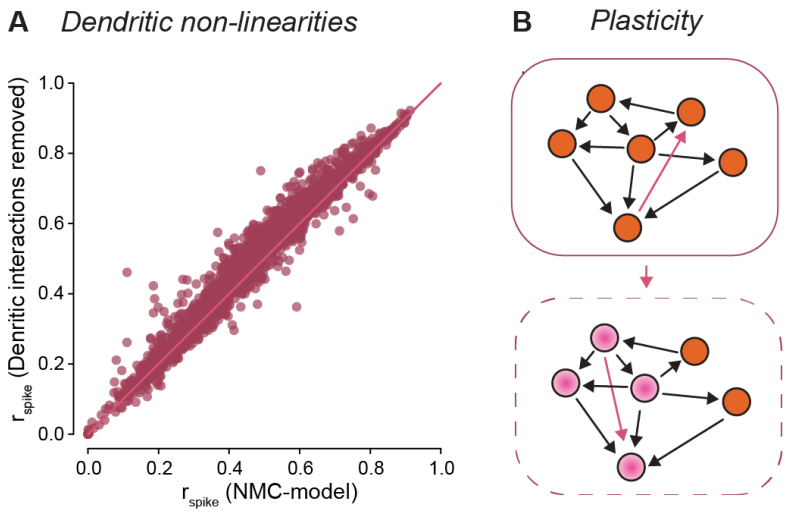

Figure 5.1 – Future directions I. (**A**) Dendritic non-linearities. Spike-timing reliability r_{spike} in response to a thalamic stimulus for the same neurons and methods as in Chapter 2 vs. r_{spike} for a decoupled replay in which synapses are directly placed on the soma. A filter accounts for the effective attenuation and delay to the synaptic current caused by the dendrite (Rössert et al., 2016). Using this second approach, the effect of the dendrite onto the synaptic current is approximately conserved for each individual synaptic input, but any interactions between different synaptic inputs are removed. (**B**) Structural and functional plasticity. Structural plasticity could lead to increased higher-order structure without violating known biological constraints.

5.2.1 Dendritic non-linearities

Nonlinear dendritic events are widespread throughout the cortex and have important computational functions (London and Häusser, 2005). For example, dendritic events shape orientation selectivity by a nonlinear response to functionally clustered synaptic inputs (Wilson et al., 2016). In the NMC-model, we can easily compare neuronal activity with and without interactions of synaptic inputs in the dendrite by using the decoupled replay mechanism introduced in Chapter 2 together with an automated synaptic filtering approach (Rössert et al., 2016). In a first preliminary investigation, we repeated the thalamic stimulus and reliability analysis from Chapter 2 with filtered synapses on the soma (i.e. with synaptic interactions removed), and found that there was a slight, but systematic increase in reliability when removing dendritic interactions (Figure 5.1). However, we observed no fundamental change in network dynamics. A specific type of nonlinear dendritic event, long lasting N-methyl-D-aspartate-mediated plateau potentials (*NMDA-spikes*), can be evoked by clustered synaptic inputs onto the dendritic tree (Schiller et al., 2000; Antic et al., 2010). These plateau potentials can facilitate faster, and perhaps more reliable, responses to inputs (Antic et al., 2018; Shai et al., 2014). However, we did not observe emergent NMDA-spikes in the NMC-model. This could have several explanations: The NMDA-receptor model used in the NMC-model (Jahr and Stevens, 1990) might not be suitable to model NMDA-spikes (Chindemi, 2018). Moreover,

while NMDA-spikes have been observed in several cortical areas and species (Antic et al., 2010), there is—to the best of our knowledge—no direct evidence yet of NMDA-spikes in the somatosensory cortex of the two-week-old rat. Finally, synaptic clustering in the NMC-model is lower than in vivo, as synapses from long-range connections are missing (around 80% of excitatory synapses, see below). The impact of dendritic plateau events on emergent cortical network dynamics thus remains to be studied in a more refined version of the NMC-model, with more accurate NMDA-receptor models, increased synaptic clustering due to inputs from other brain areas, and increased synaptic clustering due to structural and functional plasticity.

5.2.2 Structural and functional plasticity

The NMC-model uses data from different rats to build a prototypical microcircuit model. This means that any specific structure unique to one rat is lost. However, neurobiologically realistic models of functional and structural plasticity might recover some of that specific structure (Chindemi, 2018). There is reason to believe that the higher-order structure of the microcircuit could drastically increase: In Chapter 3, we approximated the in vitro 12 patch-clamp setup in silico to compare the number of simplices observed in the NMC-model to the number of simplices found in vitro (Figure 3.2). As it is difficult to exactly simulate and validate the patching process, we refrained from comparing relative frequencies of simplices in vitro and in the NMC-model. When dividing the number of observed simplices in Figure 3.2 by the number of real and simulated experiments respectively, we find that there are around $0.7-0.8$ 2D-simplices per simulated 12 patch-clamp experiment in the microcircuit, but 4.7 2D-simplices per 12 patch-clamp experiment in vivo. Similarly, there are around $0.04-0.06$ 3D-simplices per experiment in the NMC-model, compared to 0.7 in vitro. While these estimates should be treated cautiously, they suggest that the NMC-model in its naive form underestimates simplices by an order of magnitude. Simulating neurobiologically constrained structural plasticity might still take some time, but it will soon be possible to study the impact of a biophysical model of long-term functional synaptic plasticity in the NMC-model (Chindemi, 2018). Preliminary data suggest that the dependence of pairwise correlations on simplices shown in Chapter 3 increases. Following the findings of Chapter 4, we can expect that an increase in higher-order structure due to structural plasticity will further increase this dependence and shape emergent network dynamics.

5.2.3 Whole-brain integration

This thesis focused on the intrinsic dynamics of a local neocortical microcircuit. While it is certainly important to understand the structural and functional properties of individual components of the whole brain, local dynamics are of course also influenced by global inputs and long range recurrent connectivity. It is estimated that around 80% of cortical inputs to the local circuit come from other cortical areas (Reimann et al., 2017a). It might soon be possible to start untangling the impact of whole-brain integration on local microcircuit dynamics (Reimann et al., 2019). Figure 5.2 shows a *mouse* microcircuit model of similar size

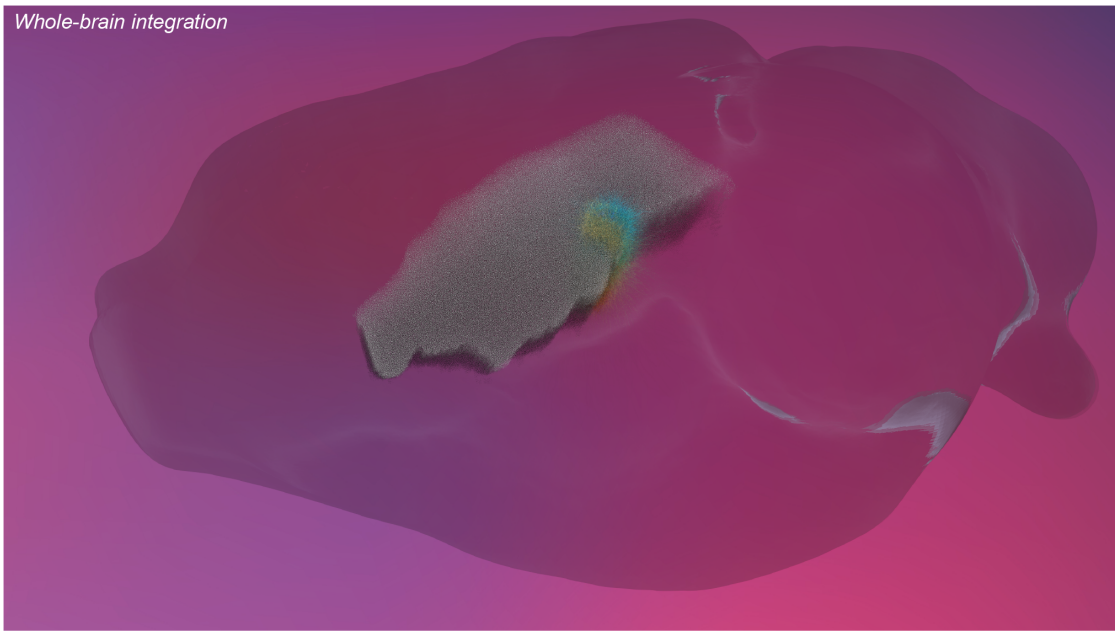

Figure 5.2 – Future directions II. Whole-brain integration: A *mouse* microcircuit (colored detailed morphologies) with a similar number of neurons as the NMC-model, embedded in a draft model of the primary somatosensory cortex (S1; point neurons), embedded in the whole brain (translucent). *Visualization: Cyrille Favreau & Blue Brain Scientific Visualization team.*

to the NMC-model (in terms of neurons; colored detailed morphologies) embedded in the primary somatosensory cortex (point neurons). Perhaps more important, especially for our predictions from Chapter 2, is integration with the thalamus, which controls cortical states (Poulet et al., 2012), including recurrent connections, which may soon be possible. Indeed, models of thalamic neurons are already available (Iavarone et al., 2019). Non-local inputs also include neuromodulators such as acetylcholine that might fundamentally alter emergent cortical dynamics with cell-type and synapse-type specific effects (Colangelo et al., 2019).

5.3 Concluding remarks

The results of this thesis are predictions that require experimental validation. Yet, we are certain that neuroscience will eventually reach a point where interpretation of some experimental results will require simulation of validated models that integrate diverse data, similar to many branches of physics. For example, in particle physics, interpretation of the data coming out of the Large Hardron Collider, and subsequently the discovery of the Higgs boson, required detailed simulations, from particle collisions to detector physics (Aad et al., 2010). Neuroscience might still be decades away from this point, however we believe that the results in this thesis are a step in that direction. Untangling emergent cortical dynamics across scales of biological detail will require models with carefully validated components and informed simplifications.

A Appendix: Cliques of neurons bound into cavities

This appendix contains the supplementary methods for joint work with Michael W. Reimann, Martina Scolamiero, Katharine Turner, Rodrigo Perin, Giuseppe Chindemi, Paweł Dłotko, Ran Levi, Kathryn Hess and Henry Markram; it has been published as "*Cliques of neurons bound into cavities provide a missing link between structure and function*" in Frontiers in Computational Neuroscience (Reimann et al. (2017b); https://doi.org/10.3389/fncom.2017.00048).

Contribution: Editing—*The appendix is included in the thesis for completeness only.* Proof of maximal directionality: M.R. and R.L.; Generation of directed flag complexes: P.D., R.L. and K.H.; In vitro slice experiments: R.P.; Optimization of the parameters: M.R.

A.1 Supplementary methods

A.1.1 Proof: Maximal directionality of directed simplices

We defined the *directionality* of $\mathcal{G}$ to be the sum over all vertices of the square of their signed degrees, i.e.,

$$\mathrm{Dr}(\mathcal{G}) = \sum_{v \in V} \mathrm{sd}(v)^2.$$

Let $\mathcal{G}_n$ denote a directed n-simplex, i.e., a fully connected directed graph on $n+1$ vertices such that every fully connected subgraph has a unique source and a unique sink, and which therefore has no reciprocal connections.

Proposition 1. *If $\mathcal{G}$ is a directed graph on $n+1$ vertices, then $\mathrm{Dr}(\mathcal{G}) \leq \mathrm{Dr}(\mathcal{G}_n)$. If additionally $\mathcal{G}$ is a fully connected directed graph without reciprocal connections, then equality holds if and only if $\mathcal{G}$ is isomorphic to $\mathcal{G}_n$ as a directed graph.*

Proof. We prove this result by induction on n. Observe that it holds trivially for $n = 1$, since

every complete directed graph on two vertices is a directed 1-simplex. Assume that the proposition holds for all $n < N$, and let $\mathscr{G}$ be a complete directed graph on $N+1$ vertices, $v_0, ..., v_N$. Without loss of generality, suppose that the signed degree of v_0 is maximal, i.e., $\mathrm{sd}(v_0) \geq \mathrm{sd}(v_i)$ for all $i \geq 1$.

Create a new graph $\mathscr{G}'$ by reversing the direction of each edge that is directed away from v_0, so that v_0 becomes a sink in $\mathscr{G}'$. Let $v_0', \ldots, v_N'$ denote the vertices of $\mathscr{G}'$, such that v_i' is the vertex corresponding to v_i. Then $\mathrm{sd}(v_0') = N$, and for each $i \geq 1$ such that the edge from v_0 to v_i was reversed, one has

$$\mathrm{sd}(v_i') = \mathrm{sd}(v_i) - 2,$$

since only edges involving v_0 can change when passing from $\mathscr{G}$ to $\mathscr{G}'$.

Let k be the number of edges in $\mathscr{G}$ that change orientation in passing from $\mathscr{G}$ to $\mathscr{G}'$. Observe that

$$\begin{aligned}
\mathrm{Dr}(\mathscr{G}') &= (\mathrm{sd}(v_0) + 2k)^2 + \sum_{\substack{\text{edge from } v_0 \\ \text{unchanged}}} \mathrm{sd}(v_j)^2 + \sum_{\substack{\text{edge from } v_0 \\ \text{reversed}}} (\mathrm{sd}(v_i) - 2)^2 \\
&= \mathrm{Dr}(\mathscr{G}) + 4 \sum_{\substack{\text{edge from } v_0 \\ \text{reversed}}} \underbrace{(\mathrm{sd}(v_0) - \mathrm{sd}(v_i))}_{\geq 0 \,\forall\, i} + 4k^2 + 4k \\
&\geq \mathrm{Dr}(\mathscr{G}),
\end{aligned}$$

where equality holds if and only if $k = 0$, i.e., if v_0 is already a sink in $\mathscr{G}$. Note that if $k \neq 0$, so that v_0 is not already a sink in $\mathscr{G}$, then no vertex of $\mathscr{G}$ is a sink, since $\mathrm{sd}(v_0) \geq \mathrm{sd}(v_i)$ for all $i \geq 1$, and a vertex v of a complete directed graph on $N+1$ vertices is a sink if and only if $\mathrm{sd}(v) = N$.

The subgraph $\mathscr{G}''$ of $\mathscr{G}'$ spanned by the vertices $v_1', \ldots, v_N'$ is a complete directed graph on N vertices. By induction, $\mathrm{Dr}(\mathscr{G}'') \leq \mathrm{Dr}(\mathscr{G}_{N-1})$, with equality holding if and only if $\mathscr{G}''$ is a directed $(N-1)$-simplex. Therefore

$$\mathrm{Dr}(\mathscr{G}) \leq \mathrm{Dr}(\mathscr{G}') = \mathrm{Dr}(\mathscr{G}'') + N^2 \leq \mathrm{Dr}(\mathscr{G}_{N-1}) + N^2 = \mathrm{Dr}(\mathscr{G}_N),$$

with equality holding only if v_0 is a sink in $\mathscr{G}$, and $\mathscr{G}''$ is a directed $(N-1)$-simplex, i.e., if and only if $\mathscr{G}$ is a directed N-simplex. □

Directionality of directed simplices is proportional to the cube of their dimension.

Lemma 2. *For each $n \geq 1$,*

$$\mathrm{Dr}(\mathscr{G}_n) = \frac{n(n+1)(n+2)}{3}.$$

Proof. Let $v_0, \ldots v_n$ be the vertices of $\mathscr{G}_n$ ordered from sink to source. It is easy to see that the

associated sequence of signed degrees takes the form

$$n, n-2, n-4, \ldots, 2, 0, -2, \ldots, 4-n, 2-n, -n,$$

if n is even, and

$$n, n-2, n-4, \ldots, 1, -1, \ldots, 4-n, 2-n, -n,$$

if n is odd. Hence

$$\mathrm{Dr}(\mathscr{G}_n) = \begin{cases} 2\left(\sum_{k=1}^{n} k^2 - \sum_{j=1}^{\frac{n}{2}} (2j-1)^2\right), & n\ even \\ 2\left(\sum_{k=1}^{n} k^2 - \sum_{j=1}^{\frac{n-1}{2}} (2j)^2\right), & n\ odd \end{cases}.$$

Recall the well known formulas

$$\sum_{k=1}^{n} k^2 = \frac{n(n+1)(2n+1)}{6}, \quad \text{and} \quad \sum_{k=1}^{n} k = \frac{n(n+1)}{2}.$$

If n is even then, using these formulas,

$$\sum_{j=1}^{\frac{n}{2}} (2j-1)^2 = 4\sum_{j=1}^{\frac{n}{2}} j^2 - 4\sum_{j=1}^{\frac{n}{2}} j + \frac{n}{2} = \frac{n(n+1)(n+2)}{6} - \frac{n(n+2)}{2} + \frac{n}{2} = \frac{n(n-1)(n+1)}{6}.$$

Similarly for n odd,

$$\sum_{j=1}^{\frac{n-1}{2}} (2j)^2 = 4\sum_{j=1}^{\frac{n-1}{2}} j^2 = \frac{n(n-1)(n+1)}{6}.$$

Hence,

$$\mathrm{Dr}(\mathscr{G}_n) = 2\left(\frac{n(n+1)(2n+1)}{6} - \frac{n(n-1)(n+1)}{6}\right) = \frac{n(n+1)(n+2)}{3},$$

as claimed. □

A.1.2 Generation of directed flag complexes

Hasse diagrams

A *Hasse diagram*, otherwise known as a directed acyclic graph, is a directed graph $\mathscr{H} = (V, E, \tau)$ with no oriented cycles (Figure 3.12B). Hasse diagrams can be used to encode various combinatorial, geometric, and topological structures, such as posets, cubical complexes and simplicial complexes. Below we explain in detail how to encode simplicial complexes via Hasse diagrams.

A Hasse diagram $\mathscr{H}$ is said to be *stratified* if for each $v \in V$, every path from v to any sink in $\mathscr{H}$

has the same length. Thus in a stratified Hasse diagram the vertices are naturally partitioned into disjoint strata, where every directed path from a vertex in the k-th stratum V_k to any sink is of length k. In particular, the 0-th stratrum V_0 is the set of sinks of $\mathscr{H}$. Moreover, for all $e \in E$, there exists $k > 0$ such that $\tau_1(e) \in V_k$ and $\tau_2(e) \in V_{k-1}$.

A Hasse diagram $\mathscr{H}$ is said to be oriented if for every vertex $v \in \mathscr{H}$, it is equipped with a linear ordering of the set E_v of edges with source v. A Hasse diagram is said to be *admissible* if it is stratified and oriented.

Vertices in the k-th stratum of a stratified Hasse diagram $\mathscr{H}$ are said to be *of level* k. If $k < n$, and v, u are vertices of levels k and n respectively, then we say that v is a *face* of u if there is a directed path in $\mathscr{H}$ from u to v. If $\mathscr{H}$ is also oriented and therefore admissible, and there is a directed path $(e_1, ..., e_{n-k})$ from u to v such that e_i is the *first* element of $E_{\tau_1(e_i)}$ with respect to the ordering on that set, for all $1 \leq i \leq n-k$, we say that v is a *front face* of u. Similarly, v is a *back face* of u if there is a path $(e_1, ..., e_{n-k})$ from u to v such that e_i is the *last* element of the set $E_{\tau_1(e_i)}$ with respect to the ordering on it, for all $1 \leq i \leq n-k$. (Supplementary Figure 3.12B(ii) and C2).

If $\mathscr{G} = (V, E, \tau)$ is a directed graph, then $\mathscr{G}$ can be equivalently represented by an admissible Hasse diagram with level 0 vertices V, level 1 vertices E, and directed edges from each $e \in E$ to its source and target. The ordering on the edges in the Hasse diagram is determined by the orientation of each edge e in $\mathscr{G}$.

Every directed simplicial complex $\mathscr{S}$ gives rise to an admissible Hasse diagram $\mathscr{H}_{\mathscr{S}}$ as follows (Supplementary Figure 3.12C1 and C2). The level d vertices of $\mathscr{H}_{\mathscr{S}}$ are the d-simplices of $\mathscr{S}$. There is a directed edge from each d-simplex to each of its $(d-1)$-faces. The stratification on $\mathscr{H}_{\mathscr{S}}$ is thus given by dimension, and the orientation is given by the natural ordering of the faces of a simplex from front to back.

A data structure for Hasse diagrams

The algorithm we use in order to produce the directed flag complex of a directed graph uses Hasse diagrams as both input and output. Hence the input directed graph $\mathscr{G} = (V, E, \tau)$ must first be turned into a Hasse diagram. The output of the algorithm is again an admissible Hasse diagram that encodes the directed flag complex of the graph.

We represent an admissible Hasse diagram $\mathscr{H}$ using vectors to store the references to the vertices of the diagram. Thus, each vertex $v \in \mathscr{H}$ stores the following information.

1. $\mathrm{Ver}(v)$: A vector of the level 0 vertices of $\mathscr{H}$ that is a list of the 0-faces of v ordered according to the orientation of $\mathscr{H}$. If v is at level 0, then $\mathrm{Ver}(v) = \emptyset$.

2. $\mathrm{Tar}(v)$: A vector of references to the vertices that are targets of edges with source v. If v is at level 0, then $\mathrm{Tar}(v) = \emptyset$.

3. Src(v): A vector of references to the vertices that are sources of edges with target v.

If $\mathscr{H}$ encodes a directed simplicial complex, then Ver(v) determines the simplex to which v corresponds, and the vectors Tar(v) and Src(v) determine the faces and co-faces of the simplex to which v corresponds, respectively.

If $\mathscr{H}$ is admissible Hasse diagram of maximal level d, then $\mathscr{H}$ is represented by an ordered set of d vectors, where for each $1 \leq n \leq d$, the n-th vector contains the references to all level n vertices.

In addition, for every vertex v in $\mathscr{H}$ of level $n \geq 1$ such that Ver(v) = $[v_0, \ldots, v_i]$, the algorithm temporarily records an auxiliary vector U_v of references to level 0 vertices u in $\mathscr{H}$ that satisfy the following properties:

1. $u \neq v_i$ for all $0 \leq i \leq n$, and
2. for every $u \in U_v$ and every $0 \leq i \leq n$, there exists an edge in $\mathscr{G}$ from v_i to u.

The vector U_v is dismissed once its function has been fulfilled.

Let S_{int} denote the size of integer data types, and for any finite set X, let $|X|$ denote its cardinality. Each edge of an Hasse diagram $\mathscr{H}$ is stored in two vertices of the diagram. If each reference requires S_{int} storage, then we require $O(|E| \cdot S_{\text{int}})$ space to store all references, where E is the edge set of $\mathscr{H}$. In addition, each vertex v in $\mathscr{H}$ the corresponding data structure stores the vectors Ver(v), Tar(v) and Src(v), as explained above, which requires an additional $O(S_{int} \cdot d)$ of space per vertex. The total size of a Hasse diagram is thus bounded by $O((S_{\text{int}} \cdot d) \cdot |V| + |E| \cdot S_{\text{int}})$, where V is the vertex set of $\mathscr{H}$. In particular, the required storage space grows linearly with the number of vertices and with the number of edges.

Directed flag complex generation algorithm

The discussion below refers to the pseudo-code given in Algorithm 1.

Line 1: The Hasse diagram $\mathscr{H}$ takes as an initial value the input Hasse diagram encoding a directed graph $\mathscr{G} = (V, E, \tau)$.

Lines 2 - 7: The *for* loop initialises the creation of the vectors U_e for level 1 vertices $e \in \mathscr{H}$. For every level 1 vertex e, the vector U_e stores the references to all the level 0-vertices that, together with e, will form a level 2 vertex.

The *if* condition (Line 3) ensures that whenever the code finds two level 1 vertices $\{e_1, e_2\}$ and a level 0 vertex u that satisfy the conditions, the vertex u will be the terminal vertex of the level 2 vertex t_u that will be created in the first iteration of the *repeat-until* loop (Line 8). Notice also that the same *if* condition ensures that each triple of level 1 vertices (e, e_1, e_2) is

Algorithm 1 : Directed flag complex generation.

Input: A Hasse diagram $\mathscr{H}_{in}$ encoding the directed graph $\mathscr{G} = (V, E, \tau)$, (cf. ST4.1.1).
Output: A Hasse diagram $\mathscr{H}$ representing the directed flag complex associated to $\mathscr{G}$.

1: Set $\mathscr{H} = \mathscr{H}_{in}$
2: **for** every level 1 vertex $e \in \mathscr{H}$ **do**
3: **if** exist e_1, e_2 such that $\tau_1(e_1) = \tau_1(e)$, $\tau_1(e_2) = \tau_2(e)$ and $\tau_2(e_1) = \tau_2(e_2) = u$ **then**
4: Add u to U_e;
5: **end if**
6: **end for**
7: $dim = 2$;
8: **repeat**
9: *next_level_nodes* – empty vector of references to nodes;
10: **for** top–level vertex $e \in \mathscr{H}$ **do**
11: **for** Every $u \in U_e$ **do**
12: Create a node t_u of a Hasse diagram;
13: $\mathrm{Ver}(t_u) = [\mathrm{Ver}(e), u]$;
14: $U_{t_u} = U_e$;
15: Add e to $\mathrm{Tar}(t_u)$;
16: Add t_u to $\mathrm{Src}(e)$;
17: **for** Every $bd \in \mathrm{Tar}(e)$ **do**
18: **for** Every $cbd \in \mathrm{Src}(bd)$ **do**
19: **if** u is the last vertex in $\mathrm{Ver}(cbd)$ **then**
20: Add cbd to $\mathrm{Tar}(t)$;
21: Add t_u to $\mathrm{Src}(cbd)$;
22: $U_{t_u} = U_{t_u} \cap U_{cbd}$;
23: **end if**
24: **end for**
25: **end for**
26: Add t_u to *next_level_nodes*;
27: **end for**
28: **end for**
29: Add *next_level_nodes* to $\mathscr{H}$;
30: $dim = dim + 1$;
31: **until** *next_level_nodes* $= \emptyset$
32: Return $\mathscr{H}$;

naturally ordered as the front, middle and back faces of a an oriented 2-simplex associated with t_u. In particular, e is the front face of t_u, and hence the ordering of $\mathrm{Ver}(e)$ can be extended to ordering of $\mathrm{Ver}(t_u)$, as in Line 13.

Lines 8 - 31: This *repeat-until* loop is where the complex is generated, where each iteration increases the dimension by 1.

Fix $n \geq 1$, and suppose by induction that all vertices of level less than or equal to n have been constructed. Fix a level n vertex s with $\mathrm{Ver}(s) = [v_0, \ldots, v_n]$ and let $u \in U_s$. By definition of the set U_s, the code creates a vertex t_u (Line 10), creates $\mathrm{Ver}(t_u)$ as $[\mathrm{Ver}(s), u] = [v_0, \ldots, v_n, u]$, so u is the last vertex in $\mathrm{Ver}(t_u)$ (Line 11), and initiates U_{t_u} as U_s (Line 12). In the next two lines (Lines 13 and 14) s becomes a target of t_u and t_u a source of s. Next, in the two *for* loops of Lines 15 and 16, the code checks for each level $n-1$ vertex bd that is a target of s, and every level n

vertex cbd that is a source of bd, whether u is the last vertex in Ver(cbd) (Line 17). In that case cbd becomes a target of t_u and t_u becomes a source of cbd (Lines 18, 19). Since u is the *last* vertex in Ver(t_u), it must be the last vertex in any face of t_u that contains it for the orientation to be preserved, whence the restriction in Line 17. This accounts of all the co-dimension 1 faces (targets) of t_u that are different from s, and by induction hypothesis these faces are already constructed. Hence t_u is declared a new level $n+1$ vertex in $\mathscr{H}$. Since in a directed simplicial complex (in particular a directed flag complex) every simplex is characterised by its ordered list of vertices, a level $n+1$ vertex t in $\mathscr{H}$ with Ver(t) = $[v_0,\ldots,v_n,u]$ can only be constructed once, and hence is equal to t_u. On the other hand, Line 20 ensures that all potential vertices of level larger than $n+1$ of which t_u is a target will be accounted for. It follows that Algorithm 1 does indeed construct construct the Hasse diagram corresponding to the directed flag complex of the input graph.

If w is a level $n+1$ vertex with Ver(w) = $[v_0,\ldots v_n,u]$, then the level n vertex v that is the front face of w is a target of w, and u is clearly not present in Ver(v). On the other hand, u is listed in U_v. From Lines 12 and 20 of the algorithm it is clear that $U_w \subset U_v$ and moreover that $u \notin U_w$, and so the inclusion is proper. The cardinalities of the sets $U_{(-)}$ are therefore strictly decreasing for the newly created vertices. New level $n+1$ vertices are created only if there exists at least one level n vertex t, such that $U_t \neq \emptyset$. Since the cardinality of the $U_{(-)}$ decreases with each iteration of the *repeat-until* loop (Line 6), the algorithm will terminate.

A.1.3 In vitro slice experiments

Slice preparation

Experiments were carried out according to the Swiss national and institutional guidelines. Fourteen- to sixteen-day-old nonanesthetized Wistar rats were quickly decapitated, and their brains were carefully removed and placed in iced artificial cerebrospinal fluid (ACSF). Slices (300 μm) were cut on an HR2 vibratome (Sigmann Elektronik). Parasagittal slices, $1.7-2.2$ mm lateral to the midline, were cut to access primary somatosensory cortex (SSC; above the anterior extremity of the hippocampus ±1 mm). Slices were incubated at 37°C for 30 to 60 min and then left at room temperature until recording. Cells were visualized by infrared differential interference contrast video microscopy using a VX55 camera (Till P-hotonics) mounted on an upright BX51WI microscope (Olympus). Layer 5 thick-tufted pyramidal cells (L5TTPCs) were selected according to their large soma size ($15-25$ μm) and their apparent large trunk of the apical dendrite. Care was taken to use only parallel slices (i.e., slices that had a cutting plane parallel to the course of the apical dendrites and the primary axonal trunk). This ensured sufficient preservation of the PCsO axonal and dendritic arborizations.

Chemicals and solutions

Slices were continuously superfused with ACSF containing 125 mM NaCl, 25 mM NaHCO3, 2.5 mM KCl, 1.25 mM NaH2PO4, 2 mM CaCl2, 1 mM MgCl2, and 25 mM D-glucose bubbled with 95% O2 and 5% CO2. The intracellular pipette solution contained 110 mM potassium gluconate, 10 mM KCl, 4 mM ATP-Mg, 10 mM phosphocreatine, 0.3 mM GTP, 10 Hepes, and 13 mM biocytin adjusted to pH 7.3-7.4 with 5 M KOH. Osmolarity was adjusted to 290-300 mOsm L_{-1} with D-mannitol ($25-35$ mM). The membrane potential values given were not corrected for the liquid junction potential, which is approximately -14 mV. Chemicals were from Sigma Aldrich or Merck.

Electrophysiological recordings

Multiple somatic whole-cell recordings (6 to 12 cells simultaneously) were performed with Multiclamp 700B amplifiers (Molecular Devices) in the current clamp mode at $34 \pm 1^{\circ}$C bath temperature. Data acquisition was performed through an ITC-1600 board (Instrutech) connected to a PC running a custom-written routine (PulseQ) under IGOR Pro (Wavemetrics). Sampling rates were 5 kHz, and the voltage signal was filtered with a 2-kHz Bessel filter. Patch pipettes were pulled with a Flaming/Brown micropipette puller P-97 (Sutter Instruments) or a DMZ puller (Zeitz Instruments) and had an initial resistance of 3-8 MΩ. Recordings were achieved with custom C++ software that controlled manipulators, amplifiers, oscilloscopes, pipette pressure, and video display.

Stimulation protocols

Monosynaptic, direct excitatory connections were identified by stimulation of a presynaptic cell with a $20-70$ Hz train of $5-15$ strong and brief current pulses ($1-2$ nA, $2-4$ ms) followed by a so-called recovery test response $0.5s$ after the end of the train (not shown in the traces), all precisely and reliably eliciting action potentials (APs).

Final somatic positions

The soma positions were recorded relative to an arbitrary reference point, and the z-axis was oriented perpendicular to the surface of the slice. After morphological stainings were ready, the y-axis axis was rotated around the z-axis axis to match the orientation of the apical dendrites. The x-axis was rotated by the same amount and remained orthogonal to the other two axes.

Connection amplitudes

The amplitude of excitatory postsynaptic potentials (EPSPs) was measured for events that followed a resting period of at least 15 s, during which time the presynaptic neurons were not

stimulated to produce APs.

A.1.4 Optimization of the parameters for the transmission-response matrices

Starting with firing data from spontaneous activity in the reconstructed microcircuit, we generated sequences of 20 transmission-response matrices for $\Delta t_i \in \{1, 2, 5, 10, 20, 50, 100\}$ ms, thus creating 49 such sequences corresponding to every possible choice of the pair $(\Delta t_1, \Delta t_2)$. We refer to each of these sequences as the *true transmission-response matrices* corresponding to the pair $(\Delta t_1, \Delta t_2)$. Here, we describe the procedure for optimizing the choice of the time intervals Δt_1 and Δt_2 so that the associated true transmission-response matrices best reflect the actual successful transmission of signals between neurons in the microcircuit.

Properties of the transmission-response matrix

The nonzero coefficients in a transmission-response matrix are a subset of those in the structural matrix. Due to the partly stochastic behavior of the *in silico* microcircuit, the subset will vary even for subsequent applications of the same stimulus. In fact, even an exact repetition of the same conditions will lead to different transmission-response matrices, if the random number generator is seeded differently. It follows that the generation of the transmission-response matrices for a given stimulus should be considered as a stochastic process. With the correct choice of the parameters Δt_i, the matrices should reflect how the microcircuit processes a stimulus and thus take into account parameters of neural processing, such as pre-/postsynaptic interaction.

To find parameters Δt_1 and Δt_2 that maximize the degree to which neural processing is captured by the transmission-response matrices, we first develop a stochastic model for synaptic firing that takes into account neural processing and that depends on Δt_1 and Δt_2. For the purpose of this analysis, we assume that the true transmission-response matrices are compatible with this model.

Based upon our model for synaptic firing, we formulate a simplified model that ignores neural processing. For this simplified model and for any choice of parameters Δt_1 and Δt_2, we explain how to obtain transmission-response matrices from actual firing data, by shuffling the firing data appropriately, then applying the algorithm for generating a transmission-response matrix of the previous section. Finally, for each choice of the parameters Δt_1 and Δt_2, we compare the true transmission-response matrices for spontaneous activity in the reconstructed microcircuit to those obtained by the simplified generation process. The parameters that we work with in the main body of the paper are the Δt_1 and Δt_2 that maximize the difference (measured by the ratio of the numbers of ones in the matrices) between the actual transmission-response matrices and those resulting from the simplified model.

Stochastic model with neural processing

Fix time intervals Δt_1 and Δt_2. Let $A = (a_{ij})$ denote the structural matrix of a reconstructed microcircuit, and let $A(n) = (a^n_{ij})$ denote the transmission-response matrix of the n-th time bin, based on firing data from a trial of simulated activity in the microcircuit, for the given intervals Δt_1 and Δt_2. If $a^n_{ij} = 1$ for any n, then $a_{ij} = 1$. It is reasonable to consider A to be static, at least over the time periods considered here.

We want to compute the probability that $a^n_{ij} = 1$, given that $a_{ij} = 1$, so we need to determine on which parameters and properties this probability depends. According to the definition of transmission-response matrices, a presynaptic and a postsynaptic spike are required for a^n_{ij} to be 1. To simplify the analysis somewhat, we assume that each neuron n_i has a *time-dependent, instantaneous firing rate* $F^i(t)$ that determines spiking probability at time t, i.e. spiking can be described as an inhomogeneous Poisson process. Under this assumption, the expected number $m^i_{\Delta t_1}(t_0)$ of spikes of neuron n_i in the interval $[t_0, t_0 + \Delta t_1]$ can be computed as

$$m^i_{\Delta t_1}(t_0) = \int_{t_0}^{t_0+\Delta t_1} F^i(u)\,du.$$

If $K^i_{\Delta t_1}(t_0)$ denotes the probability that neuron n_i spikes at least once in the interval $[t_0, t_0+\Delta t_1]$, then

$$K^i_{\Delta t_1}(t_0) = 1 - \mathscr{P}\big(m^i_{\Delta t_1}(t_0)\big) = 1 - e^{-m^i_{\Delta t_1}(t_0)},$$

where $\mathscr{P}(\lambda)$ is the Poisson probability mass function with parameter λ at 0. (Recall that if X is a random variable that counts the number of spikes of neuron n_i in the interval $[t_0, t_0 + \Delta t_1]$, then $\mathscr{P}\big(m^i_{\Delta t_1}(t_0)\big)$ is the probability that $X = 0$.) If the change in $F^i(t)$ is slow compared to Δt_1, then $m^i_{\Delta t_1}(t) \approx F^i(t) \cdot \Delta t_1$. Moreover, $1 - \mathscr{P}(\lambda) \approx \lambda$ for small values of λ. For small enough Δt_1, the expected number $m^i_{\Delta t_1}(t_0)$ of spikes of neuron n_i will certainly be small, and change in $F^i(t)$ will be slow in compared to Δt_1, so that we may assume that

$$K^i_{\Delta t_1}(t_0) \approx F^i(t_0) \cdot \Delta t_1.$$

For the postsynaptic spike the situation is more complicated. As there is a causal relation between presynaptic and postsynaptic firing, mediated by synaptic transmission, we need to estimate the conditional probability of at least one postsynaptic spike, given that at least one presynaptic spike occured. Let n_i and n_j denote neurons such that $a_{ij} = 1$. Let $s_0 \in [t_0, t_0+\Delta t_1]$ denote the time of the first presynaptic spike in this interval. Let $X^j_{\Delta t_2}(s_0)$ denote the random variable whose value is the number of times neuron n_j spiked in the time window $[s_0, s_0 + \Delta t_2]$. Let $Y^i_{\Delta t_1}(t_0)$ denote the random variable whose value is the number of times neuron n_i spiked in the time interval $[t_0, t_0 + \Delta t_1]$. We need to estimate the conditional probability

$$P\big(X^j_{\Delta t_2}(s_0) > 0 \,|\, Y^i_{\Delta t_1}(t_0) > 0\big).$$

The nature of this interaction is very intricate and depends on the identities of the presynaptic and postsynaptic neurons, the spiking history of the presynaptic neuron before s_0, and all other synaptic input the postsynaptic neuron received. It can be described as governed by some function G^{ij} modulating the spiking probability of the postsynaptic neuron n_j. This function takes as parameters the expected number of spikes of neuron n_j in the interval $[s_0, s_0 + \Delta t_2]$, the time t_0, and the "spiking history" of the presynaptic neuron n_i until s_0, which we write as a function $s^i_*(t)$ evaluated at s_0, giving rise to the expression

$$P\big(X^j_{\Delta t_2}(s_0) > 0 \,|\, Y^i_{\Delta t_1}(t_0) > 0\big) = 1 - e^{-G^{ij}(m^j_{\Delta t_2}(s_0), t_0, s^i_*(s_0))}.$$

Summarizing the analysis above, the following formula provides a good estimate of the probability that $a^n_{ij} = 1$ if $a_{ij} = 1$, for small enough Δt_1 and Δt_2, where s_0 denotes the time of the first presynaptic spike in the interval $[n\Delta t_1, (n+1)\Delta t_1]$ and $t_0 = n\Delta t_1$.

$$\begin{aligned} P\left(a^n_{ij} = 1 | a_{ij} = 1\right) &= \left(1 - e^{-m^i_{\Delta t_1}(t_0)}\right) \cdot \left(1 - e^{-G^{ij}(m^j_{\Delta t_2}(s_0), t_0, s^i_*(s_0))}\right) \\ &\approx F^i(t_0) \cdot \Delta t_1 \cdot G^{ij}\big(F^j(s_0) \cdot \Delta t_2, t_0, s^i_*(s_0)\big). \end{aligned} \tag{A.1}$$

This conditional probability encodes not only the distinctive features of the structural connectivity (via a_{ij}) but also the potentially stimulus-dependant neuron-specific firing rates (via F^i and F^j) and their co-variation. Most crucially, it captures the stimulus-dependent functional modulation of postsynaptic firing by a presynaptic spike as well. We assume that the true transmission-reponse matrices capture the actual transmission of spikes according to the model of synaptic firing described by this formula.

Null hypotheses: no neural processing

We introduce here a simplified model of synaptic spiking that is based upon Equation A.1 but that ignores any pre-/postsynaptic interaction. We then explain how to obtain transmission-response matrices that correspond to this simplified model from firing data arising from simulated activity.

We begin by setting each G^{ij} to be the projection onto the first component, ignoring the pre-/postsynaptic interaction. After this simplification, the approximation obtained in the previous section now reads

$$P(a^n_{ij} = 1 | a_{ij} = 1) \approx F^i(t_0) \cdot F^j(s_0) \cdot \Delta t_1 \cdot \Delta t_2,$$

where s_0 denotes the time of the first presynaptic spike that occurs in the interval $[n\Delta t_1, (n+1)\Delta t_1]$ and $t_0 = n\Delta t_1$, as before. Since this drastic simplification neglects the central aspect of neural computation—pre-/postsynaptic interaction—it gives rise to control cases for each pair of parameters $(\Delta t_1, \Delta t_2)$ and each choice of firing rate functions $F^i(t)$. Comparison of the true transmission-response matrices for each pair of parameters to the corresponding control ma-

trices for the same pair and a specific choice of the functions $F^i(t)$ will allow us to determine values for Δt_1 and Δt_2 for which the true transmission-response matrix optimally reflects neural processing.

We assume moreover that the individual firing rates consist of a neuron-dependent frequency that is up- or down-regulated by a global time series, i.e., that $F^i(t) = f(i) \cdot F(t)$, for some function $F(t)$ and some constant $f(i)$ for each neuron n_i. Transmission-response matrices corresponding to this simplified model for fixed Δt_1 and Δt_2, which we call *simplified transmission-response matrices*, can be generated by first shuffling all recorded spikes from simulated activity in the reconstructed microcircuit, while preserving both the number of spikes per neuron and per time bin, then applying the usual transmission-response matrix generation method.

Optimization of parameters

The difference between the true transmission-response matrices and the control case described above is a consequence of the pre-/postsynaptic interaction. Comparison with the control case enables us therefore to measure how well that interaction is captured in the true transmission-response matrices. In particular, it is reasonable to optimize the parameters Δt_1 and Δt_2 so that the difference between the true transmission response matrices arising from actual simulation data and those arising in the control cases is maximized, as a maximal difference indicates that the effect of the pre-/postsynaptic interaction is captured optimally by the true transmission-response matrices.

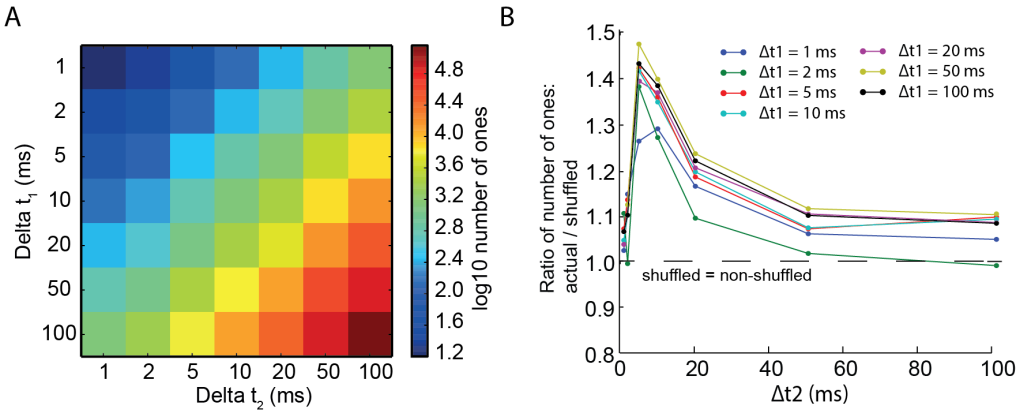

Figure A.1 – Optimization of the parameters for the transmission-response matrices

The comparison between the true transmission-response matrices and the control cases was carried out by first producing 20 true transmission-response matrices and 20 simplified transmission-response matrices based on firing data obtained from spontaneous activity in the reconstructed microcircuit for every pair $(\Delta t_1, \Delta t_2)$, where $\Delta t_i \in \{1,2,5,10,20,50,100\}$ ms for $i = 1,2$. The number of ones in each matrix was then computed and the average taken over each set of 20 matrices. Since no stimulus was applied to the microcircuit, the averages

computed are meaningful, since the firing data should be fairly homogeneous across the time bins. The average number of ones in the transmission-response matrix arising from simulated actitivity in the reconstructed microciruit, as a function of Δt_1 and Δt_2, is illustrated in the figure above, which shows the ratio of the average number of ones in the true transmission-response matrices to the average number of ones in the simplified transmission-response matrices, for various values of Δt_1 and Δt_2. In all cases we find that the maximum lies between $\Delta t_2 = 5$ ms and $\Delta t_2 = 10$ ms, leading us to choose to work with $\Delta t_2 = 10$ ms. For Δt_1 we find a maximum at 50 ms, but we use $\Delta t_1 = 5$ ms (for which the maximum ratio is only slightly lower than for $\Delta t_1 = 50$ ms) instead to avoid more than one spike per neuron per bin.

Bibliography

Aad, G., Abbott, B., Abdallah, J., Abdelalim, A. A., Abdesselam, A., Abdinov, O., et al. (2010). The ATLAS Simulation Infrastructure. *The European Physical Journal C* 70, 823–874. doi: 10.1140/epjc/s10052-010-1429-9

Abeles, M. (1982). *Local cortical circuits: an electrophysiological study* (Berlin, Heidelberg, New York: Springer)

Aharoni, R., Berger, E., and Meshulam, R. (2005). Eigenvalues and homology of flag complexes and vector representations of graphs. *Geom. Funct. Anal.* 15, 555–566. doi: 10.1007/s00039-005-0516-9

Allen, C. and Stevens, C. F. (1994). An evaluation of causes for unreliability of synaptic transmission. *Proceedings of the National Academy of Sciences* 91, 10380–10383. doi: 10.1073/pnas.91.22.10380

Antic, S. D., Hines, M., and Lytton, W. W. (2018). Embedded ensemble encoding hypothesis: The role of the "Prepared" cell. *Journal of Neuroscience Research* 0. doi:10.1002/jnr.24240

Antic, S. D., Zhou, W.-L., Moore, A. R., Short, S. M., and Ikonomu, K. D. (2010). The decade of the dendritic NMDA spike. *Journal of Neuroscience Research* 88, 2991–3001. doi:10.1002/jnr.22444

Bair, W. and Koch, C. (1996). Temporal precision of spike trains in extrastriate cortex of the behaving macaque monkey. *Neural Computation* 8, 1185–1202

Bale, M. R., Ince, R. A. A., Santagata, G., and Petersen, R. S. (2015). Efficient population coding of naturalistic whisker motion in the ventro-posterior medial thalamus based on precise spike timing. *Front Neural Circuits* 9. doi:10.3389/fncir.2015.00050

Bale, M. R. and Petersen, R. S. (2009). Transformation in the Neural Code for Whisker Deflection Direction Along the Lemniscal Pathway. *Journal of Neurophysiology* 102, 2771–2780. doi: 10.1152/jn.00636.2009

Bassett, D. S. and Sporns, O. (2017). Network neuroscience. *Nat Neurosci* 20, 353–364. doi: 10.1038/nn.4502

Bauer, U., Kerber, M., Reininghaus, J., and Wagner, H. (2017). Phat – Persistent Homology Algorithms Toolbox. *Journal of Symbolic Computation* 78, 76 – 90. doi:http://dx.doi.org/10.1016/j.jsc.2016.03.008. Algorithms and Software for Computational Topology

Beck, J., Ma, W., Pitkow, X., Latham, P., and Pouget, A. (2012). Not Noisy, Just Wrong: The Role of Suboptimal Inference in Behavioral Variability. *Neuron* 74, 30–39. doi:10.1016/j.neuron.2012.03.016

Beggs, J. M. and Plenz, D. (2003). Neuronal Avalanches in Neocortical Circuits. *Journal of Neuroscience* 23, 11167–11177. doi:10.1523/JNEUROSCI.23-35-11167.2003

Benson, A. R., Gleich, D. F., and Leskovec, J. (2016). Higher-order organization of complex networks. *Science* 353, 163–166. doi:10.1126/science.aad9029

Bienenstock, E. (1995). A model of neocortex. *Network: Computation in Neural Systems* 6, 179–224. doi:10.1088/0954-898X_6_2_004

Borst, J. G. G. (2010). The low synaptic release probability in vivo. *Trends in Neurosciences* 33, 259–266. doi:10.1016/j.tins.2010.03.003

Braitenberg, V. (1978). Cell Assemblies in the Cerebral Cortex. In *Theoretical Approaches to Complex Systems* (Springer, Berlin, Heidelberg). 171–188. DOI: 10.1007/978-3-642-93083-6_9

Brette, R. (2019). Is coding a relevant metaphor for the brain? *Behavioral and Brain Sciences* , 1–44doi:10.1017/S0140525X19000049

Brinkman, B. A. W., Weber, A. I., Rieke, F., and Shea-Brown, E. (2016). How Do Efficient Coding Strategies Depend on Origins of Noise in Neural Circuits? *PLOS Computational Biology* 12, e1005150. doi:10.1371/journal.pcbi.1005150

Britten, K. H., Shadlen, M. N., Newsome, W. T., and Movshon, J. A. (1992). The analysis of visual motion: a comparison of neuronal and psychophysical performance. *The Journal of Neuroscience: The Official Journal of the Society for Neuroscience* 12, 4745–4765

Britten, K. H., Shadlen, M. N., Newsome, W. T., and Movshon, J. A. (1993). Responses of neurons in macaque MT to stochastic motion signals. *Visual Neuroscience* 10, 1157–1169. doi:10.1017/S0952523800010269

Brody, C. D. (1999). Correlations Without Synchrony. *Neural Computation* 11, 1537–1551. doi:10.1162/089976699300016133

Brunel, N. (2000). Dynamics of Sparsely Connected Networks of Excitatory and Inhibitory Spiking Neurons. *Journal of Computational Neuroscience* 8, 183–208. doi:10.1023/A:1008925309027

Bullmore, E. and Sporns, O. (2009). Complex brain networks: graph theoretical analysis of structural and functional systems. *Nature Reviews Neuroscience* 10, 186–198. doi:10.1038/nrn2575

Calvin, W. H. and Stevens, C. F. (1968). Synaptic noise and other sources of randomness in motoneuron interspike intervals. *Journal of Neurophysiology* 31, 574–587

Chambers, B. and MacLean, J. N. (2016). Higher-Order Synaptic Interactions Coordinate Dynamics in Recurrent Networks. *PLOS Computational Biology* 12, e1005078. doi:10.1371/journal.pcbi.1005078

Chindemi, G. (2018). *Towards a unified understanding of synaptic plasticity*. Ph.D. thesis, Ecole polytechnique federale de Lausanne

Chklovskii, D. B., Mel, B. W., and Svoboda, K. (2004). Cortical rewiring and information storage. *Nature* 431, 782–788. doi:10.1038/nature03012

Churchland, M. M., Yu, B. M., Cunningham, J. P., Sugrue, L. P., Cohen, M. R., Corrado, G. S., et al. (2010). Stimulus onset quenches neural variability: a widespread cortical phenomenon. *Nature Neuroscience* 13, 369–378. doi:10.1038/nn.2501

Colangelo, C., Shichkova, P., Keller, D., Markram, H., and Ramaswamy, S. (2019). Cellular, Synaptic and Network Effects of Acetylcholine in the Neocortex. *Frontiers in Neural Circuits* 13. doi:10.3389/fncir.2019.00024

Constantinople, C. and Bruno, R. (2011). Effects and Mechanisms of Wakefulness on Local Cortical Networks. *Neuron* 69, 1061–1068. doi:10.1016/j.neuron.2011.02.040

Cox, C. L., Denk, W., Tank, D. W., and Svoboda, K. (2000). Action potentials reliably invade axonal arbors of rat neocortical neurons. *Proceedings of the National Academy of Sciences* 97, 9724–9728. doi:10.1073/pnas.170278697

Dean, A. F. (1981). The variability of discharge of simple cells in the cat striate cortex. *Experimental Brain Research* 44, 437–440. doi:10.1007/BF00238837

Denève, S. and Machens, C. K. (2016). Efficient codes and balanced networks. *Nature Neuroscience* 19, 375–382. doi:10.1038/nn.4243

Destexhe, A., Rudolph, M., and Paré, D. (2003). The high-conductance state of neocortical neurons in vivo. *Nature Reviews Neuroscience* 4, 739–751. doi:10.1038/nrn1198

Diba, K., Koch, C., and Segev, I. (2006). Spike propagation in dendrites with stochastic ion channels. *Journal of Computational Neuroscience* 20, 77–84. doi:10.1007/s10870-006-4770-0

Douglas, R. J. and Martin, K. A. (2004). Neuronal circuits of the neocortex. *Annual Review of Neuroscience* 27, 419–451. doi:10.1146/annurev.neuro.27.070203.144152

Engel, A. K. and Singer, W. (2001). Temporal binding and the neural correlates of sensory awareness. *Trends in Cognitive Sciences* 5, 16–25. doi:10.1016/S1364-6613(00)01568-0

Engelhardt, J. v., Eliava, M., Meyer, A. H., Rozov, A., and Monyer, H. (2007). Functional Characterization of Intrinsic Cholinergic Interneurons in the Cortex. *Journal of Neuroscience* 27, 5633–5642. doi:10.1523/JNEUROSCI.4647-06.2007

Erdos, P. and Rényi, A. (1960). On the evolution of random graphs. *Publ. Math. Inst. Hung. Acad. Sci* 5, 17–60

Fairhall, A. L. (2019). Whither variability? *Nature Neuroscience* 22, 329. doi:10.1038/s41593-019-0344-0

Faisal, A. A. and Laughlin, S. B. (2007). Stochastic Simulations on the Reliability of Action Potential Propagation in Thin Axons. *PLOS Computational Biology* 3, e79. doi:10.1371/journal.pcbi.0030079

Faisal, A. A., Selen, L. P. J., and Wolpert, D. M. (2008). Noise in the nervous system. *Nature Reviews Neuroscience* 9, 292–303. doi:10.1038/nrn2258

Fellous, J. M., Rudolph, M., Destexhe, A., and Sejnowski, T. J. (2003). Synaptic background noise controls the input/output characteristics of single cells in an in vitro model of in vivo activity. *Neuroscience* 122, 811–829. doi:10.1016/j.neuroscience.2003.08.027

Fiacco, T. A. and McCarthy, K. D. (2018). Multiple Lines of Evidence Indicate That Gliotransmission Does Not Occur under Physiological Conditions. *Journal of Neuroscience* 38, 3–13. doi:10.1523/JNEUROSCI.0016-17.2017

Fuhrmann, G., Segev, I., Markram, H., and Tsodyks, M. (2002). Coding of Temporal Information by Activity-Dependent Synapses. *Journal of Neurophysiology* 87, 140–148. doi:10.1152/jn.00258.2001

Gal, E., London, M., Globerson, A., Ramaswamy, S., Reimann, M. W., Muller, E., et al. (2017). Rich cell-type-specific network topology in neocortical microcircuitry. *Nature Neuroscience* advance online publication. doi:10.1038/nn.4576

Giusti, C., Pastalkova, E., Curto, C., and Itskov, V. (2015). Clique topology reveals intrinsic geometric structure in neural correlations. *Proceedings of the National Academy of Sciences* 112, 13455–13460. doi:10.1073/pnas.1506407112

Gong, P. and Leeuwen, C. v. (2004). Evolution to a small-world network with chaotic units. *EPL* 67, 328. doi:10.1209/epl/i2003-10287-7

Gütig, R. and Sompolinsky, H. (2006). The tempotron: a neuron that learns spike timing–based decisions. *Nature Neuroscience* 9, 420–428. doi:10.1038/nn1643

Harris, K. D. and Shepherd, G. M. G. (2015). The neocortical circuit: themes and variations. *Nature Neuroscience* 18, 170–181. doi:10.1038/nn.3917

Hebb, D. (1949). *The organization of behaviour* (New York: Wiley & Sons)

Hines, M. L. and Carnevale, N. T. (1997). The NEURON Simulation Environment. *Neural Computation* 9, 1179–1209. doi:10.1162/neco.1997.9.6.1179

Hires, S. A., Gutnisky, D. A., Yu, J., O'Connor, D. H., and Svoboda, K. (2015). Low-noise encoding of active touch by layer 4 in the somatosensory cortex. *eLife* 4, e06619. doi:10.7554/eLife.06619

Holtmaat, A. and Svoboda, K. (2009). Experience-dependent structural synaptic plasticity in the mammalian brain. *Nature Reviews Neuroscience* 10, 647–658. doi:10.1038/nrn2699

Hong, Y. K., Lacefield, C. O., Rodgers, C. C., and Bruno, R. M. (2018). Sensation, movement and learning in the absence of barrel cortex. *Nature* , 1doi:10.1038/s41586-018-0527-y

Hu, Y., Trousdale, J., Josić, K., and Shea-Brown, E. (2014). Local paths to global coherence: Cutting networks down to size. *Phys. Rev. E* 89, 032802. doi:10.1103/PhysRevE.89.032802

Huang, C., Ruff, D. A., Pyle, R., Rosenbaum, R., Cohen, M. R., and Doiron, B. (2019). Circuit Models of Low-Dimensional Shared Variability in Cortical Networks. *Neuron* 101, 337–348.e4. doi:10.1016/j.neuron.2018.11.034

Iavarone, E., Yi, J., Shi, Y., Zandt, B.-J., O'Reilly, C., Geit, W. V., et al. (2019). Experimentally-constrained biophysical models of tonic and burst firing modes in thalamocortical neurons. *bioRxiv* , 512269doi:10.1101/512269

Jahr, C. E. and Stevens, C. F. (1990). Voltage dependence of NMDA-activated macroscopic conductances predicted by single-channel kinetics. *Journal of Neuroscience* 10, 3178–3182. doi:10.1523/JNEUROSCI.10-09-03178.1990

Johansson, R. S. and Birznieks, I. (2004). First spikes in ensembles of human tactile afferents code complex spatial fingertip events. *Nature Neuroscience* 7, 170–177. doi:10.1038/nn1177

Jones, E., Oliphant, T., Peterson, P., and others (2001). *SciPy: Open source scientific tools for Python*. [Online; accessed 2016-11-22]

Kara, P., Reinagel, P., and Reid, R. C. (2000). Low Response Variability in Simultaneously Recorded Retinal, Thalamic, and Cortical Neurons. *Neuron* 27, 635–646. doi:10.1016/S0896-6273(00)00072-6

Kasthuri, N., Hayworth, K. J., Berger, D. R., Schalek, R. L., Conchello, J. A., Knowles-Barley, S., et al. (2015). Saturated Reconstruction of a Volume of Neocortex. *Cell* 162, 648–661. doi:10.1016/j.cell.2015.06.054

Katz, B. and Miledi, R. (1969). Spontaneous and evoked activity of motor nerve endings in calcium Ringer. *The Journal of Physiology* 203, 689–706. doi:10.1113/jphysiol.1969.sp008887

Kayser, C., Logothetis, N. K., and Panzeri, S. (2010). Millisecond encoding precision of auditory cortex neurons. *Proceedings of the National Academy of Sciences* 107, 16976–16981. doi: 10.1073/pnas.1012656107

Kempter, R., Gerstner, W., and van Hemmen, J. L. (1999). Hebbian learning and spiking neurons. *Physical Review E* 59, 4498–4514. doi:10.1103/PhysRevE.59.4498

Knoblauch, A., Palm, G., and Sommer, F. T. (2009). Memory Capacities for Synaptic and Structural Plasticity. *Neural Computation* 22, 289–341. doi:10.1162/neco.2009.08-07-588

Kohn, A. and Smith, M. A. (2005). Stimulus Dependence of Neuronal Correlation in Primary Visual Cortex of the Macaque. *Journal of Neuroscience* 25, 3661–3673. doi: 10.1523/JNEUROSCI.5106-04.2005

Lajoie, G., Lin, K. K., and Shea-Brown, E. (2013). Chaos and reliability in balanced spiking networks with temporal drive. *Physical Review E* 87, 052901. doi:10.1103/PhysRevE.87.052901

Lajoie, G., Lin, K. K., Thivierge, J.-P., and Shea-Brown, E. (2016). Encoding in Balanced Networks: Revisiting Spike Patterns and Chaos in Stimulus-Driven Systems. *PLOS Computational Biology* 12, e1005258. doi:10.1371/journal.pcbi.1005258

Landau, I. D., Egger, R., Dercksen, V. J., Oberlaender, M., and Sompolinsky, H. (2016). The Impact of Structural Heterogeneity on Excitation-Inhibition Balance in Cortical Networks. *Neuron* 92, 1106–1121. doi:10.1016/j.neuron.2016.10.027

Latora, V. and Marchiori, M. (2001). Efficient Behavior of Small-World Networks. *Phys. Rev. Lett.* 87, 198701. doi:10.1103/PhysRevLett.87.198701

Le Be, J.-V. and Markram, H. (2006). Spontaneous and evoked synaptic rewiring in the neonatal neocortex. *Proceedings of the National Academy of Sciences* 103, 13214–13219. doi:10.1073/pnas.0604691103

Loebel, A., Silberberg, G., Helbig, D., Markram, H., Tsodyks, M., and Richardson, M. (2009). Multiquantal release underlies the distribution of synaptic efficacies in the neocortex. *Frontiers in Computational Neuroscience* 3. doi:10.3389/neuro.10.027.2009

London, M. and Häusser, M. (2005). Dendritic Computation. *Annual Review of Neuroscience* 28, 503–532. doi:10.1146/annurev.neuro.28.061604.135703

London, M., Roth, A., Beeren, L., Häusser, M., and Latham, P. E. (2010). Sensitivity to perturbations in vivo implies high noise and suggests rate coding in cortex. *Nature* 466, 123–127. doi:10.1038/nature09086

Luczak, A., Barthó, P., Marguet, S. L., Buzsáki, G., and Harris, K. D. (2007). Sequential structure of neocortical spontaneous activity in vivo. *Proceedings of the National Academy of Sciences* 104, 347–352. doi:10.1073/pnas.0605643104

Luczak, A., McNaughton, B. L., and Harris, K. D. (2015). Packet-based communication in the cortex. *Nature Reviews Neuroscience* 16, 745–755. doi:10.1038/nrn4026

MacLean, J. N., Watson, B. O., Aaron, G. B., and Yuste, R. (2005). Internal Dynamics Determine the Cortical Response to Thalamic Stimulation. *Neuron* 48, 811–823. doi:10.1016/j.neuron.2005.09.035

Mainen, Z. F. and Sejnowski, T. J. (1995). Reliability of spike timing in neocortical neurons. *Science* 268, 1503–1506. doi:10.1126/science.7770778

Markram, H., Lübke, Frotscher, Roth, and Sakmann (1997a). Physiology and anatomy of synaptic connections between thick tufted pyramidal neurones in the developing rat neocortex. *The Journal of Physiology* 500, 409–440. doi:10.1113/jphysiol.1997.sp022031

Markram, H., Lübke, J., Frotscher, M., and Sakmann, B. (1997b). Regulation of Synaptic Efficacy by Coincidence of Postsynaptic APs and EPSPs. *Science* 275, 213–215. doi:10.1126/science.275.5297.213

Markram, H., Muller, E., Ramaswamy, S., Reimann, M., Abdellah, M., Sanchez, C., et al. (2015). Reconstruction and Simulation of Neocortical Microcircuitry. *Cell* 163, 456–492. doi:10.1016/j.cell.2015.09.029

Masquelier, T. (2013). Neural variability, or lack thereof. *Frontiers in Computational Neuroscience* 7. doi:10.3389/fncom.2013.00007

Mendonça, P. R., Vargas-Caballero, M., Erdélyi, F., Szabó, G., Paulsen, O., and Robinson, H. P. (2016). Stochastic and deterministic dynamics of intrinsically irregular firing in cortical inhibitory interneurons. *eLife* 5, e16475. doi:10.7554/eLife.16475

Meyer, H. S., Wimmer, V. C., Hemberger, M., Bruno, R. M., Kock, D., P.j, C., et al. (2010). Cell Type–Specific Thalamic Innervation in a Column of Rat Vibrissal Cortex. *Cereb. Cortex* 20, 2287–2303. doi:10.1093/cercor/bhq069

Miller, J.-e. K., Ayzenshtat, I., Carrillo-Reid, L., and Yuste, R. (2014). Visual stimuli recruit intrinsically generated cortical ensembles. *PNAS* 111, E4053–E4061. doi:10.1073/pnas.1406077111

Mohajerani, M. H., Chan, A. W., Mohsenvand, M., LeDue, J., Liu, R., McVea, D. A., et al. (2013). Spontaneous cortical activity alternates between motifs defined by regional axonal projections. *Nature Neuroscience* 16, 1426–1435. doi:10.1038/nn.3499

Moreno-Bote, R. (2014). Poisson-Like Spiking in Circuits with Probabilistic Synapses. *PLOS Computational Biology* 10, e1003522. doi:10.1371/journal.pcbi.1003522

Moreno-Bote, R. and Drugowitsch, J. (2015). Causal Inference and Explaining Away in a Spiking Network. *Scientific Reports* 5, 17531. doi:10.1038/srep17531

Movshon, J. A. (2000). Reliability of Neuronal Responses. *Neuron* 27, 412–414. doi:10.1016/S0896-6273(00)00049-0

Muller, L., Chavane, F., Reynolds, J., and Sejnowski, T. J. (2018). Cortical travelling waves: mechanisms and computational principles. *Nature Reviews Neuroscience* 19, 255–268. doi:10.1038/nrn.2018.20

Munkres, J. R. (1984). *Elements of algebraic topology* (Addison-Wesley Publishing Company, Menlo Park, CA)

Musall, S., Kaufman, M. T., Gluf, S., and Churchland, A. K. (2018). Movement-related activity dominates cortex during sensory-guided decision making. *bioRxiv* , 308288doi:10.1101/308288

Newsome, W. T., Britten, K. H., and Movshon, J. A. (1989). Neuronal correlates of a perceptual decision. *Nature* 341, 52. doi:10.1038/341052a0

Niell, C. M. and Stryker, M. P. (2010). Modulation of Visual Responses by Behavioral State in Mouse Visual Cortex. *Neuron* 65, 472–479. doi:10.1016/j.neuron.2010.01.033

Nogueira, R., Lawrie, S., and Moreno-Bote, R. (2018). Neuronal Variability as a Proxy for Network State. *Trends in Neurosciences* 41, 170–173. doi:10.1016/j.tins.2018.02.003

Nolte, M., Reimann, M. W., King, J. G., Markram, H., and Muller, E. B. (2018). Cortical Reliability Amid Noise and Chaos. *bioRxiv* , 304121doi:10.1101/304121

Okun, M. and Lampl, I. (2008). Instantaneous correlation of excitation and inhibition during ongoing and sensory-evoked activities. *Nature Neuroscience* 11, 535–537. doi:10.1038/nn.2105

Okun, M., Steinmetz, N. A., Cossell, L., Iacaruso, M. F., Ko, H., Barthó, P., et al. (2015). Diverse coupling of neurons to populations in sensory cortex. *Nature* 521, 511–515. doi:10.1038/nature14273

Orbán, G., Berkes, P., Fiser, J., and Lengyel, M. (2016). Neural Variability and Sampling-Based Probabilistic Representations in the Visual Cortex. *Neuron* 92, 530–543. doi:10.1016/j.neuron.2016.09.038

Pachitariu, M., Lyamzin, D. R., Sahani, M., and Lesica, N. A. (2015). State-Dependent Population Coding in Primary Auditory Cortex. *Journal of Neuroscience* 35, 2058–2073. doi:10.1523/JNEUROSCI.3318-14.2015

Pajevic, S. and Plenz, D. (2012). The organization of strong links in complex networks. *Nat Phys* 8, 429–436. doi:10.1038/nphys2257

Palm, G., Aertsen, A. M. H. J., and Gerstein, G. L. (1988). On the significance of correlations among neuronal spike trains. *Biological Cybernetics* 59, 1–11. doi:10.1007/BF00336885

Pedregosa, F., Varoquaux, G., Gramfort, A., Michel, V., Thirion, B., Grisel, O., et al. (2011). Scikit-learn: Machine Learning in Python. *Journal of Machine Learning Research* 12, 2825–2830

Perin, R., Berger, T. K., and Markram, H. (2011). A synaptic organizing principle for cortical neuronal groups. *Proceedings of the National Academy of Sciences* 108, 5419–5424. doi:10.1073/pnas.1016051108

Peters, A. and Feldman, M. L. (1976). The projection of the lateral geniculate nucleus to area 17 of the rat cerebral cortex. I. General description. *Journal of Neurocytology* 5, 63–84. doi:10.1007/BF01176183

Petersen, R. S., Brambilla, M., Bale, M. R., Alenda, A., Panzeri, S., Montemurro, M. A., et al. (2008). Diverse and Temporally Precise Kinetic Feature Selectivity in the VPm Thalamic Nucleus. *Neuron* 60, 890–903. doi:10.1016/j.neuron.2008.09.041

Petersen, R. S., Panzeri, S., and Diamond, M. E. (2001). Population Coding of Stimulus Location in Rat Somatosensory Cortex. *Neuron* 32, 503–514. doi:10.1016/S0896-6273(01)00481-0

Petilla Interneuron Nomenclature Group, Ascoli, G. A., Alonso-Nanclares, L., Anderson, S. A., Barrionuevo, G., Benavides-Piccione, R., et al. (2008). Petilla terminology: nomenclature of features of GABAergic interneurons of the cerebral cortex. *Nature Reviews. Neuroscience* 9, 557–568. doi:10.1038/nrn2402

Petri, G., Expert, P., Turkheimer, F., Carhart-Harris, R., Nutt, D., Hellyer, P. J., et al. (2014). Homological scaffolds of brain functional networks. *Journal of The Royal Society Interface* 11, 20140873–20140873. doi:10.1098/rsif.2014.0873

Poulet, J. F. A., Fernandez, L. M. J., Crochet, S., and Petersen, C. C. H. (2012). Thalamic control of cortical states. *Nature Neuroscience* 15, 370–372. doi:10.1038/nn.3035

Priesemann, V., Wibral, M., Valderrama, M., Pröpper, R., Le Van Quyen, M., Geisel, T., et al. (2014). Spike avalanches in vivo suggest a driven, slightly subcritical brain state. *Frontiers in Systems Neuroscience* 8. doi:10.3389/fnsys.2014.00108

Rajan, K., Abbott, L. F., and Sompolinsky, H. (2010). Stimulus-dependent suppression of chaos in recurrent neural networks. *Physical Review E* 82, 011903. doi:10.1103/PhysRevE.82.011903

Rakic, P. (2009). Evolution of the neocortex: Perspective from developmental biology. *Nature reviews. Neuroscience* 10, 724–735. doi:10.1038/nrn2719

Ramaswamy, S., Courcol, J.-D., Abdellah, M., Adaszewski, S. R., Antille, N., Arsever, S., et al. (2015). The neocortical microcircuit collaboration portal: a resource for rat somatosensory cortex. *Front. Neural Circuits* 9. doi:10.3389/fncir.2015.00044

Ramón y Cajal, S. (1911). Histologie du Systeme Nerveux de l'Homme et des Vertebres. *Maloine (Paris)* 2, 891–942

Reich, S. and Rosenbaum, R. (2013). The impact of short term synaptic depression and stochastic vesicle dynamics on neuronal variability. *Journal of Computational Neuroscience* 35, 39–53. doi:10.1007/s10827-012-0438-0

Reimann, M. W., Gevaert, M., Shi, Y., Lu, H., Markram, H., and Muller, E. (2019). A null model of the mouse whole-neocortex micro-connectome. *bioRxiv* , 548735doi:10.1101/548735

Reimann, M. W., Horlemann, A.-L., Ramaswamy, S., Muller, E. B., and Markram, H. (2017a). Morphological Diversity Strongly Constrains Synaptic Connectivity and Plasticity. *Cerebral Cortex* 27, 4570–4585. doi:10.1093/cercor/bhx150

Reimann, M. W., King, J. G., Muller, E. B., Ramaswamy, S., and Markram, H. (2015). An algorithm to predict the connectome of neural microcircuits. *Frontiers in Computational Neuroscience* 9. doi:10.3389/fncom.2015.00120

Reimann, M. W., Nolte, M., Scolamiero, M., Turner, K., Perin, R., Chindemi, G., et al. (2017b). Cliques of Neurons Bound into Cavities Provide a Missing Link between Structure and Function. *Frontiers in Computational Neuroscience* 11. doi:10.3389/fncom.2017.00048

Reinagel, P. and Reid, R. C. (2000). Temporal Coding of Visual Information in the Thalamus. *The Journal of Neuroscience* 20, 5392–5400

Renart, A. and Machens, C. K. (2014). Variability in neural activity and behavior. *Current Opinion in Neurobiology* 25, 211–220. doi:10.1016/j.conb.2014.02.013

Renart, A., Rocha, J. d. l., Bartho, P., Hollender, L., Parga, N., Reyes, A., et al. (2010). The Asynchronous State in Cortical Circuits. *Science* 327, 587–590. doi:10.1126/science.1179850

Reyes-Puerta, V., Sun, J.-J., Kim, S., Kilb, W., and Luhmann, H. J. (2014). Laminar and Columnar Structure of Sensory-Evoked Multineuronal Spike Sequences in Adult Rat Barrel Cortex In Vivo. *Cerebral Cortex* , bhu007doi:10.1093/cercor/bhu007

Ribrault, C., Sekimoto, K., and Triller, A. (2011). From the stochasticity of molecular processes to the variability of synaptic transmission. *Nature Reviews. Neuroscience* 12, 375–387. doi:10.1038/nrn3025

Rieke, F., Warland, D., van Steveninck, R. d. R., and Bialek, W. (1997). *Spikes: Exploring the Neural Code* (Cambridge, Mass.; London: A Bradford Book)

Ritchie, M., Berthouze, L., House, T., and Kiss, I. Z. (2014). Higher-order structure and epidemic dynamics in clustered networks. *Journal of Theoretical Biology* 348, 21–32. doi:10.1016/j.jtbi.2014.01.025

Rockel, A. J., Hiorns, R. W., and Powell, T. P. (1980). The basic uniformity in structure of the neocortex. *Brain : a journal of neurology* 103, 221–244. doi:10.1093/brain/103.2.221

Rosenbaum, R., Smith, M. A., Kohn, A., Rubin, J. E., and Doiron, B. (2017). The spatial structure of correlated neuronal variability. *Nat Neurosci* 20, 107–114. doi:10.1038/nn.4433

Rozov, A., Burnashev, N., Sakmann, B., and Neher, E. (2001). Transmitter release modulation by intracellular Ca2+ buffers in facilitating and depressing nerve terminals of pyramidal cells in layer 2/3 of the rat neocortex indicates a target cell-specific difference in presynaptic calcium dynamics. *The Journal of Physiology* 531, 807–826. doi:10.1111/j.1469-7793.2001.0807h.x

Rubinov, M. and Sporns, O. (2010). Complex network measures of brain connectivity: Uses and interpretations. *NeuroImage* 52, 1059–1069. doi:10.1016/j.neuroimage.2009.10.003

Rudolph, S., Tsai, M.-C., von Gersdorff, H., and Wadiche, J. I. (2015). The ubiquitous nature of multivesicular release. *Trends in Neurosciences* 38, 428–438. doi:10.1016/j.tins.2015.05.008

Rössert, C., Pozzorini, C., Chindemi, G., Davison, A. P., Eroe, C., King, J., et al. (2016). Automated point-neuron simplification of data-driven microcircuit models. *arXiv:1604.00087 [q-bio]* ArXiv: 1604.00087

Sato, T., Nauhaus, I., and Carandini, M. (2012). Traveling Waves in Visual Cortex. *Neuron* 75, 218–229. doi:10.1016/j.neuron.2012.06.029

Savtchouk, I. and Volterra, A. (2018). Gliotransmission: Beyond Black-and-White. *Journal of Neuroscience* 38, 14–25. doi:10.1523/JNEUROSCI.0017-17.2017

Schiller, J., Major, G., Koester, H. J., and Schiller, Y. (2000). NMDA spikes in basal dendrites of cortical pyramidal neurons. *Nature* 404, 285–289. doi:10.1038/35005094

Schreiber, S., Fellous, J. M., Whitmer, D., Tiesinga, P., and Sejnowski, T. J. (2003). A new correlation-based measure of spike timing reliability. *Neurocomputing* 52–54, 925–931. doi:10.1016/S0925-2312(02)00838-X

Sedigh-Sarvestani, M., Vigeland, L., Fernandez-Lamo, I., Taylor, M. M., Palmer, L. A., and Contreras, D. (2017). Intracellular, In Vivo, Dynamics of Thalamocortical Synapses in Visual Cortex. *Journal of Neuroscience* 37, 5250–5262

Shadlen, M. N. and Newsome, W. T. (1994). Noise, neural codes and cortical organization. *Current Opinion in Neurobiology* 4, 569–579. doi:10.1016/0959-4388(94)90059-0

Shadlen, M. N. and Newsome, W. T. (1998). The Variable Discharge of Cortical Neurons: Implications for Connectivity, Computation, and Information Coding. *The Journal of Neuroscience* 18, 3870–3896

Shai, A. S., Koch, C., and Anastassiou, C. A. (2014). Spike-timing control by dendritic plateau potentials in the presence of synaptic barrages. *Frontiers in Computational Neuroscience* 8. doi:10.3389/fncom.2014.00089

Shepherd, G. M. G., Stepanyants, A., Bureau, I., Chklovskii, D., and Svoboda, K. (2005). Geometric and functional organization of cortical circuits. *Nature Neuroscience* 8, 782–790. doi:10.1038/nn1447

Shew, W. L., Yang, H., Petermann, T., Roy, R., and Plenz, D. (2009). Neuronal Avalanches Imply Maximum Dynamic Range in Cortical Networks at Criticality. *Journal of Neuroscience* 29, 15595–15600. doi:10.1523/JNEUROSCI.3864-09.2009

Silver, R. A., Lübke, J., Sakmann, B., and Feldmeyer, D. (2003). High-Probability Uniquantal Transmission at Excitatory Synapses in Barrel Cortex. *Science* 302, 1981–1984. doi:10.1126/science.1087160

Simonyan, K. and Zisserman, A. (2014). Very Deep Convolutional Networks for Large-Scale Image Recognition. *arXiv:1409.1556 [cs]* ArXiv: 1409.1556

Singh, C. and Levy, W. B. (2017). A consensus layer V pyramidal neuron can sustain interpulse-interval coding. *PLOS ONE* 12, e0180839. doi:10.1371/journal.pone.0180839

Softky, W. R. and Koch, C. (1992). Cortical Cells Should Fire Regularly, But Do Not. *Neural Computation* 4, 643–646. doi:10.1162/neco.1992.4.5.643

Softky, W. R. and Koch, C. (1993). The highly irregular firing of cortical cells is inconsistent with temporal integration of random EPSPs. *The Journal of Neuroscience* 13, 334–350

Song, S., Sjöström, P. J., Reigl, M., Nelson, S., and Chklovskii, D. B. (2005). Highly Nonrandom Features of Synaptic Connectivity in Local Cortical Circuits. *PLoS Biology* 3, e68. doi:10.1371/journal.pbio.0030068

Steinmetz, P. N., Manwani, A., Koch, C., London, M., and Segev, I. (2000). Subthreshold Voltage Noise Due to Channel Fluctuations in Active Neuronal Membranes. *Journal of Computational Neuroscience* 9, 133–148. doi:10.1023/A:1008967807741

Stepanyants, A. and Chklovskii, D. (2005). Neurogeometry and potential synaptic connectivity. *Trends in Neurosciences* 28, 387–394. doi:10.1016/j.tins.2005.05.006

Stern, E. A., Kincaid, A. E., and Wilson, C. J. (1997). Spontaneous Subthreshold Membrane Potential Fluctuations and Action Potential Variability of Rat Corticostriatal and Striatal Neurons In Vivo. *Journal of Neurophysiology* 77, 1697–1715

Stevens, C. F. and Zador, A. M. (1998). Input synchrony and the irregular firing of cortical neurons. *Nature Neuroscience* 1, 210–217. doi:10.1038/659

Stringer, C., Pachitariu, M., Steinmetz, N., Reddy, C. B., Carandini, M., and Harris, K. D. (2019). Spontaneous behaviors drive multidimensional, brainwide activity. *Science* 364, eaav7893. doi:10.1126/science.aav7893

Stringer, C., Pachitariu, M., Steinmetz, N. A., Okun, M., Bartho, P., Harris, K. D., et al. (2016). Inhibitory control of correlated intrinsic variability in cortical networks. *eLife* 5, e19695. doi:10.7554/eLife.19695

Sudhof, T. C. (2004). The synaptic vesicle cycle. *Annual Review of Neuroscience* 27, 509–547. doi:10.1146/annurev.neuro.26.041002.131412

Tchumatchenko, T., Malyshev, A., Wolf, F., and Volgushev, M. (2011). Ultrafast Population Encoding by Cortical Neurons. *Journal of Neuroscience* 31, 12171–12179. doi:10.1523/JNEUROSCI.2182-11.2011

Thorpe, S., Delorme, A., and Van Rullen, R. (2001). Spike-based strategies for rapid processing. *Neural Networks* 14, 715–725. doi:10.1016/S0893-6080(01)00083-1

Tolhurst, D. J., Movshon, J. A., and Dean, A. F. (1983). The statistical reliability of signals in single neurons in cat and monkey visual cortex. *Vision Research* 23, 775–785. doi:10.1016/0042-6989(83)90200-6

Tsodyks, M. V. and Markram, H. (1997). The neural code between neocortical pyramidal neurons depends on neurotransmitter release probability. *Proceedings of the National Academy of Sciences* 94, 719–723

Van Geit, W., Gevaert, M., Chindemi, G., Rössert, C., Courcol, J.-D., Muller, E. B., et al. (2016). BluePyOpt: Leveraging Open Source Software and Cloud Infrastructure to Optimise Model Parameters in Neuroscience. *Frontiers in Neuroinformatics* 10. doi:10.3389/fninf.2016.00017

van Vreeswijk, C. and Sompolinsky, H. (1996). Chaos in Neuronal Networks with Balanced Excitatory and Inhibitory Activity. *Science* 274, 1724–1726. doi:10.1126/science.274.5293.1724

van Vreeswijk, C. and Sompolinsky, H. (1998). Chaotic Balanced State in a Model of Cortical Circuits. *Neural Computation* 10, 1321–1371. doi:10.1162/089976698300017214

VanRullen, R. and Thorpe, S. J. (2002). Surfing a spike wave down the ventral stream. *Vision Research* 42, 2593–2615. doi:10.1016/S0042-6989(02)00298-5

Varshney, L. R., Chen, B. L., Paniagua, E., Hall, D. H., and Chklovskii, D. B. (2011). Structural Properties of the Caenorhabditis elegans Neuronal Network. *PLoS Computational Biology* 7, e1001066. doi:10.1371/journal.pcbi.1001066

Vogels, T. P., Rajan, K., and Abbott, L. F. (2005). Neural Network Dynamics. *Annual Review of Neuroscience* 28, 357–376. doi:10.1146/annurev.neuro.28.061604.135637

Vogels, T. P., Sprekeler, H., Zenke, F., Clopath, C., and Gerstner, W. (2011). Inhibitory Plasticity Balances Excitation and Inhibition in Sensory Pathways and Memory Networks. *Science* 334, 1569–1573. doi:10.1126/science.1211095

Vreeswijk, C. v. and Sompolinsky, H. (1998). Chaotic Balanced State in a Model of Cortical Circuits. *Neural Computation* 10, 1321–1371. doi:10.1162/089976698300017214

Walton, M. E., Bannerman, D. M., and Rushworth, M. F. S. (2002). The Role of Rat Medial Frontal Cortex in Effort-Based Decision Making. *Journal of Neuroscience* 22, 10996–11003. doi:10.1523/JNEUROSCI.22-24-10996.2002

Wang, H.-P., Spencer, D., Fellous, J.-M., and Sejnowski, T. J. (2010). Synchrony of Thalamocortical Inputs Maximizes Cortical Reliability. *Science* 328, 106–109. doi:10.1126/science.1183108

Whishaw, I. Q. and Kolb, B. (1985). The mating movements of male decorticate rats: Evidence for subcortically generated movements by the male but regulation of approaches by the female. *Behavioural Brain Research* 17, 171–191. doi:10.1016/0166-4328(85)90042-7

Willshaw, D. J., Buneman, O. P., and Longuet-Higgins, H. C. (1969). Non-holographic associative memory. *Nature* 222, 960–962

Wilson, D. E., Whitney, D. E., Scholl, B., and Fitzpatrick, D. (2016). Orientation selectivity and the functional clustering of synaptic inputs in primary visual cortex. *Nature Neuroscience* 19, 1003–1009. doi:10.1038/nn.4323

Wilting, J., Dehning, J., Neto, J. P., Rudelt, L., Wibral, M., Zierenberg, J., et al. (2018). Dynamic Adaptive Computation: Tuning network states to task requirements. *arXiv:1809.07550 [nlin, q-bio]* ArXiv: 1809.07550

Max Nolte - CV

Blue Brain Project, Ch. des Mines 9, 1202 Geneva, Switzerland • +41 21 69 37609 • max.nolte@epfl.ch

EDUCATION

École polytechnique fédérale de Lausanne, Switzerland — 2014 – 2019
PhD Program in Neuroscience

The University of Edinburgh, UK — 2010 – 2014
MPhys Computational Physics
First Class Honours

University of Washington, USA — 2012 – 2013
Exchange year, Physics

Gymnasium Theodorianum Paderborn, Germany; Abitur — 2009

SUMMER SCHOOLS

- **Advanced Scientific Programming in Python 2018**, Italy
- **Summer Workshop on the Dynamic Brain 2016**, USA

RESEARCH & WORK EXPERIENCE

Blue Brain Project, EPFL, Switzerland — since 09/2014
PhD student; supervisors: Prof. Henry Markram & Dr. Eilif B. Muller

Particle Physics Experiment Group, The University of Edinburgh, UK — 09/2013 – 03/2014
Master project student; supervisor: Dr. Robert Harrington

Theoretical Electrical Engineering Group, Universität Paderborn, Germany — 08/2013 – 09/2013
Computational Nanophotonics Group, Universität Paderborn, Germany — 07/2012 – 08/2012
Summer research student; supervisor: Prof. Jens Förstner

Centre International d'Antibes, France — 06/2010 – 08/2010
Work exchange program in language school

Stephanushaus Borchen, Germany — 07/2009 – 03/2010
Zivildienst (civilian service)

TEACHING EXPERIENCE

- **General Physics I**, TA with Prof. Rolf Gruetter, EPFL
  Autumn semesters 2015/16, 2016/17 & 2017/18

- **Numerical Analysis**, TA with Dr. Simone Déparis, EPFL
  Spring semester 2014/15

PREPRINTS

1. **Nolte M**, Reimann MW, King JG, Markram H & Muller EB (2018). Cortical Reliability Amid Noise and Chaos. bioRxiv preprint bioRxiv:304121 (under review)
2. Rössert C, Pozzorini C, […], **Nolte M**, [...] & Gewaltig MO (2016). Automated point-neuron simplification of data-driven microcircuit models. arXiv preprint arXiv:1604.00087. (under review)

PUBLICATIONS

1. Reimann MW*, **Nolte M***, […] & Markram H (2017). Cliques of Neurons Bound into Cavities Provide a Missing Link between Structure and Function. Frontiers in Computational Neuroscience. 11:48. (***equal contribution**)
2. Markram H, [...], **Nolte M**, [...] & Schürmann F (2015). Reconstruction and simulation of neocortical microcircuitry. Cell, 163(2), 456-492.

SELECTED TALKS & POSTER PRESENTATIONS

- Poster: **Nolte M**, Reimann MW, Markram H, Muller EB. Neocortical circuitry supports spike-time reliability amid noise and chaos. **ELSC retreat**, Israel, February 2019.
- Talk: Cortical reliability amid noise and chaos, **1st Young Swiss Society for Neuroscience Meeting**, Geneva, January 2019
- Talk: Cortical reliability amid noise and chaos, **Allen Institute for Brain Science**, internal seminar, Seattle, July 2018
- Poster: **Nolte M**, Reimann MW, Muller EB, Markram H. Cortical reliability amid noise and chaos. **CNS 2018**, Seattle, USA. ***Student poster presentation award**
- Poster: **Nolte M**, Reimann MW, Hess K, Markram H, Muller EB. Reducing higher order connectivity in a model of neocortical microcircuitry: a comparative study. **Workshop on Topology and Neuroscience 2018**, EPFL, Lausanne, Switzerland.
- Poster: **Nolte M**, Reimann MW, Muller EB, Markram H. Cellular noise amplified by chaotic network dynamics drives high intrinsic variability in cortex. **COSYNE 2018**, Denver, USA.
- Talk: Cliques of neurons bound into cavities provide a missing link between structure and function (joint presentation with M. Reimann), **Applied Algebraic Topology**, contributed talk, Hokkaido University, August 2017
- Poster: **Nolte M**, Reimann MW, Muller EB, Markram H. Deciphering neural variability within a neocortical microcircuit. **COSYNE 2017**, Salt Lake City, USA.
- Poster: Sedigh-Sarvestani M, **Nolte M**, Mardoum P. Population coupling in the mouse visual cortex. **COSYNE 2017**, Salt Lake City, USA. (joint presentation)
- Poster: **Nolte M**, Reimann MW, Muller EB, Markram H. Limits of temporal encoding of thalamic inputs in a neocortical microcircuit. **CNS 2016**, Jeju Island, South Korea.

AWARDS

- Class Medal, MPhys Computational Physics 2013/2014
- COSYNE 2017 New Attendee Travel Grant
- CNS 2018 Student Poster Presentation Award

ORGANIZATIONS

- Society for Neuroscience
- Organization for Computational Neurosciences
- Swiss Society for Neuroscience

SKILLS

- Languages: English (fluent), German (native), French (conversational)
- Software: MacOS/Windows/Linux, Microsoft Office, Adobe Illustrator, LaTeX
- Programming languages: Python (excellent), C/C++/Fortran/Java/Matlab (experienced)

REFERENCES

Prof. Henry Markram (PhD supervisor)
henry.markram@epfl.ch
+41 21 69 39536
Professor, Blue Brain Project &
Laboratory for Neural Microcircuits,
EPFL

Prof. Kathryn Hess (collaborator)
kathryn.hess@epfl.ch
+41 21 69 34245
Professor, Laboratory for
Topology and Neuroscience,
EPFL

Dr. Eilif B. Muller (PhD co-supervisor)
Element AI, Montreal, Canada

Ce document a été imprimé au Centre d'impression EPFL,
imprimerie climatiquement neutre, certifiée myClimate.